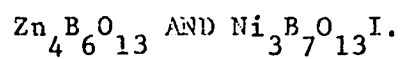


A LIGHT SCATTERING STUDY OF THE BORATES



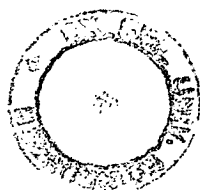
ALAN FRASER MURRAY

THESIS SUBMITTED FOR THE DEGREE OF

DOCTOR OF PHILOSOPHY

UNIVERSITY OF EDINBURGH

JUNE 1978





***I am a Bear of Very Little Brain,  
and long words Bother me.***

***A.A.Milne***

***Winnie-the-Pooh***

The research described in this thesis was the unaided work of the author, unless otherwise indicated. Where the research was done in collaboration with others, there was a significant contribution by the author.

## ACKNOWLEDGEMENTS

The preparation of this work would have been less of a pleasure, more of a chore, and probably impossible were it not for the presence of a large number of people. I would like to express my deepest thanks: to Professor R.A. Cowley, F.R.S. and Dr. W. Taylor for their supervision and encouragement;

to Drs. J.W. Arthur, A.D. Bruce and D.J. Lockwood for their collaboration at various stages;

to Drs. K.C. Bowler, H. Montgomery and R.J. Nelmes for their oft-needed advice;

to Mr. H. Vass for his technical assistance;

to all members of the Physics Department whose friendship made life pleasant;

to my wife, Glynis, for support and much more, and for proof-reading this work;

to my parents and parents-in-law, for their encouragement, and to Mrs. R.W. Chester, who bravely undertook the typing of this thesis;

to the almost-human EMAS computer system;

to the Science Research Council for financial support.

Finally I would like to thank Professor W. Cochran for his encouragement, and for the facilities of the Physics Department.

## ABSTRACT

This work describes a light scattering study of two crystalline borates, a system for automated Brillouin spectroscopy, and a theoretical investigation of incommensurate-commensurate transitions.

Firstly, the Raman spectrum of zinc metaborate ( $\text{Zn}_4\text{B}_6\text{O}_{13}$ ) is reported and discussed, and a tentative assignment is made of vibrations of the B-O framework. An interference feature in the spectrum is analysed in terms of models involving anharmonic phonon-phonon and phonon-continuum coupling.

The inelastic and elastic light scattering spectrum of nickel-iodine boracite ( $\text{Ni}_3\text{B}_7\text{O}_{13}\text{I}$ ) is presented for the first time, at temperatures between 6K and 295K. Anomalies in the phonon lifetimes and frequencies at 130K are correlated with concomitant abnormalities in the structural, elastic and magnetoelectric properties, but a structural transition at this temperature is not indicated. The dynamics of the improper paraelectric-ferroelectric transition at 68K are discussed, and possible symmetries considered. Furthermore, the data reveals a new transition at 7K, which is thought to be both structural and magnetic. Critical modes are studied, and a strongly temperature dependent mode is identified, whose behaviour cannot be fully explained.

A proven modular approach to computer control of experiments is presented, and a system for control of Brillouin scattering experiments is described. Examples of the resultant spectra are presented, along with some speculation as to future developments.

Finally, the theory of incommensurate-commensurate lock-in transitions has been studied, and the method and conclusions are detailed.

Two distinct types of lock-in transition are identified, and the corresponding distortion profiles are derived, within a simple Landau theory.

TABLE OF CONTENTS

	Page
<u>CHAPTER 1</u> <u>BASIC THEORETICAL AND EXPERIMENTAL CONSIDERATIONS</u>	1
Section 1.1 The Scattering Cross-section . . . . .	3
1.2 Normal Modes of a Crystal . . . . .	7
1.3 Symmetry Classification of the Normal Modes . . . . .	11
1.4 Selection Rules for First Order Raman Scattering . . . . .	13
1.5 Greens Functions and Raman Scattering . . . . .	15
1.6 Experimental Techniques . . . . .	22
<u>CHAPTER 2</u> <u>A RAMAN SPECTRAL STUDY OF ZINC METABORATE</u>	24
Introduction . . . . .	24
2.1 Symmetry Considerations . . . . .	24
2.2 Experimental Details . . . . .	27
2.3 Description of Spectra . . . . .	28
2.4 Molecular Potential Calculations for $XY_4$ Molecules . . . . .	31
2.5 Symmetry Conclusions . . . . .	37
2.6 The Coupled Modes Model . . . . .	38
2.7 The Fano Model . . . . .	42
2.8 Comparison with Experiment . . . . .	46
2.9 Conclusions . . . . .	48
<u>CHAPTER 3</u> <u>THE PECULIAR PARAELECTRIC PHASE OF NICKEL-IODINE BORACITE</u>	50
Introduction to Boracite Properties . . . . .	50
3.1 Properties of Cubic Ni-I . . . . .	52
3.2 Experiment . . . . .	54
3.3 Group Theory and Description of Spectra . . . . .	56
3.4 Analysis of Results . . . . .	59
3.5 Symmetry Classification of the Modes . . . . .	61
3.6 Temperature Dependence of the Modes . . . . .	65
3.7 Conclusions . . . . .	69

TABLE OF CONTENTS (Contd.)

	Page
<u>CHAPTER 4</u> <u>PHASE TRANSITIONS IN NICKEL-IODINE BORACITE</u>	71
Introduction . . . . .	71
4.1 Landau Theory and Improper Ferroelectrics . . . . .	72
4.2 The Known Transition Properties of Ni-I . . . . .	78
4.3 Experiment . . . . .	79
4.4 Presentation of Results and Analysis . . . . .	80
4.5 Symmetry Considerations . . . . .	84
4.6 Structural Information in the Raman Spectra . . . . .	93
4.7 Magnetism in Ni-I . . . . .	99
4.8 Soft Modes in Ni-I . . . . .	101
4.9 Conclusions . . . . .	104
 <u>CHAPTER 5</u> <u>A COMPUTER CONTROLLED SYSTEM FOR BRILLOUIN SPECTROSCOPY</u>	 106
Introduction . . . . .	106
5.1 The Ability of the Computer . . . . .	109
5.2 Multiplexing and Demultiplexing . . . . .	111
5.3 The Requirements of the Interferometer . . . . .	114
5.4 Interfacing the Computer to the Interferometer . . . . .	116
5.5 The Interferometer Modules . . . . .	119
5.6 The Control Programme . . . . .	122
5.7 Results . . . . .	123
5.8 Conclusions and Speculation . . . . .	125
 <u>CHAPTER 6</u> <u>INCOMMENSURATE - COMMENSURATE TRANSITIONS:</u>	
<u>A THEORETICAL STUDY</u>	127
Introduction . . . . .	127
6.1 Incommensurate Transitions: A definition . . . . .	127
6.2 Type I Transitions . . . . .	134
6.3 Type II Transitions . . . . .	140
6.4 Conclusions . . . . .	146



TABLE OF CONTENTS (Contd.)

	Page
<u>APPENDIX 1</u> <u>PERTURBATION THEORY AND THE ANHARMONIC GREENS FUNCTION</u>	148
<u>APPENDIX 2</u> <u>TABLES</u>	152
<u>APPENDIX 3</u> <u>CIRCUIT DIAGRAMS FOR THE BRILLOUIN SYSTEM</u>	159
<u>REFERENCES</u>	160
<u>APPENDIX 4</u> <u>PUBLICATIONS</u>	165

CHAPTER 1

BASIC THEORETICAL AND EXPERIMENTAL CONSIDERATIONS

The Raman effect is the inelastic scattering of electromagnetic radiation by matter, giving rise to a change of frequency. It was first reported by Raman in 1928 (1) as a new phenomenon, distinct from fluorescence, although the possibility of such a process had been theoretically envisaged (2). Raman first observed the scattering of filtered sunlight, from  $\text{CCl}_4$ , photographically. The effect is very weak, and it became necessary to use arc lamps to increase the usefulness of the technique as a probe of excitation spectra. Photographic detection techniques have now been almost universally superseded by photoelectric methods, but by far the biggest single advance in the technology of Raman scattering came with the advent of the laser (3) as a source of radiation.

The quantum mechanical theory of the Raman effect was first discussed in detail by Plazcek (4). In this treatment, the Raman scattered light was considered as the electric dipole radiation from an oscillating dipole. The incident radiation was introduced as a quantum mechanical perturbation. The discussion in §1.1 of the scattering cross-section follows a similar approach, but uses the results of second order, time dependent perturbation theory, and the formalism surrounding the quantisation of the radiation field.

Raman scattering from crystals was first investigated in 1928 (5), very soon after the original experiments. Since then it has proved a valuable tool for probing the normal mode frequency spectrum (phonon scattering), as well as scattering from other types of excitation (e.g. magnetic and electronic). Most of the available published

Raman spectra of solids were measured in the past 15 years, since the laser revolutionised Raman spectroscopy.

It is the intention of this chapter to outline the theoretical calculations relevant to the ensuing chapters, and to describe the experimental equipment used for the bulk of the work therein. There are basically two types of information to be extracted from a Raman spectrum. Firstly, one can make certain assertions about vibrational symmetries in the crystal, and secondly, one can study the interactions between excitations. These considerations can, in many cases, give clues as to why a system exists in a given state at a given point in phase space.

In §1.1 the form of the cross-section for Raman scattering from crystals is derived, giving a general expression which may be further manipulated. In §1.2, a familiar lattice dynamical calculation is presented (in the harmonic approximation) leading to the concept of a phonon. This much-documented calculation is reproduced here for completeness' sake, and also to define the notation of the rest of the chapter, which is in some places not standard to avoid confusion. In §1.3 and §1.4, an attempt is made to discuss the physics behind the classification of phonon symmetries, using some (unproved) results of formal group theory.

The introduction of some aspects of many-body theory in §1.5 and Appendix 1 may seem like using a sledgehammer to crack a nut. It is, however, useful to review the particular aspects of Greens function theory relevant to Raman scattering lineshapes, as this connection is often obscured in a more general treatment. In short, the calculations presented can all be found elsewhere, but are collected here to define the vocabulary and notation of this work.

Finally, in §1.6, the requirements of a successful Raman experiment are detailed, and the choice of equipment described and justified.

### §1.1 The Scattering Cross-section

Fermi's Golden Rule of perturbation theory, applied in first and second order, gives the probability/unit time of transitions from a state  $|\alpha\rangle$  to a state  $|\beta\rangle$  of any system as (6)

$$1.1 \quad R_{\alpha\beta} = \frac{2\pi}{\hbar} \left| \langle \beta | H_I | \alpha \rangle - \sum_{\gamma} \frac{\langle \beta | H_I | \gamma \rangle \langle \gamma | H_I | \alpha \rangle}{E_{\gamma}^0 - E_{\alpha}^0} \right|^2 \times \delta(E_{\beta}^0 - E_{\alpha}^0)$$

where the Hamiltonian of the system can be written as

$$1.2 \quad H = H_0 + H_I(t).$$

The  $\{E_{\delta}^0\}$  are the energy eigenvalues of the Schrödinger equation,  $H_0 |\delta\rangle = E_{\delta}^0 |\delta\rangle$  and  $H_I(t)$  is a small time dependent perturbation. Expressing the eigenstates  $\{|\delta\rangle\}$  as the direct products of the crystal eigenstates  $\{|D\rangle\}$  and the second quantisation representation photon field state vectors  $\{|d_1, d_2, d_3 \dots\rangle\}$ , written in shorthand form  $\{|d\rangle\}$ , we have

$$1.3 \quad R_{\alpha\beta} = \frac{2\pi}{\hbar} \left| \langle B | \langle b | H_I | a \rangle | A \rangle - \sum_{Gg} \frac{\langle B | \langle b | H_I | g \rangle | G \rangle \langle G | \langle g | H_I | a \rangle | A \rangle}{E_{Gg}^0 - E_{Aa}^0} \right|^2 \times \delta(E_{Bb}^0 - E_{Aa}^0).$$

The quantum numbers  $d_1, d_2$  etc. represent the number of photons of type 1, 2 etc.

Now the interaction energy between a dipole moment  $\underline{M}$  and an electric field  $\underline{E}$  is  $-\underline{M} \cdot \underline{E}$ . It is fruitful to express the operator of the electric field in terms of the photon creation and annihilation operators  $b^*$  and  $b$  (7).

$$1.4 \quad \underline{E}(\underline{r}, t) = \sum_n i \left( \frac{\hbar \omega_n}{2 \epsilon_0 V} \right)^{\frac{1}{2}} (b_n(t) - b_n^*(t)) \hat{\epsilon}_n .$$

The quantities  $\hat{\epsilon}_n$  and  $\omega_n$  are the polarisation and frequency, respectively, of a photon of wavevector  $\underline{k}_n$  and  $V$  is a box normalisation constant. The operators  $b_n$ ,  $b_n^*$  have the properties

$$1.5 \quad b_n |d\rangle = \sqrt{d_n} |d_1, \dots, d_n - 1, \dots\rangle \exp i (\underline{k}_n \cdot \underline{r} - \omega_n t)$$

$$1.6 \quad b_n^* |d\rangle = \sqrt{d_n + 1} |d_1, \dots, d_n + 1, \dots\rangle \exp -i (\underline{k}_n \cdot \underline{r} - \omega_n t) .$$

For first order Raman scattering, the transition is between states  $|d_i, d_f\rangle$  and  $|d_i \pm 1, d_f \mp 1\rangle$  with all other  $d$ 's unchanged and the first term in the modulus of 1.3 is zero. Thus the transition rate may be written

$$1.7 \quad R_{\alpha\beta} = \frac{\hbar \pi \omega_i \omega_f}{2 \epsilon_0^2 V^2} \left| \sum_{Gkl} \frac{\langle B | \langle a_i - 1, a_f + 1 | M_k b_i \hat{\epsilon}_{ik} | a_i, a_f + 1 \rangle | G \rangle}{\times \frac{\langle G | \langle a_i, a_f + 1 | M_l b_f^* \hat{\epsilon}_{fl} | a_i, a_f \rangle | A \rangle}{E_{GA}^0 + \hbar \omega_f}} + \frac{\langle B | \langle a_i - 1, a_f + 1 | M_k b_f^* \hat{\epsilon}_{fk} | a_i - 1, a_f \rangle | G \rangle}{\times \frac{\langle G | \langle a_i - 1, a_f | M_l b_i \hat{\epsilon}_{il} | a_i, a_f \rangle | A \rangle}{E_{GB}^0 - \hbar \omega_f}} \right|^2 \times \delta(E_{Bb}^0 - E_{Aa}^0) .$$

This is the expression describing a process in which a photon of frequency  $\omega_i$  is scattered to produce a photon  $\omega_f$ . This is a two-stage process, and the two terms in the modulus of 1.7 are represented schematically in Figures 1a and 1b. When  $\omega_i > \omega_f$  we have Stokes scattering, and when  $\omega_i < \omega_f$ , Antistokes scattering, as shown in Figure 2. Also defined are the Cartesian labels  $k, \ell$  and

$$1.8 \quad E_{DA}^O = E_D^O - E_A^O = \hbar\omega_{DA} .$$

Using 1.5 and 1.6, and defining the transition polarisability  $P$

$$1.9 \quad P_{k\ell}^{if}(BA) = \sum_G \left\{ \frac{\langle B | M_k | G \rangle \langle G | M_\ell | A \rangle}{\hbar(\omega_{GA} + \omega_f)} + \frac{\langle B | M_\ell | G \rangle \langle G | M_k | A \rangle}{\hbar(\omega_{GB} - \omega_f)} \right\}$$

equation 1.7 becomes

$$1.10 \quad R_{\alpha\beta} = \frac{\hbar \pi \omega_i \omega_f a_i (a_i + 1)}{2 \epsilon_0^2 v^2} \sum_{k\ell mn} P_{k\ell}^{if}(BA) \overline{P}_{mn}^{if}(AB) \times \hat{\epsilon}_{ik} \hat{\epsilon}_{f\ell} \hat{\epsilon}_{im} \hat{\epsilon}_{fn} \delta(\omega_{BA} + \omega_f - \omega_i) .$$

Now  $a_i$  can be written as (per unit volume)

$$1.11 \quad \frac{a_i}{V} = \frac{\epsilon_0 E^2}{2} \div \hbar\omega_i$$

and if  $a_f = 0$  initially, the intensity of scattering to a group of frequencies around  $\omega_f$  described by  $\rho(\omega_f)$  is given by

FIGURE 1: Schematic representation of the first(1a) and second(1b) terms of equation 1.7. The broad arrow represents the radiation field.

FIGURE 2: Energy levels in first order normal Raman scattering processes.

FIG.1a

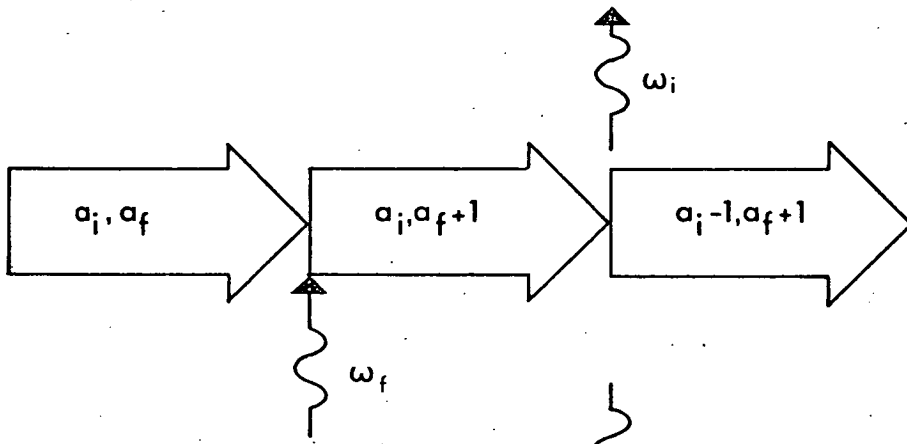


FIG.1b

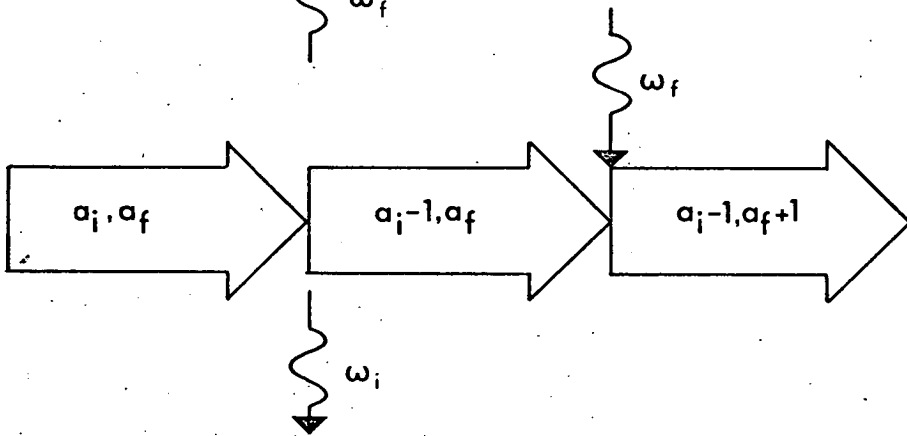
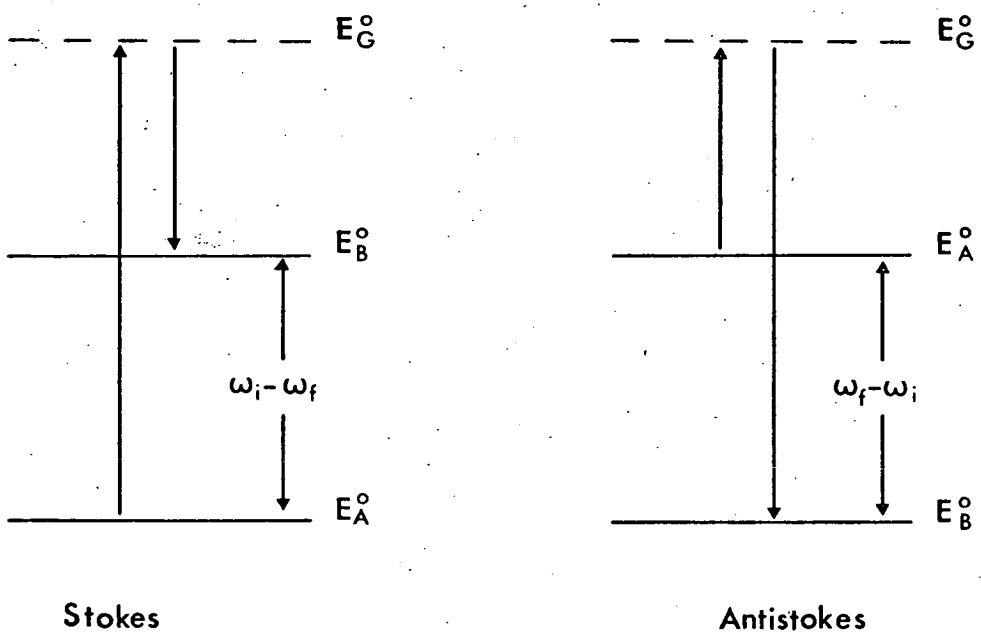


FIG.2





$$\begin{aligned}
 1.12 \quad I d\omega_f d\Omega &= \frac{\omega_f^4}{32\pi^2 c^3 \epsilon_0} \sum_{Aklmn} P_{kl}^{if}(BA) \bar{P}_{mn}^{if}(AB) E_k E_m \hat{\epsilon}_f \hat{\epsilon}_f \\
 &\times \frac{\exp(-\beta E_A)}{Z} \\
 &\times \delta(\omega_{BA} + \omega_f - \omega_i)
 \end{aligned}$$

Now,  $E_k, E_m$  are the  $k$  and  $m$  components of the incident radiation field strength, and  $Z$  the partition function ( $\beta = 1/kT$ ). 1.12 represents the total Raman scattering intensity of frequency  $\omega_f$  into an element of solid angle  $d\Omega (= \sin\theta d\theta d\phi)$  with a general input field polarisation  $\underline{E} = (E_k, E_m, 0)$ . The sum over (weighted) states  $\{|A\rangle\}$  constitutes a thermal average, and the  $\delta$ -function defines  $|B\rangle$  uniquely. The symmetry properties and the quantum mechanical definition of the terms  $P_{kl}^{if}(BA)$  are exploited in §1.4 and §1.5. In the standard notation  $a(bc)d$  used to describe a Raman experiment, (a) and (d) denote the direction of the incident and scattered light, and (b c) describe the respective polarisations, given by  $\hat{\epsilon}_i$  and  $\hat{\epsilon}_f$ .

## §1.2 Normal Modes of a Crystal

This brief discussion follows the arguments of Born and Huang (8) in analysing the internal oscillations of a crystal in terms of a set of uncoupled 'normal modes' (in the harmonic approximation). Although this calculation is now commonplace, its inclusion here is useful to define the notation and terminology of §1.3 and §1.4. It

is also necessary to provide the link between the classical description of lattice vibrations and the quantum mechanical formalism of §1.5.

The Hamiltonian of the crystal, in the harmonic approximation, may be written in terms of the momenta  $\{p_i\}$  and displacements from equilibrium positions  $\{q_i\}$  of the  $N$  atoms as:-

$$1.13 \quad H = \sum_{i=1}^N \frac{p_i^2}{2m_i} + \frac{1}{2} \sum_{i,j=1}^N q_i \cdot \phi_{ij} \cdot q_j$$

With the simple rescaling given by

$$1.14 \quad \underline{w}_i = \sqrt{m_i} q_i ; \quad \underline{\phi}_{ij} = \phi_{ij} \div \sqrt{m_i m_j}$$

and the use of the canonical equation (9)

$$1.15 \quad \dot{p}_{i\ell} = - \frac{\partial H}{\partial q_{i\ell}}$$

the equation of motion is given by

$$1.16 \quad \ddot{w}_{i\ell} = - \sum_{jm} \phi_{i\ell jm} w_{jm} \quad (\ell, m \text{ are Cartesian labels})$$

$\underline{\phi}$  is called the dynamical matrix and contains all the information about the interatomic interactions in the harmonic approximation. It transpires that a further transformation to 'normal co-ordinates' renders  $\underline{\phi}$  diagonal and thus decouples the oscillations. To this end, define firstly Fourier co-ordinates  $\{Q_{\underline{y}i\ell}\}$  :

$$1.17 \quad Q_{\underline{y}i\ell} = \frac{1}{\sqrt{N}} \sum_{\underline{I}} w_{\underline{I}i\ell} \exp(-i\underline{y} \cdot \underline{I})$$

$$1.18 \quad W_{\underline{I}i\ell} = \frac{1}{\sqrt{N}} \sum_{\underline{y}} Q_{\underline{y}i\ell} \exp(i\underline{y} \cdot \underline{I})$$

The quantity  $W_{\underline{I}i\ell}$  is now the mass weighted displacement of the  $i$ -th atom of the unit cell of origin  $\underline{I}$ . With this definition 1.16 becomes

$$1.19 \quad \ddot{Q}_{\underline{y}i\ell} = - \sum_{\underline{j}m} D_{i\ell\underline{j}m}(\underline{y}) Q_{\underline{y}jm}$$

$$1.20 \quad \left[ D_{i\ell\underline{j}m}(\underline{y}) = \sum_{\underline{J}} \Phi_{\underline{I}i\ell\underline{J}m} \exp i\underline{y} \cdot (\underline{J} - \underline{I}) \right]$$

We have thus block-diagonalised  $\underline{\Phi}$  to a set of Hermitean matrices  $\underline{D}$  which are  $3r \times 3r$  where  $r =$  number of atoms/primitive cell. A Hermitean matrix has a set of orthonormal complex eigenvectors  $\{\underline{\epsilon}_a\}$  with corresponding real eigenvalues  $\{\omega_a^2\}$ , i.e.

$$1.21 \quad \sum_{\underline{j}m} D_{i\ell\underline{j}m}(\underline{y}) \epsilon_a(\underline{j}m\underline{y}) = \omega_a^2(\underline{y}) \epsilon_a(i\ell\underline{y})$$

We can define complex normal co-ordinates from the Fourier co-ordinates  $\{Q_{\underline{y}i\ell}\}$  by:

$$1.22 \quad Q_{\underline{y}a} = \sum_{i\ell} \epsilon_a^*(i\ell\underline{y}) Q_{\underline{y}i\ell}; Q_{\underline{y}i\ell} = \sum_a \epsilon_a(i\ell\underline{y}) Q_{\underline{y}a}$$

whereupon 1.19 becomes

$$1.23 \quad \ddot{Q}_{\underline{y}a} = -\omega_a^2(\underline{y}) Q_{\underline{y}a}$$

This is the equation of motion for the displacement from equilibrium of a simple harmonic oscillator of frequency  $\omega_a(\underline{y})$ . The equation 1.16 describing 3N coupled oscillators has been decoupled to give 1.23 for a set of 3N uncoupled oscillators.

The transition from the purely classical discussion leading to 1.22 into quantum mechanical operator notation is achieved by writing the normal coordinate  $Q_{\underline{y}a}$  as a Hermitean operator  $Q_{\underline{y}a}$  and defining new operators  $b_{\underline{y}a}, b_{-\underline{y}a}^*$  by (10)

$$1.24 \quad Q_{\underline{y}a} = \left( \frac{\hbar}{2\omega_a(\underline{y})} \right)^{\frac{1}{2}} (b_{\underline{y}a} + b_{-\underline{y}a}^*)$$

$$1.25 \quad P_{\underline{y}a} = i \left( \frac{\hbar\omega_a(\underline{y})}{2} \right)^{\frac{1}{2}} (b_{\underline{y}a} - b_{-\underline{y}a}^*)$$

where  $P_{\underline{y}a}$  is the conjugate momentum to  $Q_{\underline{y}a}$ . From the classical Poisson brackets (11)

$$\{Q_{\underline{y}a}, P_{\underline{y}'b}\} = \delta(\underline{y} - \underline{y}')\delta_{ab} \quad \text{and}$$

$$\{Q_{\underline{y}a}, Q_{\underline{y}'b}\} = 0$$

$b$  and  $b^*$  can be shown to have the commutation relations

$$1.26a \quad [b_{\underline{y}a}, b_{\underline{y}'b}^*] = \delta(\underline{y} - \underline{y}')\delta_{ab}$$

$$1.26b \quad [b_{\underline{y}a}, b_{\underline{y}'b}] = [b_{\underline{y}a}^*, b_{\underline{y}'b}^*] = 0$$

and are therefore boson creation and annihilation operators respectively. The bosons in question are the quanta of the lattice vibration 'field',

called PHONONS, which are respectively created or annihilated in Stokes and Antistokes Raman experiments.

Footnote to §1.2

Although  $\underline{y}$  is used as the symbol for phonon wavevector throughout this chapter (to avoid confusion with displacement  $\underline{q}$ ), the letter  $\underline{q}$  is conventionally used for wavevector. This latter convention is adopted for the rest of this thesis.

### §1.3 Symmetry Classification of the Normal Modes

The literature of group theory is profuse, and the application of group theoretical methods to crystal vibration theory is also well documented (e.g. (12)). The purpose of this section is to emphasize the physical significance of some useful results expressed in rigorous group theoretical terms, leading to the symmetry classification of the normal modes. No purely group theoretical results are proved here, as such proofs, along with the details of the nomenclature, can be found in McWeeny (13).

Consider the eigenvalue equation 1.21, written in matrix notation:

$$1.26 \quad \underline{D} \cdot \underline{\epsilon}_a = \omega_a^2 \underline{\epsilon}_a.$$

Since the dynamical matrix  $\underline{D}$  must exhibit the symmetry of the structure, it must therefore be invariant under any operation  $C$  in the symmetry group  $G$ . Operating on 1.26 with the matrix representative  $\underline{R}_C$  of  $C$  gives

$$1.27 \quad \underline{R}_c \underline{D} \underline{\epsilon}_a = \underline{D} \underline{R}_c \underline{\epsilon}_a = \omega_a^2 \underline{R}_c \underline{\epsilon}_a .$$

This means that  $\underline{R}_c \underline{\epsilon}_a$  represents a set of eigenvectors with the same eigenvalue of  $\underline{D}$  as the original set  $\underline{\epsilon}_a$ , and are consequently linear combinations of the original set. This is true for any set of eigenvectors with a common eigenvalue, and each such set consequently forms the basis for an irreducible representation of  $G$ . Each eigenvalue  $\omega_a^2(\underline{y})$  corresponds to a normal mode, and therefore each normal mode corresponds to an irreducible representation of  $G$ . The complication of accidental degeneracies, where force constants are such that two distinct normal modes have the same frequency, is ignored here.

Now the normal coordinates  $Q_{ya}$  can be written in terms of the mass-weighted Cartesian coordinates  $W_{Iil}$  :

$$1.28 \quad Q_{ya} = \frac{1}{\sqrt{N}} \sum_{Iil} \epsilon_a^*(i\mathbf{y}) W_{Iil} \exp(-i\mathbf{y} \cdot \underline{I})$$

$$1.29 \quad \underline{Q} = \underline{T} \underline{W} \quad \text{in matrix notation}$$

where  $\underline{T}$  is unitary. This means that the matrices of a representation based on  $3N$  Cartesian coordinates are related to that based upon the normal coordinates by a similarity transformation, and the representations are therefore equivalent. A representation based on the complete set of normal mode coordinates is therefore, in general, not irreducible, and provides the same set of irreducible representations of  $G$  as does the representation based on the Cartesian displacements.

The group  $G$  has not yet been defined. In general, when  $\underline{D}$  is a function of  $\underline{y}$ ,  $G$  is the 'group of the wave vector  $\underline{y}$ ', i.e. those operations which preserve the translational symmetry of  $\underline{y}$  (14).

Fortunately, in first order Raman scattering, wave vector conservation requires  $\underline{y} \approx 0$  and this group corresponds to the point group of the structure.

The procedure for classifying the normal modes of a crystal is therefore as follows:-

- 1) Associate a set of Cartesian axes with each atom in the unit cell.
- 2) Construct the matrix representatives of the group operations with respect to these vectors, giving a representation  $\Gamma$ .
- 3) Reduce  $\Gamma$ .

For the purposes of classification of modes, the complete matrix representatives for  $\Gamma$  are fortunately not necessary, and it is sufficient to work with the characters  $\{\chi_{\Gamma}(c)\}$  of the matrices in 2) and 3), and use the orthogonality relation (13)

$$1.30 \quad n_{\gamma}^{\Gamma} = \frac{1}{g} \sum_c \chi_{\Gamma}(c) \chi_{\gamma}^*(c)$$

where  $g$  is the order of the group,  $\chi_{\gamma}(c)$  the trace of the  $c$ -matrix in irreducible representation  $\gamma$ ,  $\chi_{\Gamma}(c)$  the trace of the  $c$ -matrix in  $\Gamma$ , and  $n_{\gamma}^{\Gamma}$  the number of  $\underline{y} \approx 0$  modes of symmetry  $\gamma$  for the crystal.

#### §1.4 Selection Rules for First Order Raman Scattering

Due to the nature of the interaction between the photons and the phonons given by 1.12, only modes corresponding to certain irreducible representations can interact with the radiation. This gives rise to 'Selection Rules'. The one-phonon Raman cross-section depends on transition polarisability terms of the form 1.9

$$1.31 \quad P_{k\ell}^{if}(BA) = \frac{1}{\hbar} \sum_G \frac{\langle B | M_k | G \rangle \langle G | M_\ell | A \rangle}{(\omega_{GA} + \omega_f)} + \frac{\langle \ell \rightleftharpoons k \rangle}{(\omega_{GB} - \omega_f)}$$

It proves useful, in the case of the normal Raman effect, to use Placzek's approximation (8) which has the following physical significance.

In the adiabatic approximation, the electrons in a crystal are assumed to follow the nuclear motion. This enables the wavefunction to be written as the product of a wavefunction for the electrons in a given nuclear configuration, and the wavefunction for the given nuclear configuration. The corresponding energy eigenvalues are the sums of electronic and nuclear eigenvalues. Assuming that the states  $|A\rangle$  and  $|B\rangle$  are both electronic ground states, (i.e. no electronic Raman scattering), it is possible, to a good approximation, to divide 1.31 into ionic and electronic parts, depending on nuclear and electronic quantum numbers respectively. The conditions for this approximation to be good are that nuclear eigenvalues are much smaller than electronic eigenvalues, and that the probe frequency  $\omega_i$  ( $\approx \omega_f$ ) is not close to an electron excitation energy. With the further constraint that the probe frequency is much greater than the phonon frequencies ( $\omega_i \gg \omega_a(0)$ ), the ionic part can be ignored. This is always the case for normal Raman scattering and we can write:

$$1.32 \quad P_{k\ell}^{if}(BA) \approx \frac{1}{\hbar} \sum_{\substack{n_G \\ e_G \neq 0}} \frac{\langle 0 n_B | M_k | e_G^n \rangle \langle e_G^n | M_\ell | 0 n_A \rangle}{\omega_{e_G^0} + \omega_f} + \frac{\langle \ell \rightleftharpoons k \rangle}{\omega_{e_G^0} - \omega_f}$$



where  $e_D$  and  $n_D$  are the electronic and nuclear quantum numbers of the state  $|D\rangle$ . Now 1.32 is of the form

$$1.33 \quad P_{k\ell}^{if}(BA) = \langle 0 n_B | P_{k\ell}^{if} | 0 n_A \rangle$$

where  $P_{k\ell}^{if}$  is a unitary tensor operator. Since the numbers  $\{n_D\}$  can be taken to represent the number of phonons of each type (see §1.5), state  $|0 n_B\rangle$  differs from  $|0 n_A\rangle$  by the addition of one phonon. It can be shown that the matrix element 1.33 is zero unless the polarisability tensor element  $P_{k\ell}$  transforms according to the same irreducible representation of  $G$  as does the phonon created (15, 16). This is due to the group theoretical result that the inner product  $\langle A|B\rangle$  of two vectors is zero unless the vectors transform similarly under the group operations. The transformation properties of the second rank tensor  $P_{k\ell}$  can be derived for the 6 crystal classes, and have been tabulated in the definitive article by Loudon (15, 17).

With the information given by the calculations of §1.3 and §1.4, one can predict the symmetries of modes appearing as peaks in the Raman spectrum for a given input field  $\underline{E} = (E_k, E_\ell, E_m)$  and a given output field direction  $\hat{\underline{e}} = (\hat{\epsilon}_{fk}, \hat{\epsilon}_{f\ell}, \hat{\epsilon}_{fm})$ . These may not, of course, be visible due to absorption, or small values of the elements of  $P_{k\ell}$ .

### §1.5 Greens Functions and Raman Scattering

Useful information about the atomic vibrations of a crystal can obviously be gleaned from the Raman spectrum by applying the methods of §1.3 and §1.4, which describe the presence or absence of peaks in the

spectrum. More often than not, the shape of a peak is also of interest. For a harmonic system, simple 'response function' arguments produce an expression for the lineshape comprising delta-functions at shifts of  $\omega_f = \omega_i \pm \omega_a$  (18).

In the presence of anharmonicity, a simple 'harmonic oscillator with viscous damping' analysis gives rise to a broadening of the delta functions. This semiclassical argument is physically unrealistic, and furthermore does not describe many experimental results at all well. With the help of many-body theory, and in particular Greens function methods, however, one can derive from equation 1.12 a general expression for the lineshape without recourse to mythical damped oscillators. The fundamental assumption of the Greens function analysis of anharmonicity in solids is that the crystal may be regarded as an ensemble of bosons (phonons). These bosons interact through anharmonic terms in the Hamiltonian, and as they can be created or destroyed, 'particle number' is not conserved. Instead of considering the complete wavefunction of the system, it is necessary to go over to the second quantisation representation, which deals in the occupation numbers of the phonon states (19).

The arguments in this section follow those of Abrikosov et al. (20) and Cowley (21). It is assumed that the formalism of the three 'pictures' of quantum mechanics is familiar (11). These are the Schrödinger, Heisenberg (subscript H) and Interaction (~) pictures. The presence of anharmonicity implies the existence of terms additive to 1.13 for the Hamiltonian. These are of the form:

$$1.34 \quad H' = \sum_{\substack{ijk \\ \ell mn}} \phi \binom{\ell mn}{ijk} q_i^\ell q_j^m q_k^n .$$

This may be written in terms of the normal coordinates of 1.22 as

$$1.35 \quad H' = \sum_{\substack{\underline{y}_1 \underline{y}_2 \underline{y}_3 \\ a b c}} v(\begin{smallmatrix} \underline{y}_1 \underline{y}_2 \underline{y}_3 \\ a b c \end{smallmatrix}) Q_{\underline{y}_1 a} Q_{\underline{y}_2 b} Q_{\underline{y}_3 c}^* \delta(\underline{y}_1 + \underline{y}_2 + \underline{y}_3 + \underline{K})$$

( $\underline{K}$  = Reciprocal lattice vector)

which in turn expresses the interaction Hamiltonian  $H'$  in terms of the phonon creation and annihilation operators.

In general, the single particle Greens function is defined in terms of the second quantisation operators for creation and annihilation of a particle at a particular point in space. For phonons, however, it is convenient to define the Greens function in the momentum representation as:-

$$1.36 \quad G(\underline{y}^a, \underline{y}'^b, t) = \frac{\text{Tr}}{Z} \{ \exp(-\beta H) T_t [\psi_H(\underline{y}^a, t) \psi_H^*(\underline{y}'^b, 0)] \}$$

where  $T_t$  is the time ordering operator,  $Z$  the canonical partition function, and

$$1.37 \quad \psi(\underline{y}^a) = b_{\underline{y}^a} + b_{-\underline{y}^a}^*$$

If the crystal is to be invariant under the operations of the translation group, then the Greens function is zero unless  $\underline{y} = \underline{y}'$ . It is essential to the development of finite temperature Greens function theory to note that  $G$  is periodic in the 'complex time'  $it = \tau$ , provided  $|\tau| < \beta \hbar$ . Thus we can expand  $G$  in terms of a 'complex frequency' to give

$$1.38 \quad G(\underline{y}^a, \tau) = \sum_{n=-\infty}^{\infty} G(\underline{y}^a, i\omega_n) \exp i\omega_n \tau$$

$$1.39 \quad G(\underline{y}_{ab}, i\omega_n) = \frac{1}{2\beta\hbar} \int_{-\beta\hbar}^{\beta\hbar} G(\underline{y}_{ab}, \tau) \exp -i\omega_n \tau \, d\tau$$

where  $\omega_n = \left(\frac{2\pi}{\beta\hbar}\right) \times n$  .

The usefulness of this transformation will not become clear until it is applied in the (exactly soluble) harmonic approximation, and in the anharmonic case, when some form of perturbation theory will have to be applied. It is best, therefore, to proceed with the purely formal manipulation of  $G$  until some physically useful quantity emerges. If the time dependent properties of the Heisenberg picture operators are taken into account

$$(\psi_H(\underline{y}_{at})) = \exp \frac{iHt}{\hbar} \psi(\underline{y}_a) \exp \frac{-iHt}{\hbar} ,$$

and the trace is expanded in terms of the eigenstates  $\{|D\rangle\}$  of  $H$ , we can write:

$$1.40 \quad G(\underline{y}_{ab}, \tau > 0) = \frac{1}{Z} \sum_{A,B} \langle A | \exp(-\beta + \frac{\tau}{\hbar} H) \psi(\underline{y}_a) \exp \frac{-\tau H}{\hbar} | B \rangle \\ \times \langle B | \psi^*(\underline{y}_b) | A \rangle .$$

It is unnecessary to write  $G(\tau < 0)$  as it is uniquely defined by 1.40 and the periodicity of  $G$  along the complex time axis. Thus

$$1.41 \quad G(\underline{y}_{ab}, \tau > 0) = \frac{1}{Z} \sum_{A,B} \exp(-\beta E_A - \omega_{BA} \tau) \psi_{AB}(\underline{y}_a) \psi_{BA}^*(\underline{y}_b)$$

and if a real function  $\rho(\underline{y}_{ab}, \omega)$  is defined

$$1.42 \quad \rho(\underline{y}_{ab}, \omega) = \frac{1}{Z} \sum_{A,B} \exp -\beta E_A \psi_{AB}(\underline{y}_a) \psi_{BA}^*(\underline{y}_b) \times \delta(\omega - \omega_{BA})$$

then 1.41 can be written

$$1.43 \quad G(\underline{y}_{ab}, \tau > 0) = \int_{-\infty}^{\infty} \rho(\underline{y}_{ab}, \omega) \exp - \omega \tau \, d\omega .$$

It is now possible to relate  $\rho(\underline{y}_{ab}, \omega)$  to the Raman intensity 1.12. This expression contains matrix elements of the polarisability operator  $P_{k\ell}^{if}$  of 1.33, within the adiabatic approximation. The corresponding classical polarisability can be expanded as a Taylor series in the atomic displacements

$$1.44 \quad P_{k\ell}^{if} = P_{k\ell}^{if}(0) + \sum_{jm} P_{k\ell}^{if}(jm) q_{jm} + \dots .$$

Expressing  $\{q_j\}$  in terms of  $\{Q_{\underline{y}^a}\}$ , the normal coordinates for a phonon of wavevector  $\underline{y}$  and dispersion branch 'a', and thus in terms of  $\psi(\underline{y}^a)$ , the matrix elements in 1.12 become

$$1.45 \quad P_{k\ell}^{if}(BA) = \langle B | P_{k\ell}^{if}(0) + \sum_{\underline{y}^a} P_{k\ell}^{if}(\underline{y}^a) \psi(\underline{y}^a) \dots | A \rangle .$$

The first term obviously vanishes when  $|A\rangle \neq |B\rangle$ , and 1.12 becomes

$$1.46 \quad I d\omega_f d\Omega = \frac{\omega_f^4}{32\pi^2 c^3 \epsilon_0} \sum_{k\ell mn} E_k E_m \hat{\epsilon}_{f\ell} \hat{\epsilon}_{fn} P_{k\ell}^{if}(\underline{y}^a) \overline{P}_{mn}^{if}(\underline{y}'^b) \\ \times \left\{ \sum_A \frac{\exp - \beta E_A}{Z} \psi_{AB}(\underline{y}^a) \psi_{BA}^*(\underline{y}'^b) \right. \\ \left. \times \delta(\omega_{BA} + \omega_f - \omega_i) \right\} .$$

The expression in curly brackets is, in fact, the function  $\rho(\underline{y}_{ab}, -\omega_f + \omega_i)$  defined by 1.42 when, again,  $\underline{y}' = \underline{y}$  for translational invariance.

The Raman cross-section may therefore be written

$$1.47 \quad I d\omega_f d\Omega = \frac{\omega_f^4}{32\pi^2 c^3 \epsilon_0} \sum_{\substack{k\ell mn \\ \underline{y}_{ab}}} E_k E_m \hat{\epsilon}_{f\ell} \hat{\epsilon}_{fn} P_{k\ell}^{if}(\underline{y}_a) \bar{P}_{k\ell}^{if}(\underline{y}_b) \rho(\underline{y}_{ab}, -\omega_f + \omega_i)$$

This 'spectral function',  $\rho(\underline{y}_{ab}, \omega)$  is obtained from  $G(\underline{y}_{ab}, i\omega_n)$  by combining 1.39 and 1.43 to give

$$1.48 \quad G(\underline{y}_{ab}, i\omega_n) = \frac{1}{\beta\hbar} \int_{-\infty}^{\infty} \frac{(1 - \exp(-\beta\hbar\omega)) \rho(\underline{y}_{ab}, \omega) d\omega}{\omega + i\omega_n}$$

It is obvious that this function is not yet useful for calculating  $\rho(\underline{y}_{ab}, \omega)$  as there is an imaginary frequency involved. This problem is overcome by analytically continuing  $G(\underline{y}_{ab}, i\omega_n)$  from the imaginary axis, through the complex plane, to the real frequency axis, by writing  $i\omega_n \rightarrow \omega + i\epsilon \rightarrow \omega$  as  $\epsilon \rightarrow 0$ . This yields

$$1.49 \quad \rho(\underline{y}_{ab}, \omega) = \frac{-\beta\hbar}{2\pi i (1 - \exp(-\beta\hbar\omega))} \times \lim_{\epsilon \rightarrow 0^+} [G(\omega + i\epsilon) - G(\omega - i\epsilon)]$$

In the low momentum transfer limit ( $\underline{y} \approx 0$ ) of Raman scattering, this gives, for the cross-section:

$$1.50 \quad I d\omega_f d\Omega = - \frac{\omega_f^4 \beta\hbar}{32\pi^3 c^3 \epsilon_0} \sum_{\substack{k\ell mn \\ ab}} E_k E_m \hat{\epsilon}_{f\ell} \hat{\epsilon}_{fn} P_{k\ell}^{if}(O_a) P_{mn}^{if}(O_b) \times \text{Im}[G_{ab}(\omega)] \div (1 - \exp(-\beta\hbar\omega))$$

and the Raman scattered intensity has been related to the one-phonon Greens function matrix, indexed by a and b. In the harmonic approximation, the effect of the operators  $\psi, \psi^*$  on the states  $\{|D\rangle\}$  can be deduced from 1.24, 1.26 and the harmonic Greens function  $G^H$  can be written, from 1.42, 1.43 as

$$1.51 \quad G_{aa}^H(\omega) = \frac{2\omega_a}{\beta\hbar(\omega_a^2 - \omega^2)}$$

and also

$$1.52 \quad \rho^H(0aa, \omega) = [(n_a + 1)\delta(\omega - \omega_a) + n_a \delta(\omega + \omega_a)] .$$

The Raman spectrum therefore consists of two 'spikes' at frequencies  $\pm \omega_a$ , the energy of the  $y \approx 0$  phonon of the dispersion branch 'a' .

When anharmonicity is present, the Greens function is obtained by summation of an infinite perturbation series. This summation, and the use of diagram techniques to evaluate anharmonic Greens functions, is described in Appendix 1. The result is that  $G_{ab}(\omega)$  is given by the matrix equation

$$1.53 \quad \sum_b [(\omega_a^2 - \omega^2)\delta_{ab} + 2\omega_a(\Delta_{ab}(\omega) + i\Gamma_{ab}(\omega))]G_{bc}(\omega) = 2\omega_a \delta_{ac} \div \beta\hbar .$$

In general, the terms  $\Delta$  and  $\Gamma$  depend on the form of the Fourier coefficients  $V$  of the anharmonic potential  $\phi$ . It is not hard to see that the substitution  $\Delta = \text{constant}$ ,  $\Gamma \propto \omega$  gives the broadening and shift of the delta functions of 1.52 analogous to the response of a damped oscillator.

## §1.6 Experimental Techniques

Raman scattering in crystals is very weak, and frequency shifts  $\{\omega_2\}$  are small compared with typical visible light frequencies. The ratio of inelastic/elastic scattering is of the order of  $10^{-6}$  or smaller. This gives rise to a set of criteria for a Raman experiment.

- 1) The source of radiation must be monochromatic, very intense, well collimated, of very low bandwidth and accurately polarised.
- 2) The scattered light must be efficiently analysed and dispersed.
- 3) The detector of scattered light must be very efficient.

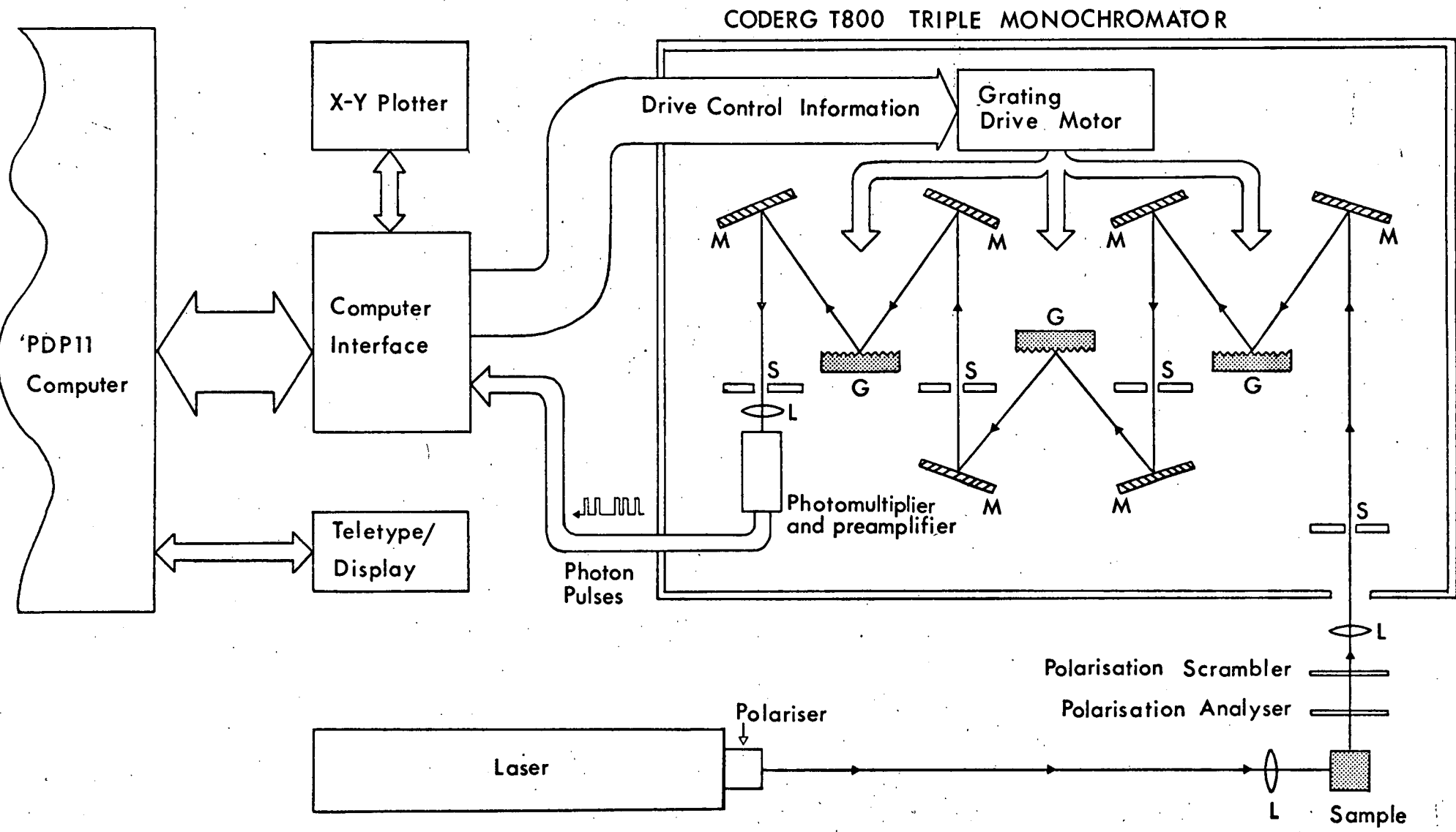
In addition, comparative studies create a further requirement

- 4) The system must collect large amounts of data in an accurate, repeatable manner. A system which fulfils all these requirements is represented by Figure 3. Requirement 1 is met by a gas ion laser (Spectra Physics model 165 argon or krypton tubes), which offers the bonus of a variety of exciting frequencies. The Coderg T800 triple grating spectrometer complies excellently with requirement 2, and a low-noise photomultiplier tube with an appropriate frequency response satisfies condition 3. The additional (optional) extra of computer control and data acquisition (23, 24) meets requirement 4 and also facilitates digital data analysis (23, 25).

In the particular case of acoustic mode scattering, the triple grating spectrometer is replaced by a higher resolution, low spectral range Fabry-Perot interferometer. This was not necessary for any of the experiments described, but the details of such a system are given in Chapter 5, as its construction formed a significant part of my thesis work.



FIGURE 3: The experimental system used for the majority of the Raman scattering work in this thesis (schematic). 'G' denotes a diffraction grating, 'M' a mirror, 'S' a slit and 'L' a lens. The flow of information between the system and the computer is also represented schematically.



A RAMAN SPECTRAL STUDY OF ZINC METABORATEIntroduction

The study of zinc metaborate,  $Zn_4B_6O_{13}$  (ZBO) was intended as a precursor to the main work of this thesis - the examination of nickel-iodine boracite,  $Ni_3B_7O_{13}I$ . ZBO contains boron atoms in exclusively fourfold coordination with oxygen atoms, while boracites have mixed threefold/fourfold B - O coordination. The intention was to classify the vibrational symmetries, and in particular to identify levels associated with the B - O framework. Some success was achieved in this, and the Raman spectrum proved interesting in its own right. In §2.1 - §2.3, the Raman spectrum of ZBO is reported and the assignment of  $q \approx 0$  normal mode symmetries is made (26). The vibrational levels of the B - O framework are tentatively identified and correlated with results from some boracite spectra in §2.4, with the aid of some simple molecular potential function calculations. The conclusions regarding symmetries of bands are summarised in §2.5, and an interesting interference feature is identified in the spectrum (27, 28). The descriptions of this phenomenon by two distinct theoretical models described in §2.6 and §2.7 are compared, and a conclusion as to applicability is reached in §2.8.

§2.1 Symmetry Considerations

$Zn_4B_6O_{13}$  has the symmorphic cubic space group  $T_d^3$  ( $\bar{I}43m$ ), with the  $BO_4$  groups linked to form an infinitely extended three-dimensional framework based on  $B_6O_{12}$  rings (29). The tetrahedral B - O coordination is unusual in that stability usually requires threefold coordination in

metaborates. All the known crystals with exclusively fourfold B - O coordination are of the form  $(M O)_m (B_2O_3)_n$ , where M is a divalent metal such as Cu (30), Sr (31), Pb (31) or, of course, Zn (29). A listing of mixed coordination borates is given by Marezio et al. (32).

A group theoretical analysis according to the methods of §1.3 predicts the following classification of the  $q \approx 0$  normal modes of ZBO in terms of the irreducible representations of point group  $T_d (\bar{4}3m, \text{see table 1})$ :

$$\Gamma = 3A_1 + 2A_2 + 5E + 7F_1 + 11F_2.$$

Furthermore, the evaluation of the selection rules of §1.4 for cubic crystals gives, for the polarisability tensors, in terms of the cubic  $\langle 100 \rangle$  axes (15, 17), X, Y and Z:

$$A_1 \begin{bmatrix} a & . & . \\ . & a & . \\ . & . & a \end{bmatrix} \quad E \begin{bmatrix} b & . & . \\ . & b & . \\ . & . & -2b \end{bmatrix} \quad \text{and} \quad \begin{bmatrix} \sqrt{3}b & . & . \\ . & -\sqrt{3}b & . \\ . & . & . \end{bmatrix}$$

$$F_2(X) \begin{bmatrix} . & . & . \\ . & . & d \\ . & d & . \end{bmatrix} \quad F_2(Y) \begin{bmatrix} . & . & d \\ . & . & . \\ d & . & . \end{bmatrix} \quad F_2(Z) \begin{bmatrix} . & d & . \\ d & . & . \\ . & . & . \end{bmatrix}$$

where the bracketed index denotes the polarisation of the phonon (given by the  $\hat{\epsilon}_a(iy)$  of §1.2). The Raman spectrum should therefore comprise  $3A_1 + 5E + 10F_2$  optic modes. A calculation similar to §1.4 for matrix elements of the dipole moment reveals that only  $F_2$  modes are also infrared active.

It is obvious that no scattering geometry with this orientation

TABLE 1

The character table for the irreducible representations of point group  $T_d(\bar{4}3m)$  (12).

	E	$8C_3$	$3C_2$	$6\sigma_d$	$6S_4$
$A_1$	1	1	1	1	1
$A_2$	1	1	1	-1	-1
E	2	-1	2	0	0
$F_1$	3	0	-1	-1	1
$F_2$	3	0	-1	1	-1

contains  $A_1$  or E modes alone. This problem is overcome (26,33) by rotating the sample about  $[0\ 0\ 1]$  such that the laser direction is  $[1\ 1\ 0]$ , or  $X'$ . The E symmetry tensors become

$$E \begin{bmatrix} b & . & . \\ . & b & . \\ . & . & -2b \end{bmatrix} \quad \text{and} \quad \begin{bmatrix} . & \sqrt{3} & . \\ \sqrt{3}b & . & . \\ . & . & . \end{bmatrix}$$

and the  $X'(Y'X')Y'$  spectrum contains only E symmetry peaks (see §1.1 for notation). Since the experimental data is in digital form (24), it is a routine matter to subtract the  $X'(Y'X')Y'$  spectrum from the  $X'(ZZ)Y'$  spectrum, with an appropriate scale factor, to lay bare the  $A_1$  modes.

## §2.2 Experimental Details

The crystal of ZBO was a byproduct in the growth of Zn - I boracite. The vapour transport method was used (34) and a shortage of  $ZnI_2$  vapour led to the production of ZBO instead of  $Zn_3B_7O_{13}I$ . The crystal growth faces were  $\langle 110 \rangle$ , so  $\langle 100 \rangle$  faces were cut and polished, using  $1\mu$  diamond powder, to facilitate both scattering geometries. Placing the sample between crossed polarisers revealed growth strains, leading to inhomogeneous optical properties. This gives rise to mixing of spectra over and above the expected intrusion of features from other spectra caused by the wide angle of the lens at the spectrometer entrance aperture. Since any spectrum is therefore, to a good approximation, a linear combination of mixed spectra, with the 'correct' spectrum

dominant, the same digital subtraction process described in §2.1 may be used to remove spurious features. Only in the case of  $F_2$  'leak through' is this impossible, due to transverse/longitudinal (TO-LO) mode frequency splittings and the corresponding intensity mismatching. The criterion for any subtraction to be possible is that some clear spectral feature is present, which can be used to determine a scale factor.

Zinc metaborate exhibits fluorescence around the 500-600 nm wavelength region (35). This was verified by survey Stokes spectra excited by 514.5 nm argon laser radiation. To avoid confusion of the Raman spectra by fluorescence, therefore, the spectra were excited by 350 mW of 476.5 nm argon laser light. The apparatus of §1.6 was used in both the  $90^\circ$  geometry as shown in Figure 3, and in  $180^\circ$  (back-scattering) geometry. The spectra are recorded to a resolution of  $1.0 \text{ cm}^{-1}$  in the  $0 - 500 \text{ cm}^{-1}$  region, and to  $1.5 \text{ cm}^{-1}$  in the  $500 - 1500 \text{ cm}^{-1}$  region. Further spectra in the  $1500 - 4000 \text{ cm}^{-1}$  frequency range revealed no further sharp features. An Oxford instruments flow cryostat was used to perform a brief study of the temperature dependence of the interference feature, although the results of this study were only qualitative.

### §2.3 Description of Spectra

In the ensuing description, and in the following chapter, the labels X, Y, Z refer to the cubic  $[1 0 0]$ ,  $[0 1 0]$  and  $[0 0 1]$  directions respectively, and X', Y' to the  $[1 1 0]$  and  $[\bar{1} 1 0]$  directions.  $\bar{X}$  represents  $[\bar{1} 0 0]$ .

The  $A_1$  spectrum:

This spectrum, shown in Figure 4, is the result of subtraction of the  $X'(Y'X')Y'$  spectrum of Figure 5 from the  $X'(ZZ)Y'$  of Figure 6. Using the E mode at  $414.5 \text{ cm}^{-1}$  as the clear feature mentioned above, a scale factor of  $1.03 \pm 0.07$  was found to give cancellation. This is not equal to the expected 1.33 from the form of the Raman tensors due to the birefringent properties of the sample, and to experimental variations between spectra. The sudden increase in the Poisson noise fluctuations in Figure 4 marks the disappearance of an E mode, and is caused by the  $\sqrt{N}$  proportionality of the photon 'particle number' fluctuations. The sharp 'differential' features, other than the resonant feature at  $122.5 \text{ cm}^{-1}$ , are due to slight calibration mismatches between the  $X'(Y'X')Y'$  and  $X'(ZZ)Y'$  spectra. There are four sharp features, and some broad second order structure. One of the discrete modes appears as the resonant interference feature at  $122.5 \text{ cm}^{-1}$ .

The E spectrum:

This spectrum, depicted in Figure 5, comprises twelve peaks, of which six are attributable to  $F_2$  admixtures, and one to another interference feature. The mode at  $89.4 \text{ cm}^{-1}$  is not the result of  $A_1$  'leak-through', and is without doubt an E mode.

The  $F_2$  spectrum:

The form of the  $F_2$  Raman tensors of §2.1 suggests that the  $X(YX)Y$  spectrum should reveal only TO modes, the  $X(YZ)\bar{X}$  only LO modes, and the  $X(YZ)Y$  both TO + LO modes. These spectra are presented as Figures 7, 8 and 9 respectively. In Figure 9, admixtures of



FIGURES 4-9: The Raman spectrum of  $\text{Zn}_4\text{B}_6\text{O}_{13}$  in the frequency regions  $0 - 500 \text{ cm}^{-1}$  and  $500 - 1500 \text{ cm}^{-1}$  at room temperature.

FIGURE 4: In  $X'(ZZ)Y' - X'(Y'X')Y'$  geometry.

FIGURE 5: In  $X'(Y'X')Y'$  geometry.

FIGURE 6: In  $X'(ZZ)Y'$  geometry.

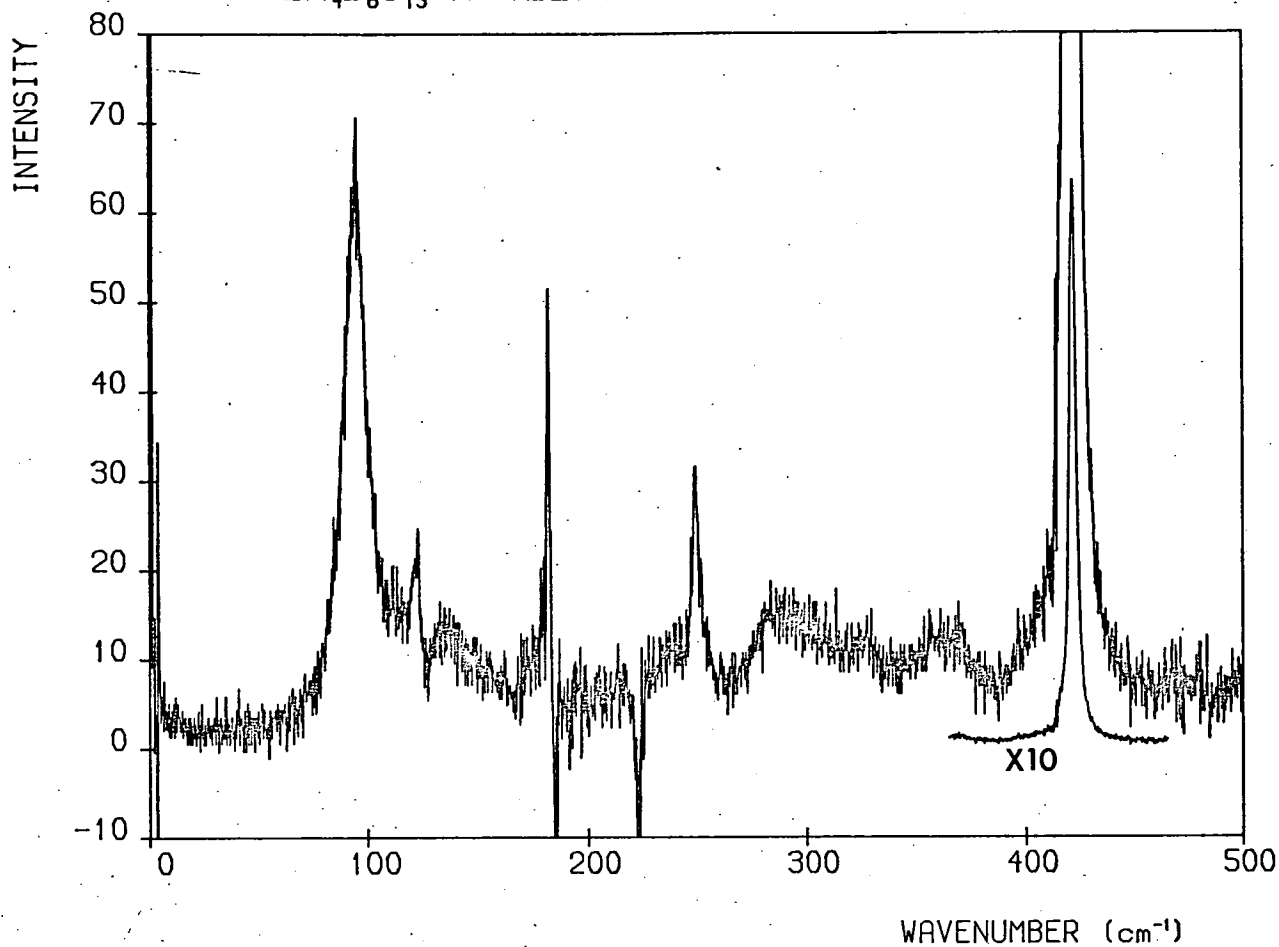
FIGURE 7: In  $X(YX)Y$  geometry.

FIGURE 8: In  $X(YZ)Y$  geometry.

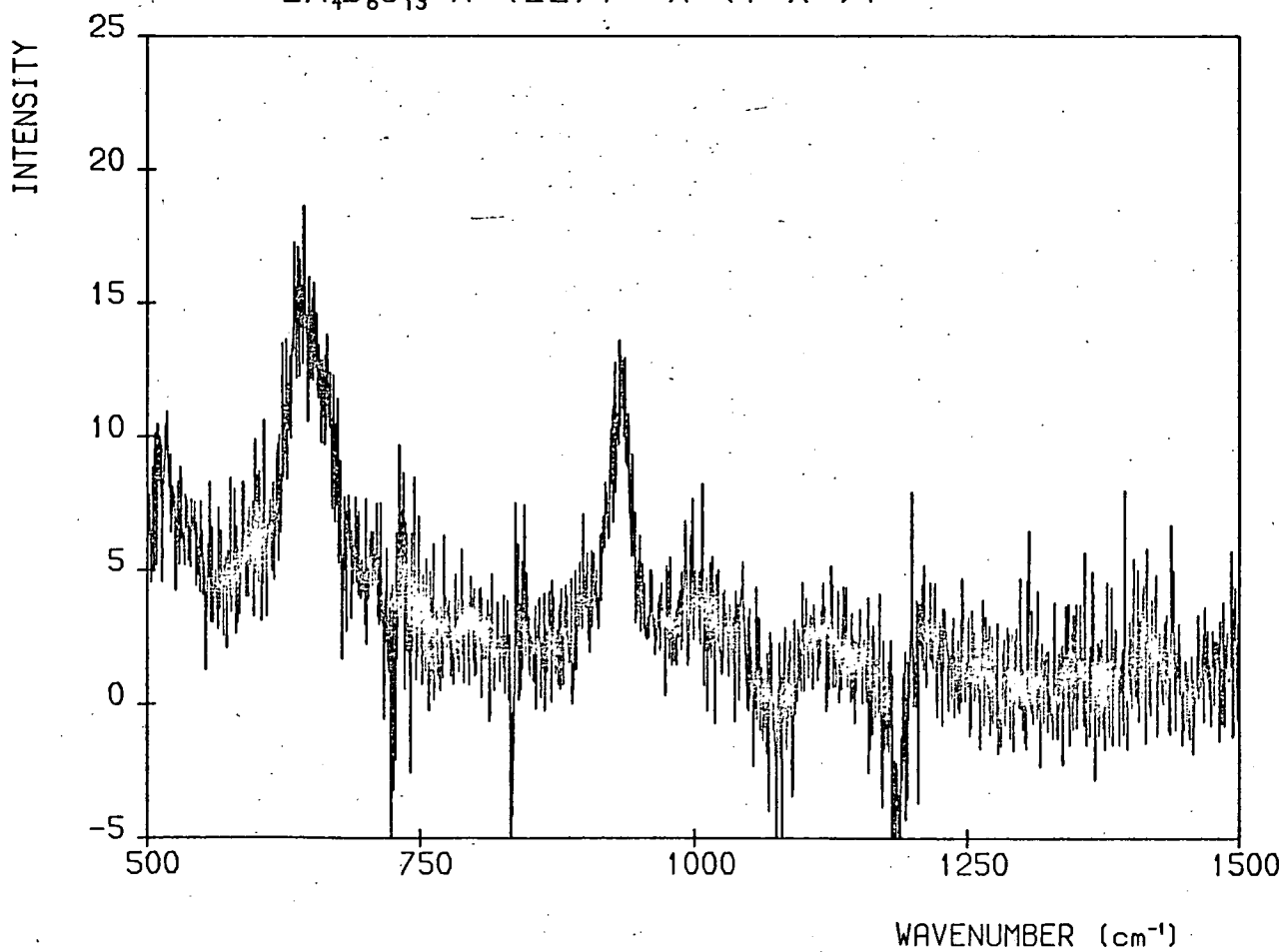
FIGURE 9: In  $X(YZ)\bar{X}$  geometry.

$Zn_4B_6O_{13} X^0 (ZZ) Y^0 - X^0 (Y^0 X^0) Y^0$

FIG 4



$Zn_4B_6O_{13} X^0 (ZZ) Y^0 - X^0 (Y^0 X^0) Y^0$



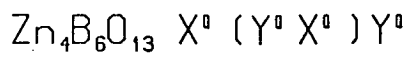
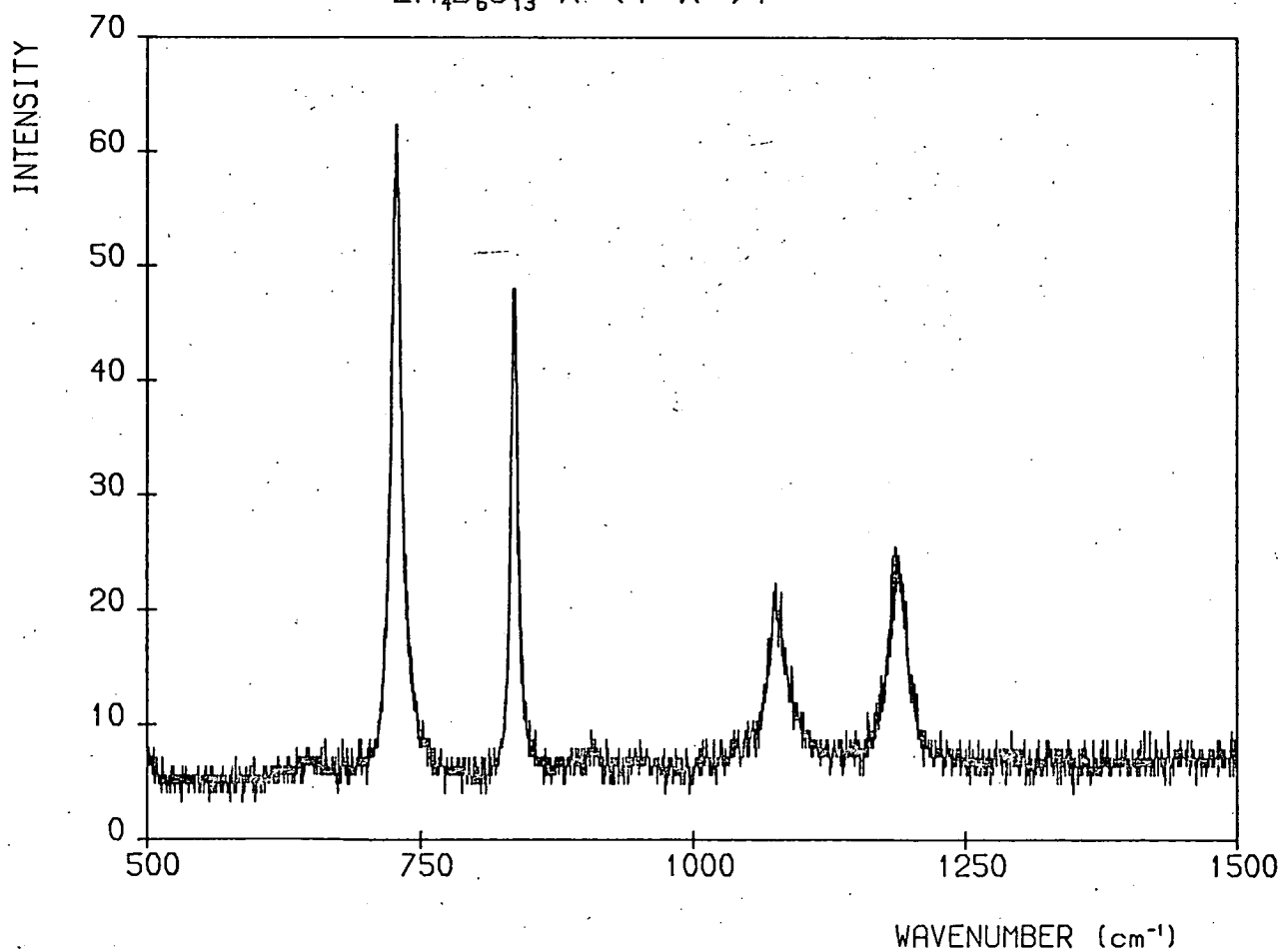
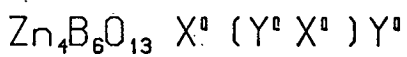
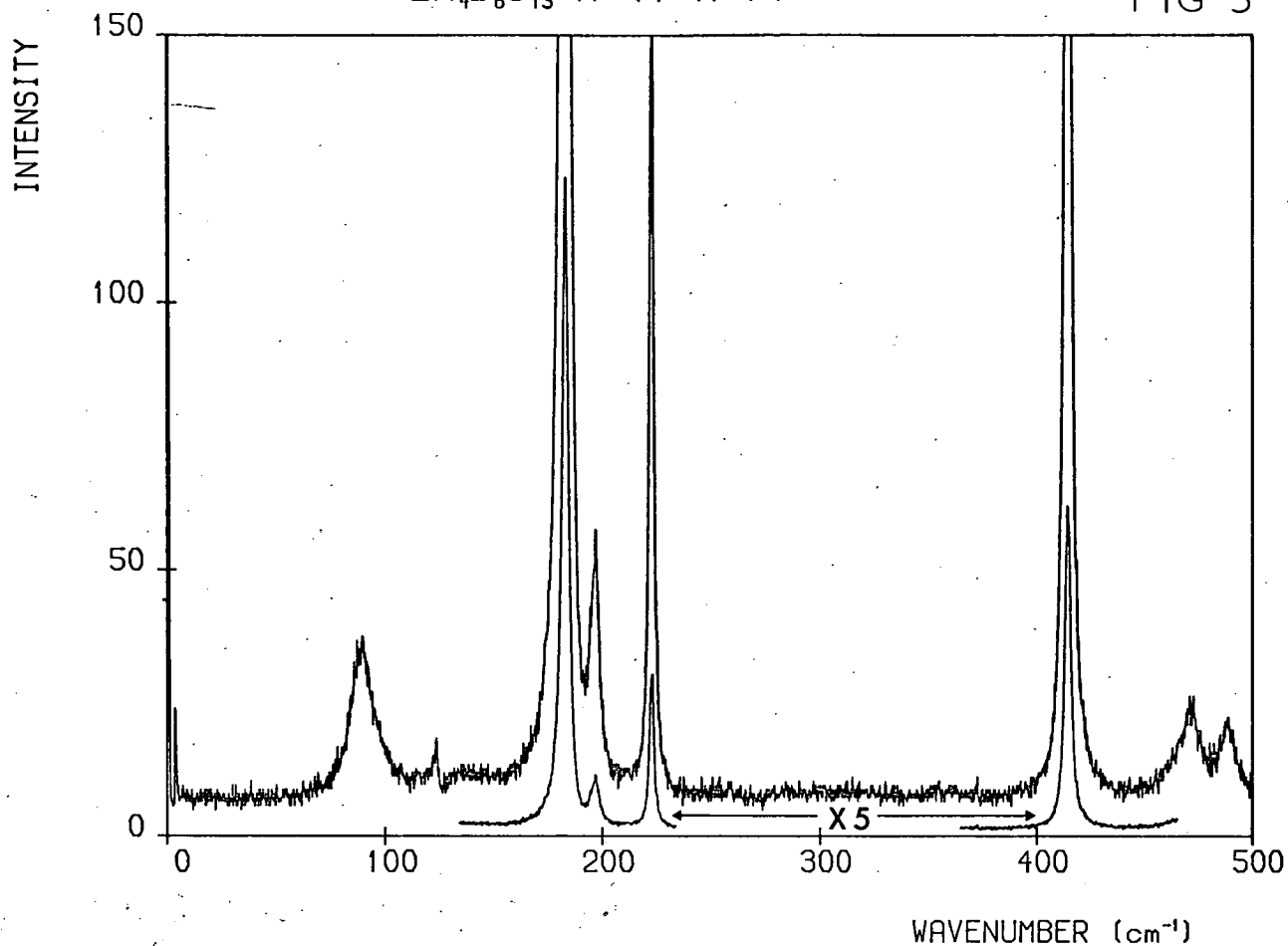
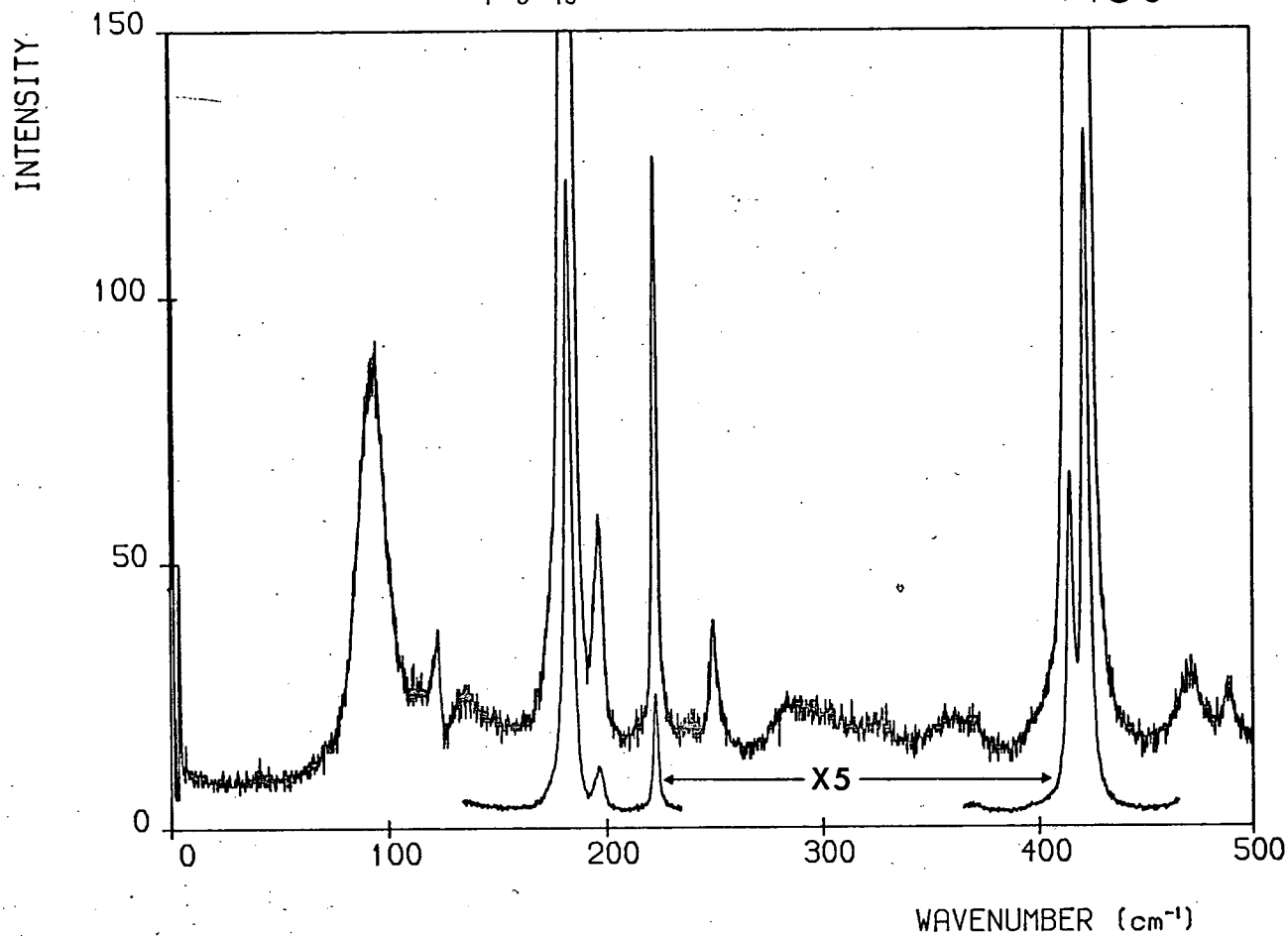


FIG 5

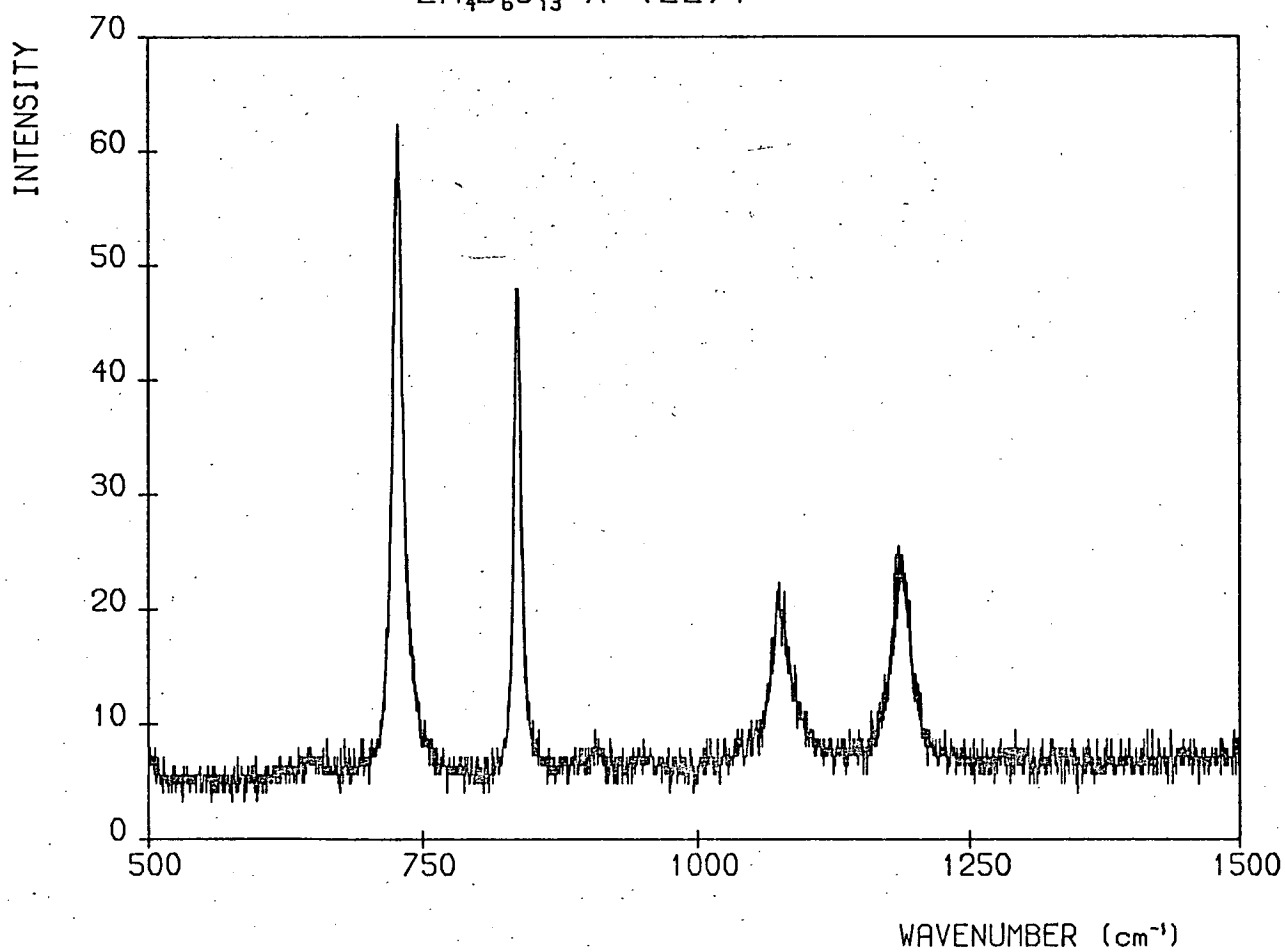


$Zn_4B_6O_{13} X^0 (ZZ) Y^0$

FIG 6

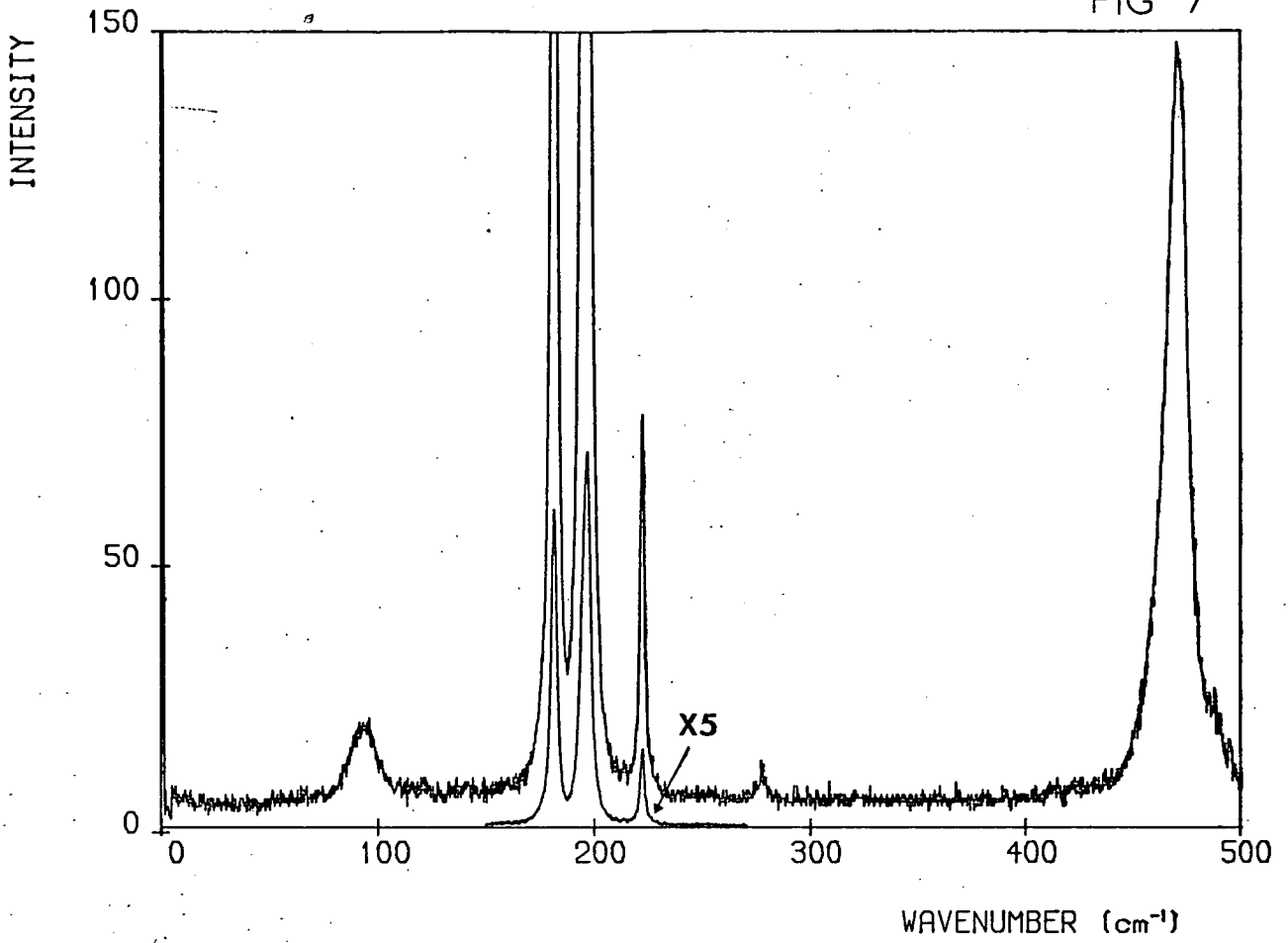


$Zn_4B_6O_{13} X^0 (ZZ) Y^0$

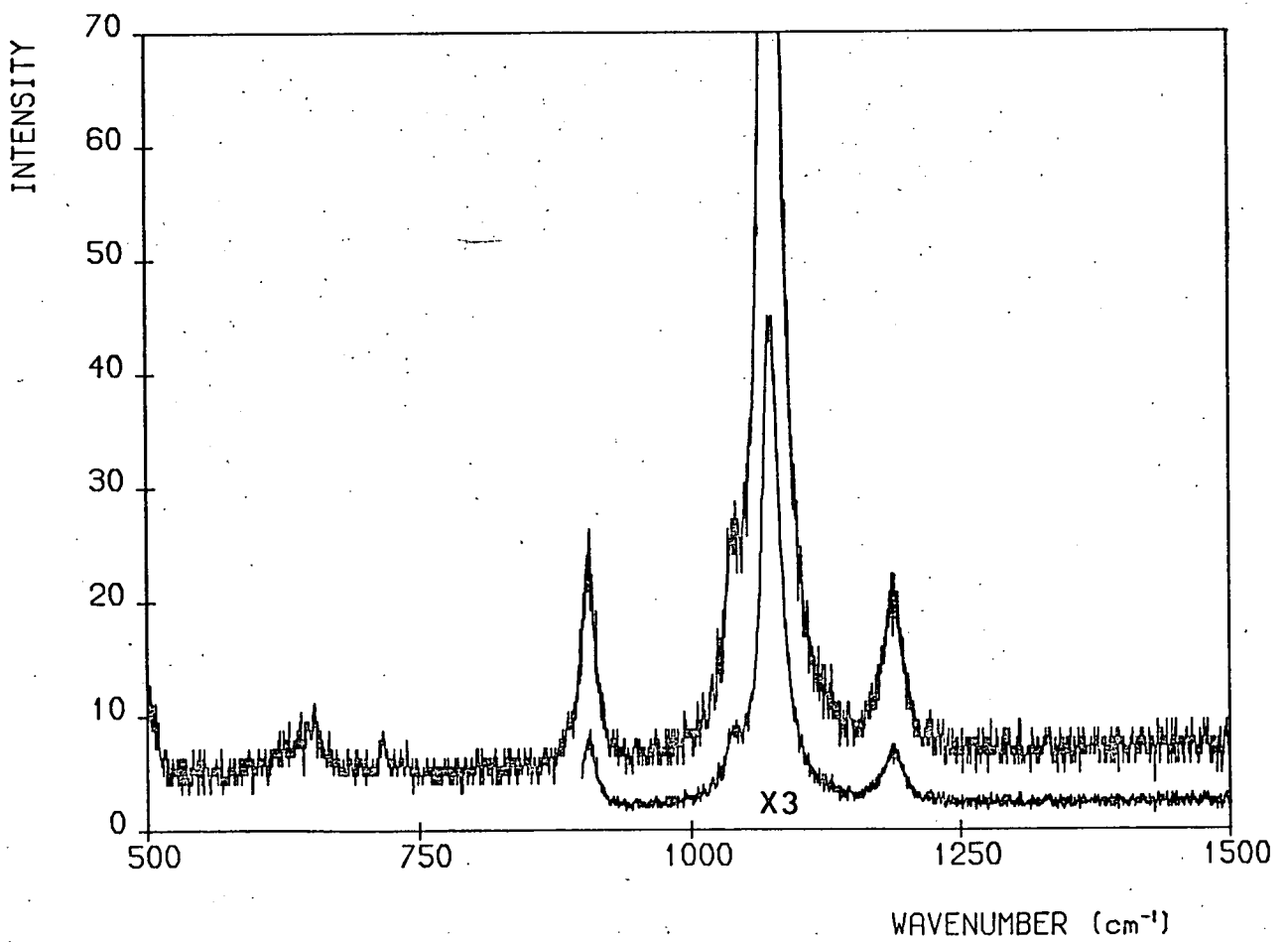


$Zn_4B_6O_{13}I$  X(YX)Y

FIG-7

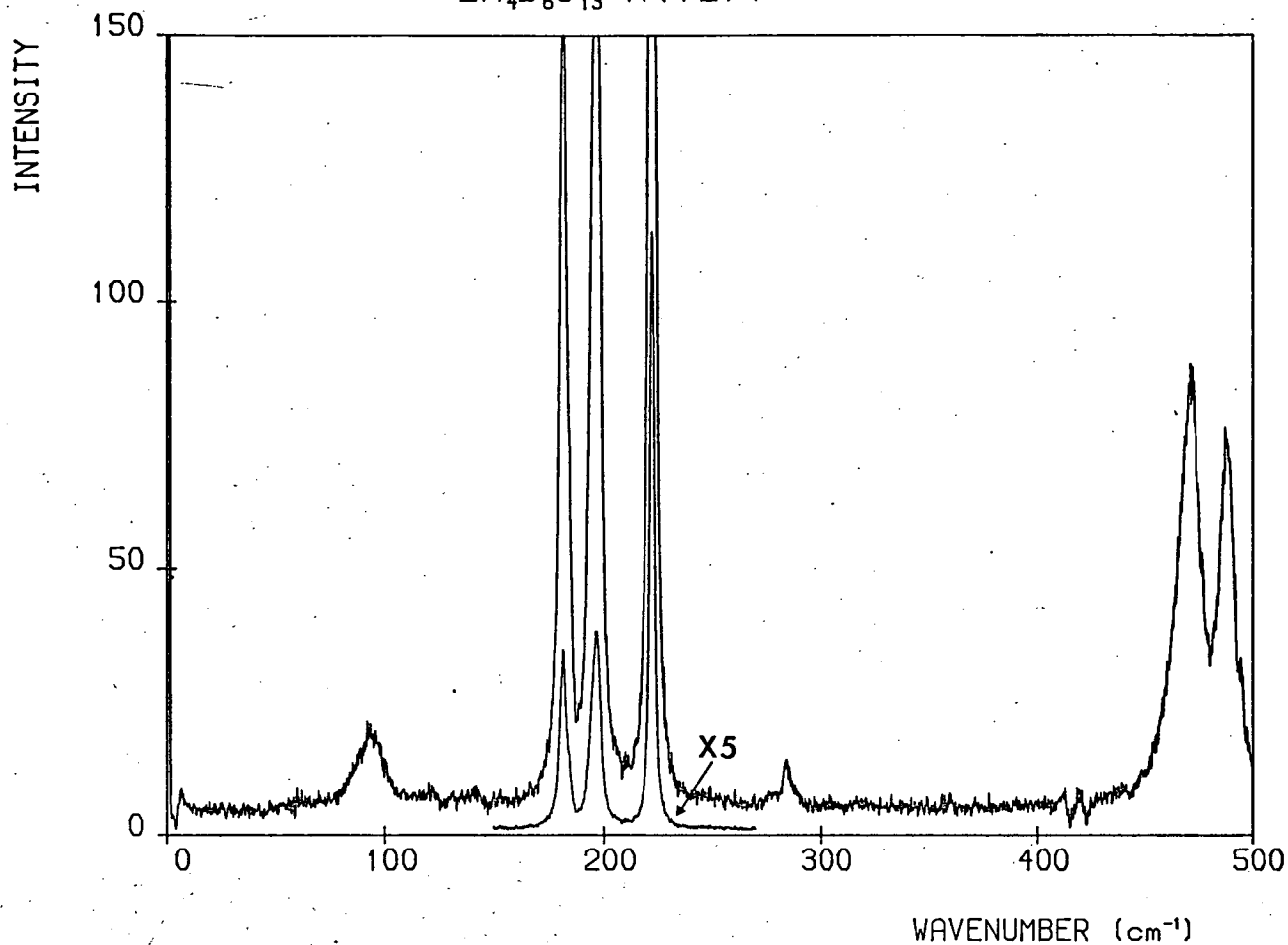


$Zn_4B_6O_{13}$  X(YX)Y

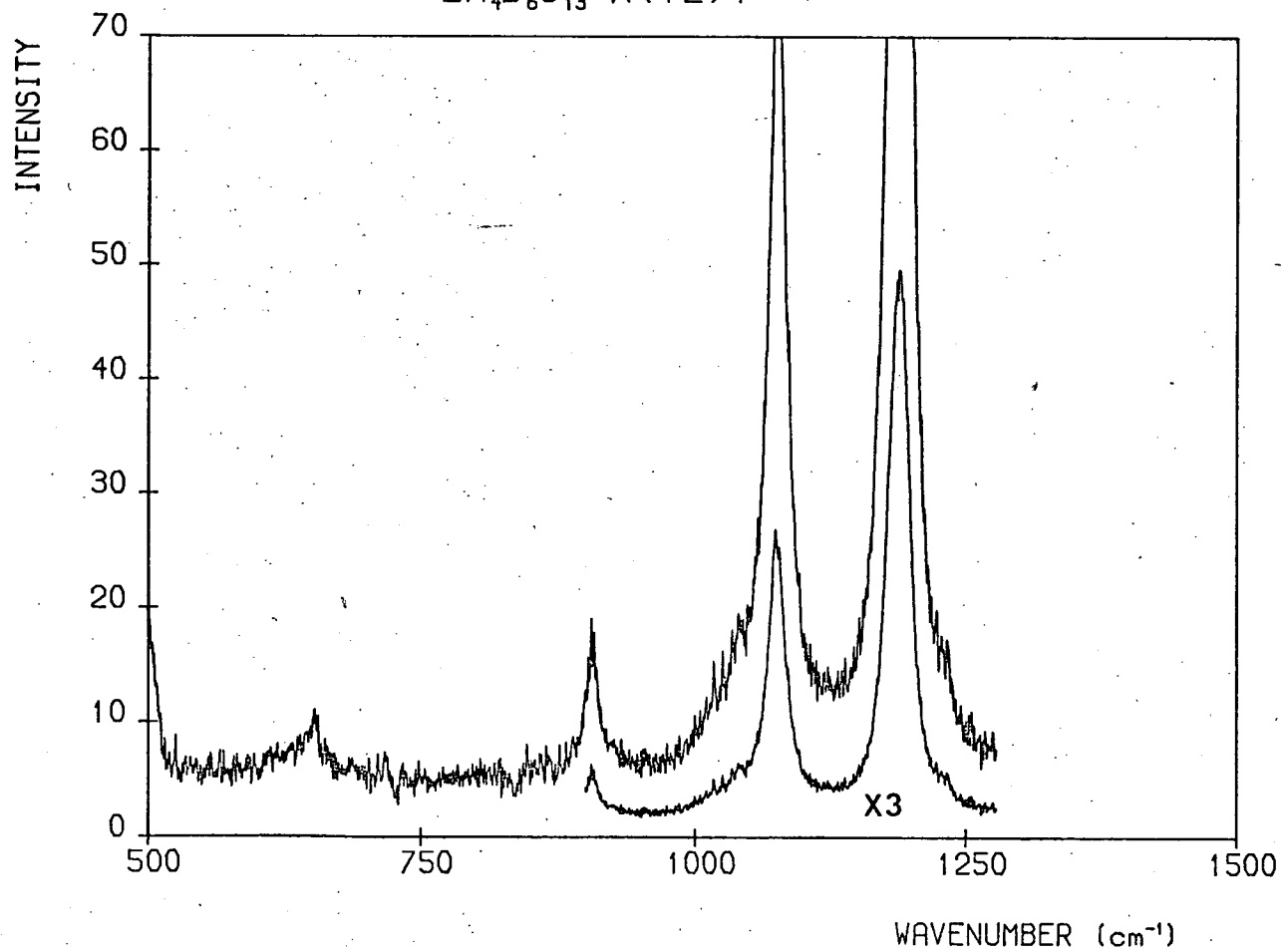


$Zn_4B_6O_{13}$  X(YZ)Y

FIG 8



$Zn_4B_6O_{13}$  X(YZ)Y



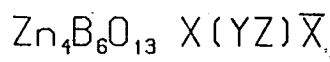
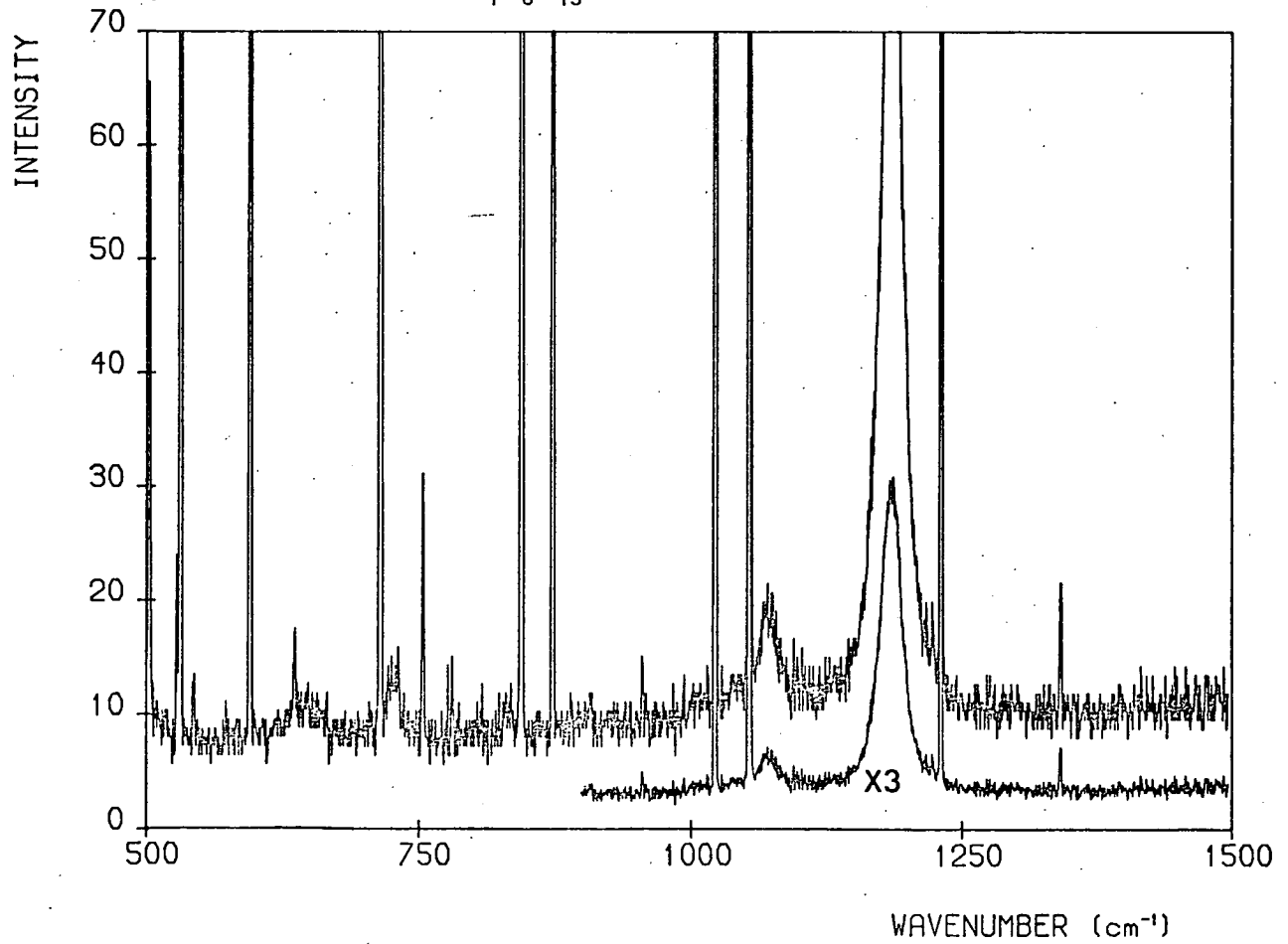
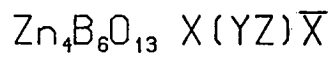
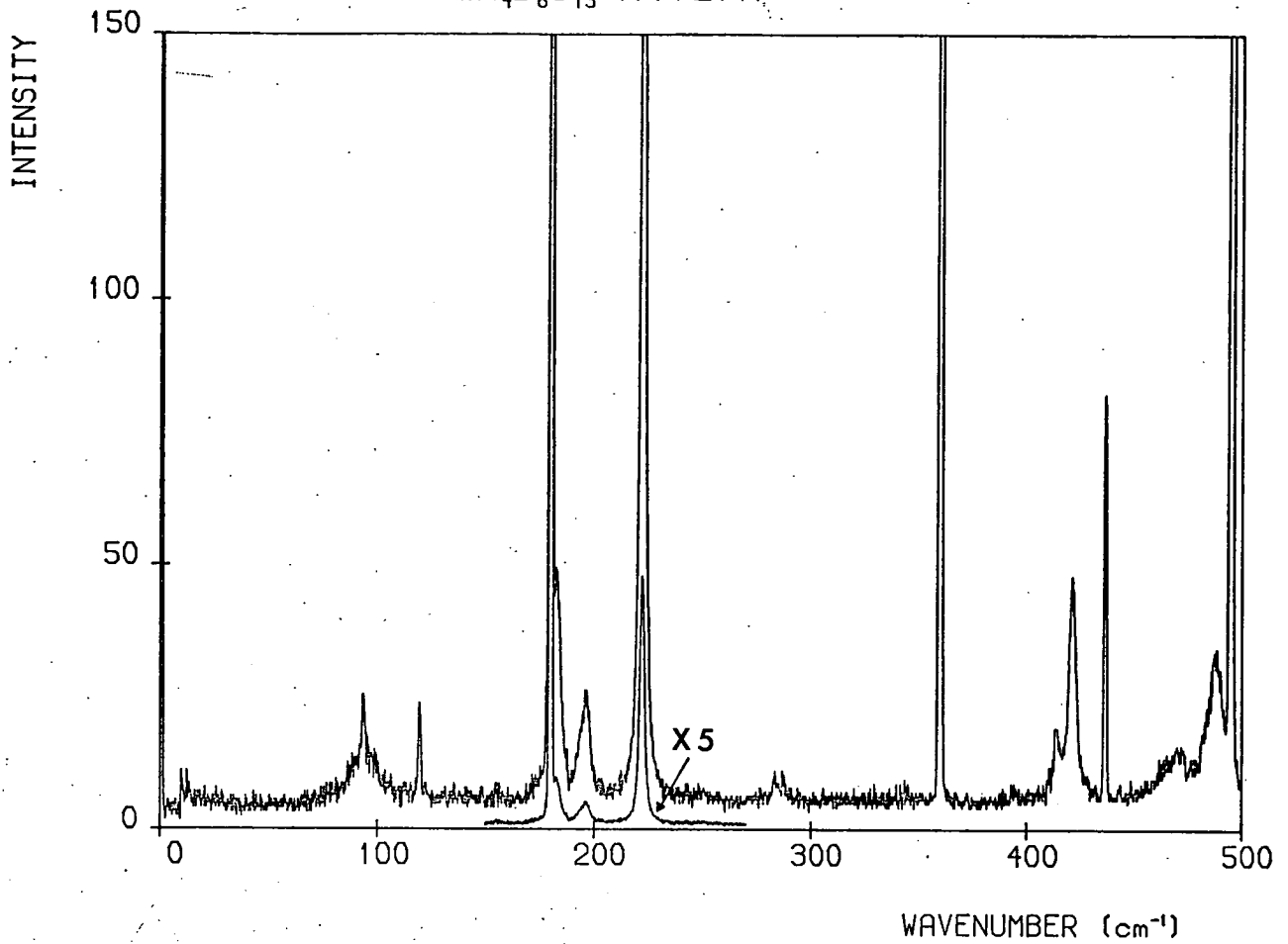


FIG 9



$A_1$  and E spectra have been subtracted out, and the intense 'spikes' in Figure 8 are the result of elastic scattering of argon laser plasma lines. This is often a problem in backscattering experiments. It is possible to identify ten  $F_2$  modes, allowing for TO - LO pairs, from a detailed study of Figures 7, 8 and 9 and use of a computer peak finding routine (25). The modes at  $93.1 \text{ cm}^{-1}$  and  $181.6 \text{ cm}^{-1}$  are worthy of remark due to their near-degeneracy with  $A_1$  and E modes.

The peak frequencies  $\omega$  and linewidths  $\gamma$  of the Raman active modes, along with their symmetry assignments, are presented in Table 2. The infrared results of Krogh-Moe (36) and Tarte (37) are also tabulated, and are discussed in §2.5.

#### §2.4 Molecular Potential Calculations for $XY_4$ Molecules

To describe molecular vibrations theoretically it is necessary to propose some phenomenological form for the potential function. Some such functions for simple molecular groups are described in Herzberg (38). The model used here for tetrahedral  $XY_4$  molecules is due to Urey and Bradley (39), and assumes harmonic forces along and perpendicular to the chemical bonds. If the distance between two Y atoms  $Y_i$  and  $Y_j$  is  $y_{ij} = y_0 + \Delta y_{ij}$ , the distance between the X atom and a particular Y atom  $Y_i$  is  $x_i = x_0 + \Delta x_i$ , and the inter-bond angle is  $\theta_i = \theta_0 + \Delta\theta_i$ , then the potential function can be written

$$2.1 \quad V = V_0 + \sum_{i=1}^4 \left[ \frac{\partial V}{\partial x_i} \Delta x_i + \frac{1}{2} \frac{\partial^2 V}{\partial x_i^2} (\Delta x_i)^2 + \frac{k_2}{2} x_0^2 (\Delta\theta_i)^2 \right] \\ + \sum_{i \neq j} \left[ \frac{1}{2} \frac{\partial V}{\partial y_{ij}} \Delta y_{ij} + \frac{1}{4} \frac{\partial^2 V}{\partial y_{ij}^2} (\Delta y_{ij})^2 \right] .$$



TABLE 2

Peak frequencies  $\omega$  ( $\text{cm}^{-1}$ ), linewidths  $\gamma$  ( $\text{cm}^{-1}$ ) and assignments for the Raman-active modes of  $\text{Zn}_4\text{B}_6\text{O}_{13}$ , with the infrared ( $F_2$ ) frequencies  $\omega_{\text{ir}}$  of references 36 and 37.

$A_1$		E		$F_2$		$\omega_{\text{ir}}$
$\omega$	$\gamma$	$\omega$	$\gamma$	$\omega$	$\gamma$	
94.7	$11.5 \pm 1.5$	89.4	$12 \pm 1$	93.1	$15 \pm 2$	
122.5	-	122.5	-			
249.3	$3 \pm 0.6$	183.0	$4 \pm 0.5$	181.6	$4 \pm 0.5$	183 <sup>c</sup>
421.9	$3 \pm 0.6$	414.5	$3.3 \pm 0.3$	196.7	$5 \pm 0.5$	204 <sup>c</sup>
		727.2	$12.5 \pm 1.5$	222.4	$2 \pm 0.5$	
		835.9	$9 \pm 1.5$	278.0	$6.5 \pm 2$	280 <sup>c</sup>
				284.2	$6.5 \pm 2$	
				471.1	$14 \pm 1.5$	478 <sup>c</sup>
				488.2	$9.5 \pm 1.5$	
				653.0	$20 \pm 6$	655 <sup>c</sup>
						750 <sup>bc</sup>
				906.2	$14 \pm 2$	930 <sup>b</sup>
				1005.0	- <sup>a</sup>	997 <sup>b</sup>
				1040.0	- <sup>a</sup>	1038 <sup>b</sup>
				1074.4	$19 \pm 1.5$	1081 <sup>b</sup>
				1189.0	$23.5 \pm 1.5$	1142 <sup>b</sup>

$\omega < 500 \text{ cm}^{-1}$ , resolution =  $1.0 \text{ cm}^{-1}$ .  
 $\omega > 500 \text{ cm}^{-1}$ , resolution =  $1.5 \text{ cm}^{-1}$ .

a) Not sufficiently resolved for meaningful measurement

b) From reference 36.

c) From reference 37.

If the potential energy  $V$  is taken to have a term  $k_3(\Delta y_{ij})^{-n}$  i.e. some inverse power of the Y-Y separation, and the requirement of equilibrium configuration stability is imposed, then:

$$2.2 \quad \frac{\partial V}{\partial x_i} = -6^{\frac{1}{2}} \frac{\partial V}{\partial y_{ij}} = \frac{6^{\frac{1}{2}n} k_3}{y_o^{n+1}} = \frac{6^{\frac{1}{2}}}{4} y_o \gamma_3 .$$

This yields a potential function in terms of three empirical force constants. These are  $k_1 = \left( \frac{\partial^2 V}{\partial x_i^2} \right)_o$ , which describes the X-Y 'central forces' interaction;  $k_2$  which relates to the bond bending; and  $\gamma_3$ , which describes the Y-Y interaction. It turns out that values of  $n$  between 5 and 9 give a good representation of the experimental results for most  $XY_4$  groups. If the determinantal equation for the normal mode frequencies  $\omega_1 - \omega_4$  is set up and solved for  $n = 7$ , these are given by the four equations:

$$2.3 \quad \omega_1^2 \equiv (k_1 + 8\gamma_3) \div m_Y$$

$$2.4 \quad \omega_2^2 \equiv (k_2 + \frac{9}{4} \gamma_3) \div m_Y$$

$$2.5 \quad \omega_3^2 + \omega_4^2 = \left( \frac{23}{2} \gamma_3 + 2k_1 + k_2 \right) \div 3m_Y \\ + (2\gamma_3 + k_1 + 2k_2) \div 3\mu$$

$$2.6 \quad \omega_3^2 - \omega_4^2 = 2 \left[ \left\{ \left( \frac{23}{2} \gamma_3 + 2k_1 + k_2 \right) \div 3 m_Y \right. \right. \\ \left. \left. - (2\gamma_3 + k_1 + 2k_2) \div 3\mu \right\}^2 + \frac{2}{9\mu m_Y} (\gamma_3 + k_2 - k_1)^2 \right]^{\frac{1}{2}}$$

where  $\mu = m_X m_Y (4m_Y + m_X)^{-1}$  is the reduced mass. The normal modes

$\omega_1, \omega_2, \omega_3$  and  $\omega_4$  transform according to the representation  $\Gamma = A_1 + E + 2F_2$  in terms of the irreducible representations of  $T_d$ . They are represented in Figure 10 and it is clear why  $\omega_1$  and  $\omega_2$  are independent of  $k_2$  and  $k_1$  respectively.

It can be seen that the three force constants can be determined from three of the equations 2.3 - 2.6, leaving the fourth as a check on the validity of the model. This was the method used by Urey and Bradley. In this work, a least squares minimisation routine was used to 'fit' the model to the frequencies  $\omega_1 - \omega_4$ , yielding three force constants and a goodness-of-fit parameter. Different combinations of the frequencies of Table 2 were tried until the best fit was obtained for ZBO, and for copper-chlorine and nickel-iodine boracite. The orders of magnitude of frequencies  $\nu_{1-4}$ , and starting values for  $k_1, k_2$  and  $\gamma_3$ , were obtained from the results of applying the fitting technique to some isolated and well known  $XY_4$  groups. This produced similar values for  $k_1, k_2$  and  $\gamma_3$  as were obtained by Urey and Bradley (39). The results for  $BO_4$  groups in ZBO and the above boracites are presented in Fig. 11 and in table 3, along with those for some other  $XY_4$  molecules. The relative intensities of the  $BO_4$  frequencies show reasonable agreement between ZBO and boracites, as do the frequencies themselves. A calculation similar to that described above, but with  $k_2 = 0$  (central forces only) produced worse fits, but the same preferred sets of frequencies  $\nu_{1-4}$ .

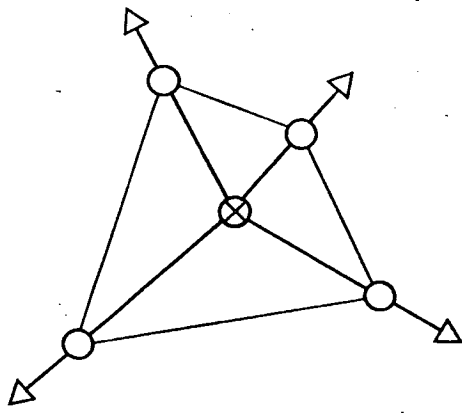
The results of this calculation must be viewed with some scepticism due to the cavalier assumption that the  $BO_4$  groups behave as free molecules. The shortcomings of this model are illustrated by the change in sign of  $\gamma_3$  from other  $XY_4$  groups. Since  $\gamma_3$  is an empirical constant, this is not altogether a damning fault, but it does indicate that the rest of the atoms in ZBO do alter the

FIGURE 10: The normal modes of vibration of a tetrahedral  $XY_4$  molecule.

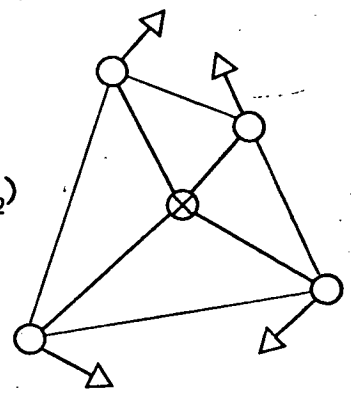
FIGURE 11: The frequencies associated with the normal vibrations of the B - O framework in  $Zn_4B_6O_{13}$ ,  $Cr_3B_7O_{13}Cl$ , and  $Ni_3B_7O_{13}I$ .

**Fig.10**

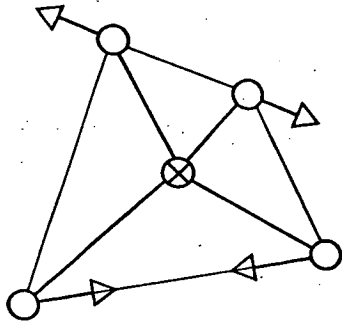
A1( $v_1$ )



E( $v_2$ )



F2( $v_3$ )



F2( $v_4$ )

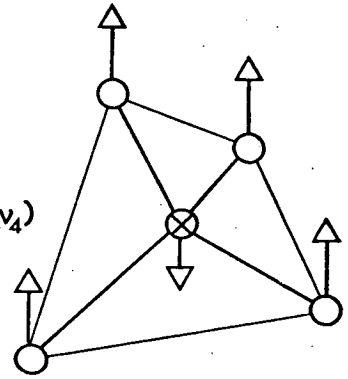


**Fig.11**

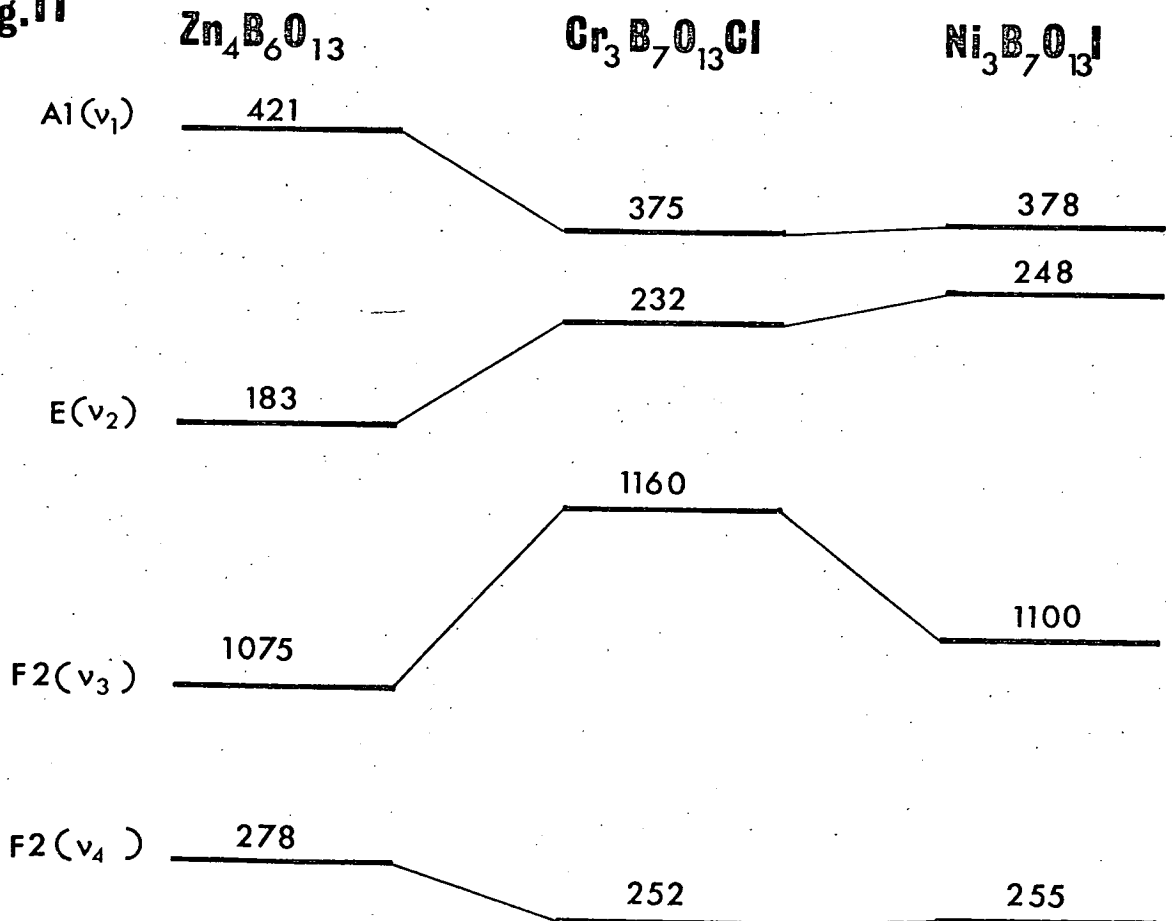


TABLE 3

Frequencies of normal modes and force constants for the Urey and Bradley model (39) for some  $XY_4$  groups (see §2.4).

Material	Frequencies ( $\text{cm}^{-1}$ )				Force constants ( $\text{Nm}^{-1}$ )		
	$\nu_1$	$\nu_2$	$\nu_3$	$\nu_4$	$k_1$	$k_2$	$\gamma_3$
$\text{CBr}_4^{\text{a}}$	265	123	667	184	141	17.8	23.8
$\text{SiCl}_4^{\text{a}}$	422	148	609	216	259	14.8	13.5
$\text{S}=\text{O}_4^{\text{b}}$	981	451	1104	613	622	111.0	35.8
$\text{Cl}=\text{O}_4^{\text{b}}$	935	462	1102	628	656	154.0	21.1
$\text{P}=\text{O}_4^{\text{b}}$	980	363	1082	515	616	42.8	36.3
$\text{Zn}_4\text{B}_6\text{O}_{13}^{\text{c}}$	421	183	1075	278	325	75.9	-19.8
$\text{Cr}_3\text{B}_7\text{O}_{13}\text{Cl}^{\text{d}}$	375	232	1160	252	345	110.0	-26.5
$\text{Ni}_3\text{B}_7\text{O}_{13}\text{I}^{\text{e}}$	378	248	1100	255	295	103.0	-20.1

- a) Reference 39
- b) Reference 38
- c) Reference 26
- d) Reference 26
- e) See Chapter 3.

environment of the  $\text{BO}_4$  groups significantly. Furthermore, the  $\nu_1$  frequency is lower than might have been expected. Nevertheless, it appears that frequencies at about  $400 \text{ cm}^{-1}$  ( $A_1$ ),  $200 \text{ cm}^{-1}$  (E) and  $1100 \text{ cm}^{-1}$ ,  $260 \text{ cm}^{-1}$  ( $F_2$ ) are characteristic of a B - O framework containing  $\text{BO}_4$  tetrahedra. It would, in theory, be possible to set up a more complicated expression for the potential of the crystal, and solve for the phonon dispersion curves at  $q \approx 0$  (10). For a crystal as complicated in structure as ZBO or the boracites, however, this is outwith the scope of this thesis.

## §2.5 Symmetry Conclusions

From table 2 it can be seen that the  $A_1$  and E Raman spectra are not totally in agreement with the group theoretical predictions, as both contain one mode too many. The Raman data would seem to suggest that the  $122.5 \text{ cm}^{-1}$  mode is spurious. However, the infrared data (36, 37) shows the presence of an  $F_2$  mode at  $750 \text{ cm}^{-1}$ , absent from the Raman spectrum. It is now thought, therefore, that the modes at around  $90 \text{ cm}^{-1}$  are the origin of the discrepancy. Apart from the  $750 \text{ cm}^{-1}$  mode, the agreement between Raman and infrared results is good. The 'extra' modes are thought to be attributable to some local vibrations associated with impurity ions. Terol and Otero (35) remarked that the 'cavities' in the B - O framework are large enough to accommodate impurity ions. Their results indicate, furthermore, that the fluorescence observed in the survey Raman spectra is due to the presence of some Mn carried over from the growth materials as an impurity, giving a luminescence peak at 540 nm. This is confirmed as a possibility by Schmid (40). The concentration of Mn would be

too small to produce an impurity mode with an appreciable normal Raman cross-section, and the spurious features are attributed tentatively to some iodine species (perhaps HI) trapped within the B - O framework.

The  $A_1$  and E symmetry interference bands are of interest, as resonant interference of this type has only rarely been observed (e.g.  $\text{SiO}_2$  (41),  $\text{AlPO}_4$  (42) and  $\text{BaTiO}_3$  (43)). Interference between modes most commonly occurs when a soft mode associated with a phase transition overlaps in frequency another mode of the same symmetry species as temperature or pressure is varied. The interaction commonly results in asymmetric peaks, and two models are used here to describe the resultant cross-section.

The first model, in §2.6, involves coupling between two phonons, via anharmonicity, whose lifetimes are widely different. The second model, described in §2.7, is due to Fano (44) and was developed to describe the phase shifts in atomic state wavefunctions, and the resultant excitation spectra, due to the configuration interaction between a discrete state and a continuum of states. This interaction produces asymmetries in the continuous absorption bands of atomic and molecular systems.

## §2.6 The Coupled Modes Model

This model exploits the properties of the one-phonon thermodynamic Greens function as described in §1.5 and Appendix 1. It is assumed for this description that the feature at  $122.5 \text{ cm}^{-1}$  is attributable to the interaction between two first-order phonons. The most general form for  $G_{ab}(\omega)$  is obtained from equation 1.53, in matrix form:



$$2.7 \quad \begin{bmatrix} \omega_a^2 - \omega^2 + 2\omega_a(\Delta_{aa} + i\Gamma_{aa}) & 2\omega_a(\Delta_{ab} + i\Gamma_{ab}) \\ 2\omega_b(\Delta_{ba} + i\Gamma_{ba}) & \omega_b^2 - \omega^2 + 2\omega_b(\Delta_{bb} + i\Gamma_{bb}) \end{bmatrix} \\ \times \begin{bmatrix} G_{aa} & G_{ab} \\ G_{ba} & G_{bb} \end{bmatrix} = \frac{2}{\beta\hbar} \begin{bmatrix} \omega_a & . \\ . & \omega_b \end{bmatrix}$$

This rather complicated expression can be simplified, within certain approximations, to provide a more tractable function for a computer fitting process.

Firstly, it is useful to consider the three lowest order contributions to the vertex part of Dyson's equation. These are represented in Figure 12. It can be shown (21) that 12a and 12b contribute a temperature dependent term  $A_{ab}(T)$  to  $S_{ab}(\omega)$ , and that the addition of 12c gives  $S_{ab}(\omega)$  of the form

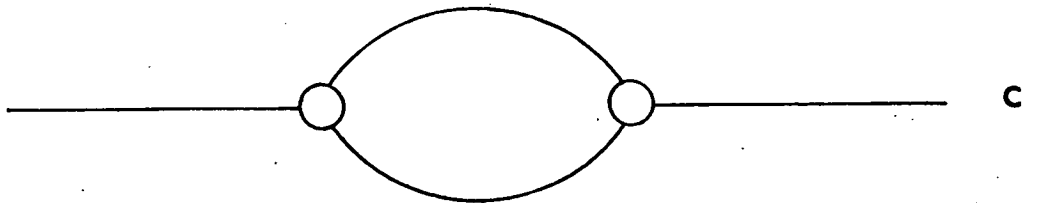
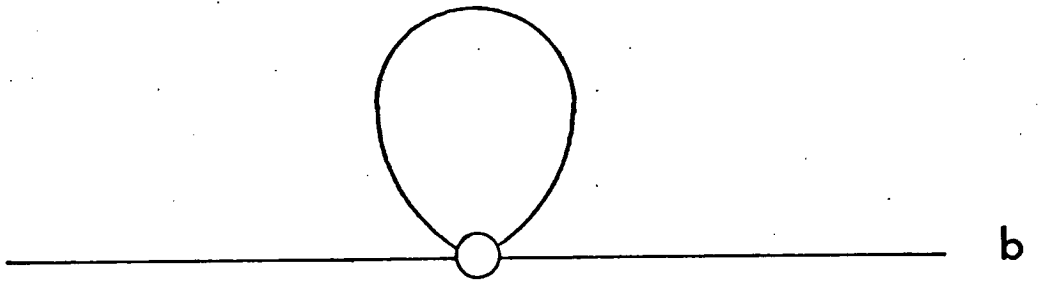
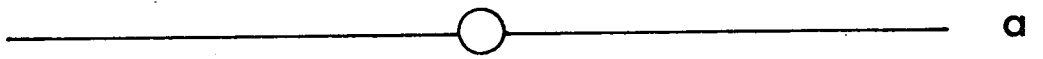
$$2.8 \quad S_{ab}(\omega) = A_{ab}(T) - \frac{18}{\hbar^2} \sum_{Y_1 Y_2 cd} v \begin{pmatrix} 0 & -Y_1 & -Y_2 \\ a & c & d \end{pmatrix} v \begin{pmatrix} 0 & Y_1 & Y_2 \\ b & c & d \end{pmatrix} \\ \times \{ (n_c + n_d + 1) \left[ (\omega_c + \omega_d + \omega)_P^{-1} + (\omega_c + \omega_d - \omega)_P^{-1} \right] \\ + (n_d - n_c) \left[ (\omega_c - \omega_d + \omega)_P^{-1} + (\omega_c - \omega_d - \omega)_P^{-1} \right] \\ + i(n_c + n_d + 1) \left[ \delta(\omega_c + \omega_d + \omega) - \delta(\omega_c + \omega_d - \omega) \right] \\ + i(n_d - n_c) \left[ \delta(\omega_c - \omega_d + \omega) - \delta(\omega_c - \omega_d - \omega) \right] \}$$

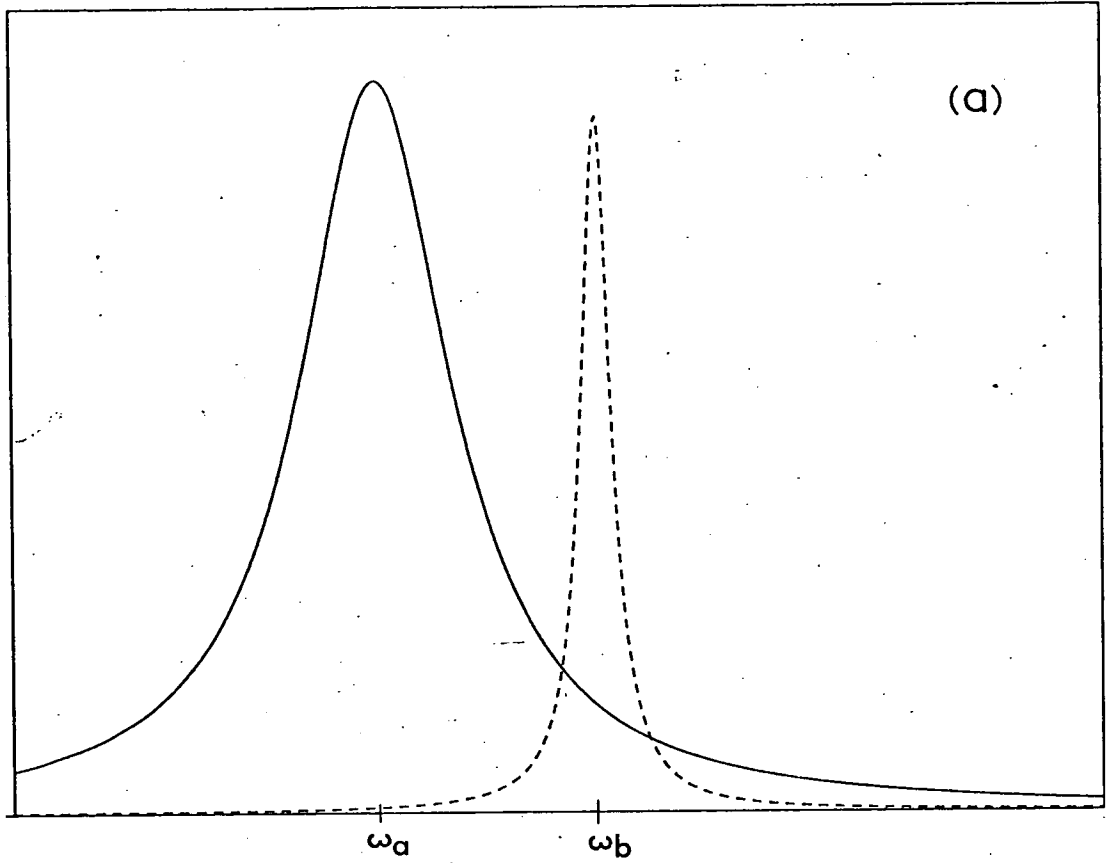
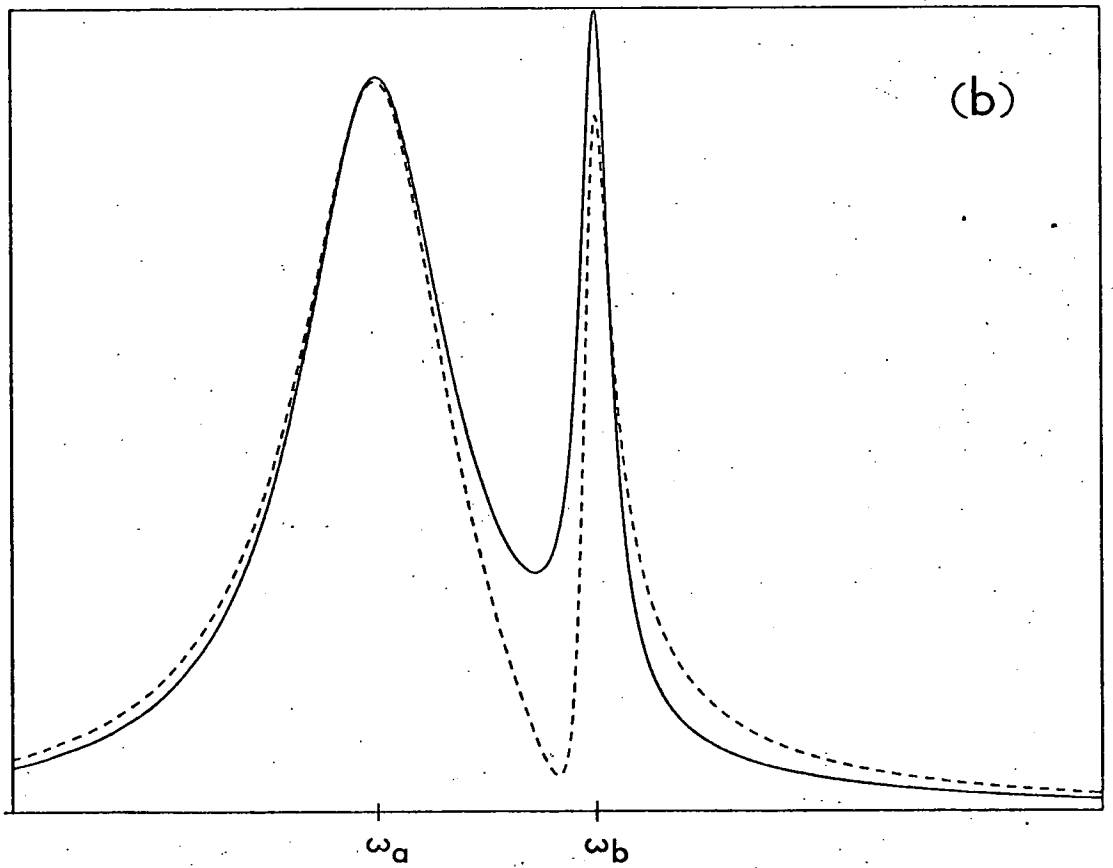
where subscript 'P' denotes 'Principal part'. In the  $(\omega, T)$  region  $\hbar\omega \ll kT$ , it can be seen that  $S_{ab}(\omega)$  can be approximated by

FIGURE 12: The three lowest order contributions to the vertex-part of equation A1.7, Dyson's equation.

FIGURE 13: The lineshape resulting from two Raman active modes where  $\Gamma_a = 5\Gamma_b$  &  $\Gamma_{ab} = 2\Gamma_a$ . Figure 13a represents modes 'a' and 'b', uncoupled and figure 13b gives the total crosssection in the uncoupled (solid line) and coupled (broken line) cases.

FIG. 12



$\text{Im}(G(\omega)) * \text{BOSEFACTOR}$  $\text{Im}(G(\omega)) * \text{BOSEFACTOR}$ 

$$2.9 \quad S_{ab}(\omega) \approx A_{ab}(T) + B_{ab}(T, \omega) + iC_{ab}(T, \omega)$$

where A, B, C are all symmetric with respect to the indices a, b.

Furthermore, B is an even function of  $\omega$ , and C is odd. If B is approximated by B(T) and C by  $\omega C(T)$ , then the large matrix of 2.7 may be written

$$2.10 \quad \begin{bmatrix} \omega_a^2 - \omega^2 + 2\omega_a(\Delta_a + i\omega\Gamma_a) & 2\omega_a(\Delta_{ab} + i\omega\Gamma_{ab}) \\ 2\omega_b(\Delta_{ab} + i\omega\Gamma_{ab}) & \omega_b^2 - \omega^2 + 2\omega_b(\Delta_b + i\omega\Gamma_b) \end{bmatrix}.$$

Apart from a constant factor  $\hbar \div 2\sqrt{\omega_a \omega_b}$ , this is  $G^{-1}(\omega)$  and  $\Delta_a, \Delta_b$  may now be interpreted as shifts in the zero position of  $(\omega_a^2 - \omega^2)$ ,  $(\omega_b^2 - \omega^2)$  and therefore in the peak position. The net result is that the intensity of Raman scattering may be written, from equations 1.50 and 2.10:

$$2.11 \quad I d\omega_f d\omega = \sum_{\substack{a,b \\ =1,2}} P_a P_b \text{Im } G_{ab}(\omega)$$

$$2.12 \quad \text{where } G^{-1}(\omega) = \begin{bmatrix} \omega_a^2 - \omega^2 + i\Gamma_a \omega & \Delta_{ab} + i\Gamma_{ab} \omega \\ \Delta_{ab} + i\Gamma_{ab} \omega & \omega_b^2 - \omega^2 + i\Gamma_b \omega \end{bmatrix}.$$

It should be noted that  $\omega_a, \omega_b$  are now the shifted characteristic frequencies, and the  $\Delta$  and  $\Gamma$  parameters have also been trivially redefined. The parameters  $\omega_a, \omega_b, \Gamma_a, \Gamma_b, \Delta_{ab}$  and  $\Gamma_{ab}$  may now be regarded as adjustable fitting parameters, and the  $P_a, P_b$  as 'strength' parameters. Performing a suitable unitary transformation

on  $G^{-1}$  renders either its real or imaginary part diagonal, corresponding to 'purely imaginary or real coupling' respectively. With a further redefinition of the remaining parameters, this gives 2.10 with either  $\Delta_{ab}$  or  $\Gamma_{ab} = 0$ . The choice of real or imaginary coupling is purely arbitrary unless a soft mode is involved, as in Chapter 3 where the distinction is discussed in detail.

Figure 13a represents a response function of the form of 2.11 and 2.12 with  $\Gamma_a = 5\Gamma_b$  and  $\Delta_{ab} = \Gamma_{ab} = 0$ . This is usually referred to as two 'uncoupled' modes. For 13b,  $\Gamma_{ab} = 2\Gamma_a$ , and the effect of 'coupling' the modes is evident in the pronounced asymmetry of the sharper feature in particular.

## §2.7 The Fano Model

This model (44) makes use of the fact that the interference of a discrete state with a continuum of states gives rise to asymmetric peaks in the excitation spectrum.

If we represent the discrete state by  $|p\rangle$ , the continuum states by  $\{|\psi_E\rangle\}$ , and the perturbed wavefunction of eigenvalue  $E$  by  $|\phi_E\rangle$ , we are concerned with the cross-section  $\sigma_1(\omega)$  for transitions from some state  $|i\rangle$  to  $|\phi_E\rangle$ , which for a transition operator component  $P_{xy}$  (see 1.33) is proportional to  $|\langle\phi_E|P_{xy}|i\rangle|^2$ . The matrix elements of the total Hamiltonian  $H$  are given as:

$$2.13 \quad H|p\rangle = E_p|p\rangle$$

$$2.14 \quad \langle\psi_E|H|p\rangle = V_E$$

$$2.15 \quad \langle\psi_{E'}|H|\psi_{E''}\rangle = E' \delta(E' - E'').$$

The state  $|\phi_E\rangle$  must now be written as an admixture of  $|p\rangle$  and  $\{|\psi_{E'}\rangle\}$ .

$$2.16 \quad |\phi_E\rangle = a(E)|p\rangle + \int b(E')|\psi_{E'}\rangle dE'$$

When this expression is applied to 2.14 and 2.15, it is found (44) that the parameter  $b$  describes a relative phase of  $|p\rangle$  and the  $\{|\psi_{E'}\rangle\}$  in 2.16, which varies by  $\pi$  as  $E$  traverses the 'resonance energy'  $E_0$ :

$$2.17 \quad E_0 = E_p + P \int |V_{E'}|^2 dE' \div (E_0 - E')$$

It is this variation of wavefunction phase that is responsible for the different contributions to  $|\phi_E\rangle$  from the  $\{|\psi_{E'}\rangle\}$  on either side of the resonance, giving rise to asymmetries. The variable  $a(E)$  describes a 'smearing out' of  $|p\rangle$  in 2.16 through a region given by, roughly,  $|E - E_0| \leq |V_E|^2$ , the region of rapid phase variation, such that the perturbed state  $|\phi_E\rangle$  contains an admixture of  $|p\rangle$  given by, in 2.16,

$$2.18 \quad a(E) \approx \frac{|V_E|^2}{(E - E_0)^2 + \pi^2 |V_E|^4}$$

It can be shown by combining 2.16 with the explicit form of the phase-shift parameter  $b(E)$ , that  $\sigma_1(\omega)$  can be obtained from the expression

$$2.19 \quad \begin{aligned} |\langle \phi_E | P_{xy} | i \rangle|^2 &= |\langle \psi_E | P_{xy} | i \rangle|^2 \\ &\times \left( \frac{\langle p | P_{xy} | i \rangle}{\pi V_E^* \langle \psi_E | P_{xy} | i \rangle} + \frac{E - E_0}{\pi |V_E|^2} \right)^2 \\ &\div \left( 1 + \left( \frac{E - E_0}{\pi |V_E|^2} \right)^2 \right) \end{aligned}$$

where

$$2.20 \quad |\tilde{p}\rangle = |p\rangle + P \int V_{E'} |\psi_{E'}\rangle dE' \div (E - E').$$

Introducing new variables  $q(E)$  and  $\Gamma(E)$ ,  $\sigma_1(\omega)$  may be written in terms of the cross-section  $\sigma_0(\omega)$  for scattering from  $|i\rangle$  to  $|\psi_E\rangle$ ,

$$2.21 \quad \sigma_1(\omega) = \frac{\sigma_0(\omega) \left( q + \frac{\omega - \omega_0}{\frac{1}{2}\Gamma} \right)^2}{\left( 1 + \left( \frac{\omega - \omega_0}{\frac{1}{2}\Gamma} \right)^2 \right)}$$

$$2.22 \quad q = \frac{\langle \tilde{p} | P_{xy} | i \rangle}{\pi V_E^* \langle \psi_E | P_{xy} | i \rangle} ; \quad \frac{E - E_0}{\pi |V_E|^2} = \frac{\omega - \omega_0}{\frac{1}{2}\Gamma}$$

Regarding the quantities  $q, \Gamma$  as constant over the range of interest, 2.21 defines a family of curves for different  $q$ , which are depicted in Figure 14. Fano also showed that when more than one continuum is present (e.g. many orders of multiphonon scattering), the cross-section may be written as

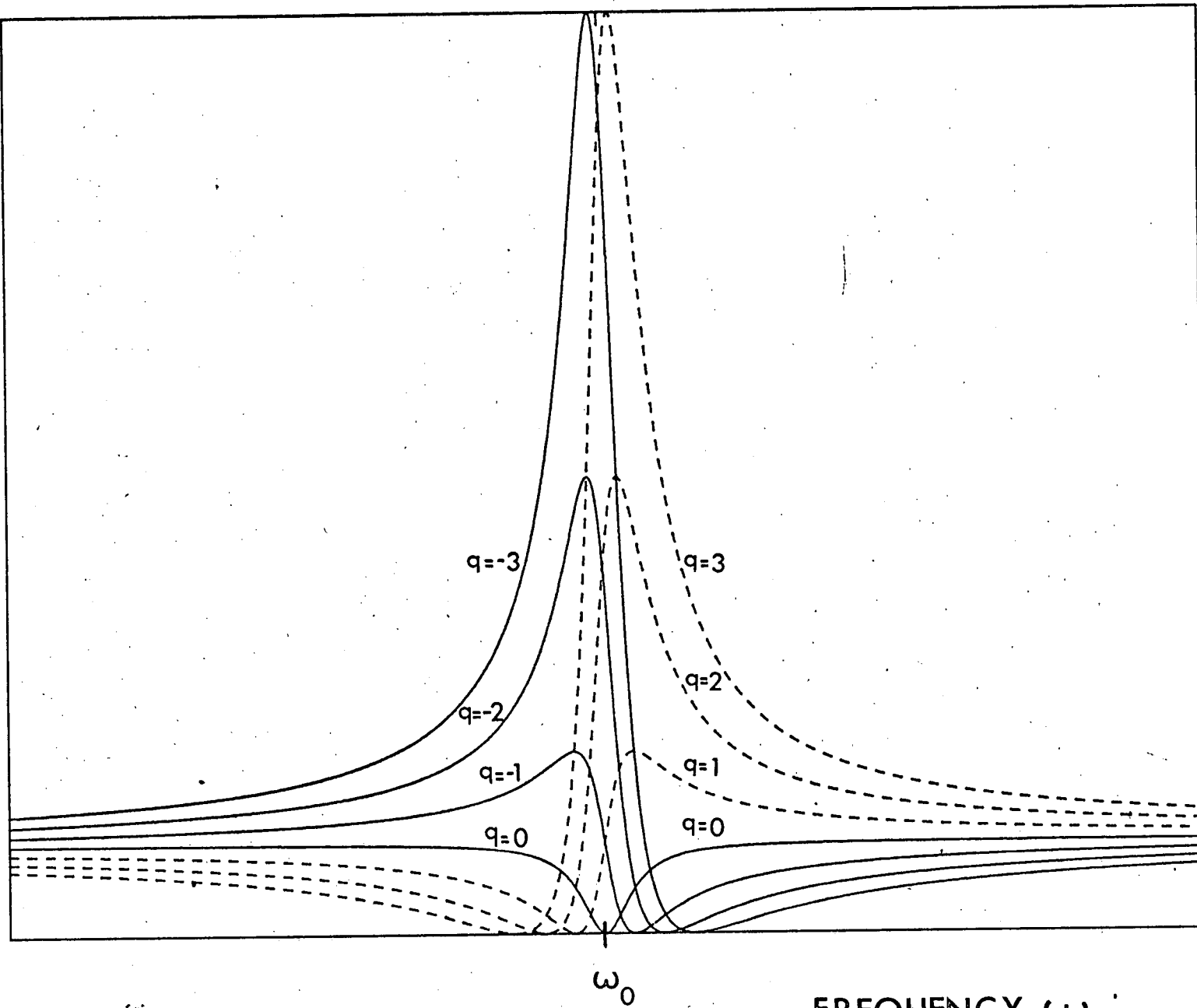
$$\sigma(\omega) = \sigma_1(\omega) + \sigma_2(\omega)$$

where  $\sigma_2(\omega)$  corresponds to the underlying noninteracting continua, and  $\sigma_0(\omega)$  is redefined as a particular linear combination of continua. It is worth remarking that the state  $|p\rangle$  is assumed to decay only into the continuum, and that this interaction alone is responsible for its noninfinite lifetime.



FIGURE 14: The shape of function 2.21 for different values of the parameter  $q$ .

$$\left[ q + \frac{\omega - \omega_0}{\Gamma/2} \right]^2 \cdot \left[ 1 + \left[ \frac{\omega - \omega_0}{\Gamma/2} \right]^2 \right]^{-1}$$



§2.8 Comparison with Experiment

Three functions derived from §2.6 and §2.7 were used to perform a computer least squares fit to the observed room temperature  $A_1$  and E spectra of ZBO (28). These are as follows:-

Coupled Modes:

A lineshape of the form 2.12 may be used to describe the spectra between  $70 \text{ cm}^{-1}$  and  $140 \text{ cm}^{-1}$ , provided it is extended to have a  $G_{cc}$  similar to  $G_{aa}$  and  $G_{bb}$ , and  $G_{ac} = G_{bc} = 0$ . With a flat, continuous background and  $\Delta_{ab} = 0$ , this corresponds to two coupled modes and one uncoupled mode, corrected for photomultiplier dark current and noninteracting continua. Figure 15 and table 4 summarise the results of this analysis.

Table 4 : Coupled mode parameters ( $\text{cm}^{-1}$ )

	$\omega_a$	$\Gamma_a$	$\omega_b$	$\Gamma_b$	$\Gamma_{ab}$	$\omega_c$	$\Gamma_c$
$A_1$	124.4	4.3	143.1	73.6	12.4	94.9	11.8
E	123.8	1.8	163.8	103.2	7.2	90.2	12.2

Fano Interference (I):

For the  $70 \text{ cm}^{-1} - 140 \text{ cm}^{-1}$  region to be described by the Fano model, a diagonal  $2 \times 2$  Greens function must be included to describe the noninteracting modes 'b' and 'c' above, as well as a constant background as before. This gives the same number of variable parameters as the coupled mode model, and results in Figure 16 and table 5.

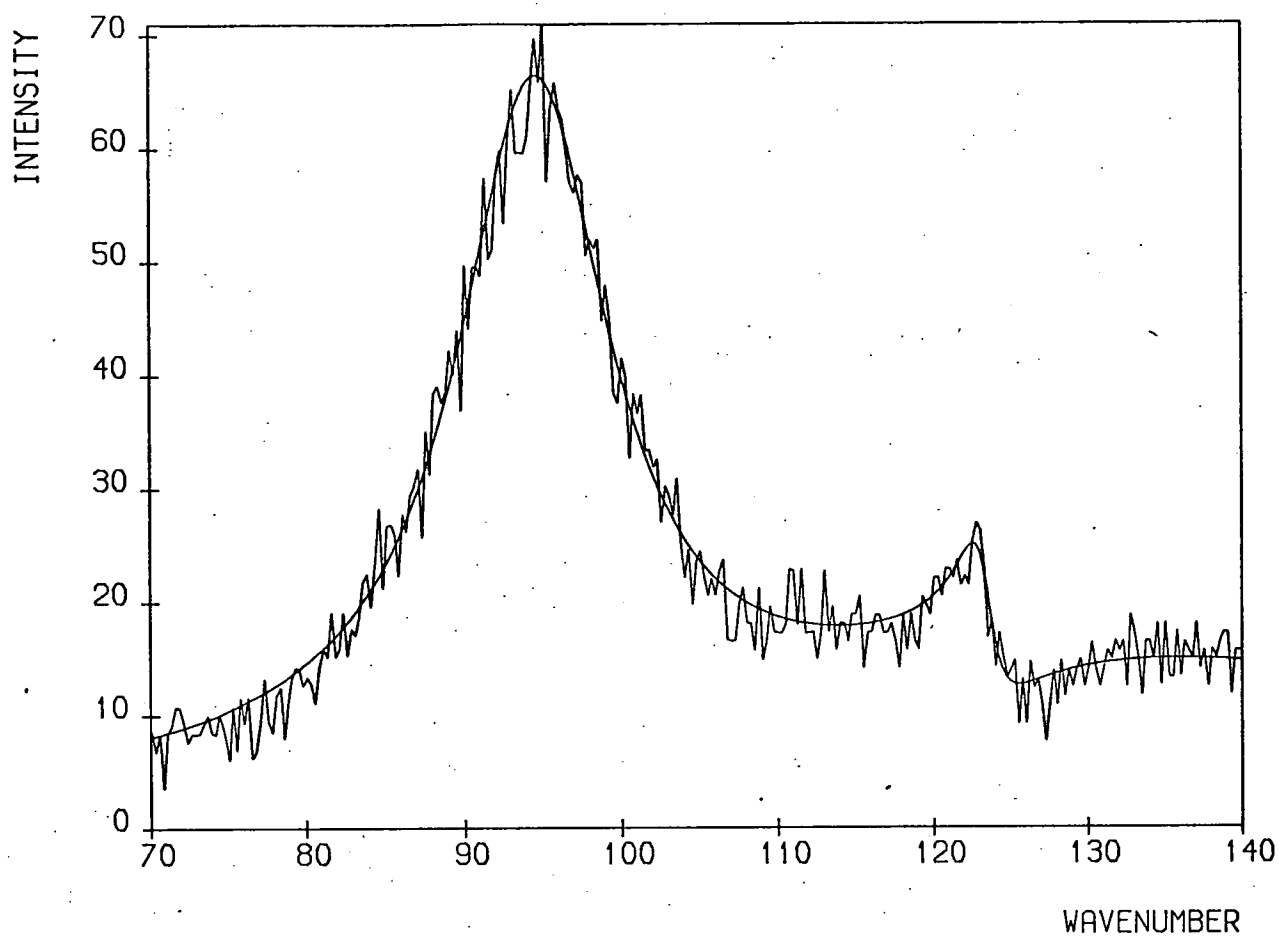
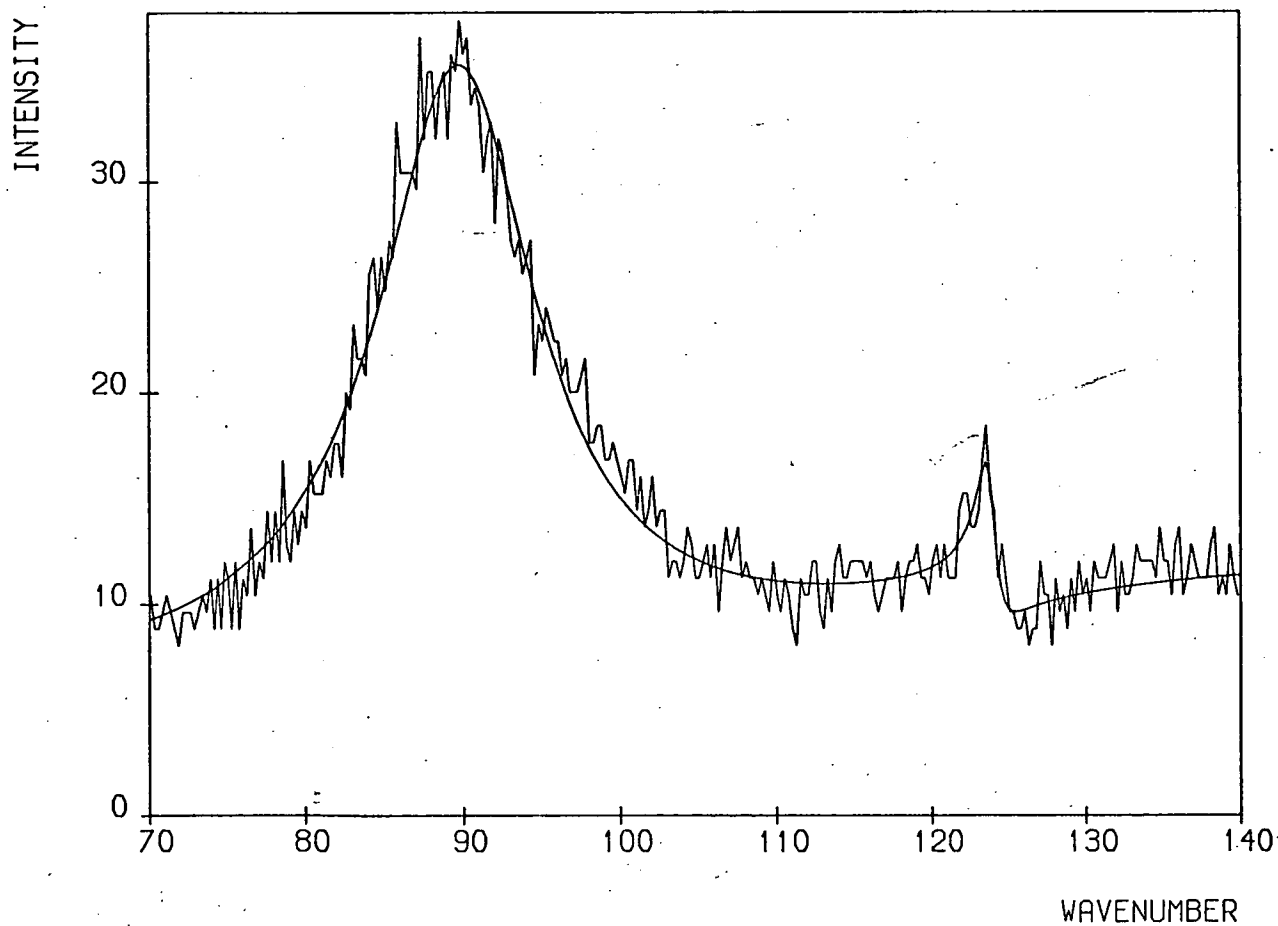
FIGURES 15 and 16: Experimental and theoretical forms for the room temperature  $A_1$  and E spectra of zinc metaborate in the frequency region  $70 - 140 \text{ cm}^{-1}$ .

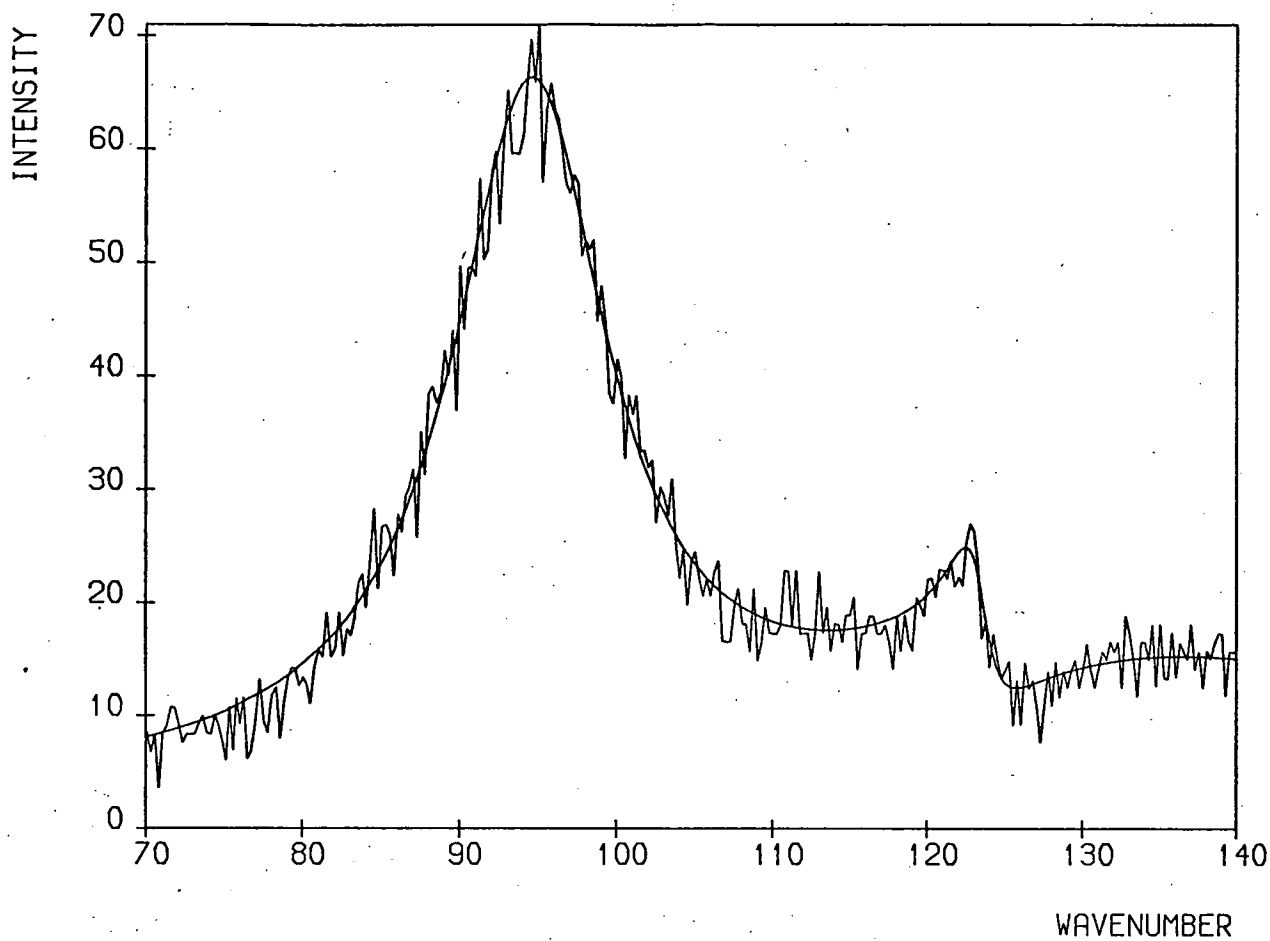
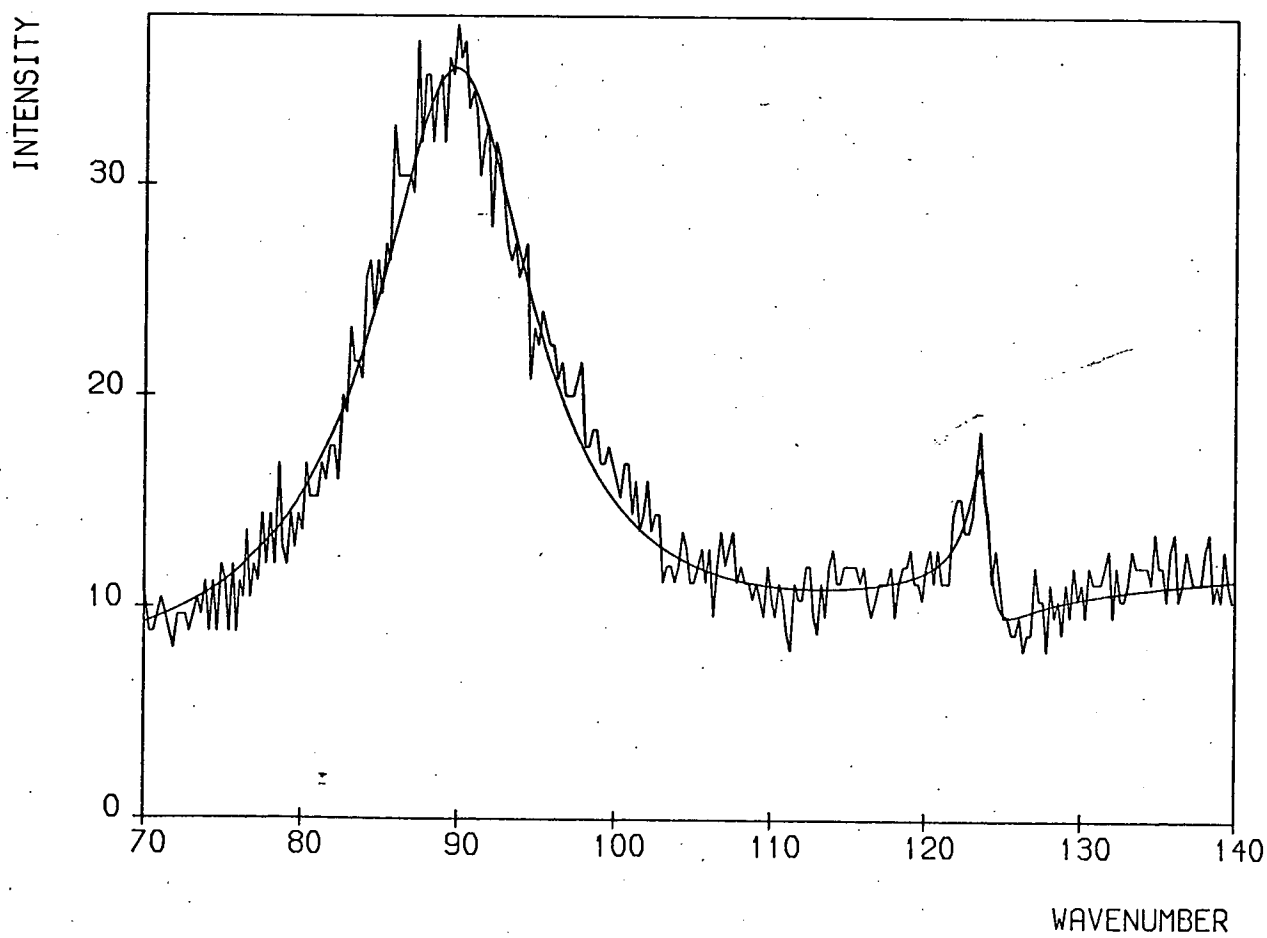
FIGURE 15: Described by the coupled modes model.

FIGURE 16: Described by the Fano model (I).

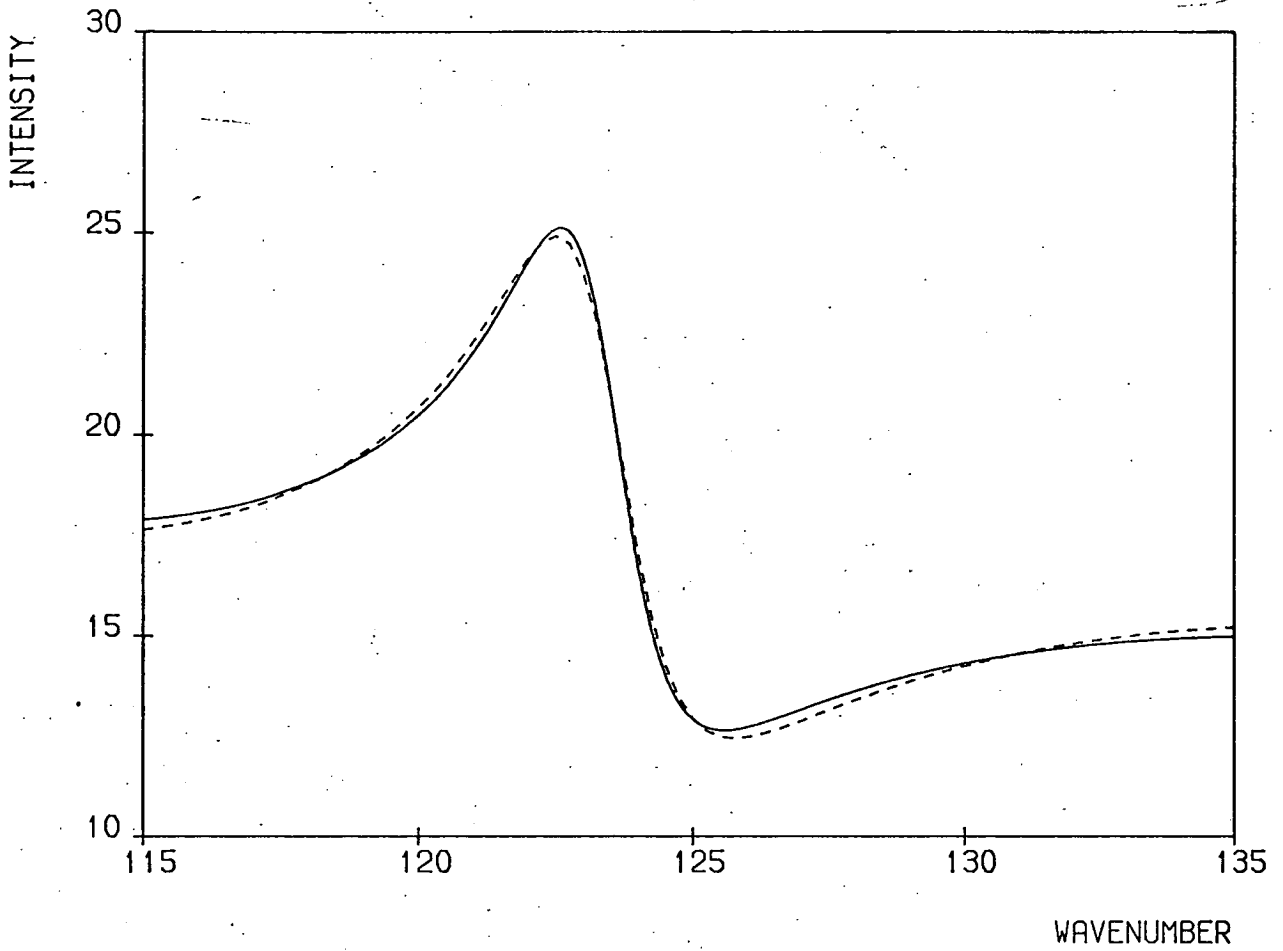
FIGURE 17: The theoretical fits of figures 15 and 16 enlarged over the frequency range  $115 - 135 \text{ cm}^{-1}$ .

FIGURE 18: Experimental and theoretical forms for the  $A_1$  spectrum of  $\text{Zn}_4\text{B}_6\text{O}_{13}$ , described by the Fano model (II).

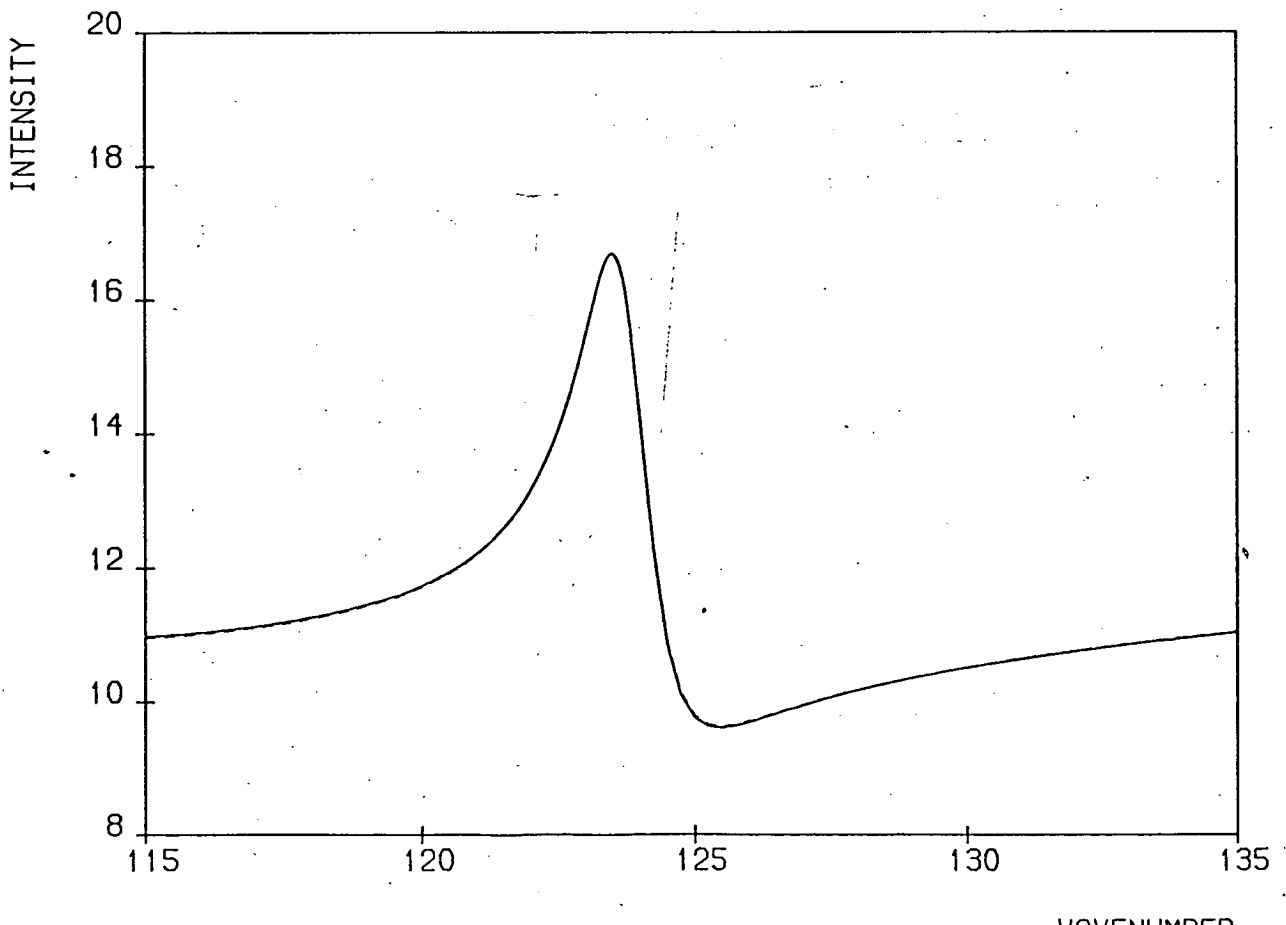
$Zn_4B_6O_{13}$  A1, COUPLED MODES $Zn_4B_6O_{13}$  X' (Y' X') Y' COUPLED MODES

$Zn_4B_6O_{13}$  A1, FANO MODEL $Zn_4B_6O_{13}$  X' (Y' X' ) Y' FANO MODEL

A1 COUPLED MODES ———, FANO - - -



E COUPLED MODES ———, FANO - - -



Zn<sub>4</sub>B<sub>6</sub>O<sub>13</sub> A1 FANO MODEL (MODIFIED)

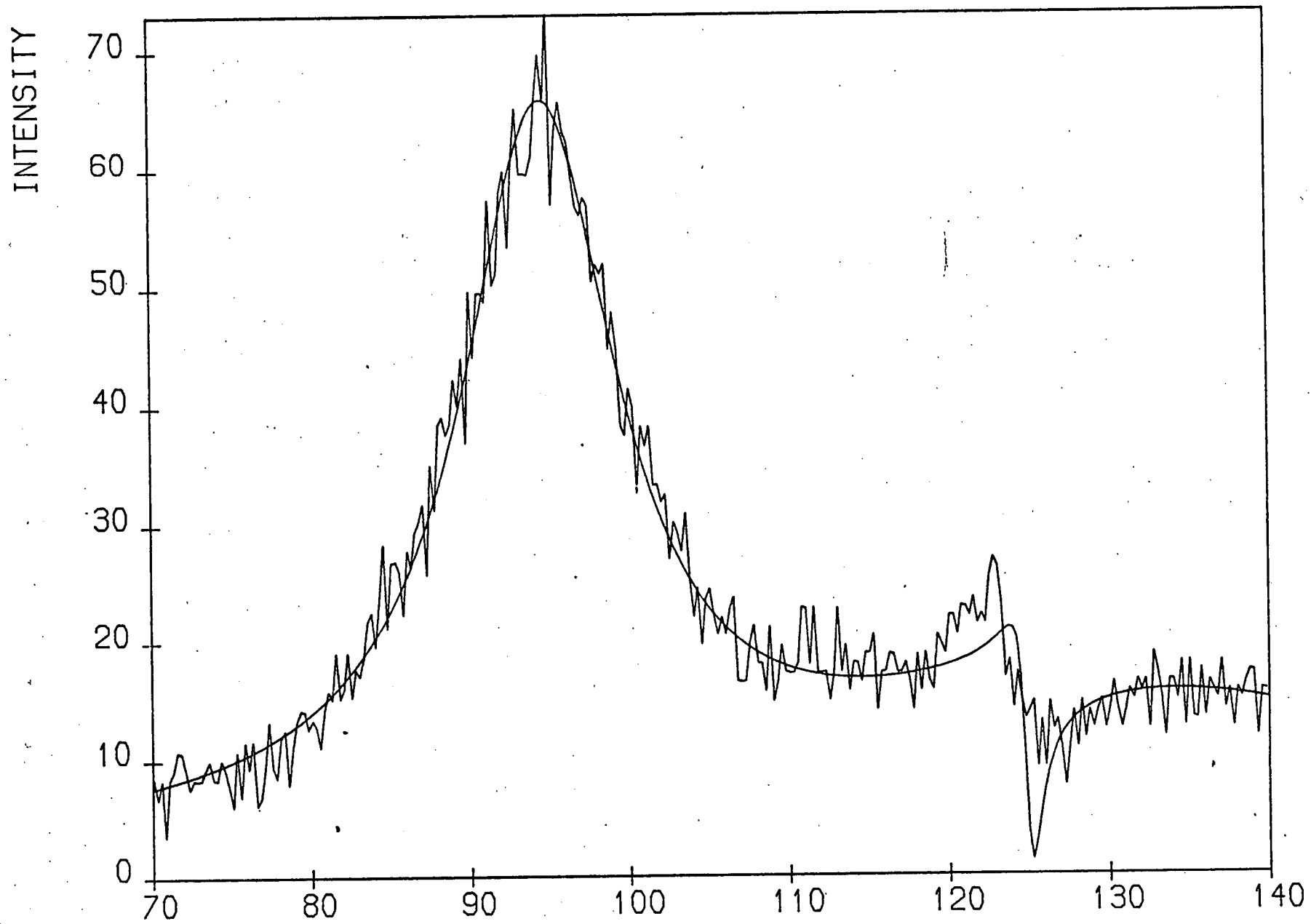


FIG 18

WAVENUMBER



Table 5 : Fano Model Parameters

	q	$\omega_o$ (cm <sup>-1</sup> )	$\Gamma$ (cm <sup>-1</sup> )	$\omega_b$ (cm <sup>-1</sup> )	$\Gamma_b$ (cm <sup>-1</sup> )	$\omega_c$ (cm <sup>-1</sup> )	$\Gamma_c$ (cm <sup>-1</sup> )
A <sub>1</sub>	-1.59	123.5	3.06	141.5	63.4	95.0	12.0
E	-2.26	123.9	1.49	163.2	101.6	90.2	12.3

The parameters describing the noninteracting modes are in good agreement with those of Table 4, although they now describe uncoupled modes. The fitted spectra of Figure 15 are indistinguishable from those of Figure 16 unless enlarged (Figure 17). The goodness-of-fit test shows that the Fano description is less than one per cent better in both A<sub>1</sub> and E symmetries, which is hardly significant.

#### Fano Interference (II):

Following the reasoning of Rousseau and Porto (43) an analysis was attempted with  $\sigma_o$  in 2.21 represented by an anharmonic oscillator function, and  $\sigma_1$  by a constant. This gave a poor fit (Figure 18), with parameter values of  $q = -0.5$ ,  $\omega_o = 125.0$  cm<sup>-1</sup> and  $\Gamma = 1.2$  cm<sup>-1</sup> for the A<sub>1</sub> spectrum. Convergence proved impossible for the E spectrum.

#### §2.9 Conclusions

Firstly, the Fano model (II) may be dismissed as an inadequate description of the interference feature in ZBO. The coupled modes model and the Fano model (I) are indistinguishable within the accuracy of the experiment. For the coupled modes model of §2.6 to be valid, the modes at 143.1 cm<sup>-1</sup> (A<sub>1</sub>) and 163.8 cm<sup>-1</sup> (E) would have to be first order.

This would mean that Figures 15 each comprises three first order bands. This would increase the number of  $A_1$  and E normal modes by one in both cases, which would further contradict the group theoretical prediction of §2.1. For this reason it is concluded that the Fano model (I) description is more significant for ZBO. A brief study of the temperature dependence of the interference feature revealed only 'normal' sharpening effects, with no evidence of decoupling.

CHAPTER 3

THE PECULIAR PARAELECTRIC PHASE OF NICKEL IODINE BORACITE

Introduction to Boracite Properties

The boracites are the family of compounds with the generalised formula  $M_3B_7O_{13}X$ , where M is a divalent metal and X a halogen or chalcogen, which exhibit intriguing ferroelectric, magnetic and structural properties. These properties are reviewed exhaustively by Nelmes (45) but a summary of the details relevant to this thesis is given below. A boracite is conveniently referred to by its metal and halogen/chalcogen only (e.g.  $Ni_3B_7O_{13}I = Ni - I$ ).

Most halogen boracites undergo a transition from a high temperature, cubic, paraelectric phase of symmetry  $T_d^5$  to a low temperature, orthorhombic, ferroelectric phase of symmetry  $C_{2v}^5$ . The transition temperature  $T_c$  can be as high as 798K (Cd - Cl, ref. 34) or as low as 68K (Ni - I, refs. 45, 46, 47), and is that of a 'coupled' transition, giving an improper ferroelectric. These terms will be defined more fully in Chapter 4, but the essential point is that the primary order parameter is not the spontaneous polarisation at an improper ferroelectric transition. The primary order parameter is defined to be a quantity whose non-zero value below  $T_c$  leads to the appropriate group symmetry change (48). The improper transition is itself a stimulus to interest in boracites, but their magnetoelectric properties provide an added basis for speculation as to device applications.

Many transition-metal boracites become ferromagnetic, with a concomitant onset of weak antiferromagnetism, at a transition (Néel)

temperature  $T_N \leq T_C$ . The interesting feature of this phenomenon is that it has been shown in Ni - I (49) that the mutually perpendicular spontaneous electric and magnetic polarisations for  $T < T_N$  ( $\underline{P}_s$  and  $\underline{M}_s$  respectively) are coupled. In fact, we can write the electric and magnetic dipole moments as:

$$\underline{P} = \underline{\chi} \cdot \underline{H} ; \quad \underline{M} = \underline{\chi} \cdot \underline{E}$$

where  $\underline{\chi}$  is the magnetoelectric susceptibility tensor, which is of the form

$$\underline{\chi} = \begin{bmatrix} \cdot & \cdot & \cdot \\ \cdot & \cdot & \chi_{yz} \\ \cdot & \chi_{zy} & \cdot \end{bmatrix}$$

Thus, switching of  $\underline{P}_s$  from  $[001]$  to  $[00\bar{1}]$  rotates  $\underline{M}_s$  from  $[110]$  to  $[1\bar{1}0]$ , and vice versa. Boracites are almost unique in displaying this property.

Since this chapter is concerned with only the idiosyncrasies of the cubic phase of Ni - I, a discussion of the known properties for  $T > T_C$  is given in §3.1. The discussion of the transition(s) in Ni - I, and of improper transitions in general, is deferred to Chapter 4. While graphical representations of the variation with temperature of normal mode frequencies and damping parameters are included in this chapter and the next, the tabulated values of these parameters are relegated to Appendix II, in most cases. This is done to avoid fragmenting the text unnecessarily, and because the actual numbers are not, in general, essential to the arguments. The details



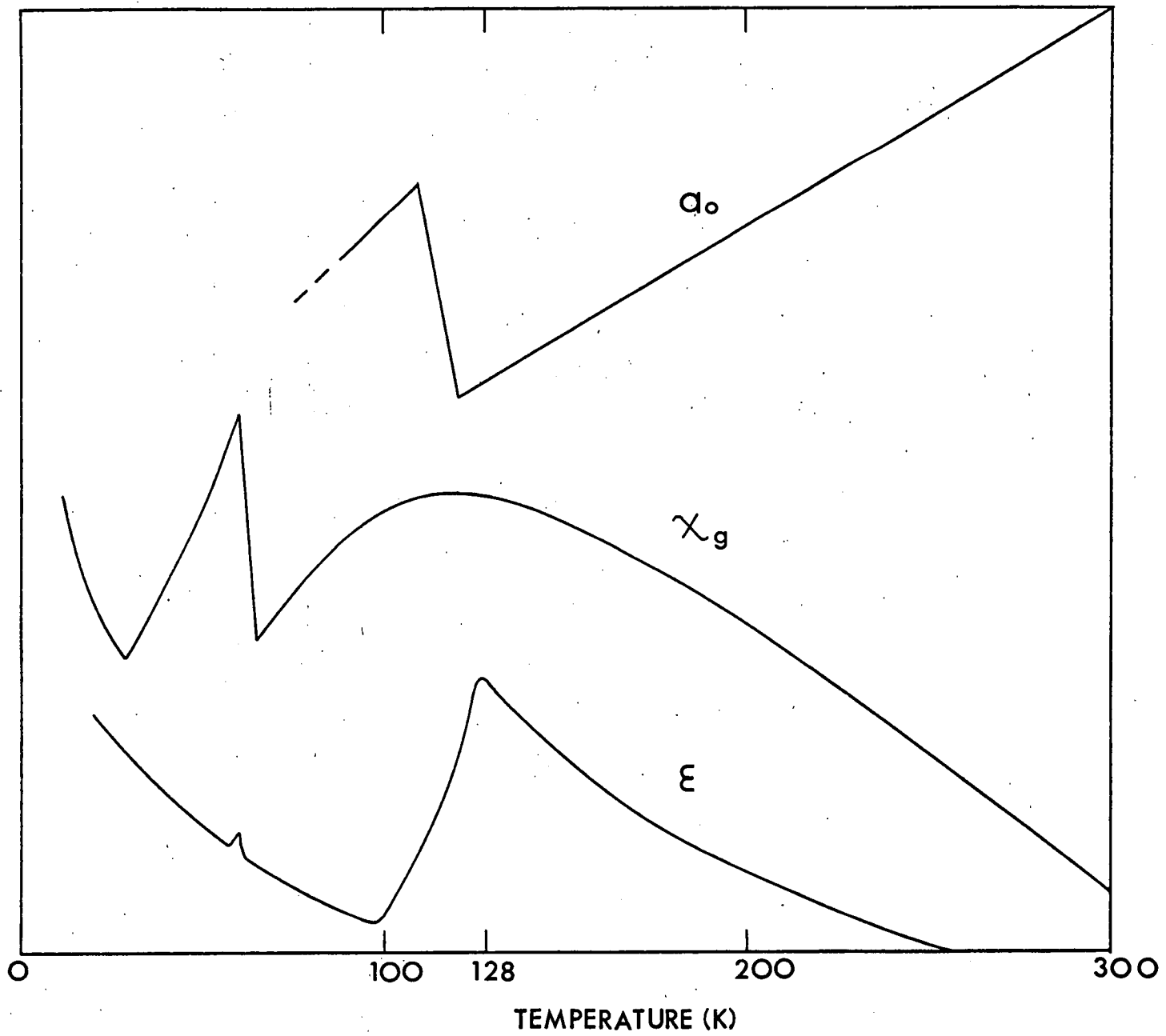
of the experiment are given in §3.2, and the group theoretical predictions and experimental results are described in §3.3. In §3.4, the analytical methods for data reduction are outlined, and in §3.5 - §3.7 the classification of cubic phase modes, and their temperature variation throughout the cubic phase are discussed, and conclusions are drawn.

### §3.1 Properties of Cubic Ni - I

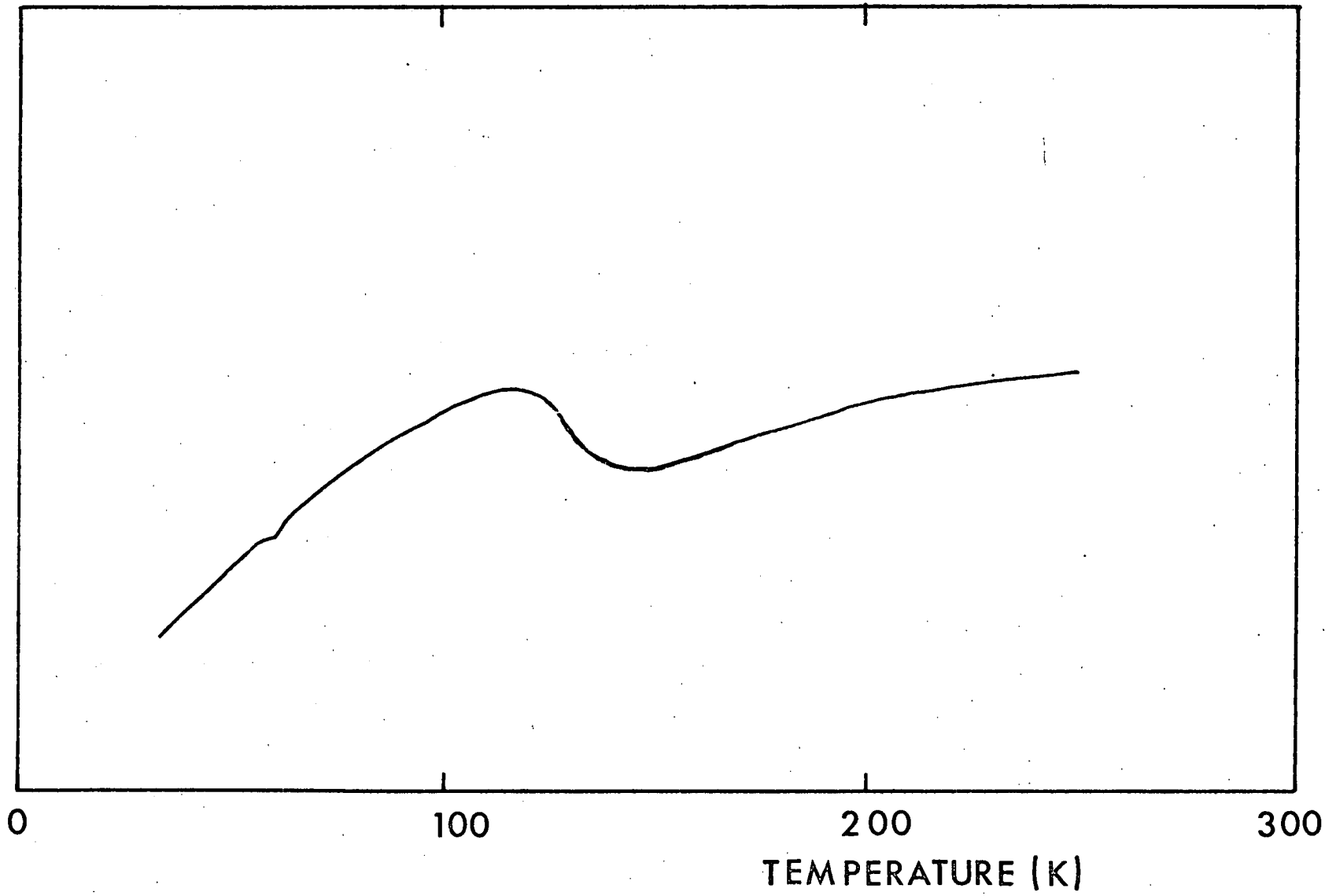
Ni - I has been shown to have the nonsymmorphic cubic space group  $T_d^5$  at room temperature (50) and 77K (51) by X-ray and neutron diffraction respectively. Cubic Ni - I is however, birefringent due to the fact that crystal growth rate is anisotropic, and different 'growth sectors' occur. This is, of course, more of a nuisance than an object of delight in Raman scattering, as it causes polarisation mixing, but careful choice of sample can minimise the inconvenience.

The interesting feature of cubic Ni - I is the anomalous behaviour of the dielectric, magnetic and structural properties at a temperature  $T \approx 130K$ . These anomalies, illustrated in Figure 19, comprise broad maxima in the magnetic and dielectric susceptibilities (49) and an increase of about 0.1% in the lattice constant (52). It might be expected that some manifestation of these abnormal magnetoelectric and structural properties would occur in the Raman spectrum. Such an expectation is reinforced by the observation of a broad maximum at 115K, and a broad minimum at 140K in the elastic stiffness component  $C_{44}$  ( $= C_{2323}$ , ref. 53). This result was obtained by piezoelectrically excited shear mode resonance measurements, and is in keeping with the broad minimum and maximum found at 120K and 150K respectively in the

FIGURES 19a and 19b: Temperature variation of the dielectric ( $\epsilon$ ), and magnetic ( $\chi_g$ ) susceptibilities and the lattice constant ( $a_0$ ) {figure 19a}, and of the elastic coefficient  $C_{44}$  { figure 19b} of  $\text{Ni}_3\text{B}_7\text{O}_{13}$  I.



$$= C_{2323}^{C_{44}}$$





elastic compliance (47). In this study the authors observed simultaneously the piezoelectric resonance frequency and the Faraday rotation of the polarisation of light in Ni - I.

In addition to these results, there is a published infrared study of Ni - I at 300K and 100K (54), which gives a further probe of  $F_2$  symmetry vibrational frequencies (see §2.1). The results of the present Raman spectral study of cubic Ni - I have been published in survey (55) and in full (56).

### §3.2 Experiment

Since Ni - I has thwarted past attempts to record its Raman spectrum the details of the sample, equipment, and methods used are given here at some length. The problematic properties of Ni - I are its opacity to most visible light frequencies, and its birefringence in the cubic phase.

The optical absorption spectrum of Ni - I (57) shows that it absorbs strongly almost all the resonant frequencies available from krypton and argon ion lasers. On transmission of white light, Ni - I appears dark brownish-green. Trials revealed a maximum intensity transmission of 11% for 676.4 nm and 5% for 647.1 nm of krypton laser light through 0.55 mm of Ni - I. For successful Stokes Raman scattering, however, it is essential to use the 647.1 nm wavelength, as absorption increases sharply for  $\lambda > 676.4$  nm (57), such that the intensity transmission for a Raman shift of  $1400 \text{ cm}^{-1}$  would be less than 3% through 0.55 mm. In addition, Raman scattered light from boracites is of low intensity, and a photomultiplier tube of high sensitivity to red light is essential. A Spectra Physics 165 krypton

laser giving 400 mW at  $\lambda = 647.1$  nm, and an RCA C31034A photomultiplier tube were used, the  $90^\circ$  scattered radiation was dispersed by the Coderg T800 triple monochromator system of \$1.6 ( $T < 295\text{K}$ ), and a Spex 1400 double monochromator digital system ( $T = 295\text{K}$ ). The resolution was  $2.5 \text{ cm}^{-1}$  in both instruments.

The crystal used was the same  $\text{B}^{11}$  enriched single crystal [100] growth sector used for the structure determination at 77K (51), which was supplied by Dr. H. Schmid, and grown by the vapour transport method (34). Although birefringence is a minimum for Iodine boracites, it is still necessary to use a [100] sector, which has a birefringence of only  $\approx 0.0003$ . The birefringence parameters for the other growth sectors (46) are  $\approx 0.0007$  ([111]) and  $0.004$  ( $[\bar{1}10]$ ). This choice of sample minimises polarisation mixing. The sample formed a cuboid of dimensions  $1.4 \times 2.2 \times 0.55 \text{ mm}^3$ , the dimensions corresponding to the cubic [110] ( $X'$ ),  $[\bar{1}10]$  ( $Y'$ ) and [001] ( $Z$ ) directions respectively. The natural growth faces were polished with  $1 \mu\text{m}$  diamond powder. To minimise the absorption, and therefore the attendant laser heating, the incident light was aligned along the shortest axis ( $Z$ ), and was placed as close to the  $[\bar{1}10]$  face as possible, to maximise heat dissipation. This orientation,  $Z$  (??)  $Y'$ , coincidentally produced the strongest Raman signal.

Cooling was achieved by use of a Thor nitrogen vapour flow cryostat, with a Thor model 3010 temperature controller, and a chromel vs. gold-iron thermocouple for temperature measurement. Approximately 5K of laser heating was detected at the thermocouple despite the above precautions, which suggests that the temperature at the beam position was a few degrees higher than that measured. An elaborate screen had to be constructed on the cold finger of the cryostat to prevent the intrusion

of the Raman spectrum of nitrogen, and the sample was clamped across the large  $\langle 001 \rangle$  faces, again to maximise heat dissipation.

### §3.3 Group Theory and Description of Spectra

A group theoretical analysis of the  $q \approx 0$  modes as described in §1.3 gives the following classification in terms of the species of point group  $T_d$  ( $\bar{4}3m$ , see Table.1):

$$\Gamma = 4A_1 + 6A_2 + 10E + 18F_1 + 20F_2 \text{ of which } 4A_1 + 10E + 19F_2$$

optic modes should be Raman-active, and  $19F_2$  infrared active (see §2.1). The spectra in the four polarisations permitted by the geometry are presented as Figures 20-23.

According to §2.1, the  $Z(Y'X')Y'$  spectrum should contain E modes only, and the  $Z(X'X')Y'$  spectrum modes of  $A_1 + E + F_2$  symmetry since the  $F_2$  Raman tensors for this geometry are of the form:

$$F_2(X') = \frac{1}{\sqrt{2}} \begin{bmatrix} . & . & d \\ . & . & d \\ d & d & . \end{bmatrix}, \quad F_2(Y') = \frac{1}{\sqrt{2}} \begin{bmatrix} . & . & d \\ . & . & -d \\ d & -d & . \end{bmatrix}$$

$$\text{and } F_2(Z) = \begin{bmatrix} d & . & . \\ . & -d & . \\ . & . & . \end{bmatrix} .$$

The E symmetry modes can be subtracted from  $Z(X'X')Y'$  to give Figure 24, with a suitable scale factor, but the  $F_2$  modes cannot be removed as no suitable scaling feature is present. The  $Z(Y'Z)Y'$

spectrum should contain  $F_2(TO + LO)$  modes and the  $Z(X'Z)Y'$  spectrum only  $F_2(TO)$  modes. As the  $F_2$  scattering is roughly ten times weaker than the  $A_1 + E$  scattering, its contribution to Figure 24 is ignored for assignment purposes. The spectra are described below:

The  $A_1$  spectrum (Figure 24):

This spectrum contains a wing feature, common to all boracites (58, 59), but less pronounced in Ni - I, such that its influence on the cross-section is negligible beyond  $\approx 100 \text{ cm}^{-1}$ . There is a broad feature centred on  $\approx 154 \text{ cm}^{-1}$ , with an indistinct but non-negligible band peaking at  $100 \text{ cm}^{-1}$ . Only two other distinct spectral features are visible at  $378 \text{ cm}^{-1}$  and  $655 \text{ cm}^{-1}$ .

The E spectrum (Figure 21):

This spectrum resembles the  $A_1$  spectrum in the region  $0 - 300 \text{ cm}^{-1}$ , with a wing feature, and broad bands peaking at  $160$  and  $84 \text{ cm}^{-1}$ . There are five additional, discrete modes.

The  $F_2$  spectrum (Figures 22 and 23):

The  $F_2$  scattering is very weak. Again, a narrow wing feature is present, with an odd scattering profile below  $200 \text{ cm}^{-1}$ , comprising apparently two bands, plus two very weak bands (a  $TO - LO$  pair) at  $255 \text{ cm}^{-1}$  and  $280 \text{ cm}^{-1}$ . It becomes clear at low temperatures that the structure around  $1000-1200 \text{ cm}^{-1}$  is a superposition of weak first order bands (see Chapter 4). The signal-attenuating effect of cryostat windows rendered the low temperature  $F_2$  spectra weaker still, which made detailed analysis impossible.

FIGURES 20 - 24: The room temperature Raman spectrum of  $\text{Ni}_3\text{B}_7\text{O}_{13}\text{I}$   
in the frequency range 0 - 1500  $\text{cm}^{-1}$ .

FIGURE 20: Z(X'X')Y' geometry.

FIGURE 21: Z(Y'X')Y' geometry.

FIGURE 22: Z(Y'Z)Y' geometry.

FIGURE 23: Z(X'Z)Y' geometry.

FIGURE 24: Z(X'X')Y' - Z(Y'X')Y' geometry.

N.B. The ordinate scales in figures 20,21 and 24

are X1 ( lower) and X5 ( upper).

N-I-B Z(X<sup>0</sup> X<sup>0</sup>) Y<sup>0</sup> SPECTRUM

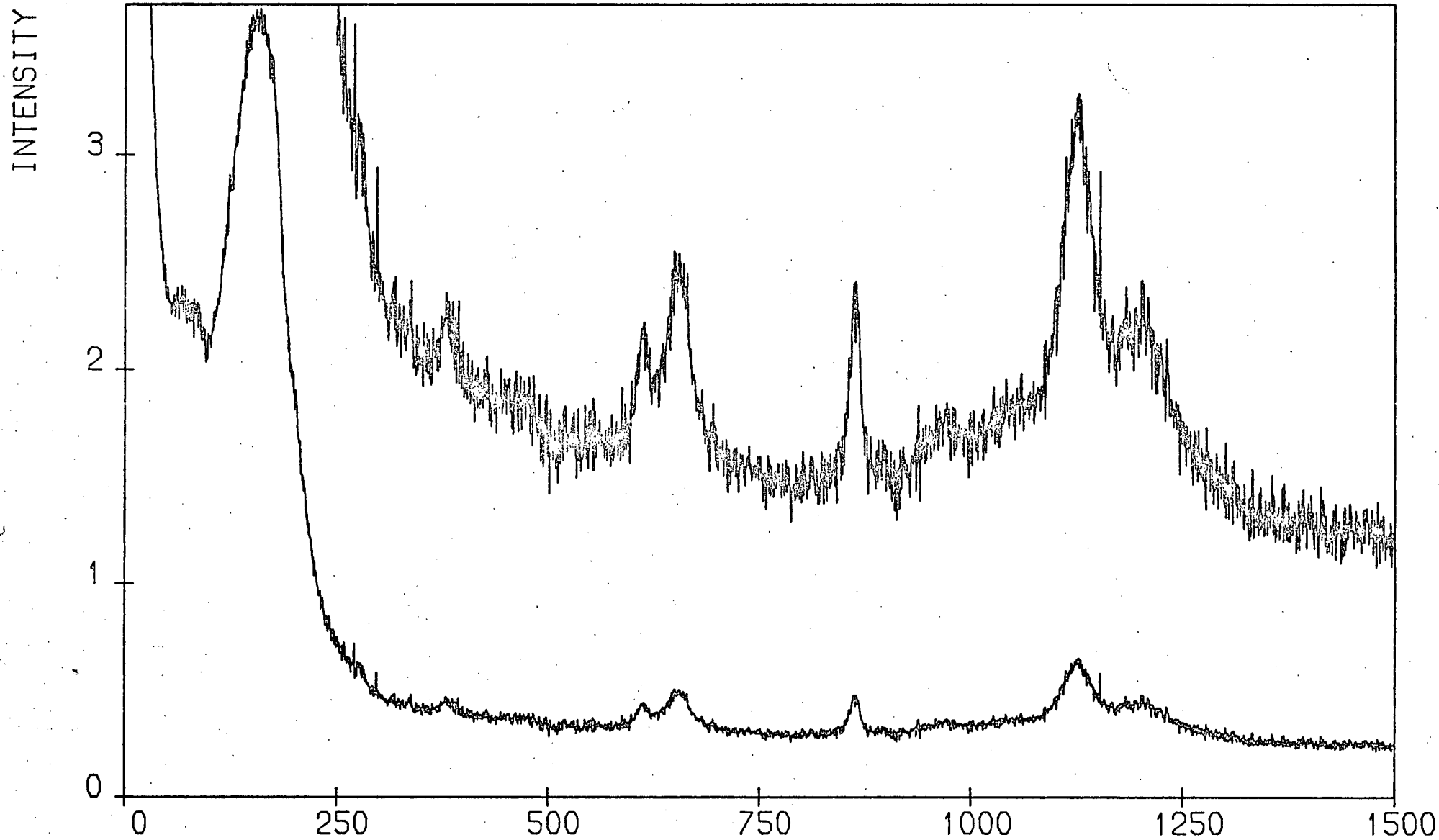
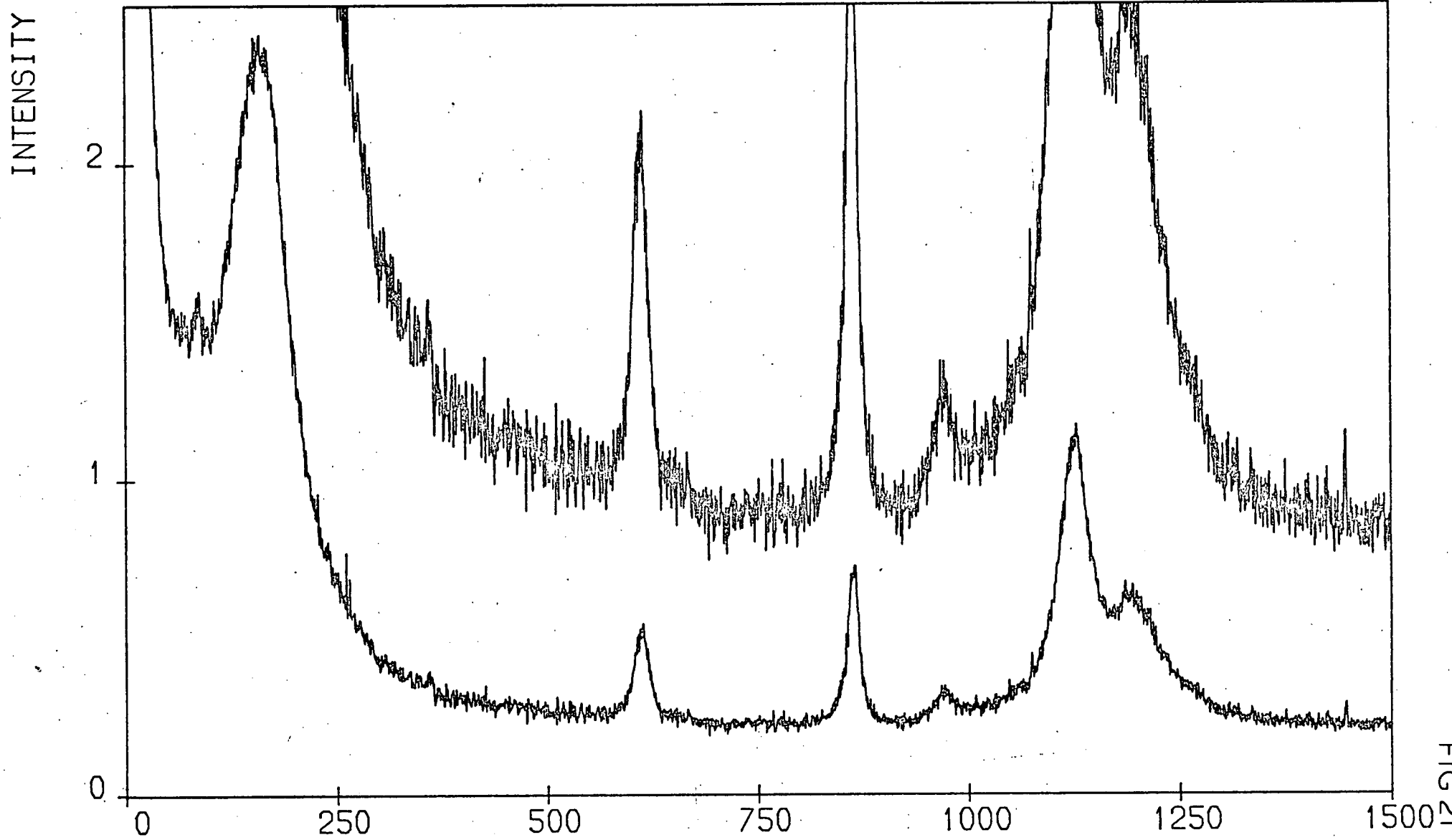


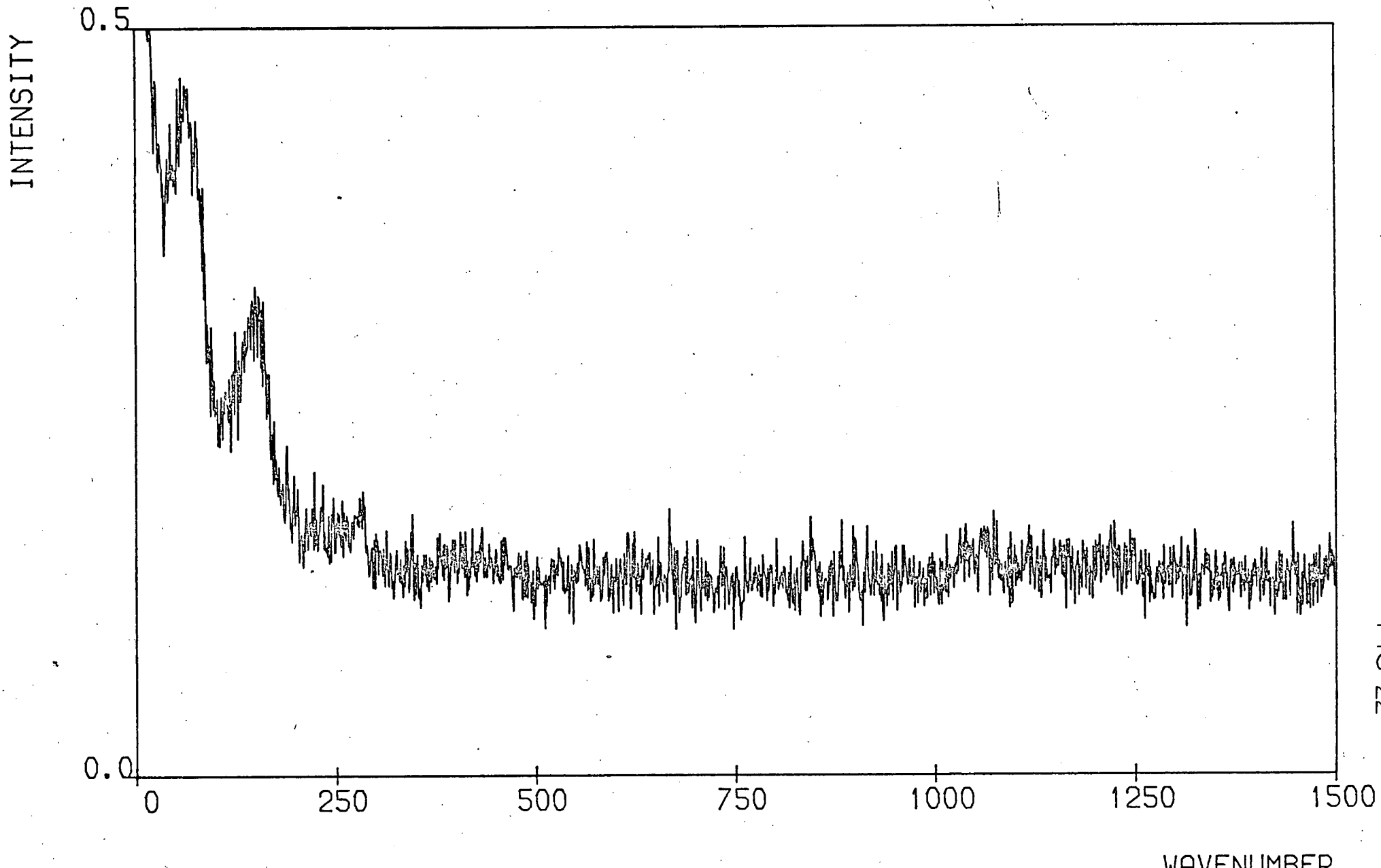
FIG 20

# N-I-B Z(Y<sup>0</sup> X<sup>0</sup>) Y<sup>0</sup> SPECTRUM



WAVENUMBER

# N-I-B Z(Y° Z)Y° SPECTRUM





# N-I-B Z(X<sup>0</sup>Z)Y<sup>0</sup> SPECTRUM

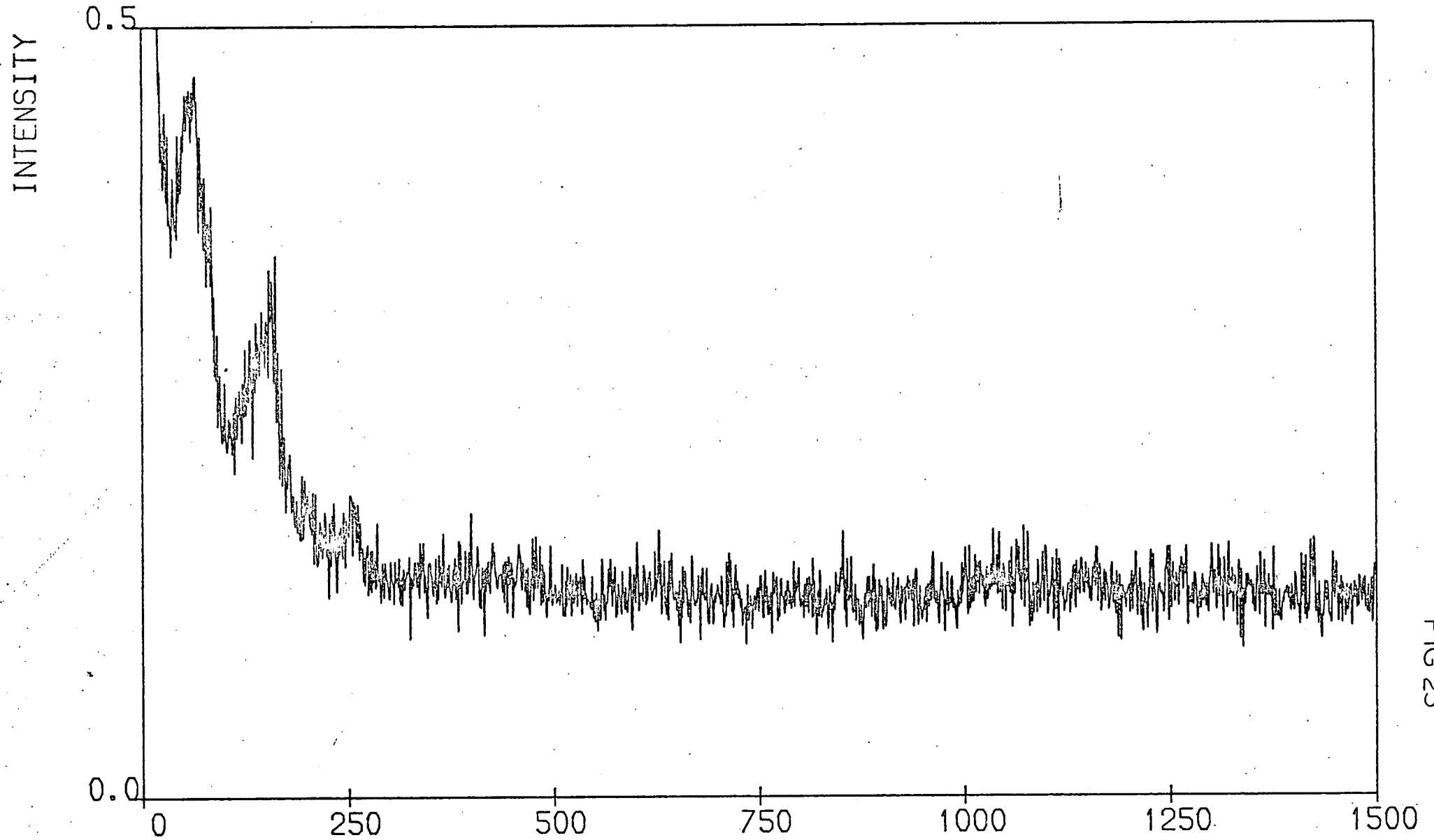


FIG 23

N-I-B A<sub>1</sub>(+F<sub>2</sub>) SPECTRUM

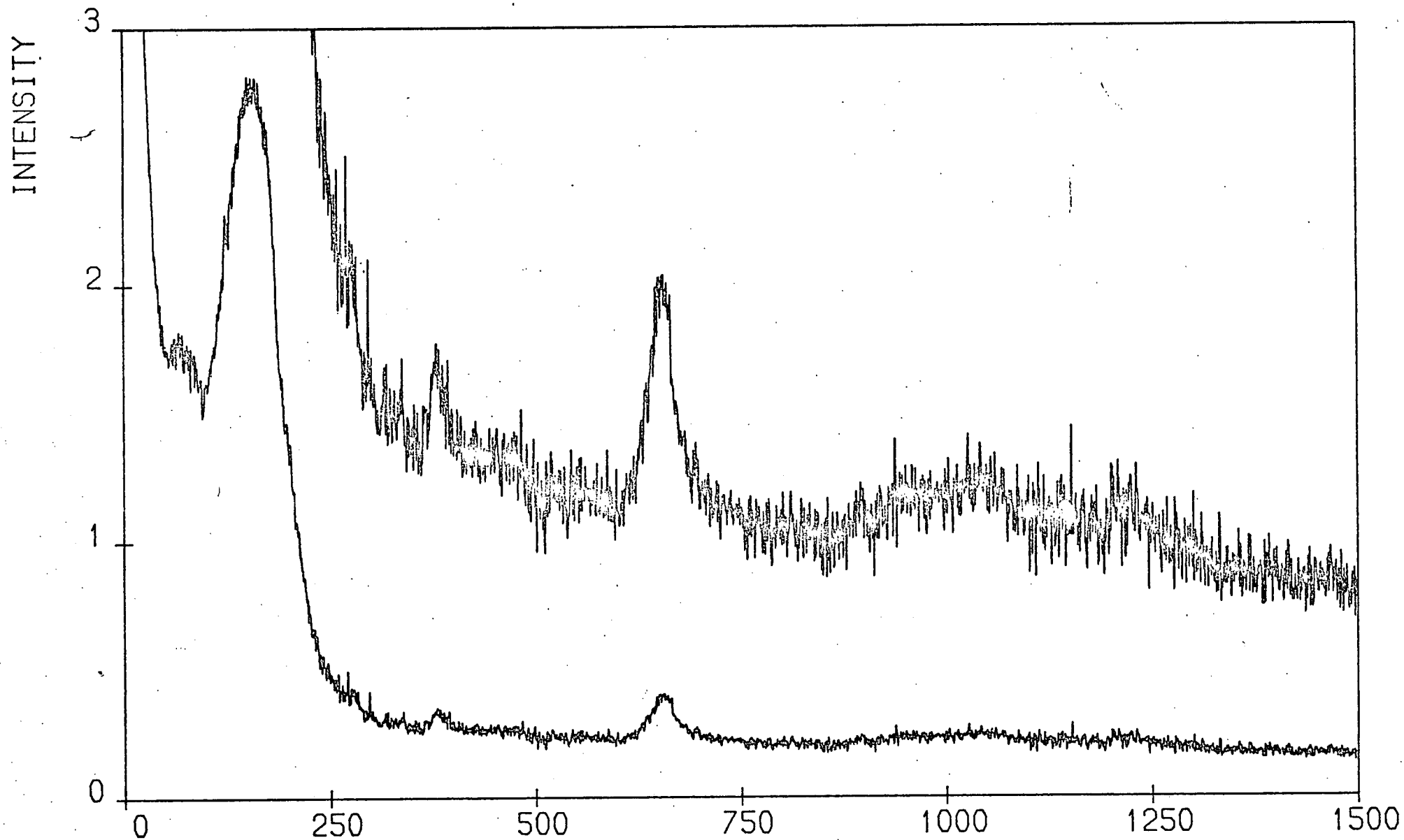


FIG 24

### §3.4 Analysis of Results

The computer least-squares fitting routine used in §2.8 proved essential to investigating the temperature dependence of the Raman spectra. Discussion of the procedure is made easier by dividing the spectra into low frequency (0 - 300 cm<sup>-1</sup>) and high frequency (300 - 1400 cm<sup>-1</sup>) regions.

The high frequency spectra:

Each of the high frequency peaks may be represented by a 1 × 1 Greens functions, giving a response function (see §1.5)

$$3.1 \quad I(\omega) = \frac{S\Gamma\omega(n(\omega) + 1)}{(\omega_0^2 - \omega^2)^2 + \Gamma^2\omega^2} ; \quad S = \text{' strength' .}$$

The low frequency spectra:

The model response function proves more problematic here. Firstly, the wing feature is described by a 1 × 1 Greens function, giving a response function 3.1, but with  $\Gamma \gg \omega_0$ . This limit corresponds to over-damped (i.e. very short lived) excitations, and reduces 3.1 to the functional form

$$3.2 \quad I(\omega) = \frac{S\omega(n(\omega) + 1)}{\omega^2 + \gamma^2}$$

where

$$3.3 \quad \gamma^2 = \frac{\omega_0^4}{\Gamma^2 - 2\omega_0^2} \quad ; \quad S = \text{'strength'}$$

Secondly, a  $2 \times 2$  Greens function must be included to account for the broad modes below  $200 \text{ cm}^{-1}$ . This can be chosen to be a diagonal matrix, giving an 'uncoupled modes' model, with two functions of the form of 3.1. Alternatively, the form 2.12 can be used, representing two coupled modes. In this case, however, the  $\omega$ -dependence of the imaginary terms in  $\underline{G}(\omega)$  means that the choice of diagonalisation convention (c.f. §2.6) is critical. In the case of a ferroelectric transition, we may be looking for a 'soft mode', whose characteristic frequency  $\omega_a$  varies as  $(T - T_c)^{\frac{1}{2}}$ . Now, it can be shown (21) that the dielectric susceptibility tensor  $\underline{\chi}(\omega)$  is given by:

$$3.4 \quad \chi_{\ell m}(\omega) \propto \underline{M}_\ell \underline{G}(\omega) \underline{M}_m \quad ; \quad \underline{G} \text{ is the Green's function of §1.5,}$$

where  $\underline{M}_\ell$  is a vector whose elements are the  $\ell$ 'th Cartesian components of the lowest order phonon expansion coefficients of the dipole moment operator (c.f.  $\{\underline{P}_i\}$  of §1.5) such that the dipole moment operator  $\underline{M}$  is given by

$$3.5 \quad \underline{M}_\ell = \sum_{\underline{ya}} M_\ell(\underline{ya}) \psi(\underline{ya}) + \dots$$

and  $\underline{y}=0$  by the translational invariance requirement. For a Curie-Weiss behaviour of  $\chi_{\ell\ell}(0)$ , we require  $\chi_{\ell\ell}(0) \propto (T - T_c')^{-1}$ , to describe the dielectric anomaly in a ferroelectric. Substituting for  $\underline{G}(0)$  in 3.4, we have for the cases of real and imaginary coupling respectively,  $\underline{\chi}^R$  and  $\underline{\chi}^I$

$$3.6 \quad \chi_{\ell\ell}^R(0) \quad \alpha \quad \frac{M_{\ell}^2(b)\omega_a^2 + M_{\ell}^2(a)\omega_b^2 - 2M_{\ell}(a)M_{\ell}(b)\Delta}{\omega_a^2 \omega_b^2 - \Delta_{ab}}$$

$$3.7 \quad \chi_{\ell\ell}^I(0) \quad \alpha \quad \frac{M_{\ell}^2(b)\omega_a^2 + M_{\ell}^2(a)\omega_b^2}{\omega_a^2 \omega_b^2}$$

Only in the second case (purely imaginary coupling) can the substitution of  $\omega_a^2 \alpha (T - T_c)$  give a denominator proportional to  $(T - T_c)$ . Thus, for real coupling,  $T_c' \neq T_c$ . For this reason, imaginary coupling is chosen.

### §3.5 Symmetry Classification of the Modes

The parameters produced by an analysis of the room temperature spectra in terms of uncoupled modes throughout are presented in table 6, along with the results of the infrared experiment (54).

It is evident that the correct number of  $A_1$  symmetry bands appears in the Raman spectrum, but that there is a dearth of E and  $F_2$  peaks. The most serious discrepancy occurs in  $F_2$  symmetry, where only five peaks can be seen, the pair at  $\approx 250 \text{ cm}^{-1}$  and  $280 \text{ cm}^{-1}$  being obviously a TO - LO pair from both the Raman and infrared data. The fitted low frequency spectra are presented in Figure 25. The infrared result suggests that the poor fit in Fig. 25a for  $F_2$  symmetry is because the 0 -  $300 \text{ cm}^{-1}$  spectrum actually comprises at least nine bands, not just four. The fit for E symmetry is good, while that for  $A_1$  symmetry is not. A coupled mode fit to this region (Figure 26a) did not improve the agreement over the 100-240  $\text{cm}^{-1}$  region as was hoped, and furthermore produced parameter inconsistencies between different temperatures (see Appendix II).

FIGURE 25: The low frequency spectra of Ni-I with theoretical fits (smooth lines) in terms of two uncoupled oscillators plus an overdamped wing.

- a)  $F_2$  symmetry.
- b) E symmetry.
- c)  $A_1 (+F_2)$  symmetry.

FIGURE 26: a) The low frequency  $A_1 (+F_2)$  spectrum of Ni-I with theoretical fit (smooth line) in terms of a coupled modes model.

- b) The  $Z(X'X')Y'$  (upper) and  $X'(ZZ)Y'$  spectra of Ni-I at low frequency.

FIG 25

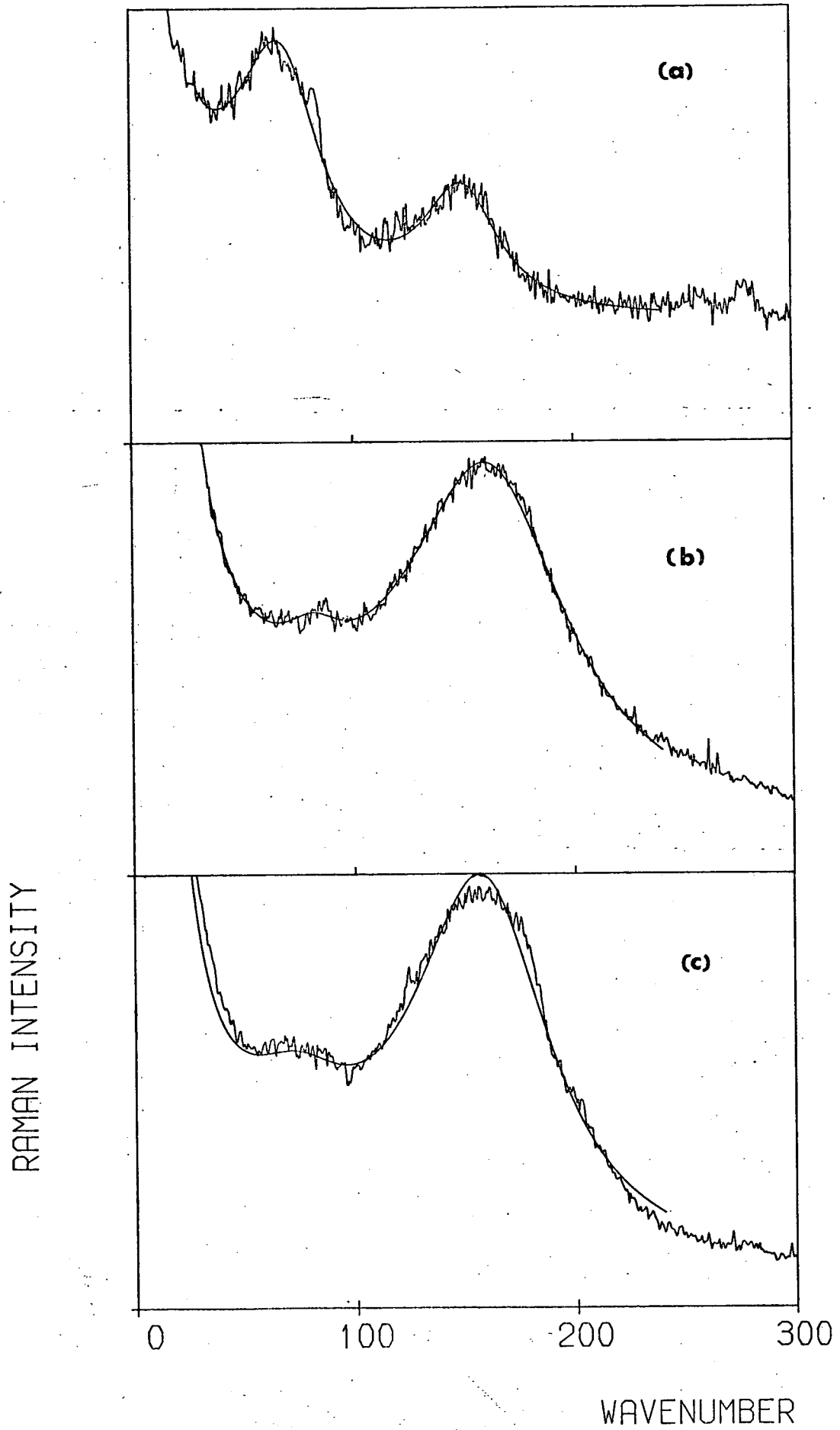


FIG 26

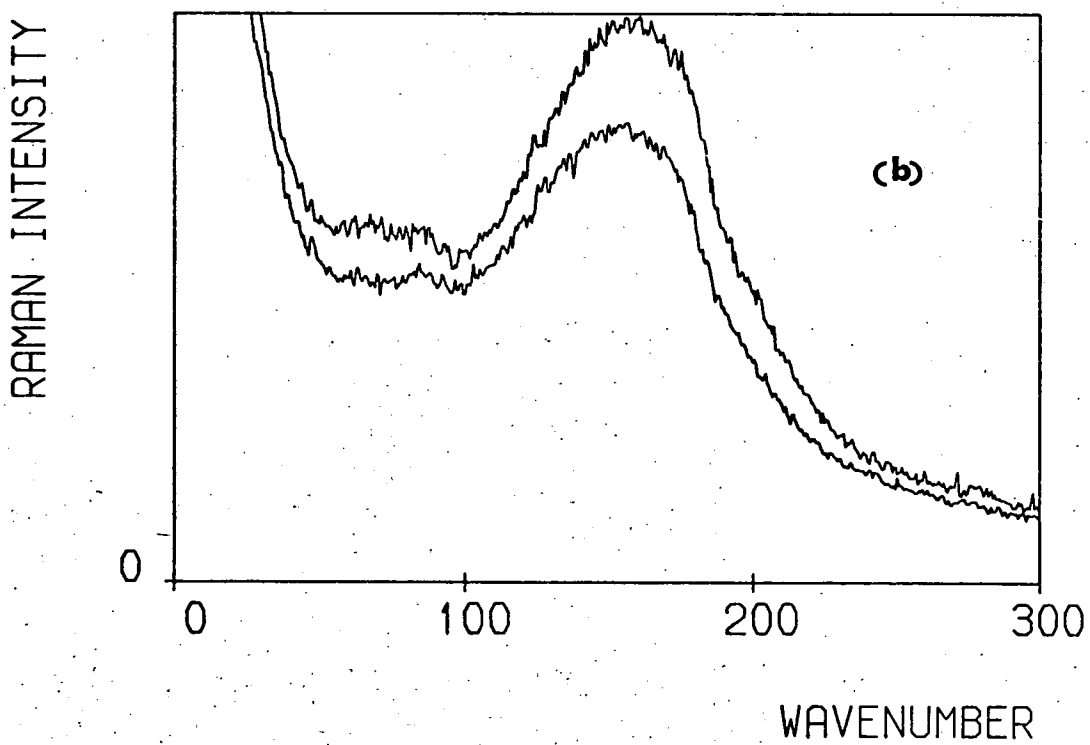
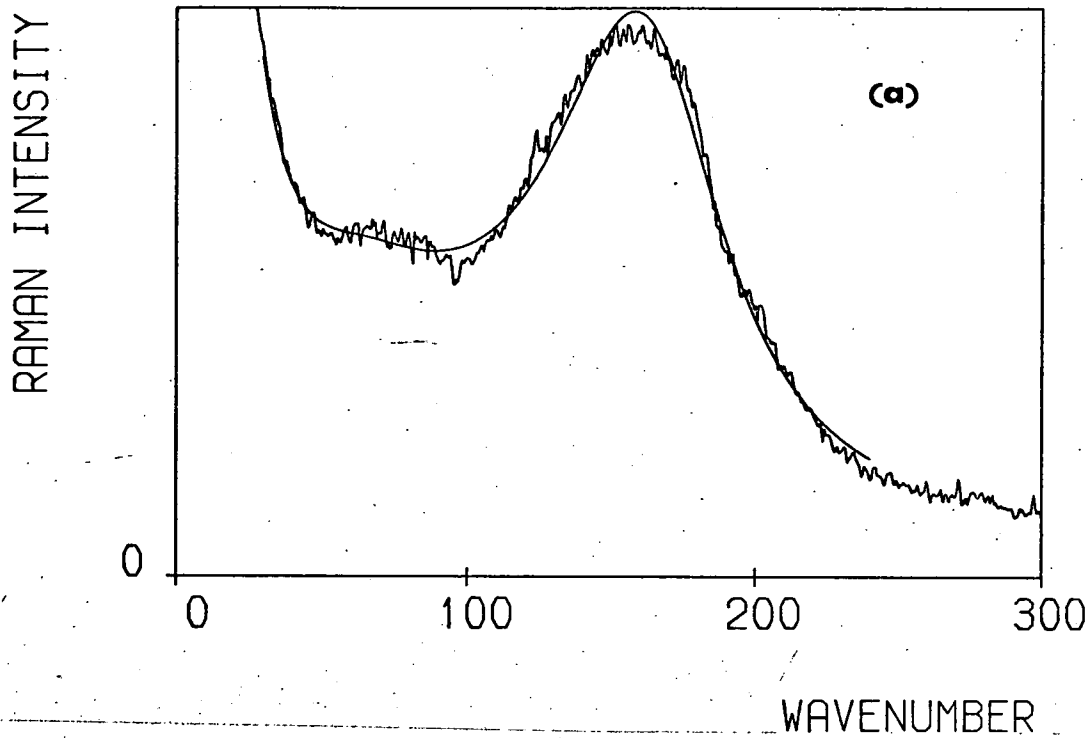




TABLE 6

Resonant frequencies  $\omega_0$  ( $\text{cm}^{-1}$ ), damping parameters  $\Gamma$  ( $\text{cm}^{-1}$ ) and assignments for the Raman active modes, and frequencies for the infrared active modes (54) of Ni - I at room temperature.

$\omega_0$	$A_1$	$\Gamma$	$\omega_0$	E	$\Gamma$	$\omega_0$	$F_2$	$\Gamma$	$F_2$ (infrared)	
									$\omega_0$	$\omega_0$
81.5		61	84.5		35	74.5		48	42	42
163.5		76	170.0		90	152.5		42	54	70
378.0 <sup>a</sup>		18 <sup>a</sup>	611.5		20	255.0 <sup>b</sup>			89	91
655.0		30	863.5		15	280.0 <sup>b</sup>			112	114
			943.0		36				135	136
			1125.5		43				168	168
			1199.5		74				195	198
									224	226
									258	286
									308	308
									320	322

All  $\omega_0$  and  $\Gamma$  are from computer fits except:

<sup>a</sup> Measured from spectrum.

<sup>b</sup> Measured from spectrum and too weak for assignment of  $\Gamma$ .

The discrepancy must therefore be attributed to the weak  $F_2$  component introduced by the form of the Raman tensors, or to other excitations (e.g. multi-phonon). An attempt to subtract the  $X'(ZZ)Y'$  spectrum ( $A_1 + E$ , Fig. 26b) from the  $Z(X'X')Y'$  spectrum (Fig. 26b) to lay bare  $F_2$  modes was unsuccessful, due to the low intensity in the  $X'(??)Y'$  geometry and the different E symmetry scale factors.

The molecular potential calculation of §2.4 suggests that the  $378 \text{ cm}^{-1}$  ( $A_1$ ) and  $255 \text{ cm}^{-1}$  ( $F_2$ ) bands are associated with B-O vibrations. Also, the presence of a first order  $F_2$  band around  $1100 \text{ cm}^{-1}$  and an E mode at about  $250 \text{ cm}^{-1}$  is indicated. This latter mode actually becomes visible at lower temperatures. These frequencies should be relatively insensitive to change of halogen or metal in the boracite formula, as such a change does not drastically disturb the B-O framework (45, 60). This is borne out by Figure 11 and the results for Cu - Cl (59) of  $385 \text{ cm}^{-1}$  ( $A_1$ )  $239 \text{ cm}^{-1}$  (E) and  $1167 \text{ cm}^{-1}$ ,  $264 \text{ cm}^{-1}$  ( $F_2$ ).

The low frequency modes for Ni - I are more heavily damped than their counterparts for other boracites, particularly in E symmetry. The lowering of characteristic frequencies from Cr - Cl and Cu - Cl to Ni - I produces a low frequency total cross-section of great complexity. This increases the probability of interactions, and thus may contribute to the shortening of phonon lifetimes, and consequently higher damping. The frequency lowering also confirms that these low frequency modes are largely attributable to metal and halogen motion, in particular the latter.

The wing feature is much narrower in Ni - I than in Cr - Cl and Cu - Cl, where it was conjectured as being due to disorder (58). X-ray structural studies have shown that this disorder, if extant, is

associated mainly with the Cl ion, being greatest in Cu - Cl, and corresponds to a displacement of the halogen ions along the  $\langle 111 \rangle$  axes (60, 61). The Raman spectra of Ni - I suggest that any disorder is much less than in the Cl boracites, in accord with structural results for Cr - Cl, Cu - Cl and Ni - I (60, 50, 51, 61). In addition, the Ni - I spectra contain a wing in all polarisations, suggesting that the disorder lacks definite symmetry, and is therefore more isotropic than in Cl boracites.

### §3.6 Temperature Dependence of the Normal Modes

The  $A_1$  and E spectra at a series of temperatures between 88K and 300K, along with the variation of the (uncoupled) mode parameters, are represented by Figures 27-31 and table 7 (see also Appendix II). The  $F_2$  spectra are too weak and too complicated to permit such a detailed study. The parameters of Figures 28, 30 and 31 are all results of fits. The normal behaviour of the parameters  $\omega_0$  and  $\Gamma$  as temperature decreases consist of a steady rise in  $\omega_0$ , with a drop in  $\Gamma$ , as the lattice contracts and anharmonicity decreases (e.g. see equation 2.8).

It can be seen from Figures 28a and 30 that this behaviour in Ni - I is interrupted by an anomalous decrease in  $\omega_0$ , and increase in  $\Gamma$  for the high frequency  $A_1$  and E modes around 128K. The parameters of Fig. 28a for the  $A_1$  mode are rather scattered, due to the proximity of the  $611.5 \text{ cm}^{-1}$  E mode. The calibration of the spectra was checked by studying the laser frequency, the krypton emission lines, and the duplication of E modes in the  $Z(X'X')Y'$  and  $Z(Y'X')Y'$  spectra (55, see Appendix II). This unusual result

FIGURE 27: The  $A_1 (+F_2)$  spectrum of Ni-I at different temperatures.

FIGURE 28: The temperature variation of the frequencies  $\omega_0$  (squares) and damping parameters  $\Gamma$  (triangles) of the  $655.0 \text{ cm}^{-1}$   $A_1$  mode (28a) and the  $163.5 \text{ cm}^{-1}$   $A_1$  mode (28b) in Ni-I.

FIGURE 29: The E spectrum of Ni-I at different temperatures.

FIGURE 30: The temperature variation of the frequencies  $\omega_0$  (squares) and damping parameters  $\Gamma$  (triangles) of some E symmetry modes in Ni-I.

FIGURE 31: The temperature variation of the frequency  $\omega_0$  (squares) and damping parameter  $\Gamma$  (triangles) of the  $170.0 \text{ cm}^{-1}$  E mode in Ni-I.

N.B. The lines in figures 30 and 31 are intended merely as a guide to the eye.

FIG 27

RAMAN INTENSITY

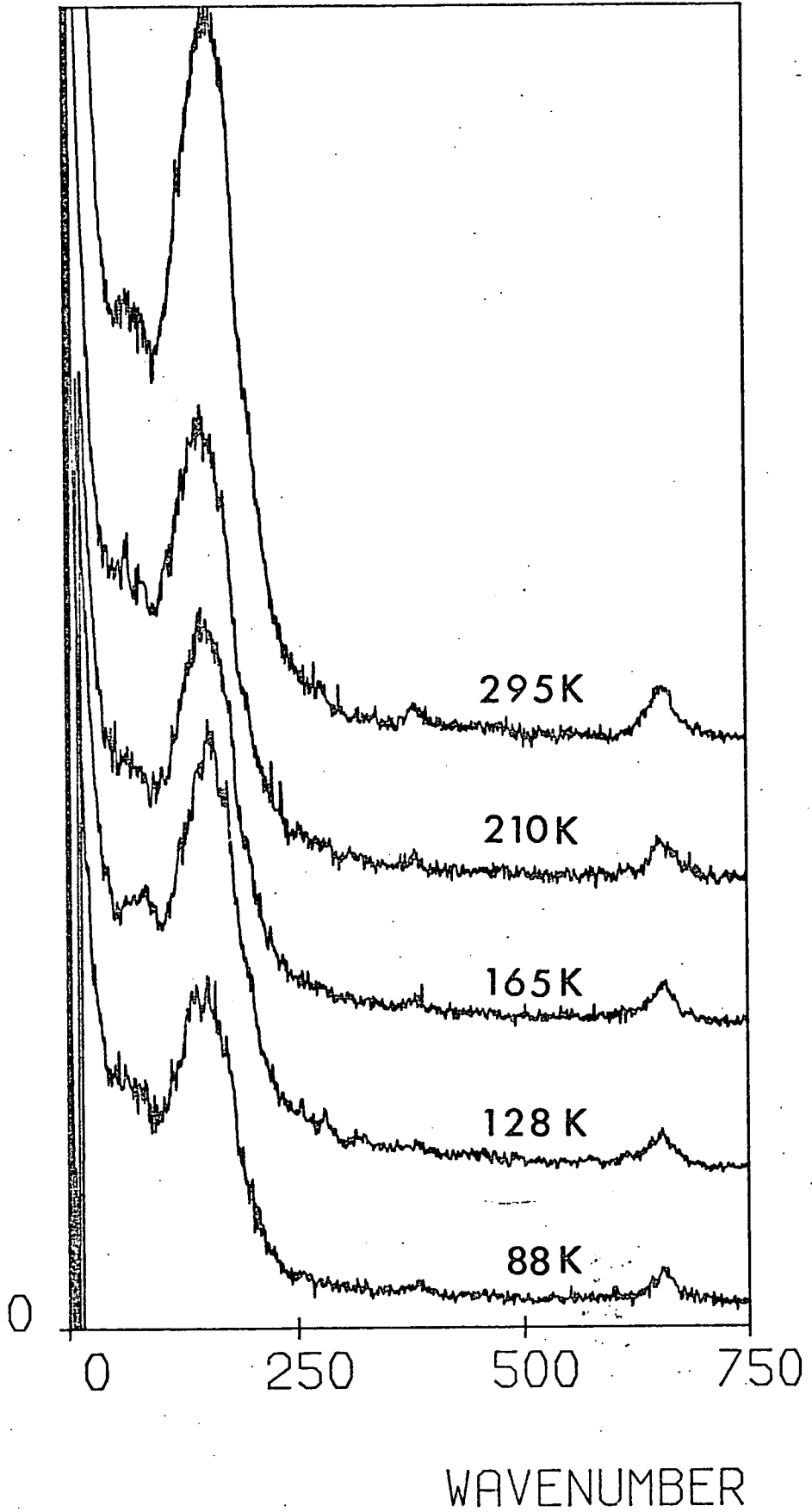


FIG 28

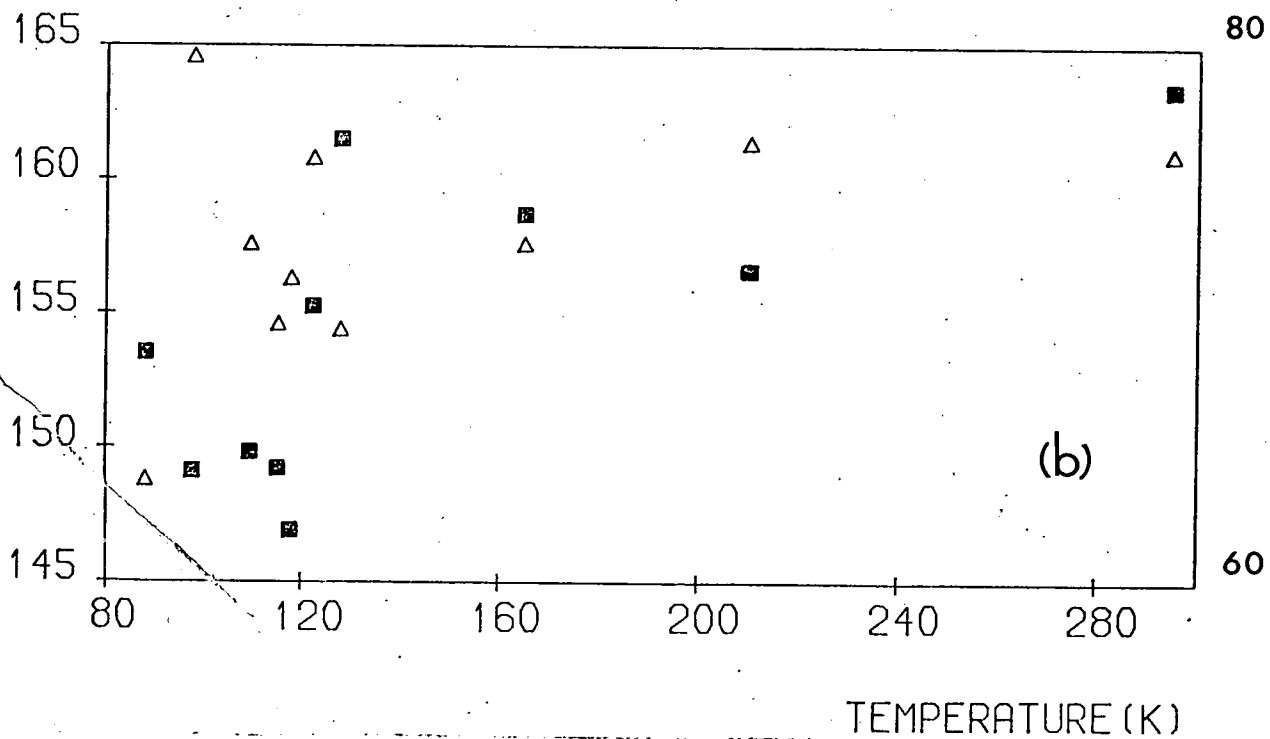
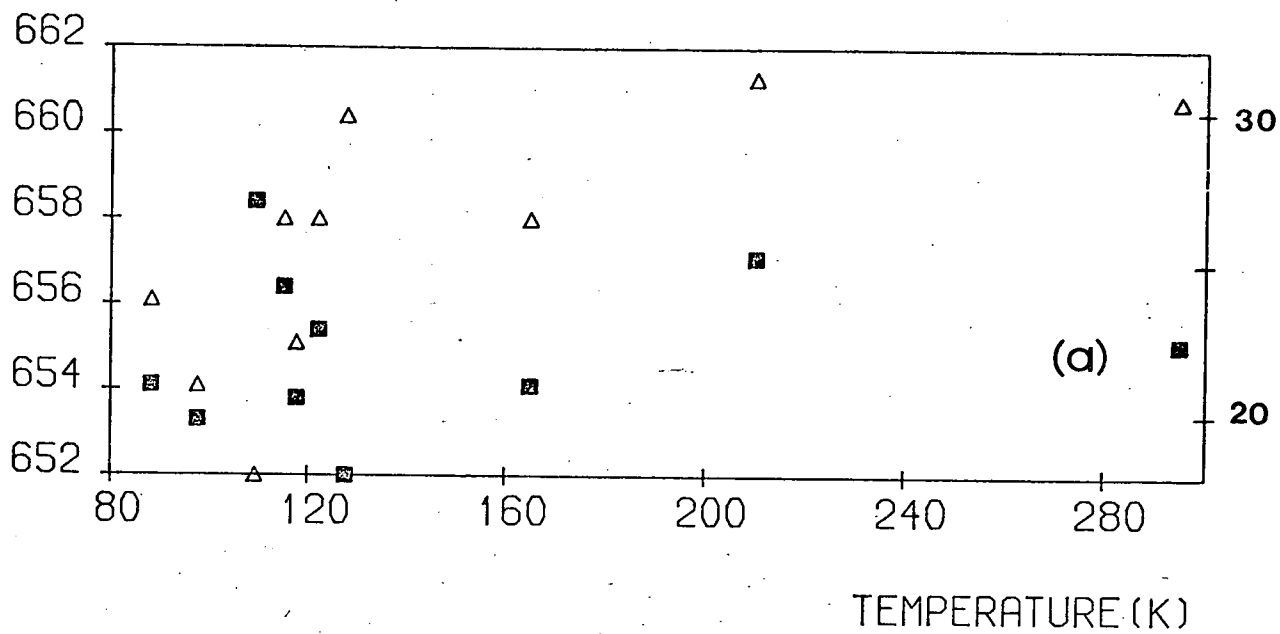


FIG 29

RAMAN INTENSITY

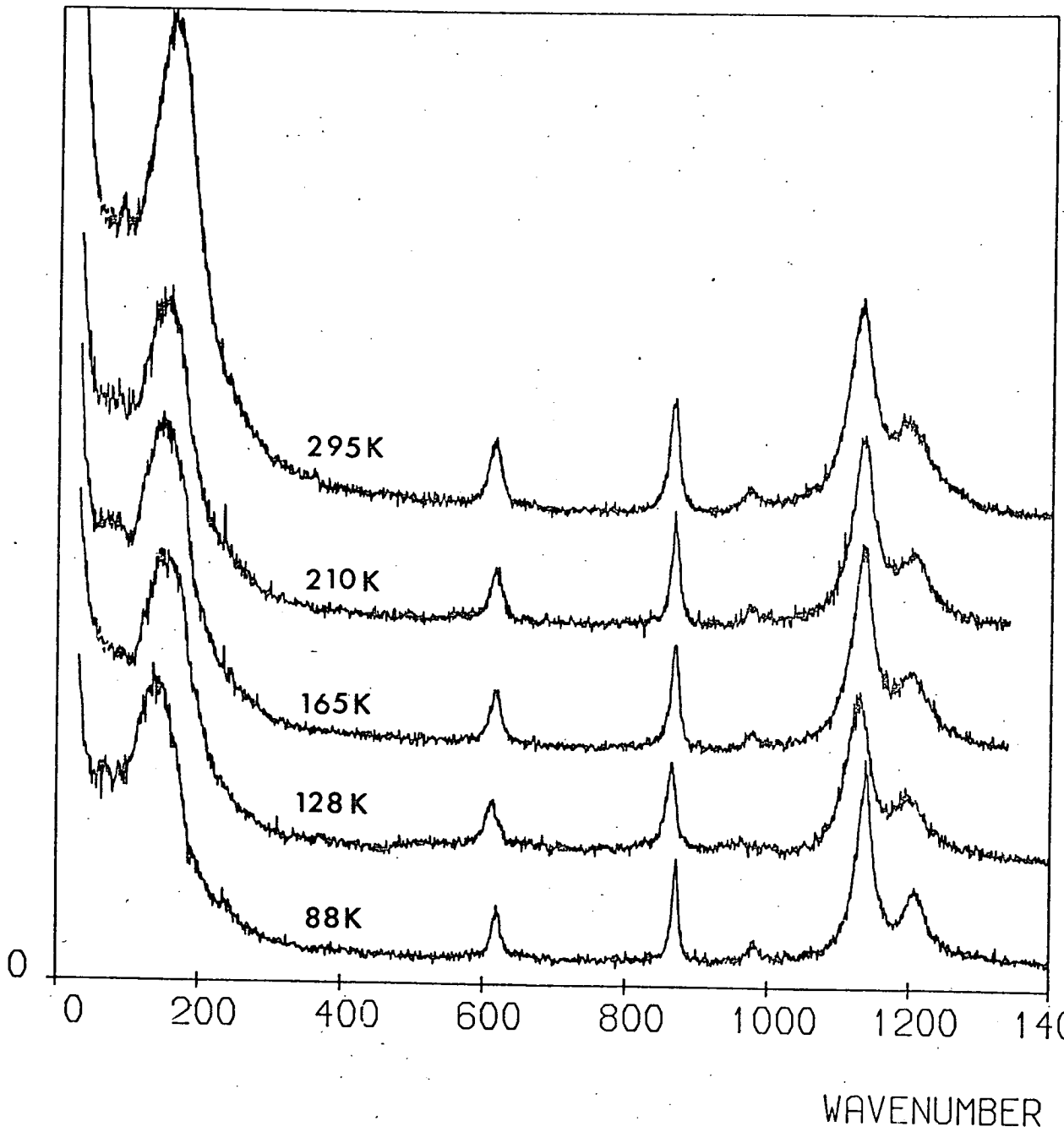
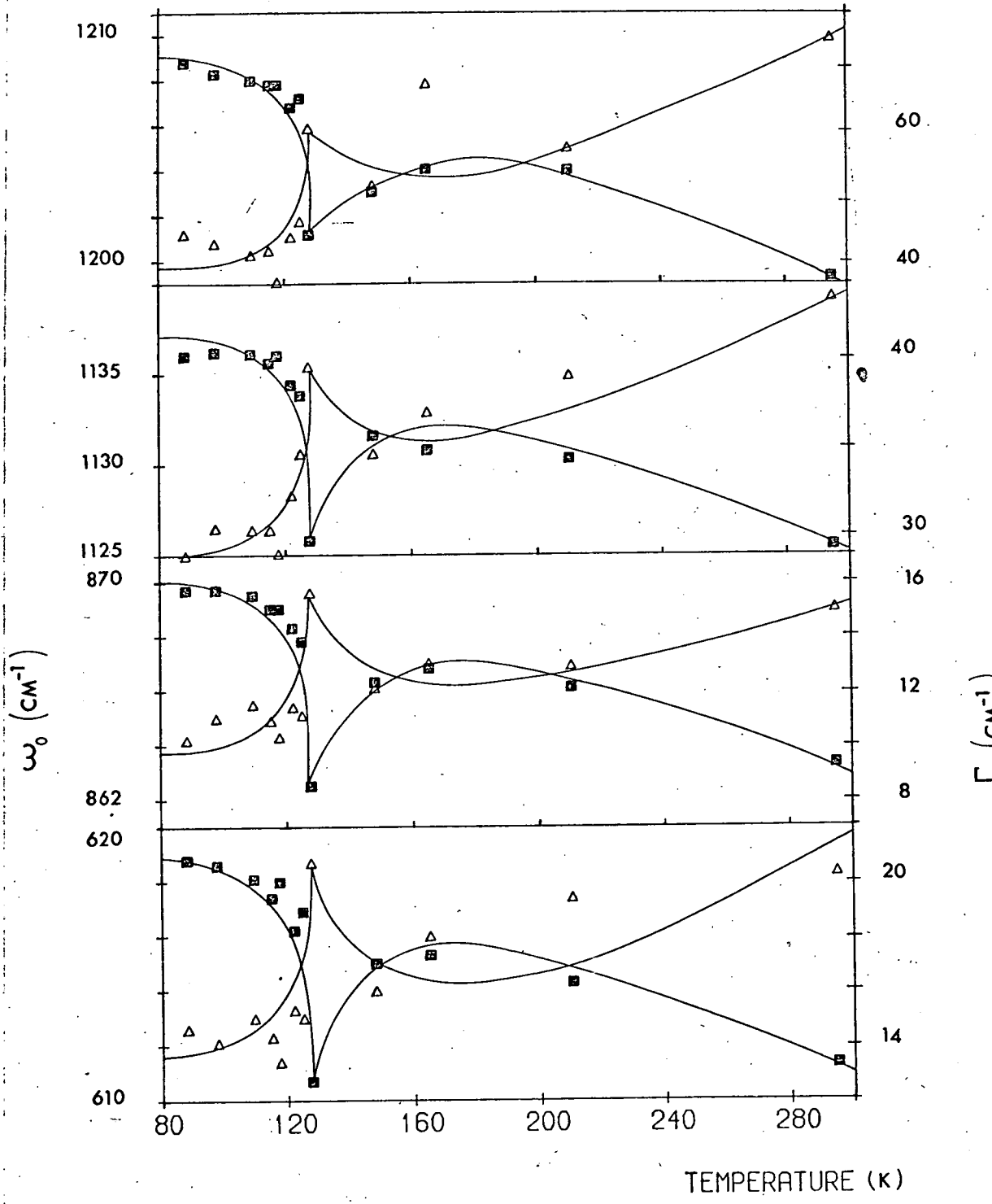


FIG 30





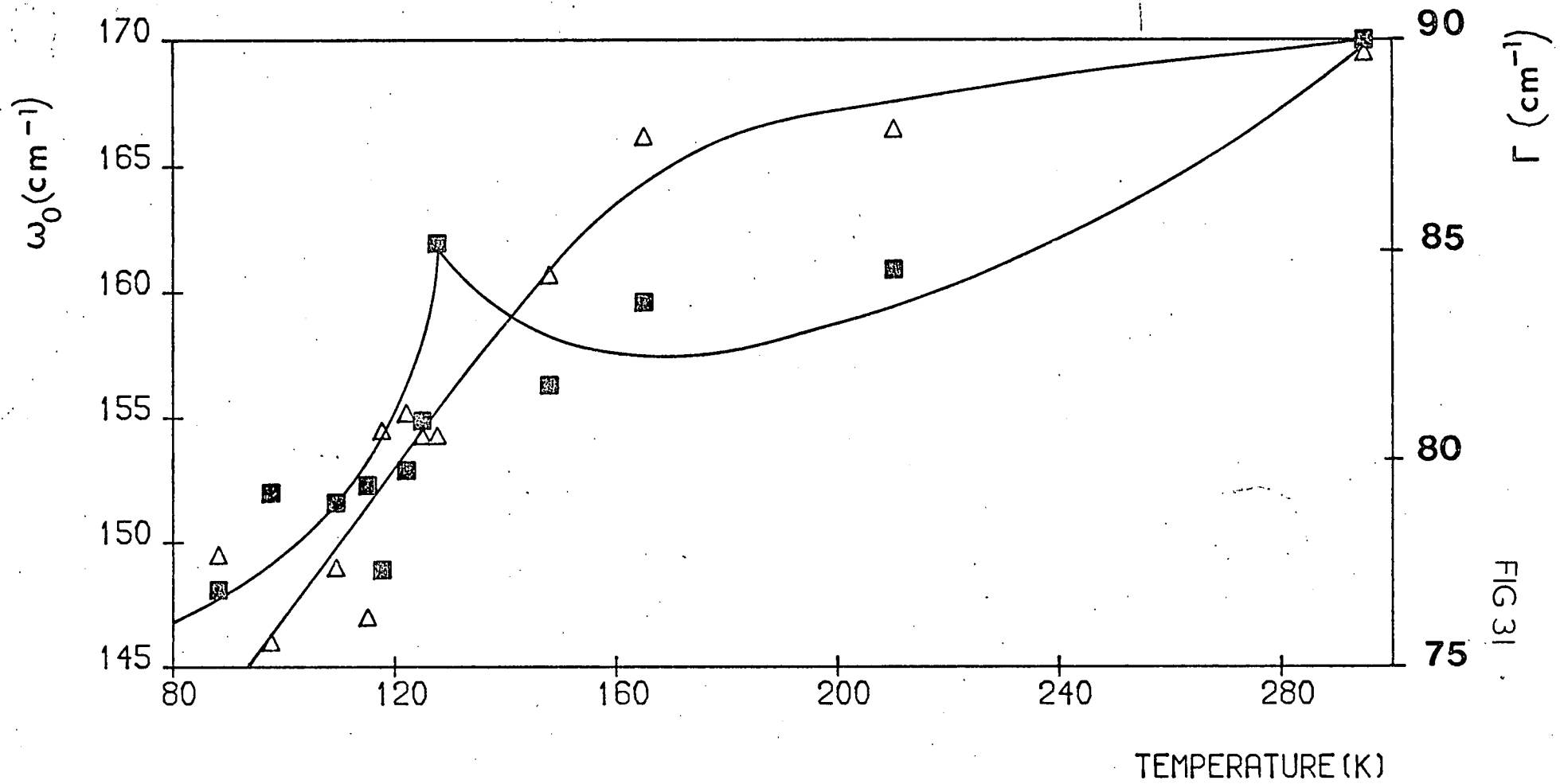


FIG 31

TABLE 7

The temperature dependence of the computer fitted frequency  $\omega_0$  ( $\text{cm}^{-1}$ ) and damping  $\Gamma$  ( $\text{cm}^{-1}$ ) parameters of the  $170.0 \text{ cm}^{-1}$  (E) and  $163.5 \text{ cm}^{-1}$  ( $A_1$ ) modes in cubic Ni - I.

Temperature (K)	E		$A_1$	
	$\omega_0$	$\Gamma$	$\omega_0$	$\Gamma$
295	170.0	89.7	163.5	76.0
210	160.9	87.9	156.6	76.4
165	160.0	87.7	158.7	72.6
148	156.3	84.4	-	-
128	162.0	80.6	161.5	69.4
125	154.9	80.5	-	-
122	152.9	81.1	155.3	85.8
118	148.9	80.7	146.9	71.3
115	152.3	76.2	149.2	69.6
109	151.6	77.4	149.8	72.6
98	151.9	75.6	149.1	79.4
88	148.1	77.7	153.5	63.8
73†	134.9	77.1		
68†	133.3	71.3		
51†	127.8	74.0		
25†	125.0	68.0		

† See ahead §4.8

is in agreement with the X-ray work of Will and Morche (52), who reported the unit cell expansion and contraction at around 130K. While this X-ray powder diffraction study was unlikely to yield accurate thermal motion parameters, the unit cell dimension would be much more reliably determined (62).

The low frequency modes behave even more strangely. The frequencies  $\omega_0$  for the  $163.5 \text{ cm}^{-1}$  ( $A_1$ ) and  $170 \text{ cm}^{-1}$  (E) modes fall with decreasing temperature, with an anomalous rise at 128K, while the damping parameters  $\Gamma$  fall more or less smoothly (Figures 28b and 31, table 7). The  $A_1$  mode parameters are again more scattered, due to the subtraction process, and to the underlying  $F_2$  (and unknown) scattering. The anomalies at 128K again suggest that some disturbance in the structure occurs at 128K, although the spectra of Figures 27 and 29 indicate cubic symmetry for  $88\text{K} < T < 300\text{K}$ , in accord with the structure refinements (50, 51). Furthermore, the  $20 \text{ cm}^{-1}$  (E) and  $15 \text{ cm}^{-1}$  ( $A_1$ ) mode softenings are completely uncharacteristic of boracite behaviour. In Cr - Cl and Cu - Cl, only the  $A_1$  wing feature is strongly temperature dependent. Softening of this magnitude is usually precursive to a phase transition, and since the low frequency modes have been associated mainly with metal and halogen motions, some displacement of these ions at a temperature below 68K seems likely. This point will be developed in Chapter 4. Discussion of the lack of a displacive transition at 128K is also deferred until then.

### §3.7 Conclusions

The number of  $q \approx 0$  normal mode frequencies visible as peaks in the Raman spectrum is in reasonable agreement with the group theoretical prediction, considering the highly absorptive nature of the material, and the low scattering efficiencies. A cubic space group is indicated at a selection of temperatures between 88K and 300K. The characteristic frequencies  $\{\omega_a\}$  and the damping parameters  $\{\Gamma_a\}$  of the Raman active modes do not behave entirely normally with varying temperature. The anomalies in these parameters are, however, consistent with the expansion of the lattice at around 128K. It would appear that the abnormal behaviour of the frequencies and damping parameters, and of the lattice parameter, is related to the irregularities in the dielectric and magnetic properties. These magnetoelectric properties seem to indicate the occurrence of a phase transition at  $\approx 128K$ , but we find no evidence of this. At temperatures not close to 128K, the high frequency modes exhibit normal temperature dependence. The interesting dynamic changes occur in the low frequency Raman spectra of boracites, in general. This region for Ni - I is very complicated, and contains many modes, so the complex interatomic interactions required to explain the observed temperature dependence cannot be determined from the Raman spectra alone. There is, in particular, an intriguing, and inexplicable 'soft mode' in this frequency region, which does not seem to be associated with the ferroelectric transition.

The dielectric properties of Ni - I are especially related to the modes of  $F_2$  symmetry. Unfortunately, these modes are very weak in the Raman spectrum, and no useful predictions concerning

dielectric variations can be made from the  $F_2$  Raman spectra. These 'polar' modes are, however, infrared active. There is, therefore, considerable scope for a useful, exhaustive infrared study of cubic Ni - I, as well as a need for further inelastic neutron scattering studies.

CHAPTER 4

PHASE TRANSITIONS IN NICKEL-IODINE BORACITE

Introduction

In Chapter 3, the properties of the cubic phase of Ni - I were discussed in some detail. It is the purpose of this chapter to present the results of a Raman spectral study of the ferroelectric transition in Ni - I, and further to report and discuss the existence of a further transition at a temperature of roughly 10K.

Since the primary reason for the study of boracites is given by their properties as improper ferroelectrics, a discussion of this class of transition is presented in §4.1. This discussion is given in terms of the phenomenological Landau theory of phase transitions. This theory is inadequate in many cases, and of limited scope in all instances, but is sufficient for a discussion at the level of sophistication of §4.1. The properties of cubic Ni - I were given in §3.1, and the known transition properties are given in §4.2 to complete the picture to date. The experimental details, and the results of both inelastic and elastic light scattering experiments, are described in §4.3 and §4.4. In §4.5 are presented the group theoretical predictions for the normal mode symmetries and for the existence of soft modes in any boracite with the assumed sequence of transitions. Although Ni - I has not been proved to follow this sequence, these predictions form a basis for further discussion of the measured spectra. In §4.6 and §4.7 are the possible inferences

to be made from the Raman spectra, with regard to structural and magnetic properties and transitions in Ni - I. There are apparent structural instabilities in the form of soft modes in the Raman spectra of Ni - I, and these are described and discussed in §4.8. Finally, in §4.9, the known transition properties of Ni - I and the results of the Raman spectral investigation are collated and conclusions are drawn.

#### §4.1 Landau Theory and Improper Ferroelectrics

Since Landau originally put forward his phenomenological theory of phase transitions in 1937 (64) there have been many excellent reviews and critiques of its methods, successes and shortcomings (e.g. 48, 64). The theory is often maligned by theoreticians, but is, in fact, a useful tool for describing many phase transition (PT) properties, provided its limitations are borne in mind. Both Landau theory and improper ferroelectric theory are complicated topics, so the following discussion is of necessity inadequate, and emphasises only the points of particular relevance to boracites. For greater detail and completeness, the articles by Cochran (64) and Dvořák (65) are most useful and concise.

The fundamental assumption of Landau theory is that the free energy  $F$  of a crystal may be written as a power series in the order parameters  $\{\xi_i\}$ . An order parameter is a quantity which is zero on one 'side' of the transition, and nonzero on the other. The fundamental characteristic of an improper transition is that more than one order parameter is critically involved. Thus we write:

$$4.1 \quad F = F_0 + \sum_i A_i \xi_i + \sum_{ij} B_{ij} \xi_i \xi_j + \sum_{ijk} C_{ijk} \xi_i \xi_j \xi_k \\ + \sum_{ijkl} D_{ijkl} \xi_i \xi_j \xi_k \xi_l + \dots$$

where all the coefficients A, B etc. are assumed to be nonsingular functions of temperature. It is largely this assertion which renders Landau's theory inadequate, particularly at temperatures close to the transition temperature  $T_0$ . The form 4.1 can be further simplified if the requirements of group symmetry and stability are imposed. Translational invariance of the crystal gives  $B_{ij} = B_i \delta_{ij}$ , and equilibrium configuration stability requires:

$$4.2 \quad \left( \frac{\partial F}{\partial \xi_i} \right)_E = 0 ; \quad \left( \frac{\partial^2 F}{\partial \xi_i^2} \right)_E > 0 ; \quad \forall i.$$

It follows that  $A_i = 0$ , or the 'high temperature' phase is always unstable. The expression 4.1 now becomes

$$4.3 \quad F = F_0 + \sum_i B_i(T) \xi_i^2 + \sum_{ijk} C_{ijk}(T) \xi_i \xi_j \xi_k \\ + \sum_{ijkl} D_{ijkl}(T) \xi_i \xi_j \xi_k \xi_l + \dots$$

and the relative values and signs of the B, C, D coefficients decide the order of the transition, and the stable configuration. This will now be illustrated in the particular case of the boracite free energy formula (in a much simplified form!). A detailed and rigorous treatment is given in refs. 66 - 68.



The essential terms required in 4.3 to produce an improper PT are:

$$4.4 \quad F' = \frac{1}{2}B_1\xi_1^2 + \frac{1}{2}B_2\xi_2^2 + C\xi_1^2 \xi_2 + \frac{1}{4}D\xi_1^4 + \frac{1}{6}E\xi_1^6$$

where the factors  $\frac{1}{2}$ ,  $\frac{1}{4}$  have been introduced for convenience. A first order transition occurs at  $T_0$  for  $B_1 \propto T - T_c$  and  $D < 2C^2/B_2$ , and a continuous (second order) transition occurs at  $T_c$  for  $D > 2C^2/B_2$ , provided  $B_2, C, D$  and  $E$  are taken as constants. The resultant forms of the free energy as a function of  $\xi_1$  are illustrated in Figures 32a and 32b. A transition is termed first order when two distinct phases are in equilibrium at the transition, and second order if these two phases are identical. For Figure 32, the stability conditions 4.1 give the following relations:

$$4.5 \quad \xi_2 = -\frac{C}{B_2} \xi_1^2$$

$$4.6 \quad \xi_1^2 = \frac{\sqrt{G^2 - EB_1} - G}{E}; \quad G = \frac{D}{2} - \frac{C^2}{B_2}$$

Therefore, if the transition is first order, it occurs at  $T = T_0 > T_c$ , and the order parameters vary as shown in Figure 33a. For a second order transition, the transition is at  $T = T_0 = T_c$ , and the variation of  $\xi_1, \xi_2$  is as shown in Figure 33b. It can be seen that the order parameter variation is continuous, while at a first order

FIGURE 32: The free energy of equation 4.4 for temperatures above, below and equal to  $T_0$ .

Figure 32a: A first order transition;

$$T_0 = T_c + \frac{3}{16E\alpha} \left( D - \frac{2C^2}{B_2} \right)^2$$

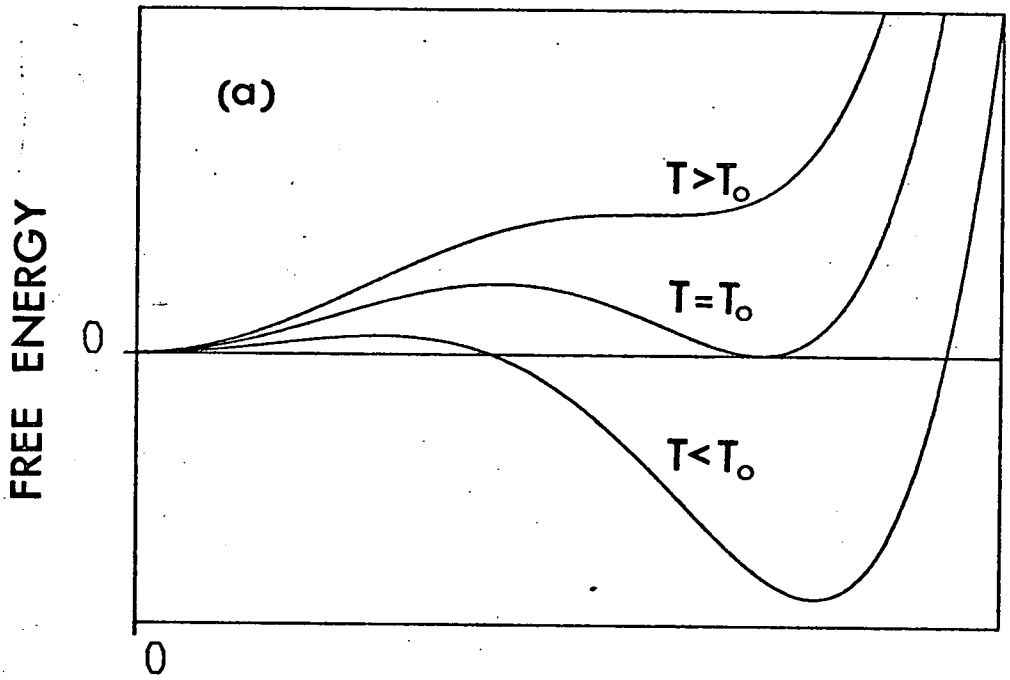
Figure 32b: A continuous transition

$$T_0 = T_c$$

FIGURE 33: The temperature variation of the energetically favoured values of the primary ( $\xi_1$ ) and secondary ( $\xi_2$ ) order parameters at:

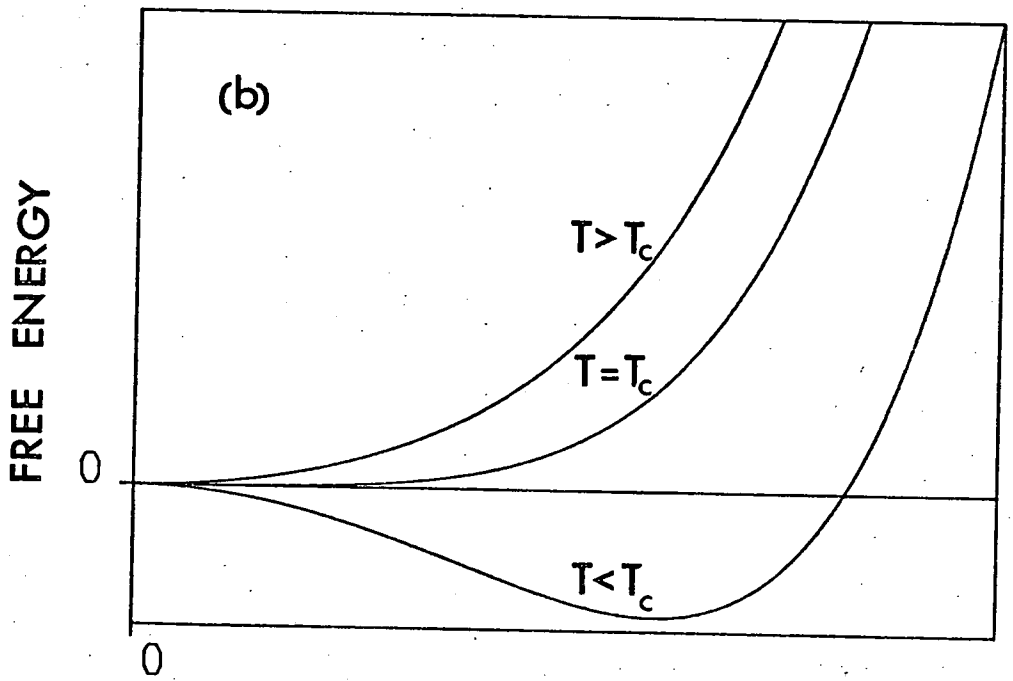
- a) a first order improper transition.
- b) a continuous improper transition.

FIRST ORDER



PRIMARY ORDER PARAMETER  $\xi_1$

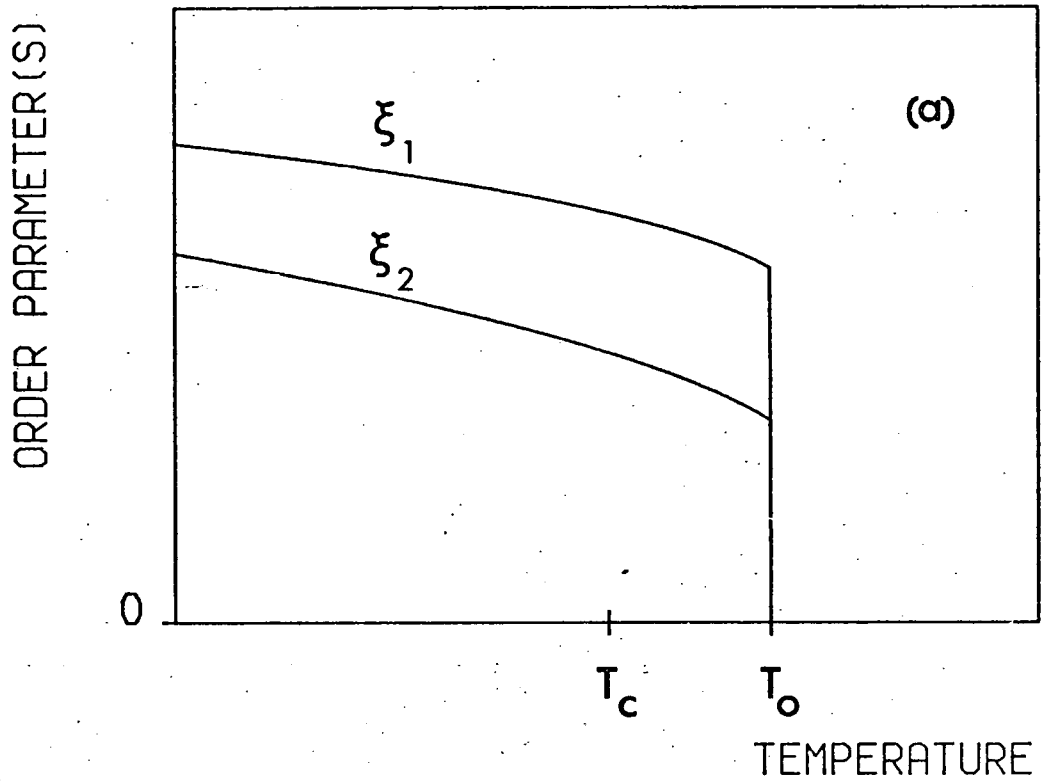
SECOND ORDER



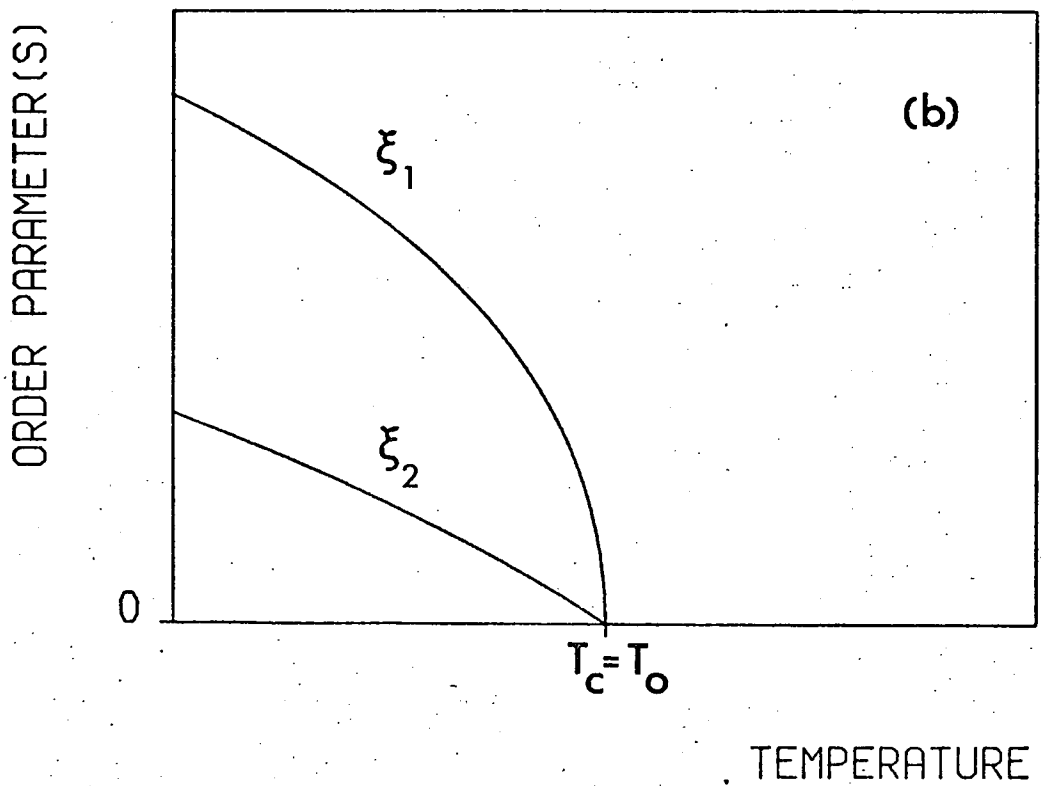
PRIMARY ORDER PARAMETER  $\xi_1$

FIG 33

FIRST ORDER



SECOND ORDER



transition, there is a discontinuous jump in  $\xi_1$  and  $\xi_2$  at  $T_0$ . It is clear, particularly in Figure 33b, that the primary order parameter is that with strongest temperature dependence close to  $T_0$ . In terms of symmetry changes, the introduction of a nonzero primary order parameter leads to the correct change of symmetry, whereas a nonzero secondary order parameter alone does not.

Dvořák and Petzelt (66) have considered the possible lowest order expansion terms for boracites which are invariant under the space group operations. They find that there are terms in the free energy of the form of 4.4, with the spontaneous polarisation  $P_s$  as secondary order parameter. Furthermore, they find cubic invariants in addition to that in 4.4, which imply that the cubic-orthorhombic transition in boracites is, of necessity, first order. The spontaneous polarisation alone cannot produce the required symmetry change.

The connection between the Landau theory, and the familiar soft mode theory of displacive transitions can be established as follows. If the anharmonic free energy of equations 1.13 and 1.35 in the  $q$ -representation is extended to higher orders, and the eigenvalue equation 1.21 is accounted for, the free energy becomes ( $K$  is a reciprocal lattice vector):

$$4.7 \quad F = \frac{1}{2} \sum_{\underline{q}^a} \omega_a^2(\underline{q}) |Q_{\underline{q}^a}|^2 + \sum_{\underline{q}_1 \underline{q}_2 \underline{q}_3} V \begin{pmatrix} \underline{q}_1 & \underline{q}_2 & \underline{q}_3 \\ a & b & c \end{pmatrix} Q_{\underline{q}_1^a} Q_{\underline{q}_2^b} Q_{\underline{q}_3^c} \\ \times \delta(\underline{q}_1 + \underline{q}_2 + \underline{q}_3 + \underline{K}) + \dots$$

This is of the form of 4.3, and a transition with  $B_i \propto (T - T_c)$  is given by  $\omega_a^2(\underline{q}) \propto (T - T_c)$ . This expansion is, of course, only valid

in the weakly anharmonic case. In the case of a second order transition, this represents a mode which 'freezes out' at the transition. For a first order transition, however, the transition occurs before this can happen (at  $T_0 > T_c$ ). In proper ferroelectrics, at a second order transition, it is a  $q \approx 0$  mode whose frequency might be expected to go to zero. This would imply a Curie-Weiss law for the static dielectric constant, provided that the Lyddane-Sachs-Teller law holds (10), i.e.

$$4.8 \quad \frac{\epsilon(0)}{\epsilon(\infty)} = \prod_b \frac{\omega_b^2(\text{LO})}{\omega_b^2(\text{TO})} = \frac{\omega_a^2(\text{LO})}{\omega_a^2(\text{TO})} \prod_{b \neq a} \frac{\omega_b^2(\text{LO})}{\omega_b^2(\text{TO})} \propto \frac{1}{(T-T_c)}$$

where a transverse mode is assumed to be 'soft'. If  $\omega^2 \rightarrow 0$ , there is no 'restoring force', and the structure is unstable against a distortion to the ferroelectric phase.

In the boracites, however, the 'soft' coordinate is associated with a zone boundary X-point mode, of wavevector (strictly a star of wavevectors (14))  $\langle \frac{2\pi}{a}, 0, 0 \rangle$ . This means there is no  $q \approx 0$  soft mode, although there will be soft modes for  $T < T_0$  (see §4.5). The physical origin of coupling of  $\underline{P}_s$  to the soft coordinate is discussed by Cochran (64). In essence, the secondary displacements giving rise to  $\underline{P}_s$  are induced by the primary displacements associated with  $\xi_1$  through anharmonic forces.

#### §4.2 The Known Transition Properties of Ni - I

Ni - I is unique among boracites in that its Néel and Curie temperatures ( $T_N$  and  $T_C$ ) are coincident. The transition at  $T_C = 68K$  (46, 47, 49, 53, 69) is therefore thought to be not only the usual boracite coupled transition, but a transition from a paramagnetic phase to an antiferromagnetic phase, with a weak ferromagnetic component. Apart from a low temperature neutron diffraction study of Ni - I (70), to determine the magnetic structure, no structural data has been published for Ni - I below 68K. Since the neutron experiment of ref. 70 was performed at a very low temperature, there is no conclusive evidence that the transition at 68K is, in fact, to an orthorhombic phase. Furthermore, light scattering data indicates the presence of a further transition at  $T < 10K$ , which is precisely the temperature régime of the neutron experiment (stated as being at 6K).

It was proposed that the anomalies in the structural and magneto-electric properties of Ni - I (see §3.1) at  $T \approx 130K$  were indicative of the phase transition (71) to an antiferromagnetic phase, but this proposition has since been invalidated by the discovery that paramagnetism persists as far as 68K (72). It has further been suggested (52) that the peculiar behaviour of the lattice parameter indicates a structural transition, although this has also been shown to be incorrect by structural (50, 51) and light scattering (55, 56, Chapter 3 of this thesis) measurements.

Finally, the results of a low-temperature study of the magnetic properties of Ni - I must be accounted for (69, 70). There is a change in the nature of the magnetisation curves (magnetisation  $\sigma$

vs. applied field  $H$ ) of Ni - I at a temperature of roughly 10K, and there is a ferromagnetic moment parallel to  $P_s$  at 6K. It has been suggested (73) that the existence of a magnetic transition in the region of 10K can be inferred from these results, and that this transition must also involve a structural change (see §4.5).

### §4.3 Experiment

The experimental details are essentially the same as those described in §3.2, so only the differences in techniques need be discussed here. The sample was the same  $[100]$  growth sector as was used for the study of the cubic phase, and the Coderg T800 system of §1.6 was used to disperse the scattered light and record the spectra, again to a resolution of  $2.5 \text{ cm}^{-1}$ .

Cooling was effected by use of a Thor flow cryostat, with nitrogen vapour flow for 88-295K, and helium vapour flow for  $T < 88\text{K}$ . Again, the  $\approx 5\text{K}$  of laser heating mentioned in §3.2 must be accounted for. In addition to the study of the Raman scattered light, a record was made of the intensity of elastic scattering as a function of temperature. The method behind this experiment entailed making a real time record of the  $\omega = 0$  scattering, with a spectral slit width of  $4 \text{ cm}^{-1}$ , as temperature varied. This induces a time lag, and consequently a temperature lag, between thermocouple and sample, and thus yields a wrong absolute temperature. Provided  $\frac{\partial T}{\partial t}$  is kept fairly constant, however, this error should be constant for all temperatures and does not render the data useless. As the laser intensity for the elastic scattering experiment was very low ( $\approx 4\mu\text{W}$ ),



laser heating is negligible, and can be ignored. This low intensity was achieved by use of a  $10^5$  filter.

Footnote to §4.3

Since all the spectra in Chapter 4 are of  $Z(??)Y'$  geometry, this will be contracted to merely ?? e.g.  $Z(Y'X')Y' \rightarrow Y'X'$ .

§4.4 Presentation of Results and Analysis

In Figures 34-37 are presented the Raman spectra in the four polarisations permitted by the scattering geometry, each at four representative temperatures. These temperatures were chosen to give the form of the cross-section in the four régimes relevant to the transition properties of Ni - I. These are:

- a) Well above the 130K anomalous region (295K).
- b) Between the anomalous region and the ferroelectric transition at  $T_c = 68K$  (100K).
- c) In the ferroelectric phase (25K).
- d) At the lowest temperature attainable with the system of §4.3 (< 7K).

It should be remembered that these temperatures may be too low by a few degrees (less than 5K, see §3.2), although they have been chosen to be at least this far from the critical temperatures where possible. The resonant frequencies and damping parameters of the bands in these spectra are presented in tables 8 and 9. Where bands are very weak, the fitting procedure giving rise to these parameters cannot

FIGURES 34-37: The Raman spectrum of Ni-I at four representative temperatures, in four polarisations.

FIGURE 34:  $Z(X'X')Y'$  geometry.

FIGURE 35:  $Z(Y'X')Y'$  geometry.

FIGURE 36:  $Z(Y'Z)Y'$  geometry.

FIGURE 37:  $Z(X'Z)Y'$  geometry.

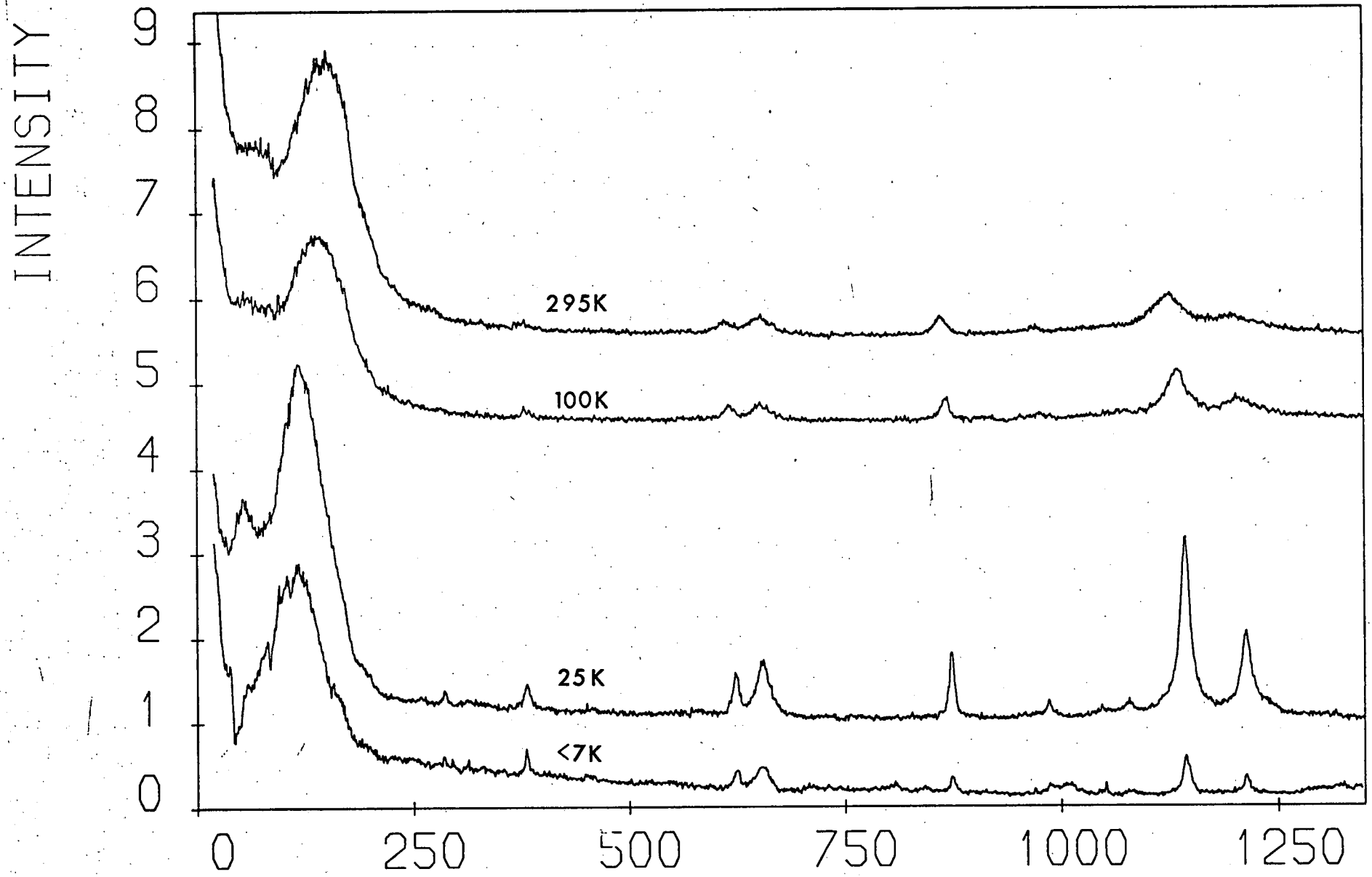
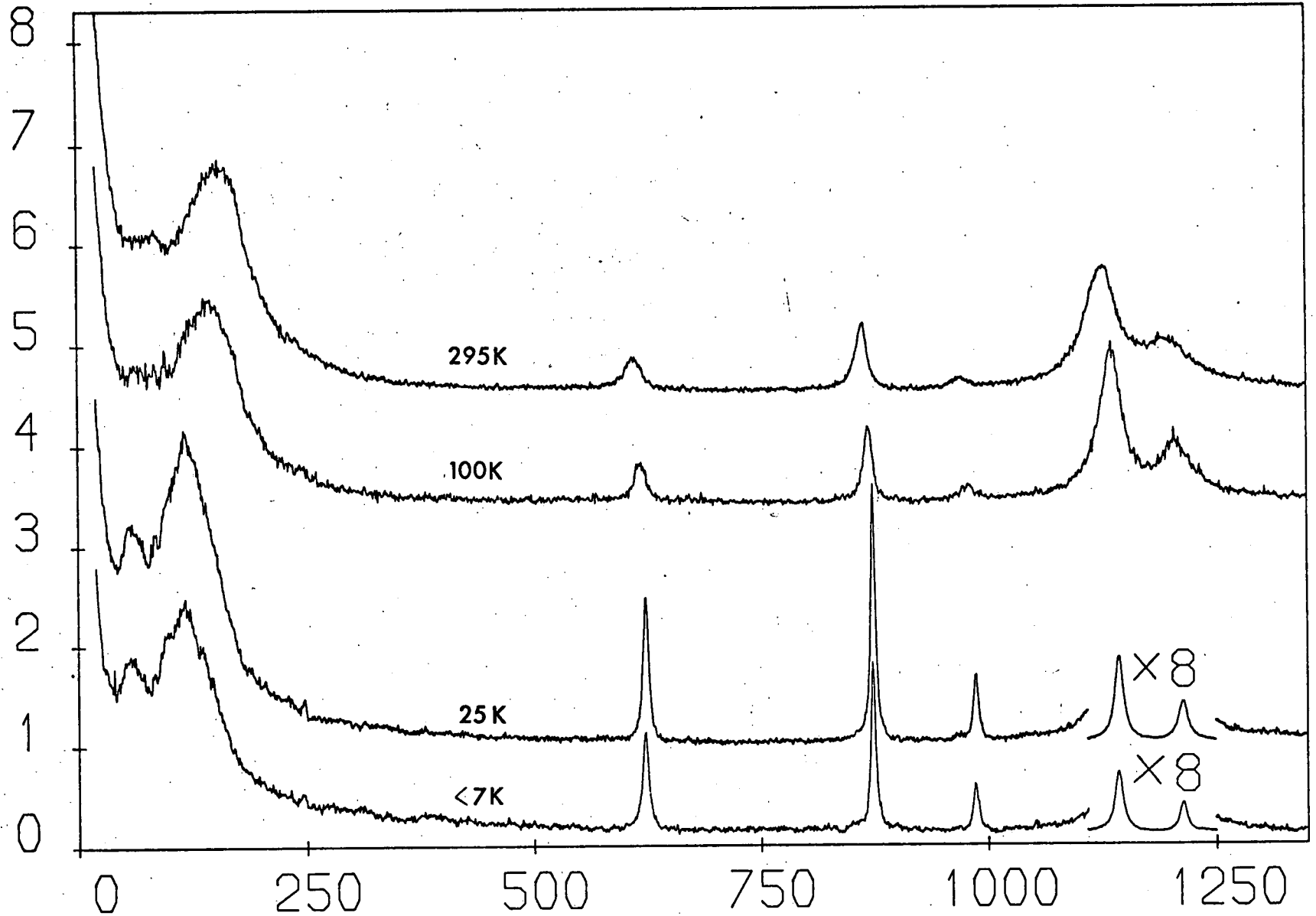


FIG 34

WAVENUMBER

INTENSITY



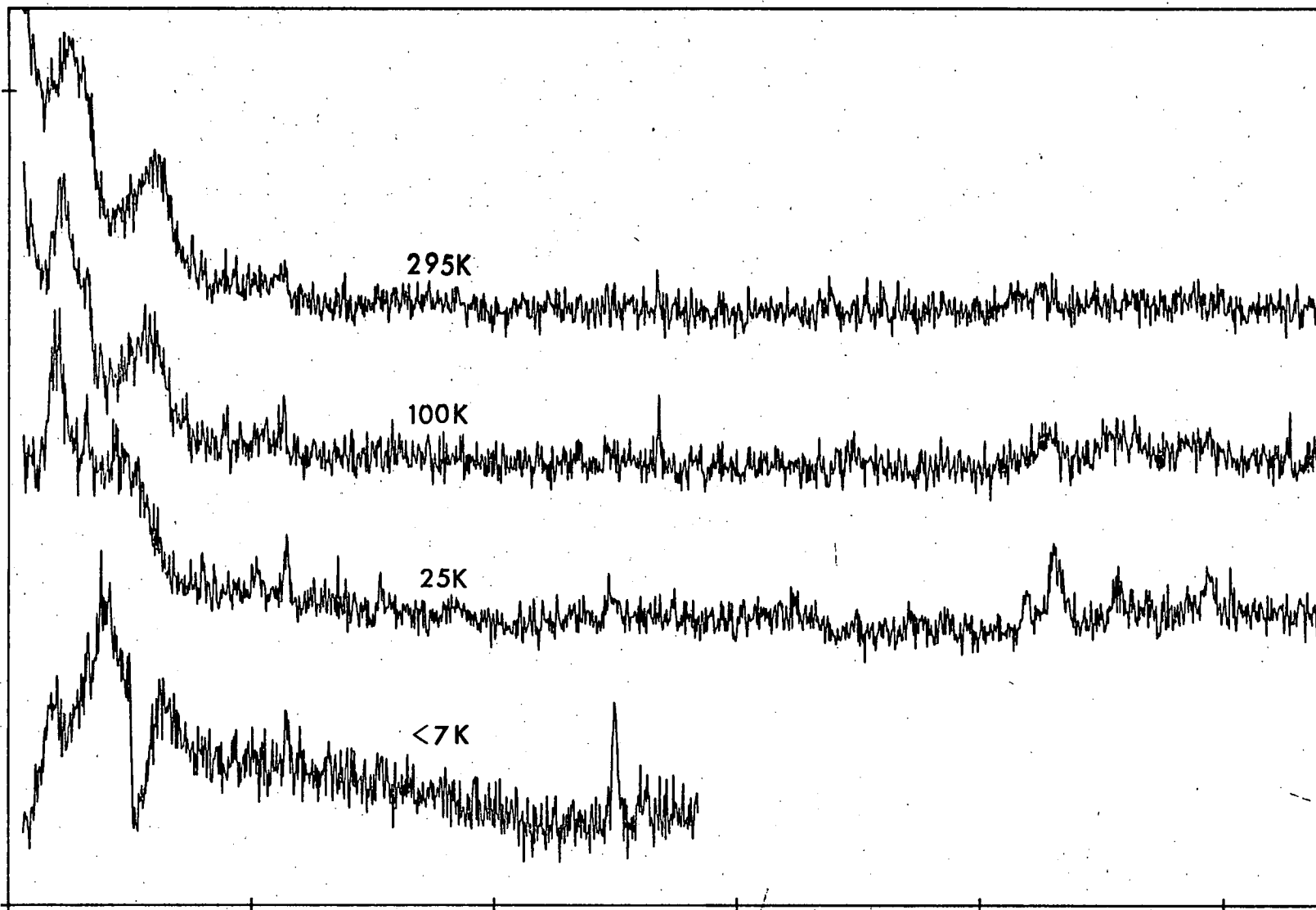
WAVENUMBER

FIG 35

INTENSITY

1

0



0 250 500 750 1000 1250

WAVENUMBER

FIG 36

INTENSITY

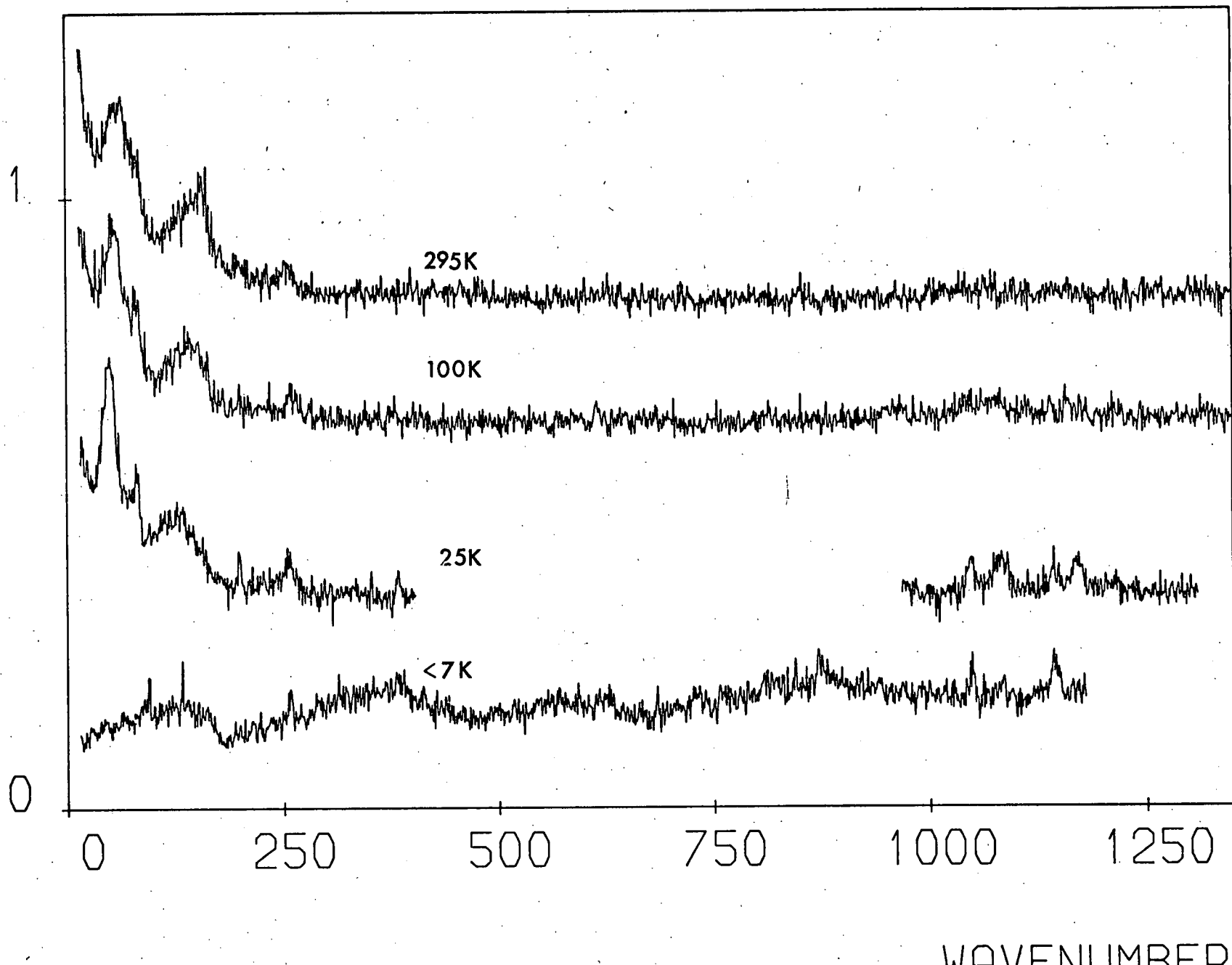


FIG. 37

TABLES 8 and 9. Frequencies and damping parameters in  $\text{cm}^{-1}$  (if appropriate) for the Raman active optic modes of Ni - I at four representative temperatures.

X'X'				Y'X'			
295 K	100 K	25 K	7 K	295 K	100 K	25 K	7 K
72.0*	68.0*	56.0*		85.0(35)	82.0(65)	59.0(23)	55.0(23)
						85.0 <sup>†</sup>	85.0 <sup>†</sup>
148.5*	144.0*	120.0*	122.0*				100.0 <sup>†</sup>
			167.0 <sup>†</sup>	170.0(90)	152.0(76)	125.0(68)	118.0 <sup>†</sup>
		194.0*	194.0 <sup>†</sup>				137.0 <sup>†</sup>
		286.0 <sup>†</sup>	286.0 <sup>†</sup>		248.0 <sup>†</sup>	248.0 <sup>†</sup>	245.0 <sup>†</sup>
378.0 <sup>†</sup>	380.0 <sup>†</sup>	383.0(9) <sup>†</sup>	381.0(5) <sup>†</sup>				
612.5(17)	616.5(13)	621.5(7)	624.0(4)	611.5(20)	618.5(13)	624.0(7)	623.0(7)
655.0(30)	653.5(21)	653.0(16)	654.0(16)				
863.0(16)	867.5(11)	871.5(6)	874.5(5)	863.5(15)	870.0(11)	874.0(6)	874.0(6)
970.0 <sup>†</sup>	977.0 <sup>†</sup>	986.0(7) <sup>†</sup>	988.0 <sup>†</sup>	970.0 <sup>†</sup>	979.5(14)	987.0(5)	986.5(6)
			1008.0 <sup>†</sup>				
		1046.0 <sup>†</sup>	1049.0 <sup>†</sup>				
		1078.0 <sup>†</sup>	1082.0 <sup>†</sup>				
1128.0(40)	1134.5(31)	1141.0(15)	1144.5(9)	1125.5(43)	1136.2(31)	1144.0(12)	1143.3(11)
1200.5(61)	1208.5(43)	1212.0(17)	1213.5(8)	1199.5(74)	1208.5(43)	1214.0(14)	1213.5(10)

\* - Known to consist of more than one band (see §2).

† - Too weak for fitting procedure (see §2).

TABLE 8

Y'Z				X'Z			
295 K	100 K	25 K	7 K	295 K	100 K	25 K	7 K
74.5*	54.0*	50.0*	45.0*	58.5*	56.0*	49.5*	
	81.0 <sup>†</sup>	79.0 <sup>†</sup>	81.0 <sup>†</sup>		81.0 <sup>†</sup>	81.0 <sup>†</sup>	90.0 <sup>†</sup>
152.5*	140.0*	106.0*	100.0*	158.0*	131.0*	131.0*	
						200.0 <sup>†</sup>	
255.0 <sup>†</sup>	257.0 <sup>†</sup>	255.0 <sup>†</sup>		257.0 <sup>†</sup>	260.0 <sup>†</sup>	257.0 <sup>†</sup>	257.0 <sup>†</sup>
280.0 <sup>†</sup>	280.0 <sup>†</sup>	286.0 <sup>†</sup>	287.0 <sup>†</sup>		378.0 <sup>†</sup>	382.5 <sup>†</sup>	382.5 <sup>†</sup>
		621.0 <sup>†</sup>	623.0 <sup>†</sup>				623.0 <sup>†</sup>
		1046.0 <sup>†</sup>			1057.0 <sup>†</sup>	1046.0 <sup>†</sup>	1045.0 <sup>†</sup>
1062.0 <sup>†</sup>	1069.0 <sup>†</sup>	1078.0 <sup>†</sup>				1080.0 <sup>†</sup>	1080.0 <sup>†</sup>
	1148.0 <sup>†</sup>	1141.0 <sup>†</sup>			1161.0 <sup>†</sup>	1143.0 <sup>†</sup>	1144.0 <sup>†</sup>
	1233.0 <sup>†</sup>	1235.0 <sup>†</sup>				1170.0 <sup>†</sup>	

\* - Known to consist of more than one band (see §2).

† - Too weak for fitting procedure (see §2).

TABLE 9



be used, and the values given in tables 8 and 9 are measured from Figures 34-37. Similarly, when features are known to consist of more than one band, these are marked in tables 8 and 9. This can occur due to overlap in frequency of contiguous bands, or to the form of the Raman tensors in the cubic phase.

The variation of the intensity of elastic scattering in the X' polarisation, as a function of temperature, is plotted in Figure 38. The dashed lines indicate extrapolated data. This extrapolation became necessary as the intensity fluctuated wildly in the critical regions, and the readings of intensity during a count-time of one second were consequently unreliable.

In Figures 39 and 40 are presented the characteristic frequencies,  $\omega_0$  and the damping parameters  $\Gamma$  respectively, of four 'high frequency' Y'X' modes. Figure 41 portrays the temperature dependence of these parameters for the  $170.0 \text{ cm}^{-1}$ , Y'X' mode. The parameters are, of course, those of equation 3.1. The solid lines in Figures 38-40 are intended merely as a guide to the eye.

#### §4.5 Symmetry Considerations

It is thought that the sequence of translational symmetries of boracites, with decreasing temperature, is:

cubic  $\rightarrow$  orthorhombic  $\rightarrow$  monoclinic  $\rightarrow$  trigonal (45).

This sequence is, however, far from complete in many boracites. The space group sequence corresponding to the above transitions is:

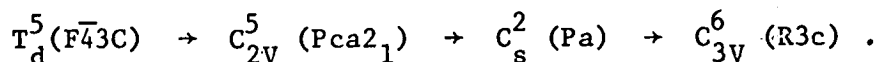


FIGURE 38: Temperature variation of the intensity of elastic scattering in Ni-I (intensity in arbitrary units).

FIGURE 39: Temperature variation of the resonant frequencies of four Y'X' modes in Ni-I.

FIGURE 40: Temperature variation of the damping parameters of the four modes of figure 39, with corresponding symbols.

FIGURE 41: Temperature variation of the frequency (squares) and damping parameter (triangles) of the  $170.0 \text{ cm}^{-1}$  Y'X' mode in Ni-I. The ordinate calibration is in units of  $(\omega_0 - 125) \text{ cm}^{-1}$  for frequency and  $(\Gamma - 65) \text{ cm}^{-1}$  for damping.

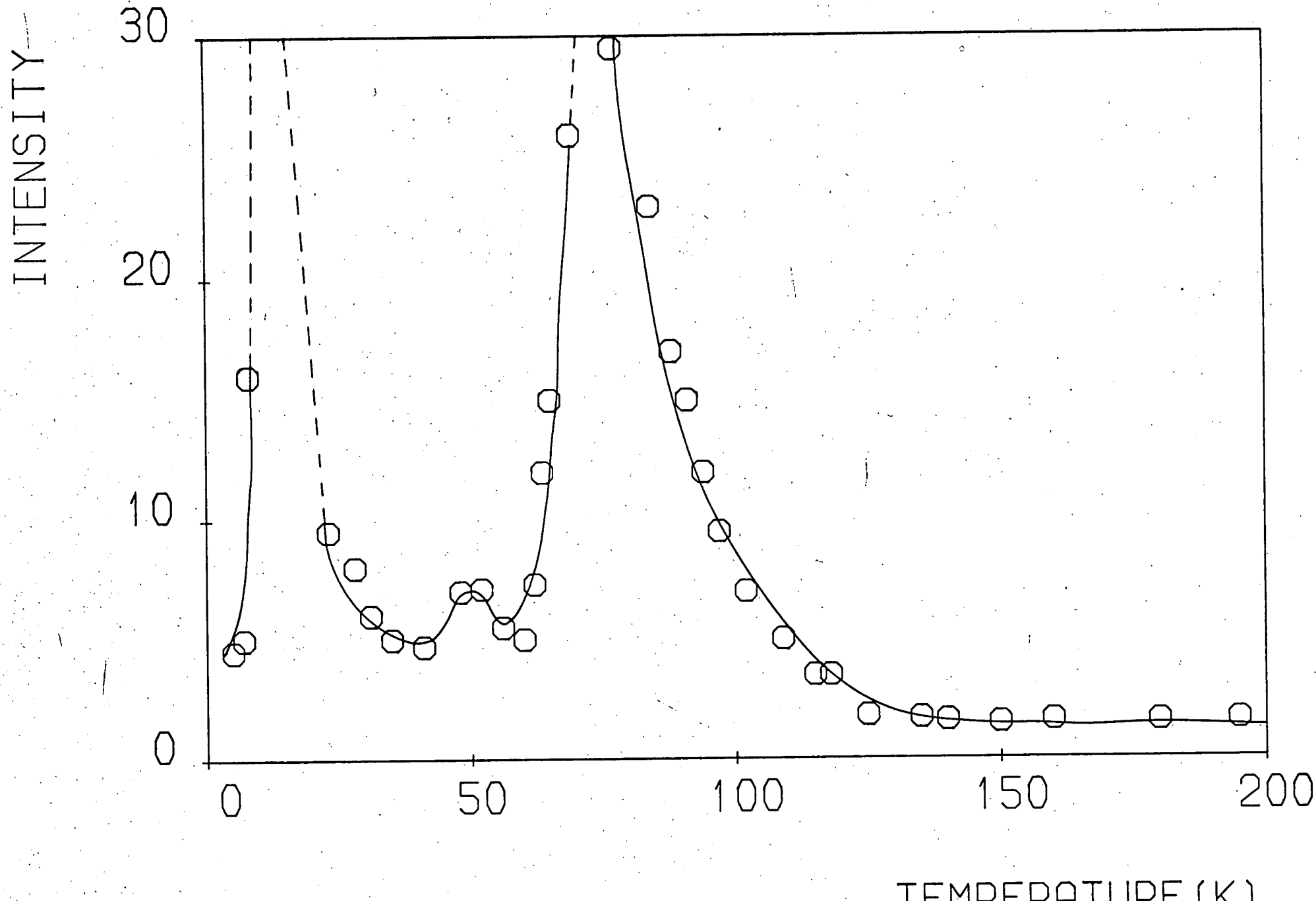


FIG 38

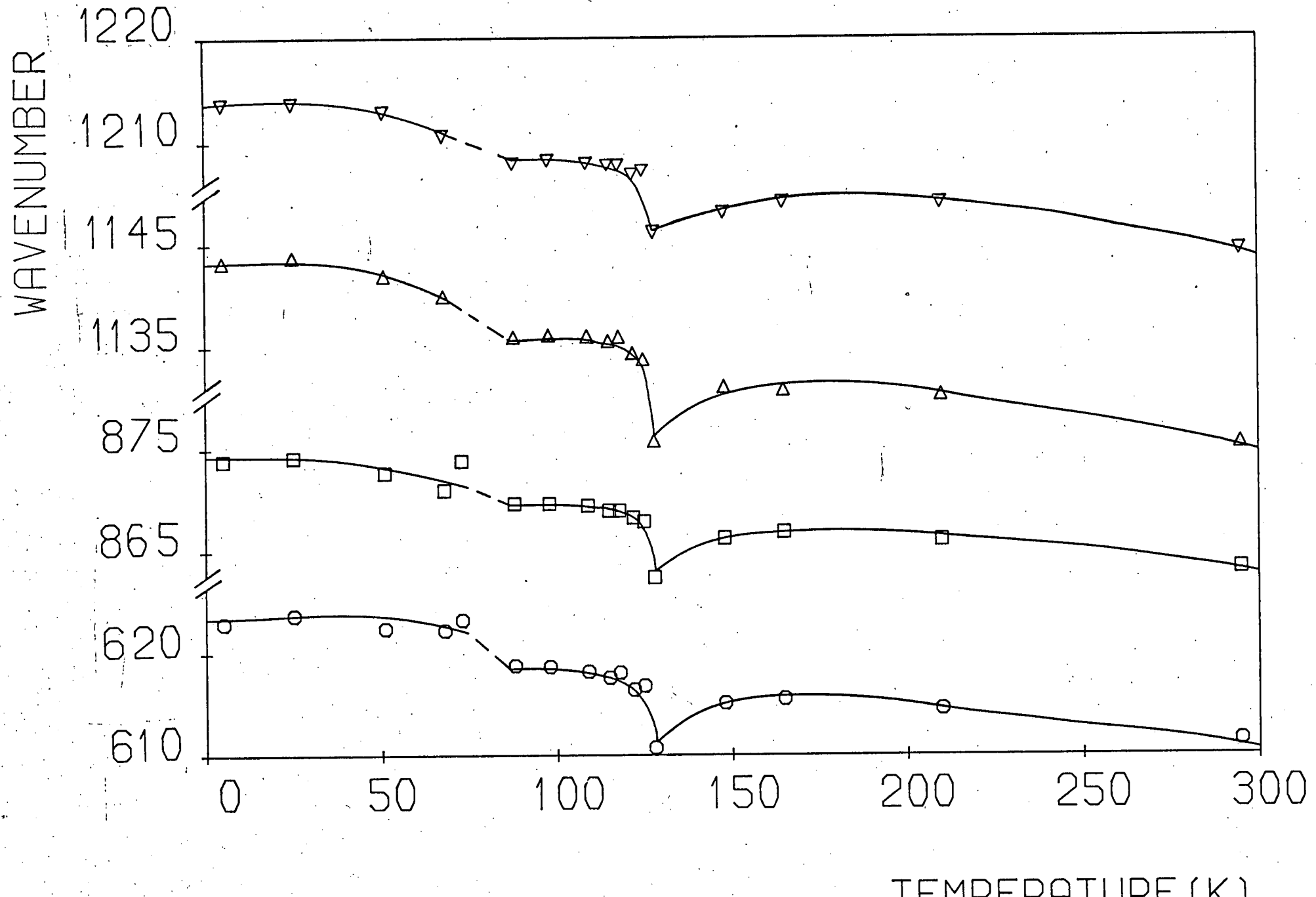


FIG 39

WAVENUMBER

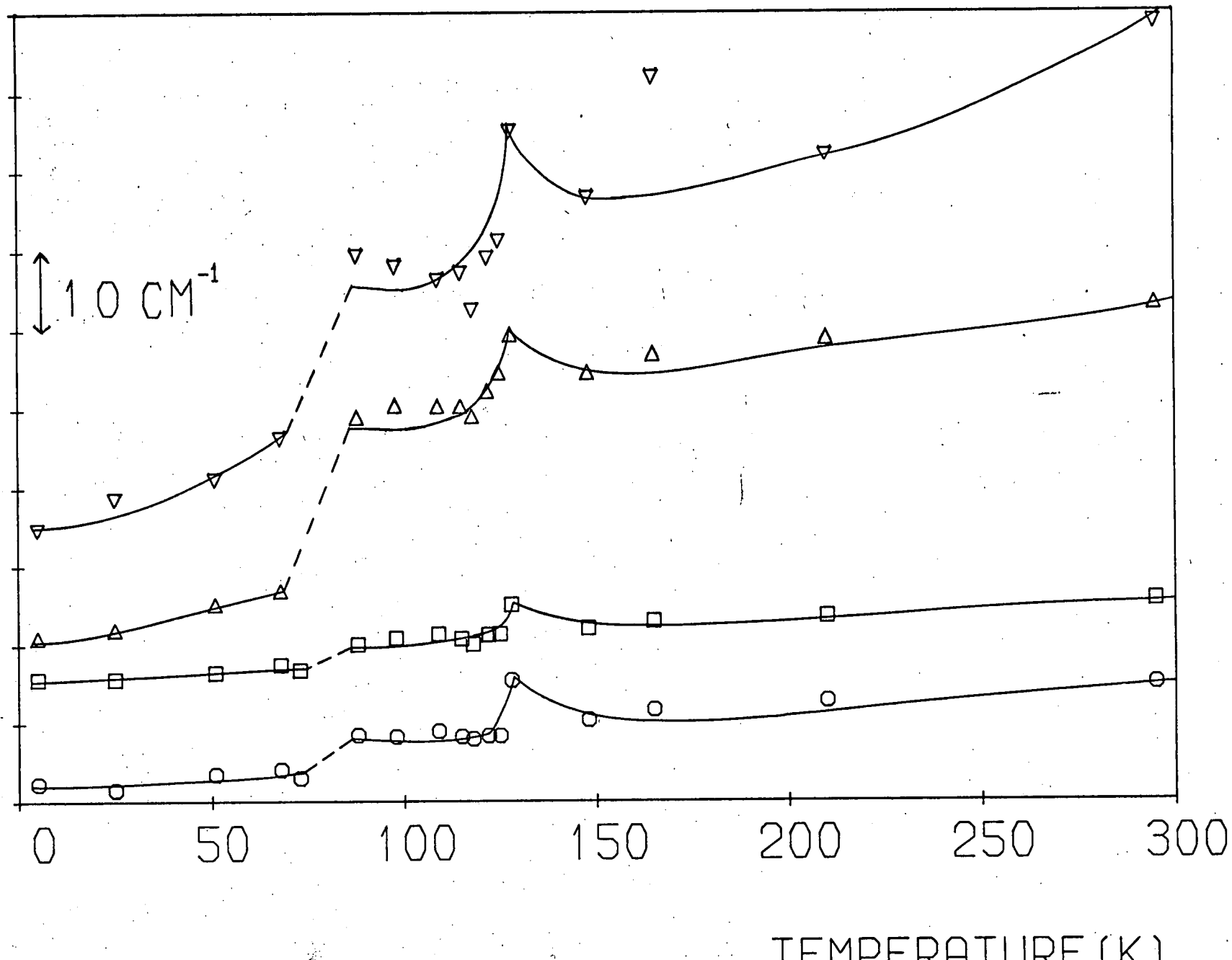


FIG. 40

WAVENUMBER

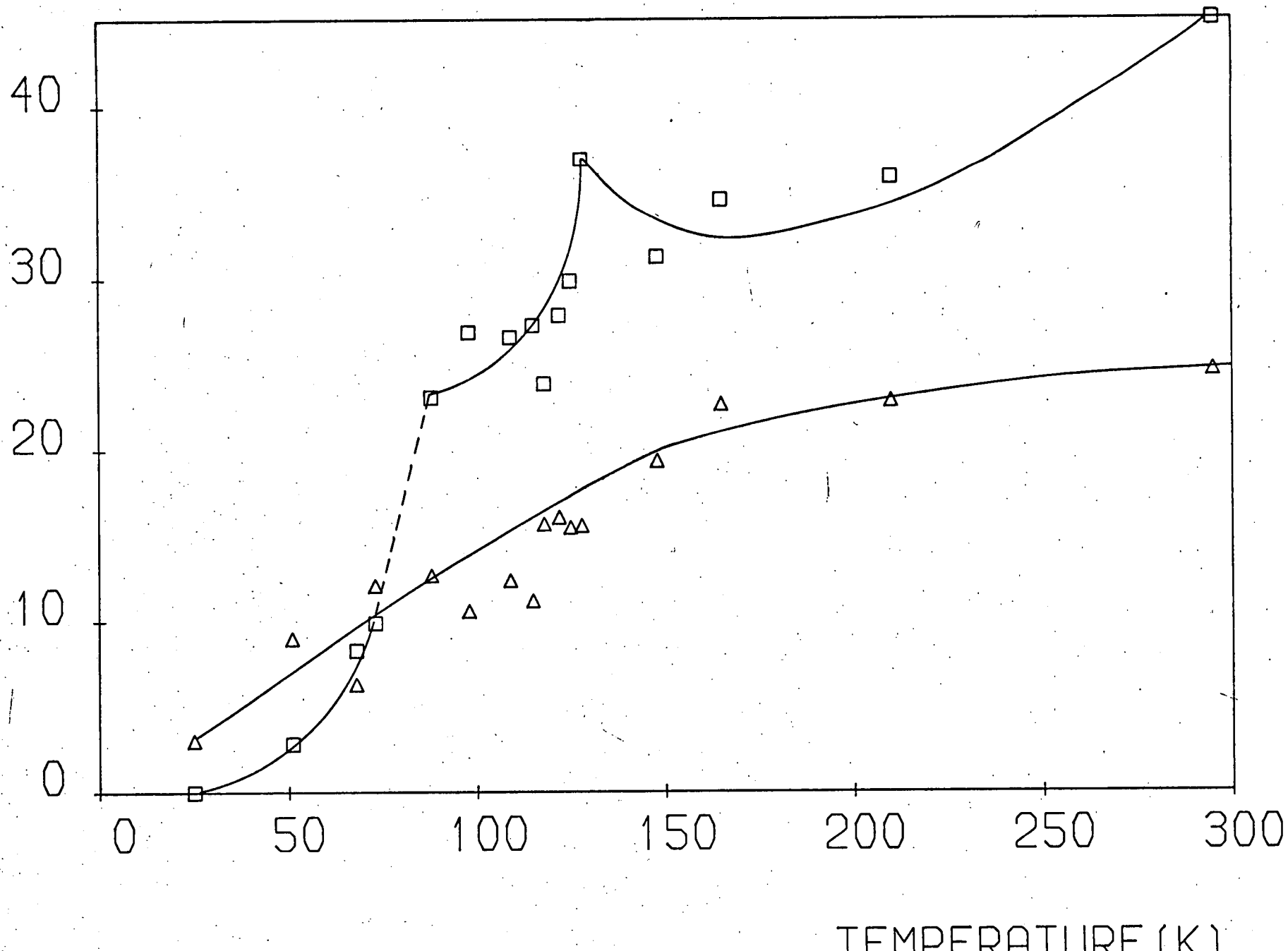


FIG 41

If the primitive unit cell in the cubic phase has volume  $V$ , the primitive cell volume changes according to the sequence

$$V \rightarrow 2V \rightarrow 4V \rightarrow V \quad (45, 74).$$

Applying the methods of §1.3 and §1.4, there should be  $4A_1 + 10E + 20F_2$  Raman active optic modes for cubic Ni - I, and  $72A_1 + 72A_2 + 72B_1 + 72B_2$  (including acoustic modes) for orthorhombic Ni - I. The respective point groups are  $T_d$  and  $C_{2V}$  (see tables 1 and 10). Since no detailed analysis of the atomic positions in the monoclinic boracite phase exists, a classification of the  $\underline{q} = 0$  normal modes in this phase is not possible. It is possible, however, to construct a correlation table for the normal mode symmetries between the cubic, orthorhombic and monoclinic phases (table 12, also see table 11). The indices (ZX) indicate that the (ZX) mirror plane of the  $C_{2V}$  point group has been chosen as the plane for the  $C_s$  group. The Raman tensors for these three phases, with respect to the cubic ( $X', Y', Z$ ) axes are given in table 13 (15, 17, 33). It can be seen that the cubic  $X'$  and  $Y'$  axes have been chosen to be the new orthorhombic axes, while  $Z$  defines the orthorhombic c-axis. The composition of the Raman spectrum is given in table 14, with this choice of axes.

It has been shown (66) that the primary order parameter for the transition is associated with a doubly degenerate X-point (zone boundary) mode corresponding to representation  $\tau_5$  of the group of  $\underline{q} = (0, \frac{2\pi}{a}, 0)$  or  $(\frac{2\pi}{a}, 0, 0)$  in space group  $T_d^5$ . Furthermore, this critical mode splits into homogeneous modes of  $A_1 + A_2$  symmetry with  $\underline{q} = 0$  in the new, 'folded' Brillouin zone. These should appear in the Raman spectrum as features with a frequency-temperature dependence similar to the  $\xi_1$ -temperature dependence of Figure 33a (i.e. strongly temperature dependent near  $T_0$ , constant for  $T \ll T_0$ .)

TABLE 10

The character table for the irreducible representations of point group  $C_{2v}$  (mm2) (12).

	E	$C_2$	$\sigma_v(ZX)$	$\sigma_v'(YZ)$
$A_1$	1	1	1	1
$A_2$	1	1	-1	-1
$B_1$	1	-1	1	-1
$B_2$	1	-1	-1	1



TABLE 11

The character table for the irreducible representations of the point group  $C_s(ZX)$ , (12).

	E	$\sigma_h(ZX)$
A'	1	1
A''	1	-1

TABLE 12

The correlations between the species of the point group  $T_d$  and those of its subgroups  $C_{2v}$  and  $C_s$ .

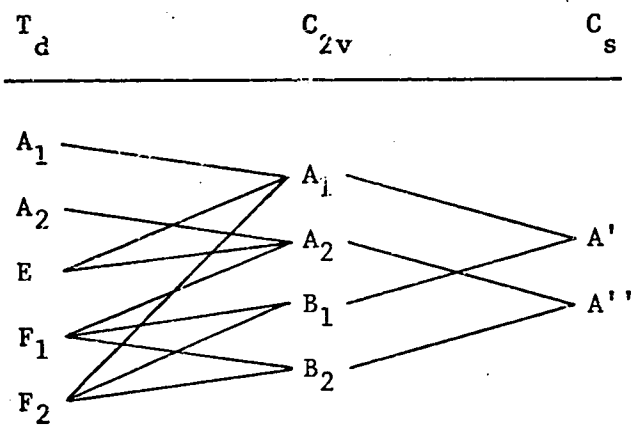


TABLE 13

The Raman tensors for the cubic, orthorhombic and monoclinic symmetry classes (15).

Table 13a) Cubic Raman tensors (axes X', Y', Z, see §2.5)

$$A_1 \begin{bmatrix} a & \cdot & \cdot \\ \cdot & a & \cdot \\ \cdot & \cdot & a \end{bmatrix} ; \quad E \begin{bmatrix} b & \cdot & \cdot \\ \cdot & b & \cdot \\ \cdot & \cdot & -2b \end{bmatrix} \quad \text{and} \quad \begin{bmatrix} \cdot & \sqrt{3}b & \cdot \\ \sqrt{3}b & \cdot & \cdot \\ \cdot & \cdot & \cdot \end{bmatrix}$$

$$F_2(X') \frac{1}{\sqrt{2}} \begin{bmatrix} \cdot & \cdot & d \\ \cdot & \cdot & d \\ d & d & \cdot \end{bmatrix}, \quad F_2(Y') \frac{1}{\sqrt{2}} \begin{bmatrix} \cdot & \cdot & d \\ \cdot & \cdot & -d \\ d & -d & \cdot \end{bmatrix}$$

$$\text{and } F_2(Z) \begin{bmatrix} d & \cdot & \cdot \\ \cdot & -d & \cdot \\ \cdot & \cdot & \cdot \end{bmatrix}$$

Table 13b) Orthorhombic Raman Tensors

$$A_1 \begin{bmatrix} a & . & . \\ . & b & . \\ . & . & c \end{bmatrix} ;$$

$$A_2 \begin{bmatrix} . & d & . \\ d & . & . \\ . & . & . \end{bmatrix}$$

$$E_1 \begin{bmatrix} . & . & e \\ . & . & . \\ e & . & . \end{bmatrix} ;$$

$$B_2 \begin{bmatrix} . & . & . \\ . & . & f \\ . & f & . \end{bmatrix}$$

Table 13c) Monoclinic Raman Tensors

$$A'(ZX) \begin{bmatrix} a & . & d \\ . & b & . \\ d & . & c \end{bmatrix} ;$$

$$A''(ZX) \begin{bmatrix} . & e & . \\ e & . & f \\ . & f & . \end{bmatrix}$$

TABLE 14

Symmetries of modes present in the four scattering polarisations in the cubic, orthorhombic and monoclinic phases of Ni - I.

	X'X'	Y'X'	Y'Z	X'Z
T <sub>d</sub>	A <sub>1</sub> + E + F <sub>2</sub>	E	F <sub>2</sub> (TO + LO)	F <sub>2</sub> (TO)
C <sub>2v</sub>	A <sub>1</sub>	A <sub>2</sub>	B <sub>2</sub>	B <sub>1</sub>
C <sub>s</sub>	A'	A''	A''	A'

#### §4.6 Structural Information in the Raman Spectra

A transition at 130K? :

Firstly, it can be stated that the Raman spectra, as discussed in §3.6, indicate that although there is a disturbance to the lattice at a temperature  $\approx 130\text{K}$  there is no structural transition at this temperature. This result, that Ni - I is cubic above 88K, is in agreement with the structural work at 77K (51) and 300K (50), but not with the speculation of Will and Morche (52) that a displacive transition occurs at 130K. It can be seen from tables 6 and 8, 9 that  $4A_1 + 8E + 8F_2$  modes have been detected, while  $4A_1 + 10E + 19F_2$  are predicted. The asterisks in tables 8 and 9 indicate the multiple  $F_2$  bands and reflect the dearth of low frequency Y'Z and X'Z modes. The 100K spectra of  $F_2$  symmetry confirm the tentative suggestion of §3.5 that the structure around  $1100\text{ cm}^{-1}$  contains first order bands, as these are considerably 'sharper' at 100K. Also, gratifyingly, a very weak E symmetry band can be discerned at  $248\text{ cm}^{-1}$ . One could not presume to have identified this without the retrospective knowledge of its presence in the 25K spectrum (Fig. 35). The eye of faith can discern its presence in Figure 29!

The ferroelectric transition at 68K:

At the ferroelectric transition, new bands appear in all the spectra. There should, in fact, be  $71A_1 + 72A_2 + 71B_1 + 71B_2$  Raman active optic modes, if the transition is to the normal boracite orthorhombic phase, which would require 204 new modes to appear below

68K. About one half of the Raman-active modes have been identified in the orthorhombic phases of Cr - Cl (75), Cu - Cl (59) and Mn - Cl (76), but only a few of the 204 new modes can be identified in Ni - I. This is due partly to the weak scattering properties of boracites, and the highly absorptive nature of Ni - I, and partly to the complicated low frequency ( $\omega < 300 \text{ cm}^{-1}$ ) profiles. The failure to resolve the low frequency Y'Z and X'Z modes is a function of the intrinsic near-degeneracies and bandwidths, not of the spectrometer resolution which was, again,  $2.5 \text{ cm}^{-1}$ .

The wing feature in Ni - I for  $T > T_c$  does not reduce at, or below, the ferroelectric transition (Figures 34-37) and it appears in all polarisations. In other boracites there is a broader, more prominent wing for  $T > T_c$ , and this wing appears in  $A_1$  symmetry only. A further disparity between Ni - I and other boracites is seen in the fact that the  $A_1$  wing in Cr - Cl and Cu - Cl reduces as the ferroelectric phase is reached, and subsequently disappears for  $T < T_c - 80\text{K}$ . Unfortunately, for Ni - I, the wing is so narrow that the insertion of filters during scanning over the laser frequency removes much of the information about the width and strength of the wing. The result is that the parameter  $\gamma$  and the strength  $S$  in equation 3.2 do not show consistent temperature behaviour. This is because a wide variety of  $S$  and  $\gamma$  describe any one spectral wing in Ni - I equally well. No quantitative statements can therefore be made regarding the behaviour of the wing at the transition. The  $A_1$  wing in Cr - Cl and Cu - Cl was conjectured as being due to disorder (see §3.5) associated mainly with the Cl ion. Qualitatively, the dissimilar nature and behaviour of of the wing in Ni - I suggests that it is either (i) not due to

disorder at all or (ii) the disorder in Ni - I lacks definite symmetry, is considerably less than in Cr - Cl and Cu - Cl, and persists well below  $T_c$ .

The frequencies associated in Chapter 4 with  $BO_4$  vibrations of around  $250 \text{ cm}^{-1}$  ( $E$ ),  $378 \text{ cm}^{-1}$  ( $A_1$ ) and  $255.0 \text{ cm}^{-1}$ ,  $1100.0 \text{ cm}^{-1}$  ( $F_2$ ) are confirmed by the lower temperature spectrum. The first three are clearly measurable and show little frequency shift through the ferroelectric transition. The rigidity of the B - O framework to metal and halogen substitution makes this discovery not too surprising.

It can be seen from Figure 39 that the characteristic frequencies of most of the Y'X' modes rise fairly abruptly at  $T_c$ , with the notable exception of the  $170 \text{ cm}^{-1}$  (at 295K.) Y'X' mode, which actually drops in frequency by  $13 \text{ cm}^{-1}$  at the transition (Figure 41). The  $655.0 \text{ cm}^{-1}$  X'X' mode shows no frequency shift. The linewidths of the X'X' and Y'X' modes reduce by approximately a factor of two at the transition (Figure 40) with again the measurable exceptions of the  $655.0 \text{ cm}^{-1}$  X'X' mode, and the  $170.0 \text{ cm}^{-1}$  Y'X' mode (Figure 41) which show no sharp variation in  $\Gamma$  at  $T_c$ . The frequency and damping parameter shifts indicate that there is indeed a transition at a temperature of about 70K. Furthermore, the shifts imply that anharmonic interactions in Ni - I must, on average, decrease below  $T_c$ , to account for the general reduction in the phonon self energies, and thus the reduced 'damping'. It is this reduction in the parameters  $\{\Gamma_a\}$  that is wholly responsible for the increase in intensity of the high frequency modes in Figures 34 and 35, as the parameters  $S$  of equation 3.1 do not show any significant increase at  $T_c$ . This means that the polarisabilities of the modes do not change significantly at  $T_c$ . The persistent



softening of the  $170 \text{ cm}^{-1}$  mode in Y'X' is remarkable, and is discussed elsewhere (§4.8). The  $A_1$  soft mode in the cubic phase (Figure 28b) cannot be 'followed' into the ferroelectric phase as the subtraction process of §3.3 is no longer possible, and the composition of the  $\omega < 300 \text{ cm}^{-1}$  region in the X'X' spectrum below  $T_c$  is no longer clear. The Y'Z' and X'Z' spectra for  $T < T_c$  are still similar in appearance, and do not have any strongly temperature dependent mode frequencies, although again the damping decreases in general, and some new modes do appear.

A detailed investigation of the spectra at a temperature just below  $T_c$ , and at 25K, revealed no discernible splitting in frequency or damping parameter of any of the modes to correspond to the correlations  $E \rightarrow A_1 + A_2$ ,  $F_2 \rightarrow A_1 + B_1 + B_2$  between groups  $T_d$  and  $C_{2V}$ . These spectral results are consistent with a distortion at a temperature of about 70K, from a cubic to an orthorhombic phase. It must be remarked, however, that other crystal classes cannot be precluded from the Raman spectra alone. The lack of frequency or linewidth splittings between spectra indicate that the magnitude of the deviation from cubic symmetry is small. The actual temperature of the transition may be seen to be  $73\text{K} \pm 4\text{K}$  from the central peak result of Figure 38. Superficially, this temperature might appear to be at variance with the accepted value of 68K (47) but the discrepancy is the result of the time-lag mentioned in §4.4, and the consequent temperature lag between thermocouple and sample. It can further be seen from the central peak result that, whatever is the cause of the central peak, or peaks, at the transition, domain walls did not cause parasitic scattering

below  $T_c$ , as the intensity of elastic scattering returns to its 'cubic' value. A similar effect was observed in Cr - Cl (75). This, along with the lack of spectral 'mixing' in the 25K spectrum suggests that the sample formed a single ferroelectric domain in the region of the laser beam path, with the axes chosen in § 4.5. The 'choice' of which two of the cubic  $\langle 110 \rangle$  axes become the orthorhombic 'a' and 'b' axes may have been affected by the boundary conditions, in which the faces of the sample were  $[110]$ ,  $[\bar{1}10]$  and  $[001]$ , as the sample was not poled.

A transition at  $\approx 7K$ :

At a temperature below 7K ( $\pm 2.5K$ ), a further phase can be seen to exist from the Raman spectra, which has a different symmetry from the phase between 7K and 68K. The existence of this 'new' transition can be verified from the elastic scattering intensity of Figure 38 where there is a further maximum at 12 K ( $\pm 5K$ ). This temperature is again too high due to the time lag alluded to above, and the -5K correction gives a transition temperature of 7K ( $\pm 5K$ ). The most marked changes in spectral lineshape occur in the previously non-critical Y'Z and X'Z spectra. These are quite different from their counterparts in the orthorhombic phase, and from each other. The wing feature in Y'Z polarisation has disappeared below 7K, and the lineshape in this spectrum around  $135 \text{ cm}^{-1}$  is most peculiar, with an apparent anti-resonance dip. The X'Z spectrum also has no wing feature below  $T_c$ , and shows an extremely unusual (particularly at low temperature) broad structure, comprising asymmetric humps. There are also some new sharp features. In the X'X' spectrum again more new bands appear, and there are considerable intensity changes in some modes. The intensity

changes in the high frequency modes at  $1144 \text{ cm}^{-1}$  and  $1214 \text{ cm}^{-1}$  in the  $X'X'$  spectrum are not attributable to a change in the  $\Gamma$  parameters, but to a reduction in the mode strength  $S$ , which indicates a changing polarisability tensor element. The broad, low frequency modes in both  $X'X'$  and  $Y'X'$  polarisations are now split into obvious superpositions of several modes. There are no further measurable changes in the  $Y'X'$  spectrum, and the  $X'X'$  and  $Y'X'$  wing features are undiminished below 7K. The disappearance of the overdamped wing in the  $Y'Z$  and  $X'Z$  spectrum indicates that if dynamic disorder is the origin of the wing (see §3.5) this disorder has acquired a definite symmetry in the new phase. The modes do not appear to sharpen at this transition, indicating that there is no reduction in the anharmonicity as there was at the ferroelectric transition.

If this new phase is the monoclinic boracite phase of §4.5 one would expect from table 14 that the  $X'X'$  and  $X'Z$  spectra should contain the same ( $A'$ ) modes, and the  $Y'X'$  and  $Y'Z$  the same ( $A''$ ) modes. The relative sizes of the polarisability tensor elements  $a \rightarrow f$  in table 13(c) are unknown, however, and can contrive to make the two spectra for either of the monoclinic mode symmetries quite different in appearance from each other. This appearance of modes in, for instance,  $Y'X$  and  $Y'Z$ , can be seen to occur at (e.g.)  $623 \text{ cm}^{-1}$ . If this were merely spectral mixing due to birefringence, the mode at  $874 \text{ cm}^{-1}$  in  $Y'X'$  would also appear in  $Y'Z$ , and more strongly. It does not do this. A similar argument can be applied for the  $X'X'$  and  $X'Z$  spectra in relation to the modes at, for instance,  $1144 \text{ cm}^{-1}$  and  $167.0 \text{ cm}^{-1}$  ( $X'X'$  only). This lack of obvious depolarisation, along with the

result of the elastic scattering experiment, indicates again a lack of disorientated domains, with no domain wall effects to cause parasitic scattering. This may seem improbably fortuitous, but the size of the region of sample probed by the beam must be borne in mind. The spectral results are not inconsistent with a monoclinic crystal class, and the differences between A' and A'' spectra can be accounted for by the values of the tensor elements  $a \rightarrow f$ . Again, it must be said that an irrefutable assignment of a crystal class cannot be made from the Raman spectra alone for  $T < 7K$ . A later experiment produced a highly birefringent sample below 7K, with an elastic scattering intensity which remained high below the transition. This would support the above discussion of domain wall effects at this (7K) transition, and suggest that a multi-domain sample had been produced in the later experiment.

#### §4.7 Magnetism in Ni - I

Magnetic ordering at 130K? :

As a structural transition does not occur at 130K, the suggestion first put forward by Quèzel and Schmid (77) seems most plausible. They proposed that the magnetic susceptibility maximum at 130K was attributable to short range magnetic ordering. There is no evidence of long range magnetic order in the form of new excitations at 130K in the Raman spectrum. The disturbance to the lattice (52) has, however, been verified by the Raman result, and it seems reasonable to put forward the phenomenological argument that this disturbance might well affect the spin-spin correlations

and give rise to a change in the degree of short range magnetic ordering, and thus to a change in susceptibility.

Magnetic ordering at 68K? :

Since Ni - I becomes antiferromagnetic, with a weak ferromagnetic component, at 68K, one might expect to see evidence of the long-range magnetic ordering involved in the Raman spectrum. As one-magnon scattering from zone-centre magnons would be at low frequency, any such evidence might be in the form of multi-magnon scattering. The lineshape of this scattering would depend on the density of magnon states, but it would certainly produce broad features. There is nothing in the Raman spectra to attribute to such a scattering mechanism, but there are no results elsewhere from which to estimate the energy of magnon scattering in Ni - I.

Magnetic ordering below 7K :

The magnetic structure determined by von Wartburg (70) predicts that at 6K, the space group is  $C_{2V}^5$  (orthorhombic) and that there is a weak ferromagnetic moment  $m_z$  in the direction of the spontaneous polarisation, [001]. Previously (46, 49) the magnetic moment was thought to be in the xy plane. This result, coupled with the change in the nature of the magnetisation curves (69) at 10K stimulated a group theoretical study of the magnetic structure at 6K (73) to investigate the possibility of a magnetic transition at 10K. The authors constructed a phenomenological free energy expression (c.f. equation 4.1) in terms of the antiferromagnetic vectors

invariant under the group operations of  $C_{2V}^5$ . They found that the term necessary for the existence of an energetically-favoured non-zero  $m_z$  was not allowable within  $C_{2V}^5$  (this term is proportional to  $m_z \ell_\alpha$ , where  $\ell$  is one of the antiferromagnetic vectors). They argued that any magnetic transition at  $\approx 10K$  must also be structural, and to a lower symmetry (e.g. monoclinic) phase. This would contradict the nuclear structure determination of von Wartburg (70), although the orthorhombic  $\rightarrow$  monoclinic distortion could merely be very small. It is possible that the peculiar X'Z Raman spectral lineshape at  $T < 7K$  is attributable to magnetic excitations, but no temperature dependent spectra (in this phase) exist to substantiate this notion. What is almost certain, however, is that the transition at 10K suggested by the magnetic studies corresponds to the 7K structural transition indicated by the Raman spectra.

#### §4.8 Soft Modes in Ni - I

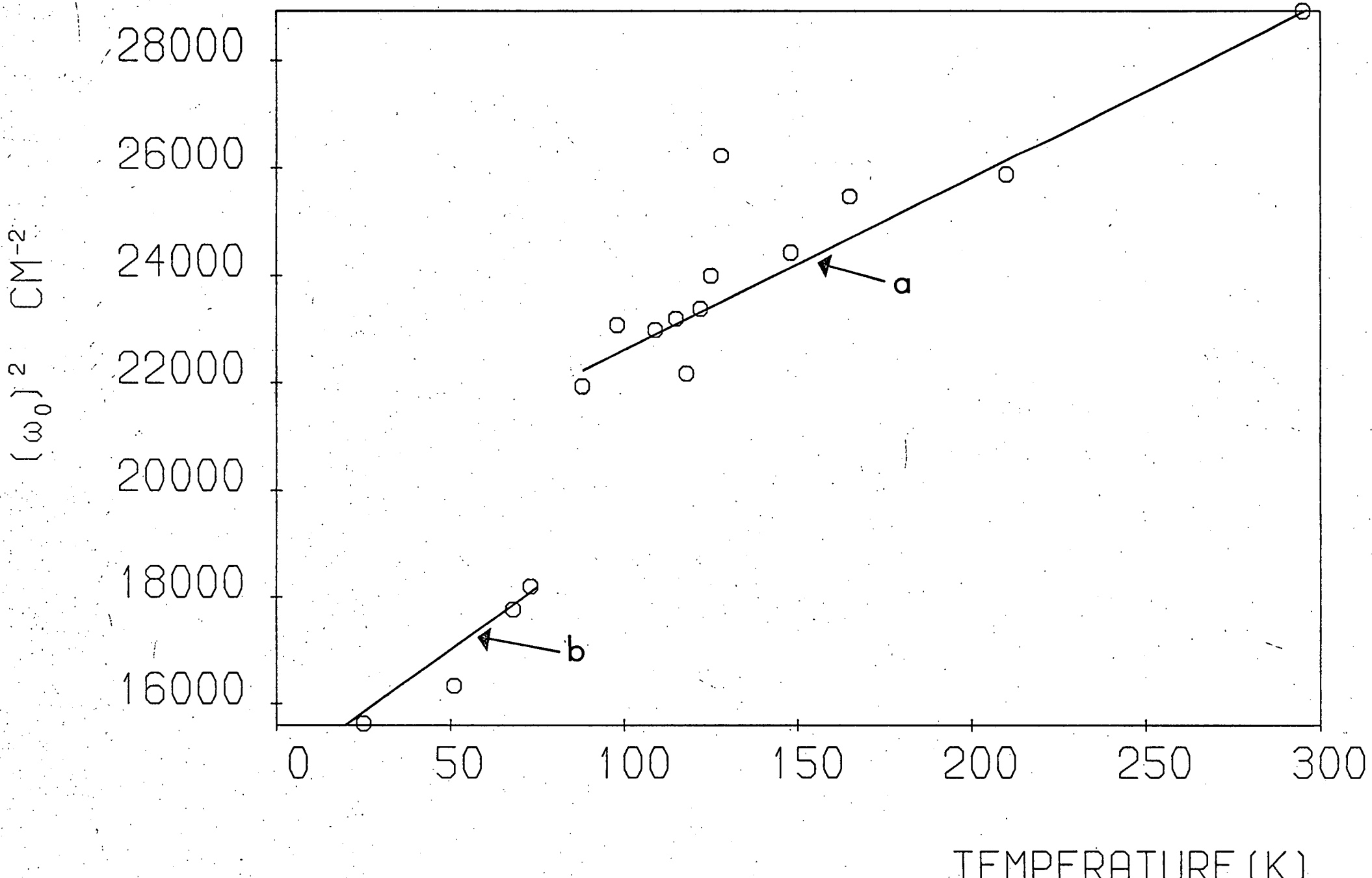
The  $A_1$  and  $A_2$  soft modes for  $T < 68K$  have been discussed in §4.5, and should appear in the X'X' and Y'X' Raman spectra respectively. Such modes have been observed in Cr - Cl at  $149.5 \text{ cm}^{-1}$  ( $A_1$ ) and  $91 \text{ cm}^{-1}$  ( $A_2$ ), (75), and in Cu - Cl at  $136.0 \text{ cm}^{-1}$  ( $A_1$ ) and  $67.0 \text{ cm}^{-1}$  ( $A_2$ ). Bearing in mind the general lowering of frequencies between chlorine boracites and Ni - I, the appearance of a distinct 'shoulder' at about  $194 \text{ cm}^{-1}$  on the side of the  $120.0 \text{ cm}^{-1}$  X'X' band in Ni - I is tentatively assigned to the  $A_1$  critical mode. The feature at  $82.0 \text{ cm}^{-1}$  (at 100K) in the Y'X' spectrum can also be seen to sharpen below  $T_c$ , and subsequently to undergo

a complicated change of shape for temperatures close to and below  $T_c$ . Although the level of Poisson 'noise' fluctuations obscures the details of this behaviour, this sharpening is thought to be due to the appearance of the  $A_2$  soft mode, superimposed upon the existing band or bands. The subsequent variation in shape could be due to the temperature dependence of the soft mode frequency. The complexity of this frequency region in Ni - I makes an unequivocal assignment impossible.

The mode in the Y'X' spectrum whose temperature frequency is  $170 \text{ cm}^{-1}$  is an enigma. Its frequency does conform approximately to a  $\omega_0^2 \propto (T - T_t)$  law (Figure 42), with two regions of different  $T_t$ , but the values of  $T_t$  involved are both negative (approximately -600K for line 'a', and -370K for line 'b' in Figure 42.) The mode is certainly not an order parameter for either of the transitions dealt with in §4.6 and §4.7. It does not correspond to the same dispersion branch at  $q \approx 0$  as the zone boundary soft mode for the 68K transition, and is not an obvious precursor to the trigonal phase. It can be shown (16) that, within Landau theory, the soft mode for the cubic-trigonal transition would have to have  $F_2$  symmetry. It may represent some competing instability which is 'beaten' by both of the above transitions, but the nature of this instability is not clear. The  $A_1$  soft mode in the cubic phase can, of course, no longer be studied in the ferroelectric phase, as it is no longer separable from other modes at low frequency.

FIGURE 42: Temperature variation of ( frequency)<sup>2</sup> for the 170.0 cm<sup>-1</sup> mode in Ni-I. The straight lines are of  $\omega_0^2 \propto (T - T_c)$  where  $T_c$  is -600K (a) and -370K (b).





#### 54.9 Conclusions

The results of the elastic and inelastic light scattering spectra of  $\text{Ni}_3\text{B}_7\text{O}_{13}\text{I}$  indicate that it is cubic for all temperatures between 68K and room temperature, and that no displacive transition occurs at 130K, as has been suggested. At 68K there is a transition to a lower symmetry crystal class which is almost certainly orthorhombic by analogy with other boracites. At a temperature of  $\approx 7\text{K}$ , a further transition is seen to occur, which is structural, and probably magnetic.

That the ferroelectric transition exists is obvious from the new modes which appear in the Raman spectrum below 68K. This is confirmed by the presence of a central peak at  $\approx 70\text{K}$ , the mode frequency shifts, and the reduction in phonon damping below 68K. The lack of mode splitting below 68K suggests that the lattice distortion is small, and that the orthorhombic phase is therefore almost cubic. The reduction in damping indicates a reduction in anharmonicity, and the sample studied was a single ferroelectric domain in the region of the beam path. This is consistent with the results of Raman spectroscopic studies of other boracites. If the wing feature for  $T > 68\text{K}$  is caused by some kind of dynamic disorder, the disorder persists well below  $T_c$ , and lacks definite symmetry. This is not consistent with the results in other boracites. There is no direct evidence in the Raman spectra of magnetic excitations associated with the short range magnetic order postulated to account for the susceptibility maximum at 130K. Neither is there any direct spectroscopic evidence of the onset of antiferromagnetic/weak ferromagnetic order known to set

in at 68K. The critical modes associated with the primary order parameter for the improper ferroelectric transition can be tentatively identified in the orthorhombic phase.

The second, new transition can be seen from the Raman spectra to be to a lower symmetry, consistent with the primitive unit cell doubling at the orthorhombic to monoclinic transition in boracites, as more new modes appear and intensities and lineshapes alter dramatically. This transition is almost certainly the magnetic and structural transition predicted at about 10K in Ni - I. The structural nature of the transition would indicate that the direction of the ferromagnetic moment in Ni - I at 6K was correctly determined by von Wartburg (70) but that the nuclear structure was not, in that it was given as orthorhombic,  $C_{2v}^5$ . Again, if the wing feature is attributable to dynamic disorder, the disorder acquires a well defined symmetry in the new phase. From the spectral data and the elastic scattering data it can be seen that the sample formed a single domain once more below 7K.

Finally, the puzzlingly persistent soft mode must be left as an unknown mechanism. It is associated with neither of the two transitions mentioned above, and is not an obvious precursor to any of the known boracite transitions. What is more, the 'transition temperature' apparently associated with this mode is negative, and the 'transition' must therefore be considered 'virtual'.

The results of this chapter are to be published in summary (78) and in full (79).

CHAPTER 5

A COMPUTER CONTROLLED SYSTEM FOR BRILLOUIN

SPECTROSCOPY

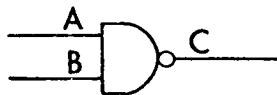
Introduction:

This system for automatic Brillouin spectroscopy represents essentially the culmination of a programme of work which began several years ago with the automation of two double grating Raman spectrometers (23, 80). In both cases, control is effected by pre-setting rows of switches, and the data is output in digital form on paper tape. This original work has provided the basis for a more versatile and complex computer controlled system (23, 24) which offers automatic control of Raman experiments, graphical equipment, temperature scanning experiments, and now Brillouin spectroscopy. This system is now fully operational, although possible extension to control of further experimental parameters can be envisaged. It is the purpose of this chapter to give a fairly brief description of the methods involved in the particular case of the Brillouin system. While programme development for the other computer controlled facilities formed part of my thesis work, the design, construction and programming for the Brillouin system represents a far greater part (performed in collaboration with Dr. J.W. Arthur).

Any attempt to describe and discuss the operating cycle of a logic circuit is almost doomed to become verbose. In an attempt to avoid this pitfall, therefore, the discussion in this chapter is kept one or more stages removed from the actual circuit diagrams, and a presentation is made in terms of schematic diagrams. The

diagrams themselves, in full detail, are included in Appendix 3. At this stage, therefore, a short discussion of the very basic philosophy of logic circuit design is appropriate.

Every point in a logic circuit is at a potential '1' or '0'; 'on' or 'off'. In the case of TTL system circuits, logic level 1 represents 5V. Designing a logic circuit involves putting together circuit elements with known properties such that a predetermined sequence of logic level changes occurs and produces some desired result. One of the simplest logic circuit elements is the NAND gate. This device is represented by the symbol and 'truth table' shown below.



NAND

A	B	C
0	0	1
1	0	1
0	1	1
1	1	0

The truth table implies that, if wire A and wire B are both at a potential of +5V ('1'), then and only then is wire C at 0V.

Logic circuit elements represent Boolean algebraic forms, and NAND means 'not A and B' or  $\overline{A \cup B}$ . The basic circuit elements are put together to form arbitrarily complex circuits to perform complicated functions.

In §5.1, the ability of the computer is described in general terms, as far as it is relevant to this system. It has, of course, abilities in addition to those mentioned. The nature of this particular computer placed constraints upon the design philosophy in

that it is a time shared computer, which is used by several research groups. While this means that a costly, dedicated computer is not required, it also means that the system does not command the undivided attention of the computer. This problem is overcome by the use of multiplexing techniques, as described briefly in §5.2. This section is not essential to the rest of the chapter and, indeed, the multiplexing/demultiplexing network existed before the Brillouin system, and so did not form part of this chapter's project. Its inclusion, however, is useful to justify the approach adopted to the control circuitry, although this approach was largely determined by the need to be compatible with the existing equipment.

In §5.3 are described the requirements of the Fabry-Perot interferometer. The basic theory of this high resolution device is well documented (e.g. 81). §5.4 puts together the computer's abilities and the interferometer's requirements in a manner compatible with the existing equipment, and suitable for operating within a nondedicated (time shared) computer environment. In §5.5, some of the details of the blocks or modules used in building up the complete system are described, and the discussion is in terms of 'black boxes'. Detailed understanding is left to contemplation of Appendix 3.

The logical structure of the operating control programme for the Fabry-Perot system is described in §5.6, and the results of its operation in two distinct modes are presented in §5.7. These results demonstrate both the simplicity of operation for the control of the system and the convenient format of the results produced. Finally, in §5.8, the scope of the system is critically examined, and possible future developments are proposed. These proposed developments take

the form both of additions to the existing system, and total re-designing of the entire system (24).

### §5.1 The Ability of the Computer

The computer is a Digital Equipment Corporation PDP11/45 16-bit machine. It is best regarded as a transmitter and receiver of 16 digit binary numbers or 'words' (83). These words may, on transmission from the computer, carry information regarding the running of the experiment. The words received by the computer may contain the data resultant from the experiment, and any experiment is seen by the computer as a system with which to exchange words.

The additional and vital ability of the computer is, of course, the ability to perform arithmetic and logical functions, and to store data. The computer is thus able to concoct a 16-bit word from information supplied to it by the experimentalist and/or by a programme running in the computer. Since this word has the function of controlling the experiment it is known as the 'controlword', and it is assumed that the transmission of a controlword by the computer initiates some action on the part of the experiment. The subsequent word transmitted from experiment to computer is a 'dataword'. This exchange of controlwords and datawords between computer and experiment takes place along a common set of 16 wires, and is illustrated schematically in Figure 43. (The set of cables is often called the data 'bus'.)

Included in Figure 43 is a representation of a technique which is employed here to synchronise transmission and receipt of words

FIGURE 43: Schematic representation of the flow of 16-bit binary 'words' between computer and experiment.

FIGURE 44: Schematic diagram of the multiplexing/ demultiplexing network implemented according to table 15.



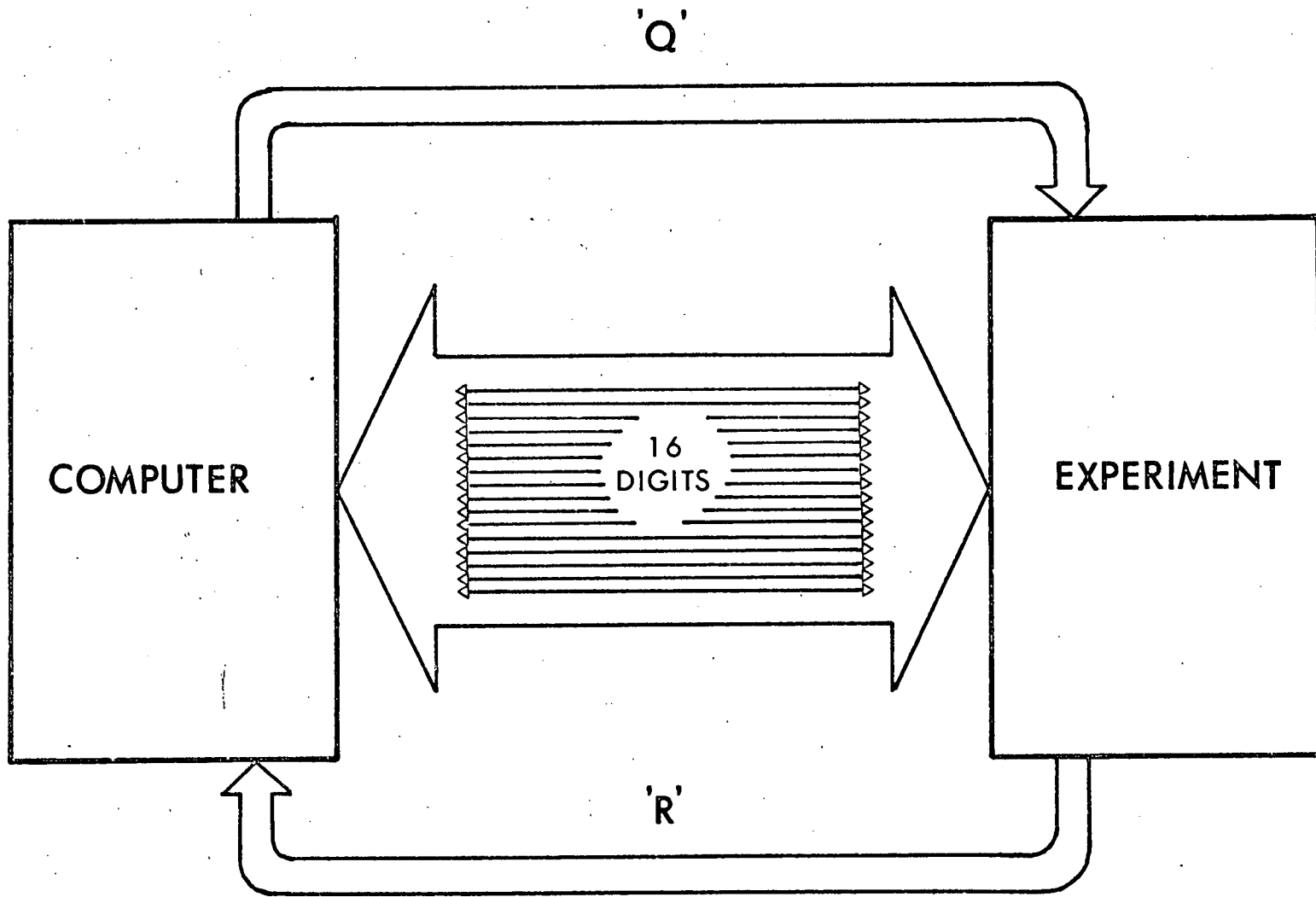


FIG43

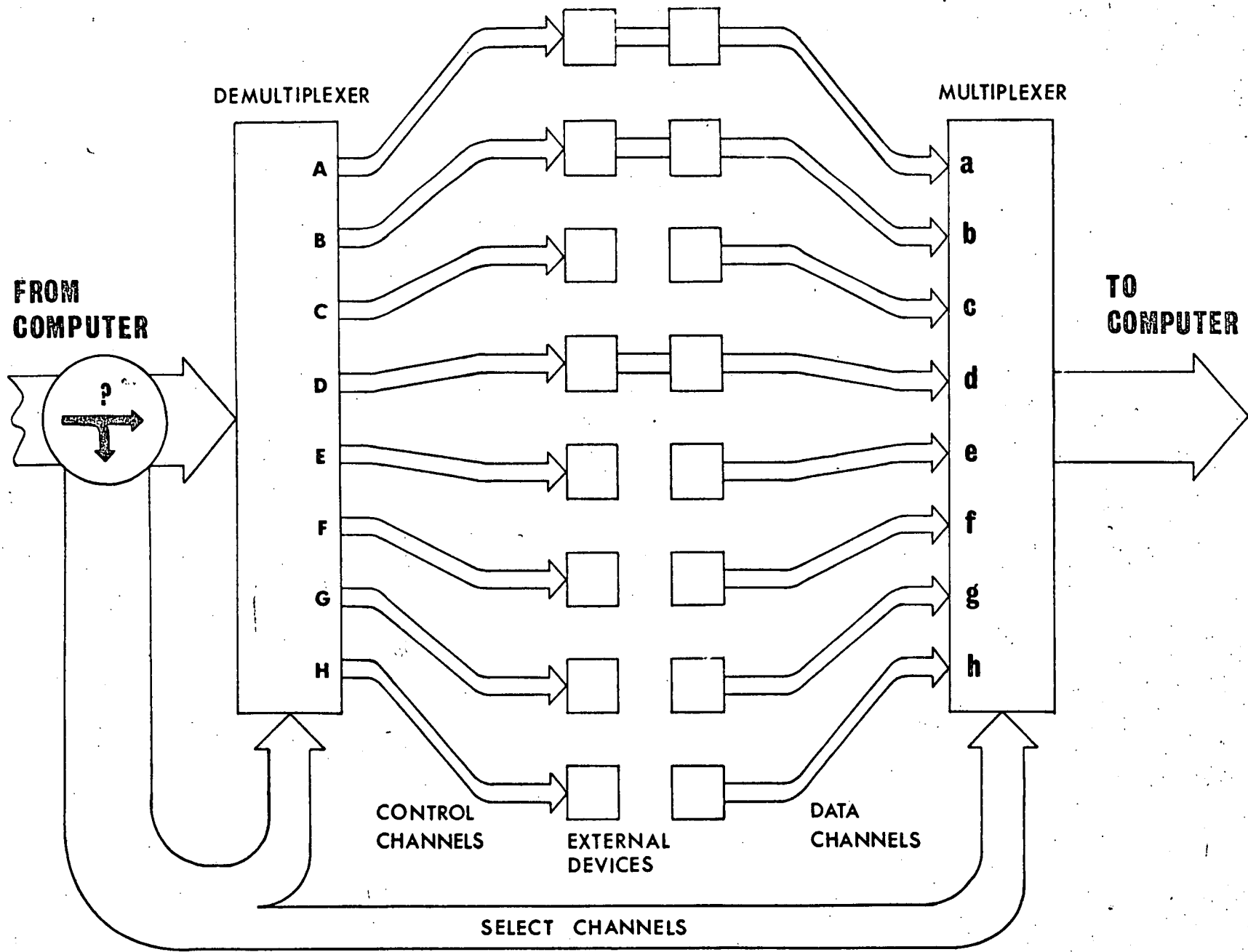


FIG 44

by the computer, but is also applied at many levels of the control circuitry. When the computer has generated a controlword as prescribed by the experimentalist, it signals to the experiment that there is a controlword ready for use. This signal takes the form of an electronic pulse 'Q' along an extra wire. The controlword is transmitted by the computer, and a subsequent signal 'R' along a further wire informs the computer that the controlword has been received. There is an exactly analogous pair of signals associated with the receipt, by the computer, of a dataword, except that the functions of 'Q' and 'R' are reversed. This exchange of signals is a common contrivance in data transmission circuitry, and the signals 'Q' and 'R' can be seen to form a 'message-boy' service which ensures that events occur in the correct order (for instance, the computer will certainly not send a new controlword until the 'R' signal is returned to indicate that the previous controlword has been received by the experiment.) This pair of signals is sometimes known as a 'handshake loop'.

## §5.2 Multiplexing and Demultiplexing

Multiplexing and demultiplexing techniques are essential when the computer is of the nondedicated variety, and its time must therefore be shared between users. The computer must then be able to exchange controlwords and datawords with many experiments by switching its single controlword transmission channel to many experimental channels (demultiplexing), and switching many experimental data channels to the one computer data receipt channel (multiplexing).

The enormous advantage of this scheme of operation is that the computer may exchange words with several different experiments belonging to several different users, apparently simultaneously, due to the high operation speed of the computer. Under normal circumstances, different experiments have no adverse effects upon each other.

In the system implemented here, the techniques of multiplexing/demultiplexing are also applied at the level of the particular control system, which allows the design of the on-line control circuitry to be approached on a 'modular' basis. The single computer 'transmit' and 'receive' channels allocated to light scattering experiments are thus split further into eight channels for controlwords and eight for datawords. This level of operation is represented by Figure 44 and by the table of subchannel allocation, Table 15. The lower 'select channels' route for the controlword in Figure 44 expresses the fact that it is an extra controlword which is sent prior to the controlword for the experiment which defines the control channel A → H and the data channel a → h relevant to the experiment in question (23, 24). Not all devices require to return data to the computer (e.g. an X-Y plotter, channel C), and the unallocated channels of Table 15 indicate the scope for expansion to further control of experiments (see §5.8) without further connections to the computer itself. Devices corresponding to A → D and a → d do not interfere with one another and may be controlled simultaneously and independently, or disconnected completely, as required.

TABLE 15. Allocation of control and data subchannels at control system level, as implemented (see Figure 44).

A	Coderg T800 triple monochromator	a	Photon counter for A
B	Digital voltmeter input	b	Digital voltmeter output
C	X - Y plotter	c	Not allocated
D	Fabry-Perot interferometer	d	Photon counter for D
E	] Not allocated	e	] Not allocated
F			
G			
H			

### §5.3 The Requirements of the Interferometer

In order to explain the generation and the meaning of the controlwords and datawords of §5.1 for the interferometer experiment it is necessary to give an account of the 'manual' operation of the interferometer, that is before the computer is introduced.

The interferometer is a Burleigh RC42 piezoelectrically scanned etalon, with three piezoelectric elements or 'stacks'. The expression for the angular position  $\theta$  of a maximum of intensity in the pattern produced by multiple reflection at an etalon is:

$$5.1 \quad 2nd \cos \theta = m\lambda$$

where  $n$  is the refractive index of the material between the plates,  $d$  the plate separation,  $m$  an integer and  $\lambda$  the wavelength. In the RC42 etalon,  $n$ ,  $\theta$  and  $m$  are held fixed while  $d$  is changed by the application of a 1 KV 'ramp' voltage to the stacks. This results in a scan over a range of  $\lambda$  which is small compared to the range of a grating spectrometer, but the resolution is much higher. In some other instruments,  $\lambda$  is scanned by altering the gas pressure between the plates, and consequently  $n$ . Since the ramp voltage  $V$  evolves linearly in time, a plot of intensity vs. time on a 'Y - t' chart recorder corresponds to a spectral scan. This same time linearity can be exploited in interfacing the system to a multichannel analyser (MCA), which has (say) 100 channels and 'strokes' the photon count over a time  $= T \div 100$  into each successive channel, where  $T$  is the ramp duration (in time). Each

MCA channel therefore corresponds to an integrated intensity over a range of wavelength  $\delta\lambda$  equal to

$$5.2 \quad \delta\lambda = (\text{Free spectral range}) \div 100.$$

The data in the MCA can then be recorded on paper tape and subsequently transferred to a computer memory. The plates are then tracked back by the reduction of the stack voltage to 0V, and a fresh scan can be initiated manually.

There are some disadvantages to this method, and these are as follows:

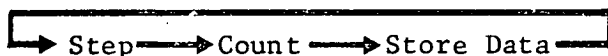
- i) The transfer of data from MCA  $\rightarrow$  paper tape  $\rightarrow$  computer is cumbersome and time-wasting.
- ii) Large amounts of data  $\Rightarrow$  large amounts of papertape.
- iii) Comparative studies cannot be performed immediately.
- iv) The data format is not immediately compatible with existing data-handling routines (84).
- v) Each data point corresponds to an integration over a non-zero wavelength range  $\delta\lambda$ .
- vi) The etalon plates will drift axially due to temperature effects and mechanical instabilities, destroying calibration.
- vii) The etalon plates will deviate from parallelism for reasons as in vi) above, degrading finesse (81).

The scheme of computer control implemented here takes care of i)  $\rightarrow$  vi), and could be extended to remove vii) (see §5.8).

§5.4 Interfacing the Computer to the Interferometer

It would be possible, if a dedicated computer were available, merely to use such a computer as a glorified MCA. This would remove disadvantages i) + iv) of §5.3. The computer is, as has been said, not dedicated, and some means must be devised whereby the multiplexing/demultiplexing system can be allowed to switch the computer's attention off the interferometer experiment, and on to another user or experiment (temporarily). This makes linear time evolution impossible.

The problem is overcome by substituting a 'staircase' voltage for the 'ramp' voltage. Such a voltage is depicted in Figure 45. In this mode, while the voltage  $V$  is constant, the photon count can be recorded for a given length of count time, and the computer can devote its attention to some other experiment. The fact that the count occurs when the voltage is constant, and therefore the etalon plates stationary, carries with it the added advantage that each data point now corresponds to a single setting, and not to an integral over a range  $\delta\lambda$ . This discontinuous mode of operation is essential to the scheme of things. The sequence of events is thus:

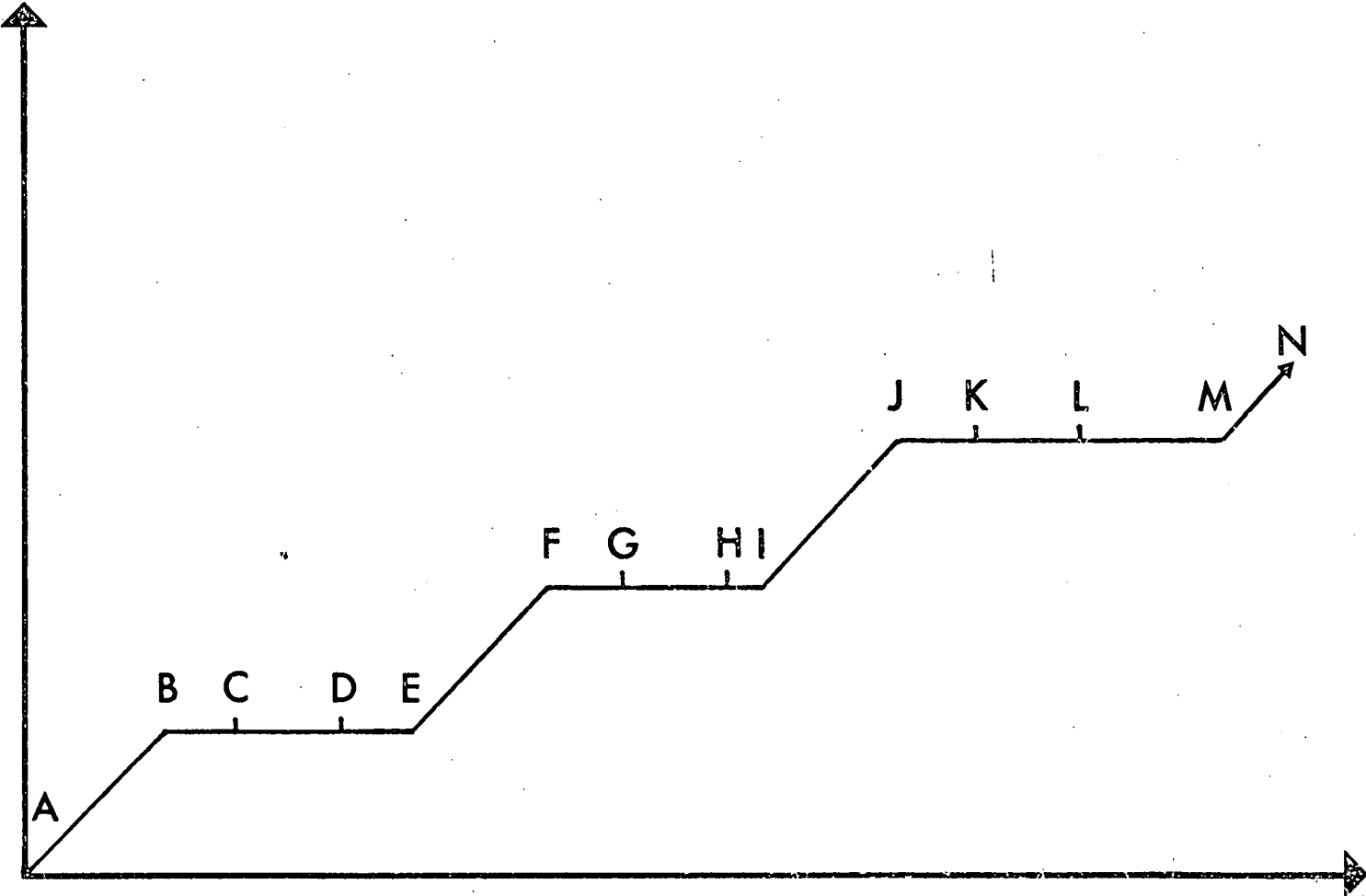


In Figure 45, the intervals AB, EF, IJ and MN represent an increase  $\delta V$  in  $V$  and therefore a step  $\delta\lambda$  in  $\lambda$ . Intervals CD, GH and KL are 'count times' and are therefore of equal



FIGURE 45: The evolution in time of the etalon 'stack' voltage within the on-line control system.

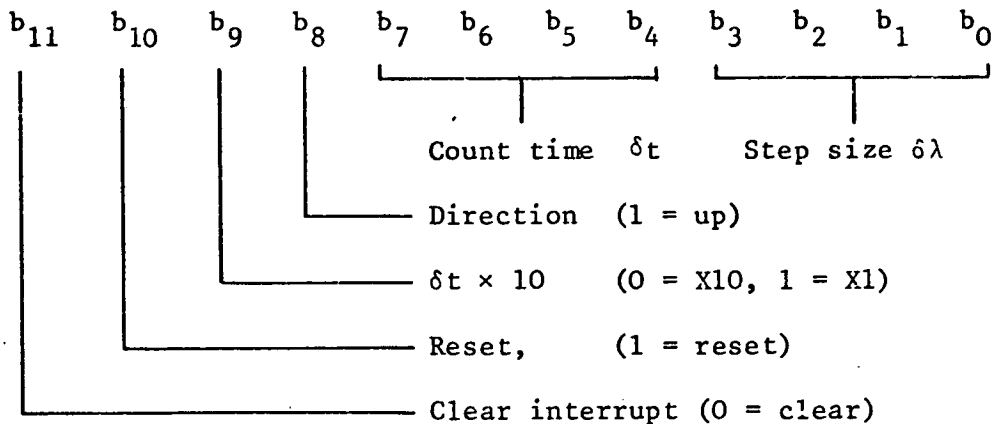
VOLTAGE  
TO  
ETALON



TIME

length  $\delta t$ , and intervals BC, FG and JK are 250  $\mu s$  waits induced by the computer to allow for mechanical 'ringing' of the etalon plates to be damped out. The intervals DE, HI and LM are deliberately drawn as unequal time intervals, as these are the junctures at which the system releases the computer to attend to other users. At these times, the waiting periods enforced by the computer have no adverse effect, provided the etalon remains stable. We are now in a position to detail the controlword and dataword associated with a complete step-count operation (e.g. A  $\rightarrow$  E of Figure 45).

The experiment requires to know the step size, the length of time for each photon count operation and the direction of scanning (i.e. is  $\frac{\partial V}{\partial t}$  positive or negative). The convention for the allocation of controlword bits adopted here is given below.



Bit 8 gives the sign of  $\frac{\partial V}{\partial t}$ , bit 9 allows the option of either  $\delta t$ , or  $\delta t \times 10$  being used as the count time. Bit 10 ensures that the ramp generator is reset properly (see §5.5) and bit 11 clears an optional manually-induced interrupt. This interrupt is arranged to occur during the 'dead' interval (e.g. DE, HI and LM of Figure

45) and is useful if something goes wrong, or adjustments must be made during a scan. Bits 12 → 15 are redundant in this case.

The computer generates this controlword by use of the following algorithm:-

$$\begin{aligned} 5.3 \quad \text{Controlword} = & 2^0 \times \text{stepsize} + 2^4 \times \text{count time} + 2^8 \times \text{direction} \\ & + 2^9 \times (\delta t \times 10) + 2^{10} \times \text{reset} + 2^{11} \times \text{clear interrupt.} \end{aligned}$$

The values of the parameters are therefore  $0 < \text{stepsize} < 15$ ;

$0 < \text{count time} < 15$ ;  $\text{direction} = \pm 1$ ;  $\delta t \times 10 = \pm 1$ ;

$\text{reset} = \pm 1$ ;  $\text{clear interrupt} = \pm 1$ .

The dataword is much more simply explained. When the system has acted upon the controlword, the number of photons counted is relayed back to the computer as a 16-bit binary dataword, so that the maximum number of photons counted during  $\delta t$  must be kept below  $2^{16} = 65536$  (or  $2^{16} \times 8 = 524288$  if the  $\div 8$  facility is used, see §5.5).

### §5.5 The Interferometer Modules

The basic modules are illustrated schematically in Figure 46, and the circuits are given in full in Appendix 3 (Figures A3a → A3c). It would be uninformative in this context to try to explain in detail the operation of the individual circuits in terms of their component parts, as this is best understood by staring at the circuit diagrams with the aid of the Texas instruments TTL data book (82). In essence, however, the controlword is acted upon by the modules as follows.

FIGURE 46: The modules for the Fabry - Perot interferometer (F/P) and Coderg T800 spectrometer interfaces, with the flow of information between modules, and to /from the computer.

FIGURE 47: The overall architecture of the computer-controlled system for Brillouin spectroscopy.

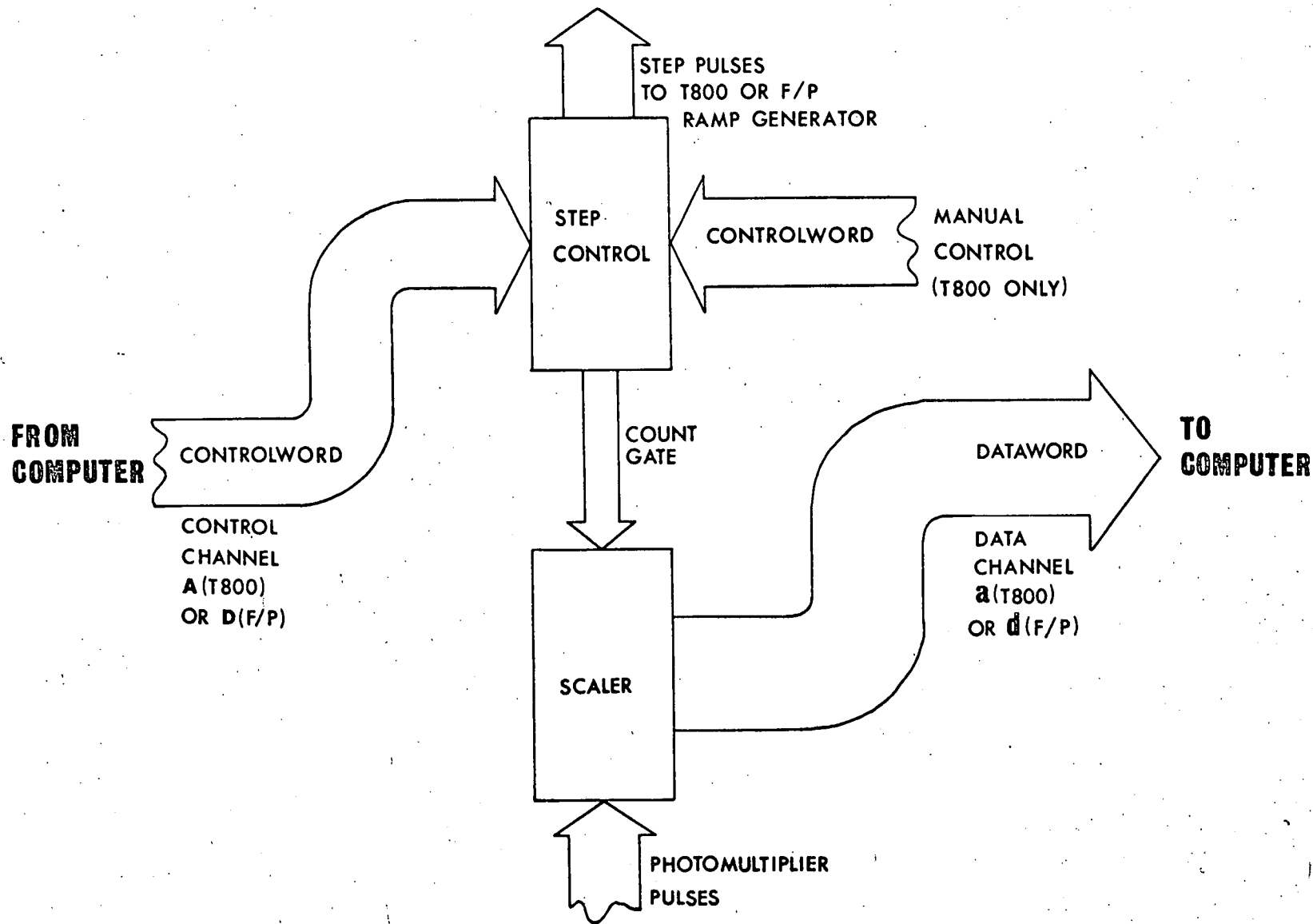


FIG 46

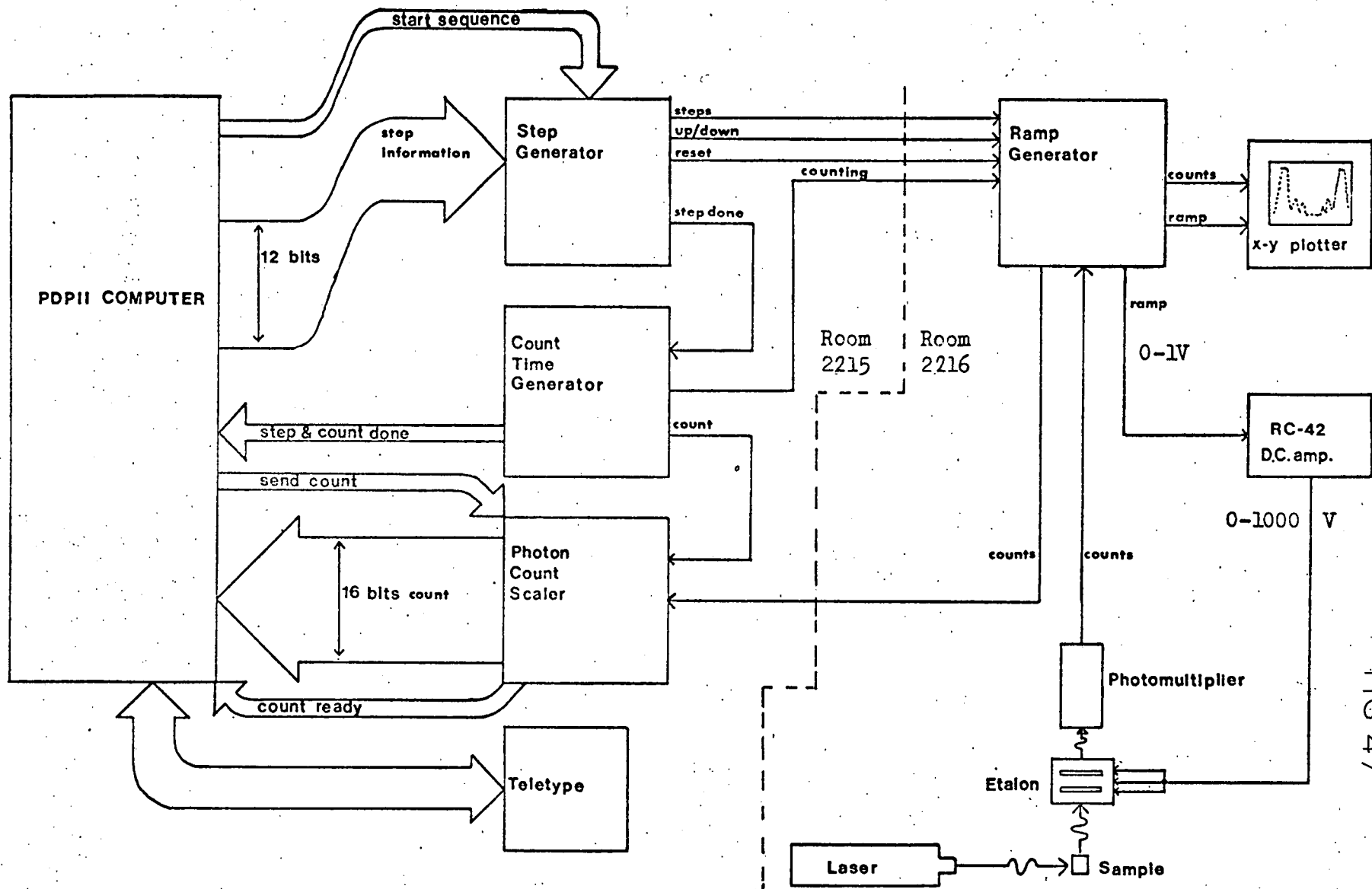


FIG 47

Firstly, the step control module interprets  $\delta V$  as an integer, and generates a sequence of  $\delta V$  pulses, which are subsequently summed up, and converted to an analogue increment of 1 Volt by the ramp generator, the sign being determined by bit 8. This increment is input to the 'external' socket of the interferometer's own ramp generator, which now operates merely as a D.C. amplifier of gain 1000X. Before the stream of pulses is summed by the computer ramp generator, however, the 'counters' are reset to zero by bit 10 of the controlword (see §5.4). After the 250  $\mu$ s wait mentioned in §5.4 to stabilise the etalon, a pulse of duration  $\frac{\delta t}{10}$  seconds (or  $\delta t$  if bit 9 = 0) is sent to the photon scaler. This pulse, the 'count gate' of Figure 45, effectively 'opens' the scaler for  $\frac{\delta t}{10}$  seconds. At the end of this gate pulse, the accumulated photon count is relayed back to the computer via channel d. There is a 'message-boy' loop of signals (c.f. §5.1) associated with the step pulse generation/count pulse generation in addition to the 'Q' and 'R' of Figure 43. These are labelled 'step done' and 'count done' respectively in Figure A3a.

The step size has been chosen such that the voltage cannot possibly evolve in time faster than the maximum  $\frac{\partial V}{\partial t}$  of manual operation, and the digital  $\rightarrow$  analogue conversion is such that 1 step represents 2V. The total number of single steps in a scan is therefore given by  $(1KV) \div (2V) = 500$ . It can be seen that the count time has alternative ranges of  $0 \rightarrow 1.5$  seconds or  $0 \rightarrow 15$  seconds, depending on the value of bit 9. The additional facility of an optional predivision of the photon count by eight, switchable manually, allows for high-statistic counting to be performed.



It is, perhaps, useful to present two sample controlwords and their interpretation. Firstly, in

b <sub>11</sub>	b <sub>10</sub>	b <sub>9</sub>	b <sub>8</sub>	b <sub>7</sub>	b <sub>6</sub>	b <sub>5</sub>	b <sub>4</sub>	b <sub>3</sub>	b <sub>2</sub>	b <sub>1</sub>	b <sub>0</sub>
0	1	0	1	0	1	0	1	1	1	0	0

referring to §5.4,  $\delta t = 0101$ ,  $\delta t \times 10 = 0$ , so count time = 5 seconds; step size =  $1100 = 12$ , so the scan will comprise  $500 \div 12 = 41$  steps, and thus 42 data points. Similarly,  $011100100101$  gives a count time of 0.2 seconds and a stepsize of 5.

The overall architecture of the Fabry-Perot system is represented by Figure 47.

Footnote to §5.5:

The modules in Figure 45 are the same, essentially, for the Coderg T800 system, except that the pulses generated by the step control module are used directly as stepper motor pulses for the grating drive motor (23, 24).

### §5.6 The Control Programme

A complete spectral scan is represented by Figure 45, extended to 1KV. This is therefore composed of a sequence of controlwords, and their corresponding datawords. The flow diagram for a computer programme which creates such a sequence is presented in Figure 48, with an additional, useful facility.

If 'scans' = 1 in the diagram, the programme controls a single scan, measuring photon counts for a period of  $\delta t$  seconds, at a

set of frequencies  $\nu_i$  in regular steps of  $\delta\nu$ . If, however, 'scans'  $> 1$ , the programme corrects for axial drift of the plates by refraining from storing any counts until a threshold level is reached. It is therefore possible, under programme control, to accumulate multiple scans with threshold triggering at some intensity between the maximum Brillouin intensity and the maximum Rayleigh intensity. This is a particular advantage when the scattering is weak, as it automatically compensates for axial drift of the etalon plates, which would destroy the frequency calibration in a single scan of long duration. Thus, disadvantage vi) of §5.3 has been overcome. In Figure 48, the stars indicate junctures at which the computer is effectively released by the control programme. This programme was written in the assembly language of the PDP11 computer (83) but there is no reason why it could not have been written in a high level language and compiled on a special compiler.

### §5.7 Results

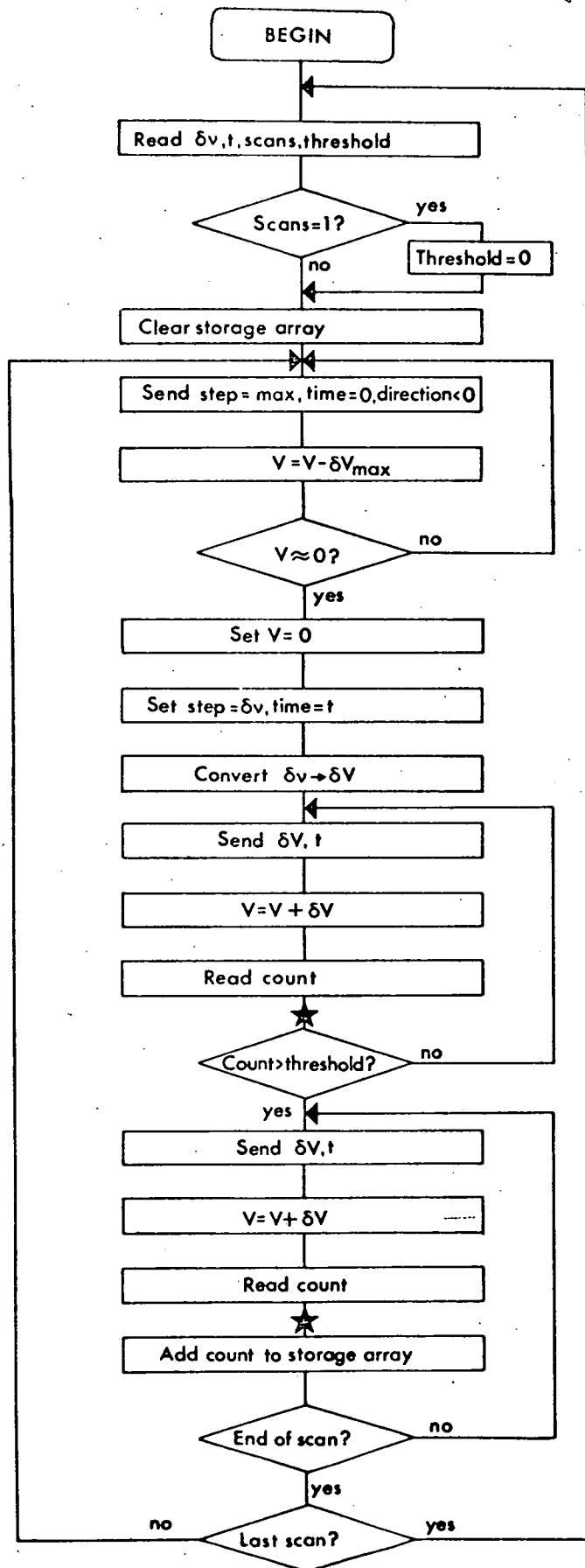
In Figures 49 and 50 are presented the results of two separate Brillouin scans of  $\text{BaMnF}_3$ . Firstly, the sequence of control instructions is presented, along with the resultant stored data file. Below these are plots of the corresponding spectra, drawn by the X - Y plotter in Table 15, controlled by a graphics programme compatible with both the Coderg T800 system and interferometer system files. Figure 50 is of particular interest, as it represents a multiple scan. It can be seen that the stored data begins

FIGURE 48: Flow diagram for the interferometer control programme, including the 'multiscan' option. The scan will actually be linear in wavelength  $\lambda$ , but also linear in frequency  $\nu$  to within 0.3%.

FIGURE 49: Command sequence, resultant datafile and plot for a Brillouin scan in 'single scan' mode. The underlined sections are computer prompts.

FIGURE 50: Command sequence, resultant datafile and plot for a Brillouin scan in 'multiscan' mode. The underlined sections are computer prompts.

FIG 48.



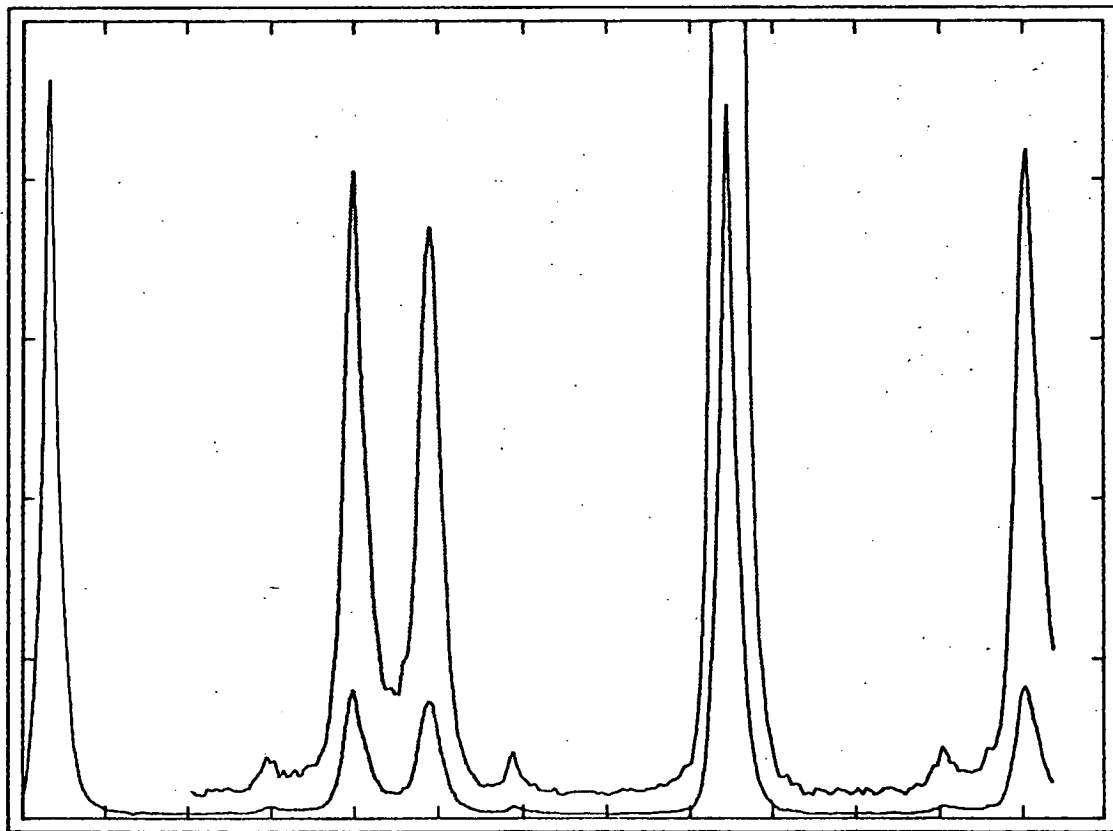
.RUC//BRIL  
FILE:TEST01,  
STEP=2, TIME=4, TEMP=400, SCANS=1,  
NOTES : DEMONSTRATION FOR MANUAL  
G3?Y

FIG 49

SCAN COMPLETE(BRILLOUIN)

FILE:TEST01  
START=0 , END=500 , STEP=2, TIME=4, TEMP=400, SCANS=1,  
NOTES : DEMONSTRATION FOR MANUAL

DATA=  
23 38 83 137 236 399  
709 813 576 385 282 203 142 85  
53 35 25 18 14 13 9 8  
8 8 7 8 6 4 8 7  
7 5 7 6 6 5 6 5  
7 6 6 6 5 5 5 7  
6 7 6 7 7 6 6 6  
7 7 9 10 11 14 12 13  
9 11 9 10 11 9 11 12  
12 12 14 16 21 31 40 64  
100 130 142 115 92 76 62 46  
39 30 28 29 27 27 35 36  
47 64 96 123 130 122 99 73  
56 36 27 18 15 12 10 9  
7 7 8 7 8 8 9 13  
15 11 9 8 7 8 6 6  
6 6 7 5 5 6 6 6  
6 6 6 6 5 6 5 5  
6 6 7 6 7 6 6 6  
7 7 7 8 7 8 9 9  
10 12 12 13 20 33 60 123  
200 347 579 784 607 419 311 226  
137 90 62 39 31 20 17 12  
9 9 10 7 8 7 5 6  
5 7 6 6 5 6 7 6  
6 5 6 7 5 7 6 5  
6 7 7 7 6 6 5 7  
7 8 7 8 10 12 12 16  
14 12 12 10 11 10 10 11  
11 13 16 15 17 21 30 48  
67 101 137 147 132 108 39 69  
54 42 36  
SCAN COMPLETE(BRILLOUIN)



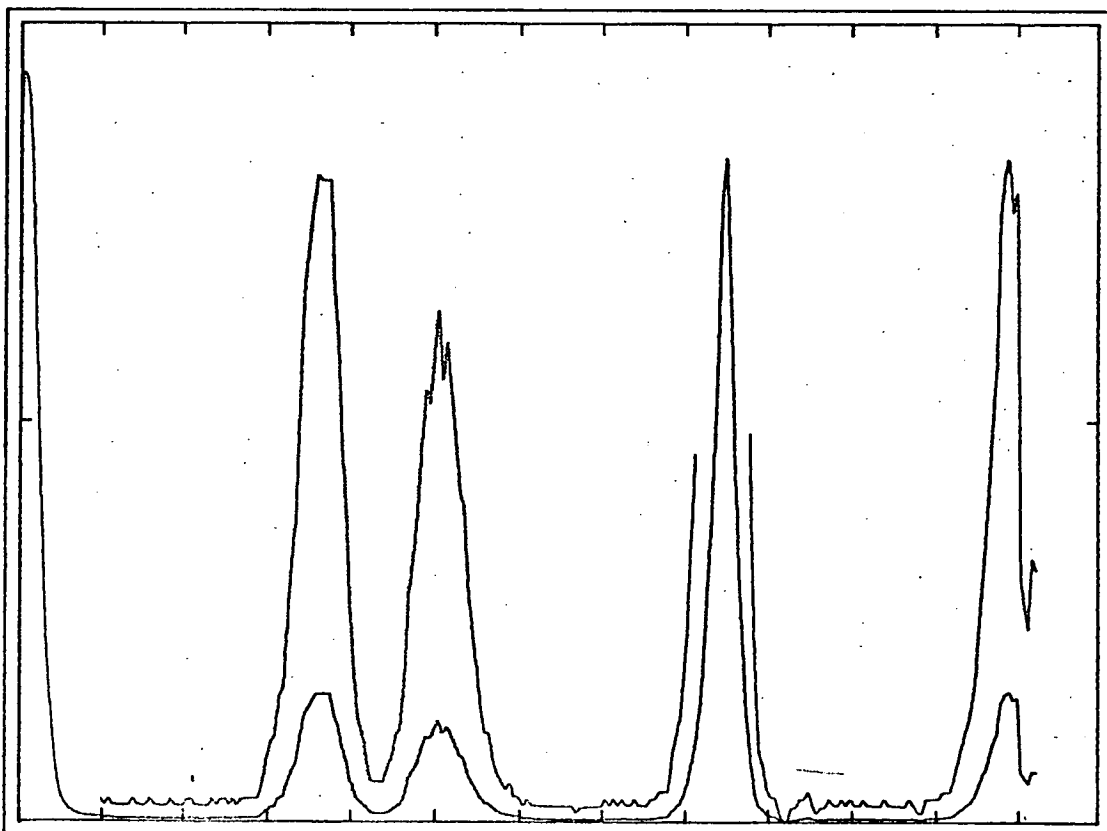
.RUC//BRIL,  
 FILE:TEST02,  
 STEP=2, TIME=2, TEMP=400, SCANS=2, THRESHOLD=1600,  
 NOTES : DEMONSTRATION OF MULTISCAN  
 GO?Y

SCAN COMPLETE(BRILLOUIN)

FILE:TEST02  
 START=0 , END=500 , STEP=2, TIME=2, TEMP=400, SCANS=2, THRESHOLD=1600,  
 NOTES : DEMONSTRATION OF MULTISCAN

DATA=  
 600 745  
 841 748 522 373 271 187 113 65  
 43 32 26 21 16 14 12 10  
 9 9 7 8 8 8 6 7  
 7 8 8 8 7 7 7 5  
 6 8 8 8 7 6 6 8  
 7 7 8 7 8 7 6 8  
 7 9 8 11 12 14 15 14  
 12 11 11 10 11 13 12 13  
 13 14 15 18 24 35 58 80  
 113 123 122 105 95 70 52 46  
 40 36 31 32 32 33 34 44  
 54 78 112 135 130 106 79 61  
 42 27 21 18 12 12 10 9  
 8 8 7 7 8 10 11 13  
 12 11 8 9 8 7 7 6  
 6 6 7 6 8 7 8 7  
 7 6 7 5 7 7 7 7  
 7 9 8 8 7 6 8 9  
 7 8 8 10 10 12 10 11  
 14 15 18 24 41 83 166 323  
 606 1045 1066 753 546 402 259 147  
 97 66 47 35 24 23 16 12  
 12 9 9 10 8 9 8 7  
 8 7 7 7 7 7 7 7  
 8 8 7 7 7 7 6  
 6 6 7 7 7 7 8  
 7 8 10 9 11 14 16 13  
 14 11 10 10 10 11 11 11  
 11 13 16 18 22 30 49 72  
 103 128 126 111 90 78 58 48  
 42 38 34

SCAN COMPLETE(BRILLOUIN)



at the threshold level, on the 'leading edge' of a Rayleigh peak. The methods of processing these data files are discussed in references 23, 25 and 84.

## §5.8 Conclusions and Speculation

The system described in the preceding sections of this chapter certainly provides a reliable, working facility for high resolution light scattering spectroscopy. The data is collected in a useful format, and in a precisely controlled and repeatable manner. The design of the system requires only that a data handling terminal and a time shared computer be available, so that the scope is not limited by the cost of a dedicated computer. The computer provides the additional facilities of disc storage, programme compilers and data links to a larger job-processing computer, so the large amount of data created by comparative studies does not present a problem. The data is readily available for immediate manipulation, or for later analysis on the larger computer.

The control method incorporates an ability to minimise the detrimental effects of axial drift of the etalon plates. Non-axial drift still presents a problem, however, in that the resultant loss of plate parallelism degrades finesse and thus renders very low statistic experiments impractical due to the long times involved. This could, in principle, be rectified within the scope of the existing system, by the application of a small 'trimming' voltage to each of the piezoelectric stacks independently. The decision as to the magnitude and sense of these voltages could be made by

the computer. This might involve a multiscanning mode of operation in which the computer compares each successive scan with its predecessor and decides whether or not finesse is deteriorating. The trimming voltages could then be adjusted by the computer (via digital/analogue convertors) to converge upon optimal plate alignment. The criterion for such a convergence could simply be that the height of the Rayleigh peak be maximised. A more sophisticated method, however, would be to study the shape and width of the Rayleigh peak, and to regard high peak intensity and narrowness as desirable qualities. There are a number of ways in which this criterion might be applied. This proposed addition to the scope of the system could be made within the framework of the existing multiplexing network, using channel E of Table 15. Obviously some further circuitry would be required and a more complicated control program would result.

A much more drastic development, however, would be the introduction of a microprocessor (85), and the complete replacement of the entire Raman/Brillouin system control circuitry. Although the combined system at present offers more than adequate capabilities, it is not independent of the vagaries of the computer itself. The circuitry would be simpler, as much of the work currently done by circuits would be done by microprocessor programmes, and a link to a computer could, of course, be included. The future of automatic spectroscopic systems must surely lie in the direction of the microprocessor.



CHAPTER 6

INCOMMENSURATE - COMMENSURATE TRANSITIONS: A THEORETICAL STUDY

Introduction

There has been considerable interest in recent years in the class of transition leading to an aperiodic system, known as an incommensurate phase, which is not strictly amorphous. Many of the properties and characteristics of such materials have been summarised by Axe (86).

The analysis reported in this chapter forms part of a current programme of study involving several aspects of incommensurate transition theory (87, 88, 89). I am particularly grateful to Professor R.A. Cowley and Dr. A.D. Bruce for encouraging my collaboration in this exciting project.

§6.1 Incommensurate Transitions: a Definition

The dictionary definition of 'commensurate' (actually commensurable) is "capable of being measured exactly by the same unit." The unit of measurement for a crystal lattice is the unit cell dimension (e.g. 'a' in Figure 51(i)). If a distortion of such a simple structure occurs (as temperature is lowered) which can be described by a displacement field  $u(z) = u_1 \cos q_c z + u_2 \sin q_c z$  and  $q_c$  is a simple rational fraction of  $\tau = \frac{2\pi}{a}$ , the transition is said to be from a disordered to a commensurate phase. The classification 'disordered' is borrowed from the terminology of magnetic transitions. Such a disordered-commensurate transition is given by imposing a

- FIGURE 51: i) A linear monatomic chain of primitive cell dimension 'a'.  
ii) A distortion of the form  $u(z) = U \cos q_c z$ , where  $q_c = \frac{2\pi}{3a}$ .  
iii) The structure produced by a distortion 51(ii) on 51(i).

- FIGURE 52: i) A distortion of the form  $u(z) = U \cos q_c z$ , where  $q_c = \frac{2\pi}{3a}$ .  
ii) The structure produced by a distortion 52(i) on 51(i).  
iii) A distortion of the form  $u(z) = U \cos q_i z$ , where  $q_i$  is close to, but not equal to  $\frac{2\pi}{3a}$ .  
iv) The structure produced by a distortion 52(iii) on 51(i).  
v) A distortion of the form  $u(z) = U \cos(q_c z + \phi(z))$ , where  $q_c = \frac{2\pi}{3a}$  and  $\phi(z)$  'contains two phase solitons'. The soliton regions are marked 'S'.  
vi) The structure produced by a distortion 52(v) on 51(i). The solitons can be seen as regions of local aperiodicity separated by regions of local ordering as in 52(ii).

- FIGURE 53: i) The form of  $\phi(z)$  corresponding to a two-soliton distortion of 51(i) close to a lock-in transition to  $q_c = \frac{2\pi}{3a}$ .  
ii) A distortion of the form  $u(z) = U \cos(q_c z + \phi(z))$ , where  $q_c = \frac{2\pi}{3a}$  and  $\phi(z)$  contains two phase solitons as given by 53(i). (identical to 52(v)).  
iii) The structure produced by a distortion 53(ii) on 51(i). (identical to 52(vi)).

distortion  $u(z)$  given by 51(ii) on the disordered structure 51(i) to produce 51(iii) (commensurate). Clearly the new unit cell dimension is  $3a$ , and the structure 51(iii) can indeed be measured by the same unit 'a'. The wavevector  $q_c$  is here equal to  $\frac{\tau}{3}$ .

The modulation in the structure can be thought of in terms of a 'soft' phonon with wavevector  $q_c$  which condenses to  $\omega_c = 0$  to produce the commensurate structure. Obviously, a distortion where the minimum in the soft mode dispersion occurs at  $q_c = \tau = 0$  is homogeneous, and the unit cell dimension does not change. The class of transition termed incommensurate occurs when the soft mode located by the minimum in  $\omega(q)$  has a wavevector  $q_i$  which cannot be expressed as a simple fraction of  $\tau$ , and the distortion induced by the condensation of the soft mode produces an aperiodic system. Such a system obviously cannot be measured exactly by the unit 'a'. A distortion of Figure 51(i) of the form  $u(z) = U \cos q_i z$  is plotted in 52(iii) and (iv), with  $q_i$  close to but not equal to  $\frac{\tau}{3}$ . This phase is not strictly crystalline. In fact, anharmonic terms in the Hamiltonian ensure that to some extent, the incommensurate distortion will include harmonics of  $q_i$  (90). The extent of the contribution from these harmonics depends on the detail of the soft mode dispersion (see §6.2 and §6.3).

In the case of an incommensurate transition in a conductor, the presence of a Fermi surface associated with the conduction electrons can provide an excuse for incommensurability. It is well known (91) that the proximity of a phonon wavevector to the Fermi surface results in Kohn anomalies - points of inflection in the dispersion curve. It is plausible that the enhanced screening of phonon frequencies caused by the electron-phonon interaction at the Fermi surface could

also affect the temperature dependence of the frequencies to provide an incommensurate soft mode. Instances of incommensurate transitions with characteristic wavevectors identical to the wavevectors of marked Kohn anomalies have been reported, particularly in quasi-one-dimensional conductors (e.g. (92)).

By no means all structurally incommensurate transitions occur in conductors, however, and for illustrative purposes the disordered-incommensurate transition at  $T_i = 130\text{K}$  in  $\text{K}_2\text{SeO}_4$  is relevant here. The temperature dependence of the soft mode branch of the dispersion relation of  $\text{K}_2\text{SeO}_4$  (from inelastic neutron scattering (93)) is presented schematically in Figure 54. It can be seen that the soft phonon condenses to zero frequency at 130K at a wavevector of  $0.31\underline{\tau}$ , producing an incommensurate structure (c.f. Fig. 52(iii) and (iv), where  $q_i = 0.323\underline{\tau}$ ). When the incommensurate distortion occurs in  $\text{K}_2\text{SeO}_4$ , there is a concomitant appearance of satellite Bragg peaks in the neutron scattering cross-section at  $q_i$  (or X-ray scattering cross-section). This is due to the fact that the distortion is itself periodic (c.f. Fig. 52(iii)) although the structure it produces is not. If the modulation were commensurate, of course, the new Bragg peaks would occur at  $q_c$ , some rational fraction of  $\underline{\tau}$ . A study of the elastic scattering therefore provides a probe of the value of  $q_i$ . In  $\text{K}_2\text{SeO}_4$ ,  $q_i$  is close to  $\underline{\tau}/3$ , and may be expressed as  $q_i = \underline{\tau}/3 - \underline{\delta} = q_c - \underline{\delta}$ , where  $\underline{\delta}$  is small. A study of the temperature dependence of  $q_i$  in  $\text{K}_2\text{SeO}_4$  (93) is represented by Figure 55. At  $T_i$ , the satellite reflections appear at  $q_i \approx (1 - 0.07)\underline{\tau}/3$  and shift to  $q_i \approx (1 - 0.02)\underline{\tau}/3$  over the following  $\approx 40\text{K}$ .

At  $T_c = 93\text{K}$ , a further transition can be seen to occur, at which  $\underline{\delta} \rightarrow 0$  apparently discontinuously and therefore  $q_i \rightarrow q_c$ .

FIGURE 54: The form of the soft-mode dispersion at temperatures above and equal to the disordered-incommensurate transition  $T_i$  for  $K_2SeO_4$  (schematic). The parameter  $\delta$  measures the deviation from commensurate,  $\frac{1}{3}$  ordering (reference 93).

FIGURE 55: The variation with temperature of the parameter  $\delta$  for  $K_2SeO_4$ . At a temperature  $T_c$ ,  $\delta \rightarrow 0$ , apparently discontinuously, corresponding to a lock-in to commensurate  $\frac{1}{3}$  ordering.

FREQUENCY

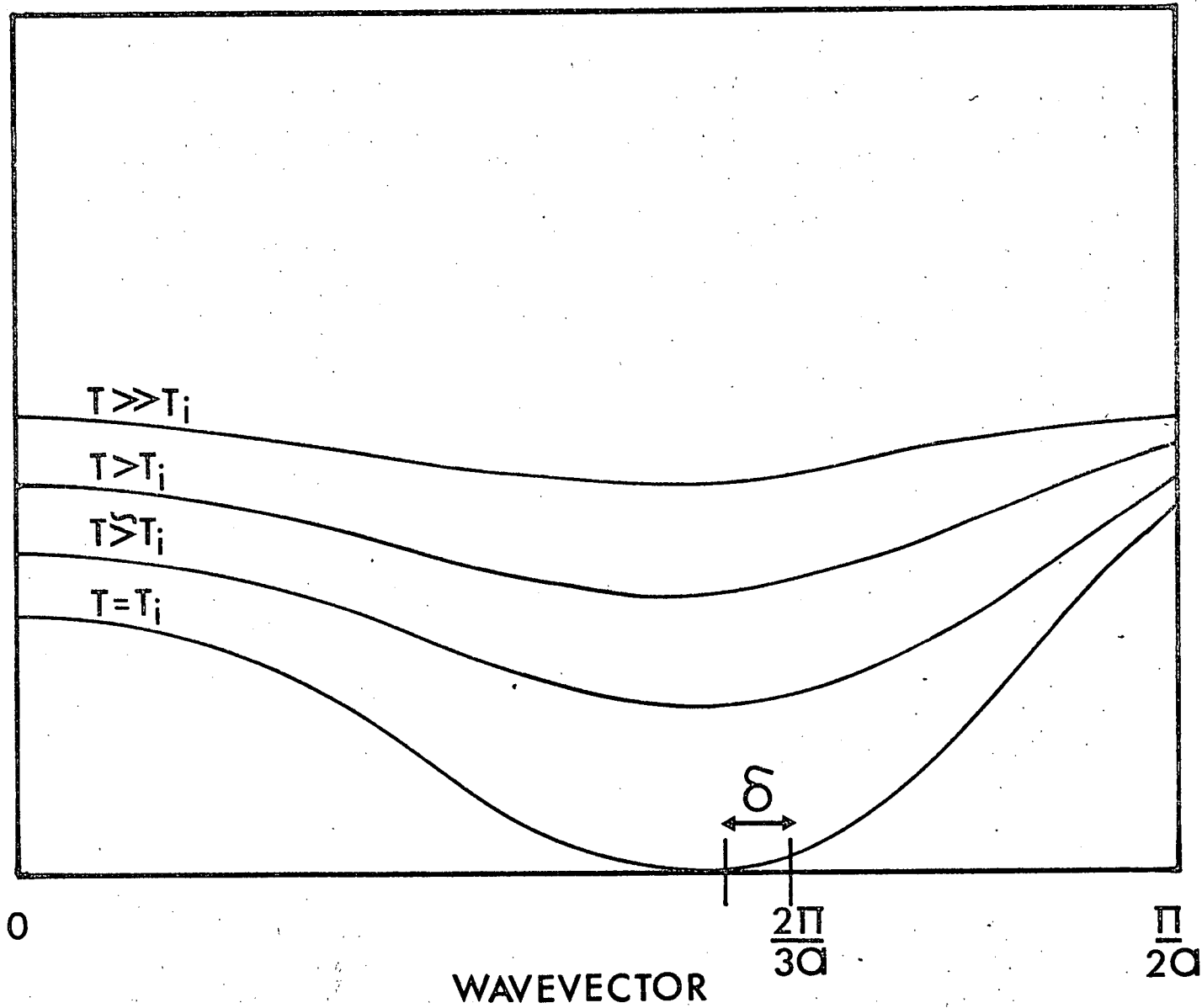


FIG 54

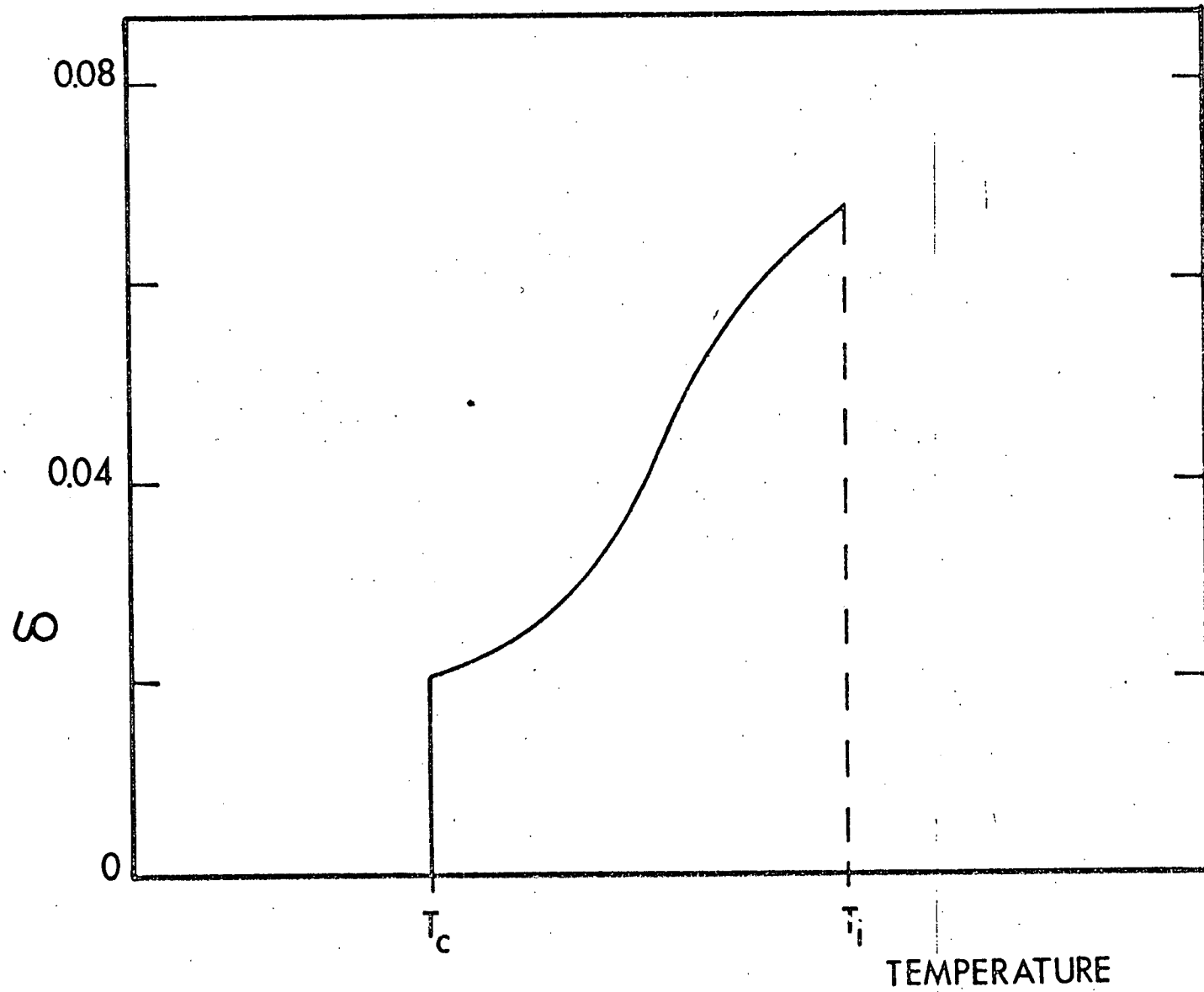


FIG 55

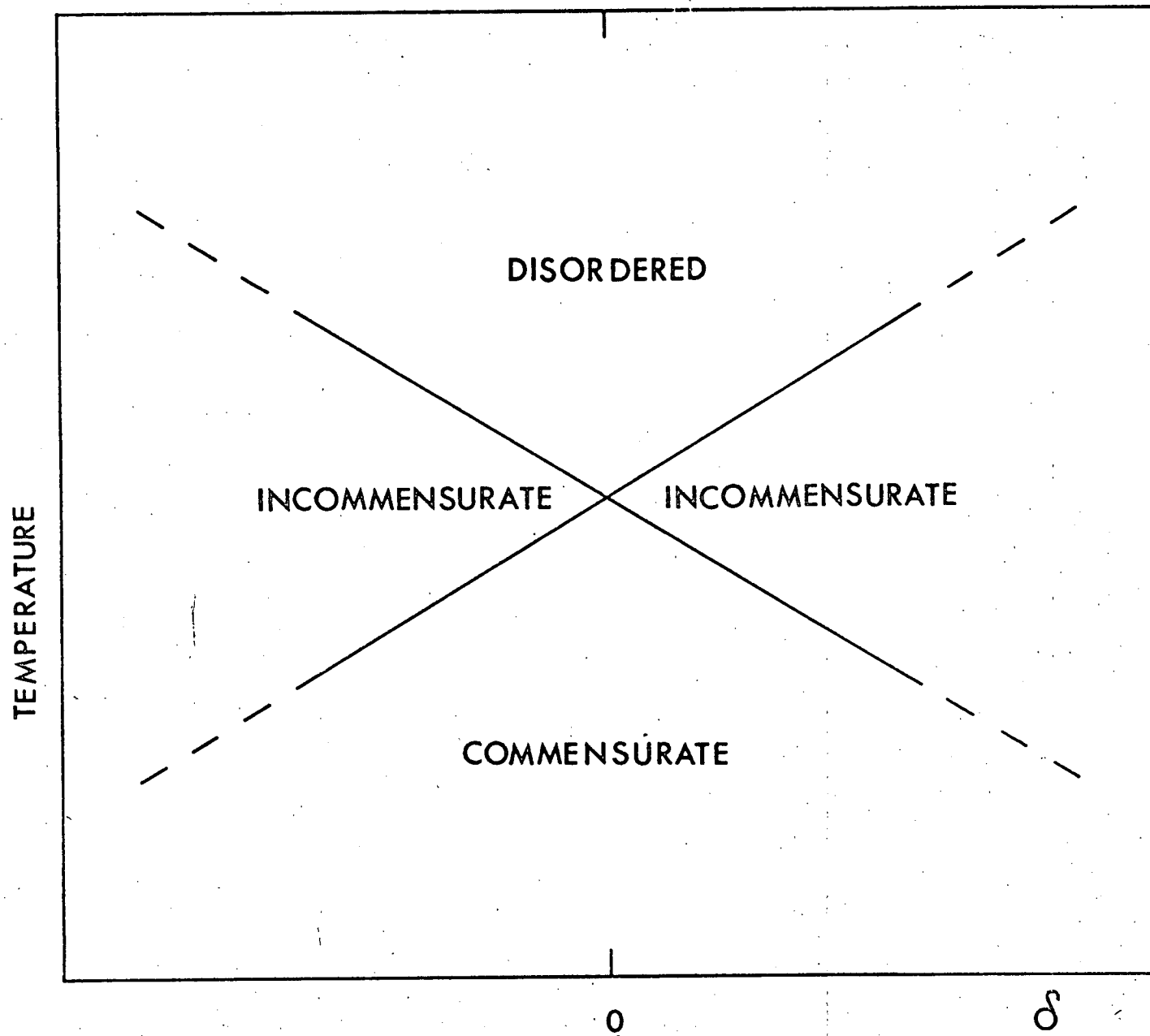
The structure below  $T_i$  is consequently commensurate, and has a unit cell dimension  $3X$  that of the disordered phase (above  $T_i$ ). The sequence of transitions in  $K_2SeO_4$  as temperature is lowered is thus analogous to the one-dimensional sequence from Figure 51(i) to 52(iv) at  $T_i$ , and finally to 52(ii) at  $T_c$ . The transition at  $T_c$  where the wavevector of the distortion jumps to a commensurate value is commonly termed a lock-in transition. It is the purpose of this chapter (and reference (88)) to elucidate the nature of the distortion just above  $T_c$ , the lock-in transition temperature.

No detailed argument is offered here to explain the existence of irrational wavevectors for soft modes in insulators. Intuitively, it is not surprising that, in some materials, zone boundary or zone centre modes become unstable, as these are obvious critical points on the dispersion curve, and it seems reasonable to expect other high symmetry points to provide lock-in wavevectors. The existence of energetically favourable incommensurate modulations is controlled by the nature of the atomic forces. The philosophy of this chapter, therefore, is to investigate model Hamiltonians with suitable minima in the soft mode dispersion branch, and to adjust the harmonic parameters to induce phase transitions. This Landau-style manipulation will be applied to the lock-in transition. A discussion of the disordered-incommensurate transition is given in reference 87.

The phase diagram with respect to the parameter  $\delta$  is essentially given by Figure 56. For  $\delta = 0$ , the transition is directly from the disordered phase to a commensurate phase. Otherwise there is an intervening incommensurate phase which is traversed as temperature is lowered. It must be remarked that not all incommensurate phases lock in to commensurability (e.g.  $NbSe_2$  (90)). For the purposes of this work, incommensurate lock-in transitions can be classed



FIGURE 56: Schematic phase diagram for a system exhibiting disordered-commensurate, disordered-incommensurate, and incommensurate-commensurate ('lock-in') transitions, in terms of the parameter  $\delta$ .



as being one of two types. At type II transitions, the lock-in wave-vector  $q_c$  defines a point of inversion symmetry (e.g.  $q_c = 0$ ;  $q_c = \pi/2$ ), at type I transitions it does not (e.g.  $\pi/3$ ). These two cases have a different Hamiltonian, and consequently a different incommensurate distortion profile.

A simplified reformulation is given in §6.2 of the analysis of the type I Hamiltonian, as studied by McMillan (94) and Bak and Emery (95). In §6.3, the Hamiltonian is constructed and analysed for type II transitions, and the form of the distortion profile derived. In §6.4, conclusions are drawn.

### §6.2 Type I Transitions ( $q_i \approx \pi/p$ ; $p > 2$ )

So far, the illustrative example has been a monatomic linear chain. It turns out that examining the form of the incommensurate modulation in one dimension (the direction of  $q_i = [0, 0, q_i]$  does not obscure any of the physics, provided the generalisation to 3D is carefully considered.

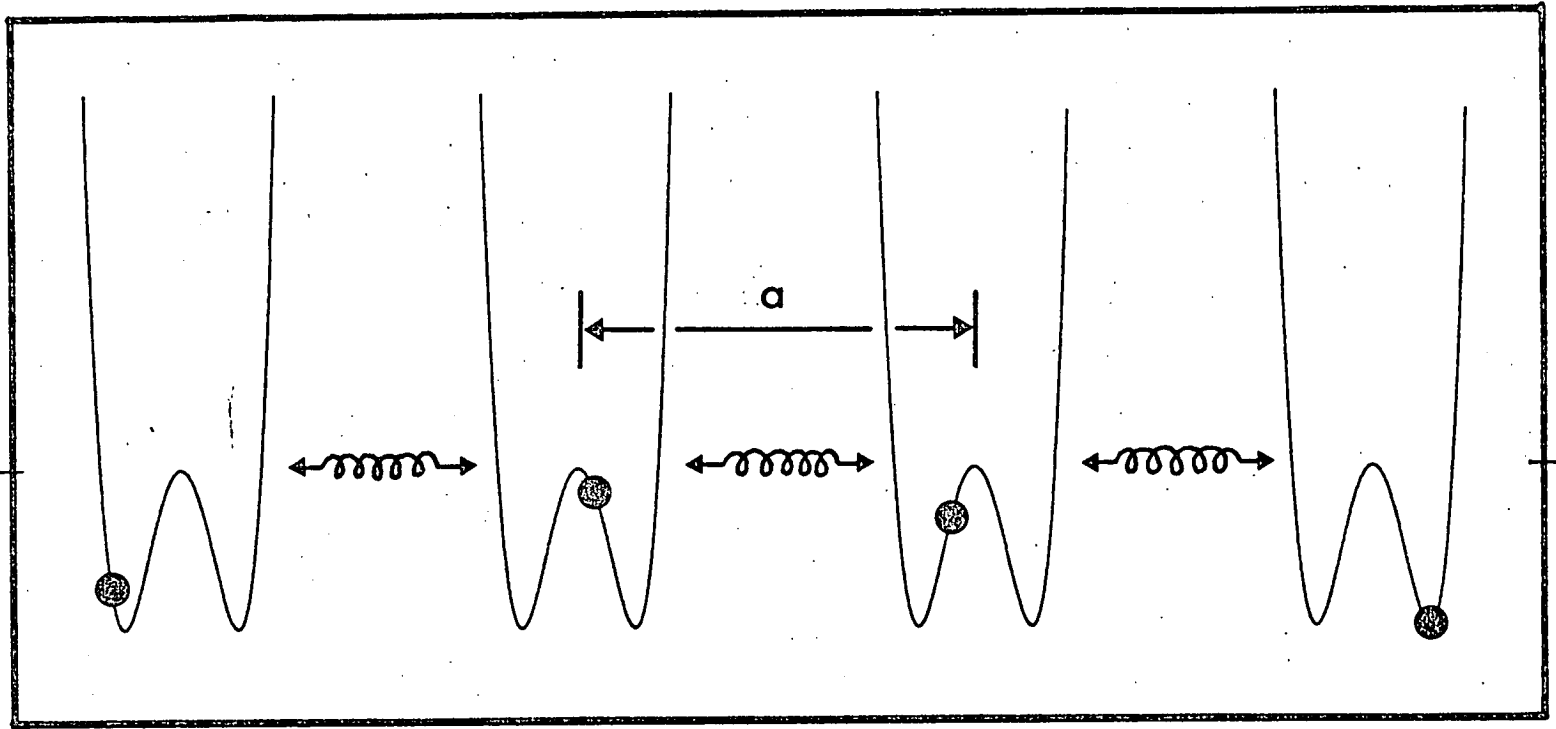
The basic model for both types I and II transitions is illustrated schematically in Figure 57. In this model (96) the atoms are assumed to move in double well potentials, localised on the undistorted positions, and of the form  $A u^2(z) + B u^4(z)$ , where  $u(z)$  is the displacement of the atom at  $z$  from its undistorted position. Furthermore, there are assumed to be (generally anharmonic) interatomic interactions.

Since we know that  $q_i$  is close to some  $q_c$  at the lock-in boundary, let us represent  $u(z)$  by:

$$6.1 \quad u(z) = \sqrt{2} U(z) \cos(q_c z + \phi(z)).$$

FIGURE 57: A simple model for a system undergoing displacive phase transitions. The parameters characterising the double wells and the interatomic forces can be adjusted to produce an energetically favoured incommensurate phase. The circles represent atoms, and the 'springs' atomic forces.

POTENTIAL



z

The essential anharmonic terms in the Hamiltonian density in terms of these variables are

$$6.2 \quad H_{an}(z) = BU^4(z) + C U^p(z) \cos p \phi(z)$$

where  $q_c = \frac{\tau}{p}$  and  $H = \int H(z) dz$ . The exact forms of these terms are most conveniently obtained by expressing the full Hamiltonian in the form of equation 4.7, i.e. (excluding kinetic energy)

$$6.3 \quad H = \frac{1}{2} \int \omega^2(q) |Q_q|^2 dq \\ + \iiint V_3(q_1 q_2 q_3) Q_{q_1} Q_{q_2} Q_{q_3} \delta(q_1 + q_2 + q_3 + K) dq_1 dq_2 dq_3 \\ + \dots$$

Considering the anharmonic terms, and restricting the range of  $q$  to small regions around  $\pm q_c$  by means of the transformation:

$$6.4 \quad Q_{\pm q_c + \tilde{q}} = (P_1(\tilde{q}) \pm i P_2(\tilde{q})) / \sqrt{2}$$

then expressing the Fourier transforms of the  $P$ 's as

$$6.5 \quad P_1(z) = U(z) \cos \phi(z); \quad P_2(z) = -U(z) \sin \phi(z)$$

yields equations 6.1 and 6.2. The first and second terms in 6.2 can be identified respectively with the  $B u^4(z)$  term in the double potential well, and the  $p$ -th order anharmonic interatomic coupling term in the model. It is clear that the  $\delta(\sum_j q_j + K)$  associated with each term of 6.3 restricts the order of anharmonicity in which

coordinates with  $q_i \sim q_c = \tau/p$  can appear.

The form of the harmonic term is critical, as it essentially defines the difference between type I and type II transitions. When  $q_c$  does not define a centre of inversion symmetry for the dispersion curve,  $\omega^2(q)$  can be represented for the regions around  $\pm q_i$  by the form

$$6.6 \quad \omega^2(q) = \omega_0^2 + (q - q_i)^2$$

and  $\omega_0^2 \propto T - T_i$  gives the required variation. It is important to note that this is not a valid approximation for type II transitions (see 6.3). With the same set of variable changes as described for the anharmonic terms in  $H(z)$ , we have for the harmonic terms:

$$6.7 \quad H_0(z) = \frac{1}{2}\omega_0^2 U^2(z) + \frac{1}{2}(\nabla U(z))^2 + \frac{1}{2}U^2(z)(\nabla\phi(z))^2 \\ + \frac{1}{2}U^2(z)\delta^2 - U^2(z)\delta\nabla\phi(z)$$

where  $\nabla = \frac{\partial}{\partial z}$  and

$$6.8 \quad q_i = q_c + \delta.$$

The full (essential) Hamiltonian density is now given by  $H = H_0 + H_{an}$  and we can attempt to adjust the form of  $u(z)$  to minimize the corresponding free energy. With no loss of generality, we may restrict our discussion to  $q_c = \tau/3$ . Before presenting the result of this procedure, it is fruitful to consider the single plane wave incommensurate distortion of Figures 52(iii) and 52(iv). This

corresponds to  $U(z) = \text{constant}$ ,  $\phi(z) = \delta z = 0.01z$  in equation 6.1, and the only  $z$ -dependent term in  $H$  is  $CU^3 \cos(0.03z)$ . This term provides equal positive and negative contributions to the free energy, depending on the value of the cosine. A net lowering of the free energy can be obtained by modulating the amplitude  $U$  or the phase  $\phi$  (or both). Since the term in 6.7 which lowers the free energy for  $\delta \neq 0$  (i.e. which favours incommensurability) depends only on  $\nabla\phi(z)$ , it seems plausible that phase modulation is more important. McMillan (90) noted also that modulating the amplitude increases the positive  $U^2, U^4$  terms of 6.2 and 6.7, more than does a variation of  $\phi$ , such that in his language, 'amplitude modulation costs more energy'. Accordingly, the phase-modulation-only hypothesis is adopted, although it must be borne in mind that  $U(z)$  may vary. Indeed the fact that  $U$  must at least vary from zero above  $T_i$  to some small nonzero value below  $T_i$  suggests that the phase-modulation-only form should not be applied near  $T_i$ . With this reservation, therefore, setting  $u(z) = \sqrt{2}U \cos(\frac{2\pi}{3a}z + \phi(z))$  for a monatomic chain of length  $L$  we have a free energy/ unit cell

$$6.9 \quad F = \frac{U^2}{L} \int_0^L \left( \frac{\phi^2}{2} + UC \cos 3\phi \right) dz - \frac{U^2}{L} (\phi_L - \phi_0) \delta + \frac{U^2 \delta^2}{2}$$

Within this expression, there is a 'competition' between the integral term, which is minimised for  $\phi(z) = \text{constant} = 0, \frac{2\pi}{3}, \frac{4\pi}{3} \dots$  (remember  $C < 0$ ), and the term in  $(\phi_L - \phi_0)$ , which provides a negative contribution to  $F$  if  $\phi(z)$  varies along  $L$ . Given that  $\phi(z)$  should vary, therefore, the minimisation of the integral demands



that the variation of  $\phi(z)$  be in steps of  $\frac{2\pi}{3}$  and that the steps satisfy the sine-Gordon equation (SGE)  $\phi'' = +3UC\sin 3\phi$ , one of whose solutions is the SOLITON (97)

$$6.10 \quad \phi(z) = \frac{4}{3} \tan^{-1} \exp(-9UCz^2)^{\frac{1}{2}} .$$

A two-soliton distortion of the structure of Figure 51(i) is given by Figure 52(vi), and the corresponding form of  $u(z)$  by Figure 52(v) (also Figure 53(ii)). The corresponding variation of  $\phi(z)$  is given in Figure 53(i). Clearly, this distortion corresponds to regions of commensurate, periodic  $\frac{\tau}{3}$  ordering where  $\phi$  is constant, separated by regions of local rapid phase variation (phase solitons, marked s) giving rise to localised aperiodicity. The soliton regions may be regarded as 'domain walls' between the locally commensurate regions.

At a lock-in transition to  $q_c = \frac{\tau}{3}$  the solitons must space out until  $\phi = \text{constant}$  over the whole crystal, so the soliton density must go to zero continuously as  $T \rightarrow T_c^+$ . The order parameter for the lock-in transition is therefore the soliton density. McMillan (90) has shown analytically that  $\delta$ , and therefore soliton density goes continuously to zero at  $T_c$  and the lock-in transition is continuous. In the event that macroscopic strain appears in the Hamiltonian as a coupling to the soliton density, the strain acts as an intermediary between widely separated solitons and it can be shown (88) that the transition is then of necessity first order (cf. Figure 32a). In practice this will almost certainly be the case.

A further inadequacy of the theory above is that it does not take any account of the underlying lattice. Obviously a soliton is not a useful concept when its width is comparable to the lattice spacing,

as it would then represent a dislocation, and not merely a discommensuration (94). Furthermore, the lattice may well provide preferred soliton locations. Work is currently in progress to study the nature of incommensurate distortions (if they exist) without regarding  $u(z)$  as a continuous field. This is algebraically messy, and numerical methods will have to be used. An attempt to analyse the model by analogy with the description of a submonolayer film on a substrate (98) failed due to the singular nature of the double well potential.

### 56.3 Type II Transitions ( $q_i \sim 0$ )

As has been said, when  $q_i = 0 + \delta$ , the expansion  $\omega^2(q) = \omega_0^2 + |q - q_i|^2$  is not valid since  $\frac{\partial \omega}{\partial q}$  must  $\rightarrow 0$  as  $q \rightarrow 0$ . This means that steps 6.6 - 6.7 are impossible, and 6.3 - 6.5 unhelpful for type II transitions. It is most useful to consider the model of Figure 57, with nearest and next-nearest neighbour harmonic interactions, explicitly. The model Hamiltonian is therefore, in a real-space notation

$$6.11 \quad H = \sum_{\ell} \left[ \frac{A}{2} u_{\ell}^2 + \frac{B}{4} u_{\ell}^4 + C_1 (u_{\ell+1} - u_{\ell})^2 + C_2 (u_{\ell+2} - u_{\ell})^2 \right]$$

where  $u_{\ell}$  is the displacement of the  $\ell$ 'th atom. Using that fact that, for the type II incommensurate distortion, wavelength

$\lambda_i = \frac{2\pi}{q_i} \gg a$ , we can expand  $u$  as a Taylor series and thus go to the continuum limit, i.e.  $u_{\ell+n} = u(\ell a) + na \nabla u(\ell a) + \frac{(na)^2}{2} \nabla^2 u(\ell a) + \dots$

This projects out a Hamiltonian density

$$6.12 \quad H(\mathbf{x}) = \frac{\tilde{\lambda}}{2} U^2(\mathbf{x}) + \frac{1}{4} U^4(\mathbf{x}) \\ + \frac{1}{2} C (\nabla U(\mathbf{x}))^2 - \frac{1}{2} [(\nabla^2 U(\mathbf{x}))^2 + \frac{4}{3} \nabla U(\mathbf{x}) \nabla^3 U(\mathbf{x})]$$

where

$$6.13 \quad U = B^{\frac{1}{4}} u ; \quad x = -2B^{1/8} z / ((C_1 + 16C_2)a^4)$$

and  $\tilde{\lambda}$ ,  $C$  have been similarly defined.

Equation 6.12 provides a suitable function to investigate the energetically stable configuration for  $U(\mathbf{x})$  by integrating over a length  $L$  of 'crystal', and minimising the resultant free energy. This calculation will be performed within two hypotheses.

56.3(i) A single-Fourier-component distortion (SPW)

This form for  $U(\mathbf{x})$  is represented by

$$6.14 \quad U(z) = U \cos q x$$

and gives a free energy/unit cell of:

$$6.15 \quad F_L = \frac{U^2}{4} \omega^2(q) + \frac{3U^4}{32} + \frac{\delta(q)}{4} \left( \frac{\tilde{\lambda}}{2} U^2 + \frac{5U^4}{8} \right)$$

$$6.16 \quad \omega^2(q) = \tilde{\lambda} + Cq^2 + \frac{1}{3}q^4$$

This form for the harmonic term clearly describes a system which, for

$C < 0$ , can have an energetically favoured phase with  $q =$

$q_i = \delta = \left(-\frac{3C}{2}\right)^{\frac{1}{2}}$ , i.e., a minimum in the dispersion at  $\delta$ .

It can be seen that the disordered (d) phase corresponds to  $U = 0$ , the incommensurate (i) phase to  $U \neq 0$ ,  $q_i = \delta$  and the commensurate (c) phase to  $U \neq 0$ ,  $q = q_c = 0$ . Within the single plane wave approximation, therefore, we have

$$6.17a \quad (F_L)_d = (F_L)_i \quad \text{when } C < 0 < \tilde{A}; \quad G^2 = \frac{4}{3} \tilde{A}$$

$$6.17b \quad (F_L)_i = (F_L)_c \quad \text{when } C, \tilde{A} < 0; \quad G^2 = \left(1 - \sqrt{\frac{3}{2}}\right) \frac{4}{3} \tilde{A}$$

$$6.17c \quad (F_L)_d = (F_L)_c \quad \text{when } C > 0; \quad \tilde{A} = 0$$

and the phase diagram is given by Figure 58 where  $\tilde{A}$  is regarded as the temperature dependent parameter. It now seems reasonable to apply a more general trial form for  $U(x)$  incorporating harmonics.

§6.3(ii) A multi-plane wave distortion (MPW)

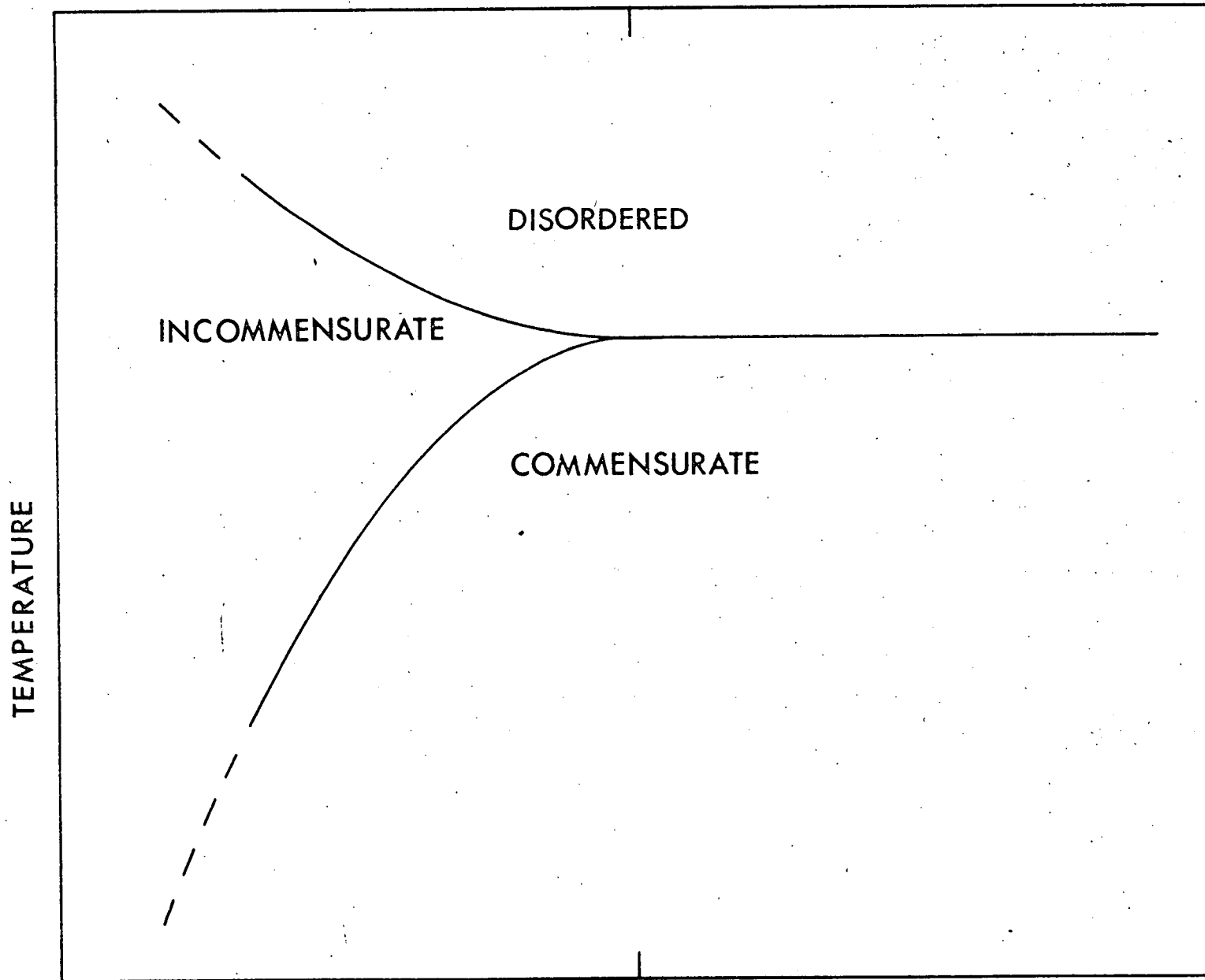
Substitution of a multiple-component Fourier series for  $U(x)$ :

$$6.18 \quad U(x) = \sum_m U_m \cos m q x$$

projects out as free energy/unit length from 6.12

$$6.19 \quad F_L = \frac{\tilde{A}^2}{2} U_0^2 + \frac{1}{4} \sum_{m>0} U_m^2 \omega^2(mq) + \frac{U_0^4}{32} + \frac{1}{32} \sum_{mnop} U_m U_n U_o U_p [4\delta(m-n-o-p) + 3\delta(m+n-o-p)]$$

FIGURE 58: Phase diagram for a system exhibiting a type II lock-in transition, within the simple single-Fourier-component distortion (SPW) model of §6.3(i).



C

where  $\omega^2(mq)$  is given by 6.16.

A computer minimisation programme was used to minimise 6.19 for a particular  $C, \tilde{A}$  in terms of 1, 2, 3, ... 7-component Fourier distortions with a view to a soliton-like form. Substitution of the Fourier components of a soliton does produce a minimum in  $F_L$ , but not an absolute minimum (i.e. the SPW free energy is always lower). A further multi-component series does yield a lower  $F_L$  than the SPW, but the series is rapidly convergent, and therefore the form of  $U(x)$  almost sinusoidal. The variation of the SPW and MPW free energies with  $C$  is shown in Figure 59(i) and (ii) respectively, along with the commensurate free energy 59(iii). It can be seen that the lock in transition occurs at a value of  $\bar{C} = C \sqrt{\frac{3}{|\tilde{A}|}} = -0.92$  between a MPW state and a commensurate state. The MPW series has  $U_m = 0$  for  $m$  even, and  $U_3 \sim -0.035U_1$ . The self-consistency of this solution can be checked analytically in terms of a two-plane-wave distortion with this ratio of  $U_1: U_3$

It can also be shown (88) that the rescaled displacement field:

$$6.20 \quad W(\tilde{x}) = (-\tilde{A})^{\frac{1}{2}} U(x|3\tilde{A}|^{\frac{1}{2}})$$

obeys a fourth order, nonlinear differential equation

$$6.21 \quad W'''' - C \sqrt{3}/\tilde{A} W'' + (W^2 - 1)W = 0$$

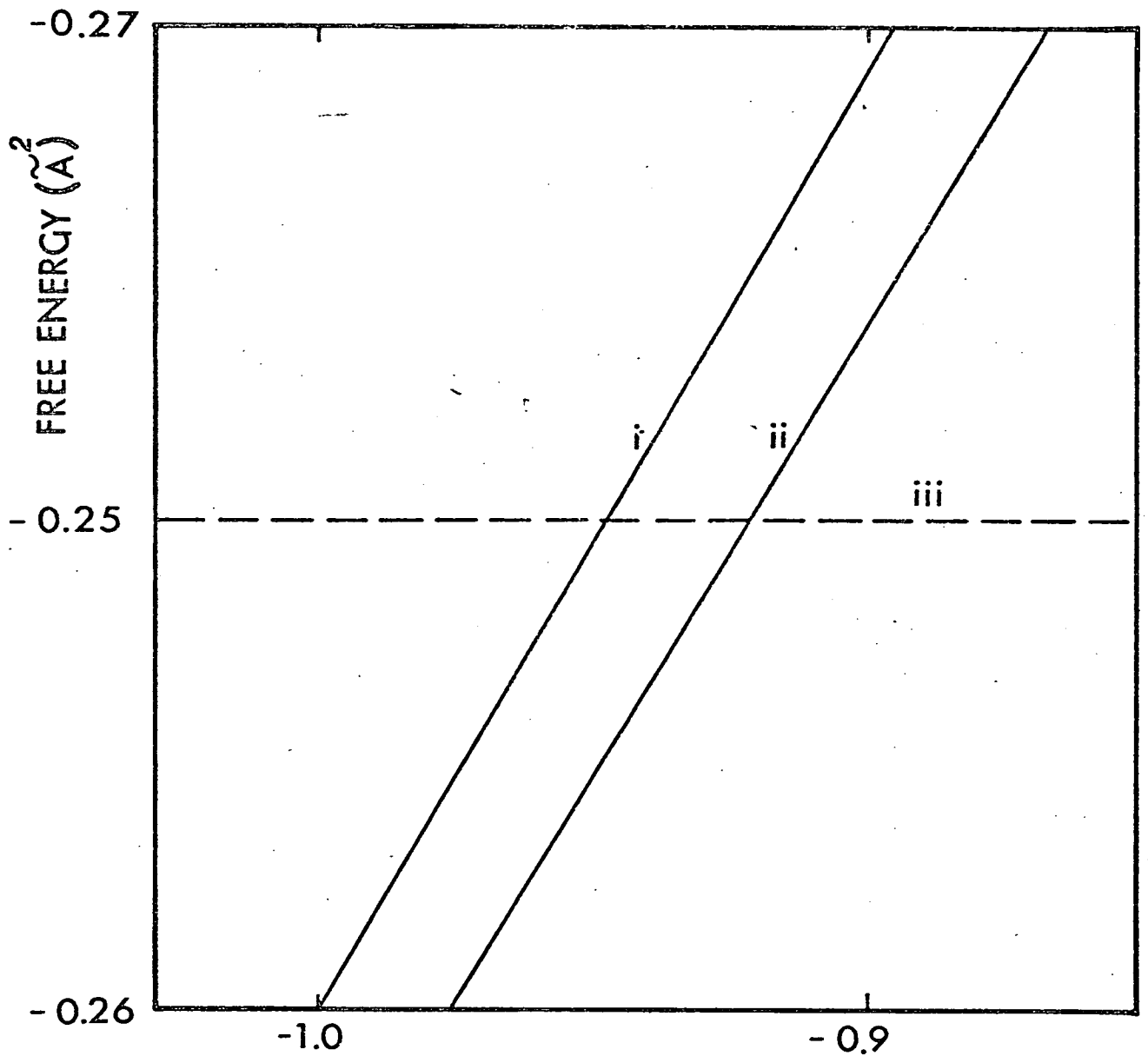
This equation is the type II transition analogue of the SGE, but does not appear to have a simple analytic solution. A numerical analysis of 6.21, looking for a domain wall solution, shows that such a solution

FIGURE 59: The variation with parameter  $C$  of equation 6.12 of the incommensurate phase free energy within the single-Fourier-component model (SPW) of §6.3i (line i), and the multi-plane-wave model of §6.3ii (line ii). Line iii represents the commensurate phase free energy.

FIGURE 60: The variation with parameter  $C$  of equation 6.12 of the energy of a domain-wall type solution (soliton-like) to equation 6.21. Note that for  $C > -1.14$ , the disordered phase free energy ( $=0$ ) is less than that of a domain wall, and that for  $C < -0.98$ , the MPW incommensurate phase is already favoured. This means that the domain-wall solution is never favourable in type II transitions.



FIG 59



$$\bar{C} = C \frac{\sqrt{3}}{\sqrt{|\tilde{A}|}}$$

# DOMAIN WALL ENERGY

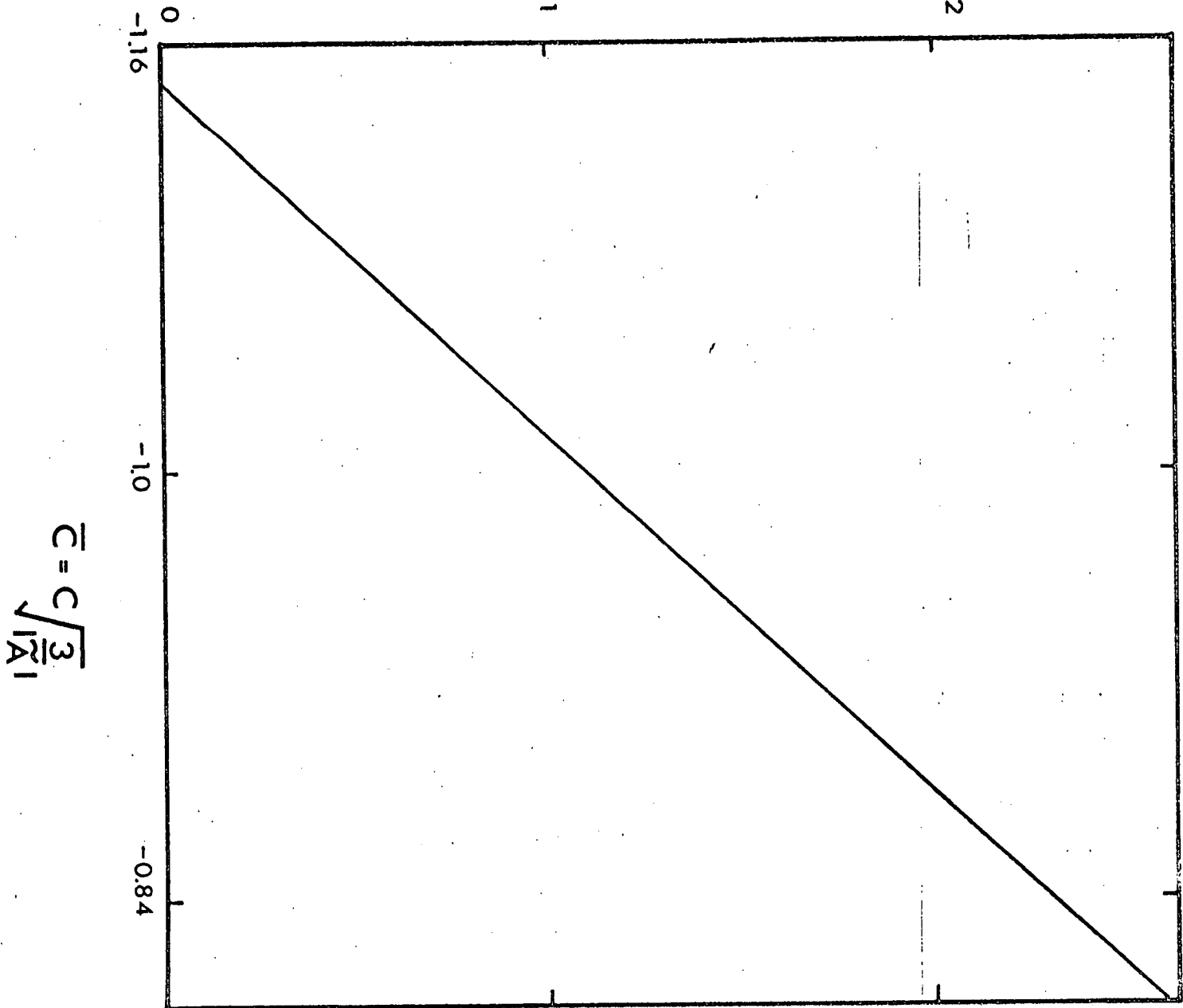


FIG 60

does exist, but that its free energy is never lower than that of either a disordered, commensurate, or incommensurate SPW phase. In other words, although a soliton phase does 'exist', as a minimum in  $F_L$ , it is never energetically favourable. This is clear from Figure 60, in that by the time the soliton energy is less than the disordered phase energy at  $\bar{C} < -1.14$ , the SPW phase has already become favourable. This is entirely consistent with the results of the MPW analysis and Figure 59.

It seems, therefore, that the different form of the soft mode dispersion in type II materials leads to a qualitatively different distortion profile in the incommensurate phase from that of type I materials. The fact that the lock-in transition occurs at  $\bar{C} = -0.92$  means that, even within an MPW model, the deviation from commensurability  $\delta (= (-\frac{3C}{2})^{\frac{1}{2}})$  must vary discontinuously to zero at  $T_c$  and that the lock-in transition is first order regardless of coupling to strain degrees of freedom.

#### §6.4 Conclusions

Types I and II transitions have been shown to have qualitatively different distortion profiles, corresponding to the extremely un-sinusoidal modulation characterised by an array of phase solitons, and a nearly sinusoidal form respectively. This qualitative difference demands that a type I lock-in transition can in principle, be continuous, as soliton density goes to zero, although in practice it will almost certainly be first order. A type II transition is, of necessity, first order.

In three dimensions, the solitons and plane waves become infinitely extended planar wavefronts. There is no a priori reason why discommensurations cannot occur in more than one direction, and the 'crossing' of solitons may lead to dislocations (90).

The modes of excitation of any incommensurate single-plane-wave ground state (89) correspond to a local phase modulation (phason) or a local amplitude modulation (ampliton?). An attempt to detect phasons (whose dispersion should resemble acoustic modes) in  $\text{BaMnF}_4$  by Brillouin spectroscopy failed, although a critically temperature dependent mode of vibration was found. This temperature dependence has been conjectured by Scott (99) to be due to acoustic mode-phason coupling, although no direct observation of phason scattering has yet been reported. There is, therefore, a need for high resolution Brillouin and neutron scattering studies at  $T < T_i$  to verify directly the presence of a phason dispersion branch, whose frequency  $\rightarrow 0$  as  $q \rightarrow q_i$ . Possible materials for such studies are  $\text{BaMnF}_4$ ,  $\text{K}_2\text{SeO}_4$  (type I) and  $\text{NaNO}_2$  (type II). The failure of the Brillouin experiments to observe phason scattering directly may be due to inadequate resolution. Alternatively, there may be a gap in the phason dispersion, due to pinning effects (particularly in the soliton limit). This could shift phason peaks out of the free spectral range of the interferometer. Neutron and Raman studies, along with a detailed lattice dynamical study, should resolve this question.

APPENDIX 1      Perturbation Theory and the Anharmonic Greens Function

In the Schrodinger picture of Quantum Mechanics, the wave function evolves in time according to the equation:

$$A1.1 \quad |\psi(t)\rangle = \exp \frac{-i H t}{\hbar} |\psi(0)\rangle = U(t,0) |\psi(0)\rangle$$

which, in the interaction picture becomes

$$A1.2 \quad |\tilde{\psi}(t)\rangle = \exp \frac{i H_0 t}{\hbar} \exp \frac{-i H t}{\hbar} |\tilde{\psi}(0)\rangle \\ = \tilde{U}(t,0) |\tilde{\psi}(0)\rangle$$

where  $U(t_2, t_1)$ ,  $\tilde{U}(t_2, t_1)$  are the time evolution operators between times  $t_1$ ,  $t_2$  ( $= 0, t$  in A1.1 and A1.2).  $\tilde{U}$  has the property

$$A1.3 \quad \tilde{U}(t_3, t_2) \tilde{U}(t_2, t_1) = \tilde{U}(t_3, t_1) .$$

Now consider expression 1.36 for  $G(\underline{y}ab, \tau)$ . Using the definition of the interaction picture (11) and the properties of  $T_t$ , this gives

$$A1.4 \quad G(\underline{y}ab, \tau) = \frac{\text{Tr}}{Z} \{ \exp -\beta H_0 T_t [ \tilde{\psi}(\underline{y}a, \tau) \tilde{\psi}^*(\underline{y}b, 0) \tilde{U}(\beta \hbar, 0) ] \}$$

Differentiating A1.2 gives a differential equation for  $\tilde{U}$ ,

$$A1.5 \quad \hbar \frac{\partial \tilde{U}(\tau, 0)}{\partial \tau} = -\tilde{H}' \tilde{U}(\tau, 0)$$


where  $\tilde{H}'$  is the additive term 1.35 to the harmonic Hamiltonian. This can be solved iteratively to give (20), (22):

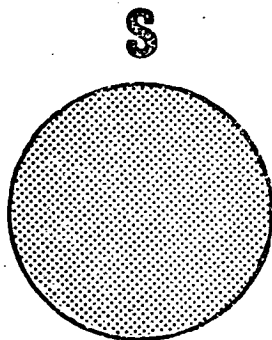
$$A1.6 \quad \tilde{U}(\tau, 0) = 1 + \sum_n \frac{1}{n!} \left( \frac{-1}{\hbar} \right)^n \int_0^\tau \rightarrow \int_0^\tau T_t (\tilde{H}'(\tau_1) \rightarrow \tilde{H}'(\tau_n)) d\tau_1 \rightarrow d\tau_n$$

When substituted into A1.4, this gives

$$\begin{aligned}
 \text{A1.6} \quad G(\underline{y}_{ab}, \tau) &= G^H(\underline{y}_{aa}, \tau) \\
 &+ \text{Tr} \sum_n \frac{1}{Zn!} \left(-\frac{1}{\hbar}\right)^n \int_0^\tau \rightarrow \int_0^\tau T_t [\exp - \beta H_0 \tilde{H}'(\tau_1) \rightarrow \tilde{H}'(\tau_n) \\
 &\quad \times \tilde{\psi}(\underline{y}_a, \tau) \tilde{\psi}^*(\underline{y}_b, 0)] d\tau_1 \rightarrow d\tau_n .
 \end{aligned}$$

When expression 1.35 is used for  $H'$ , and  $V$  is redefined such that  $Q_{\underline{y}_a} \rightarrow \psi(\underline{y}_a)$ , we have, for [ ] in A1.6, a string of  $\tilde{\psi}$  and  $\tilde{\psi}^*$  operators at all the dummy 'times'  $\{\tau_n\}$ , with their respective  $\{V_n(\underline{y}_1 \underline{y}_2 \underline{y}_3)\}$  coefficients, as well as  $\tilde{\psi}(\underline{y}_a, \tau)$  and  $\tilde{\psi}^*(\underline{y}_b, 0)$ . Wick's theorem (20) allows this to be written as a series of products of harmonic Greens functions, and obviously we must have an even number of  $\tilde{\psi}$  and  $\tilde{\psi}^*$  for a particular  $(\underline{y}_a)$ , or the trace is zero. Going over to the frequency Greens function  $G(\underline{y}_{ab}, i\omega_n)$ , we have a series of  $\tilde{\psi}$  operators, separated by  $V$  coefficients. For each  $V(123)$  there is a term  $\beta \hbar \delta(\omega_1 + \omega_2 + \omega_3)$ , as well as the  $\delta(\underline{y}_1 + \underline{y}_2 + \underline{y}_3)$  of 1.35. There is also a term  $(-1)^n$  associated with the properties of  $T_t$  (20). It can be shown (20) that terms with more than two  $\tilde{\psi}$  for any  $(\underline{y}_a)$  disappear as  $n \rightarrow \infty$ . We can now generalise to higher order anharmonicity, and represent the series diagrammatically. If each  $V(123\dots)$  constitutes a circle, and each  $G_{aa}^H(i\omega_n)$  a line, with  $\tau$  running left to right, then some terms of the frequency Greens function are illustrated in Figure Ala. Two useful simplifications can be made. It can be shown that the  $(n!)^{-1}$  in A1.6 can be dropped if only topologically distinct diagrams are drawn (Ala ii and iii are not) and the  $Z^{-1}$  can be ignored if disconnected diagrams (e.g. Ala iv) are ignored.

From the above considerations, one can work backwards and calculate a term in  $G$  from a diagram. The diagram has thus become the manipulative tool, instead of equation A1.6. We can construct 1.53 for infinite order as follows. If  is taken to represent the full Green's function and



is taken to represent  $\hbar S(\underline{y}_{ab}, i\omega_n)$ , the vertex contribution for all connected diagrams, then 'equation' Fig. Albi is true. Thus equation 1.6 may be written as Fig. Albii, which gives for  $G(\underline{y}_{ab}, i\omega_n)$

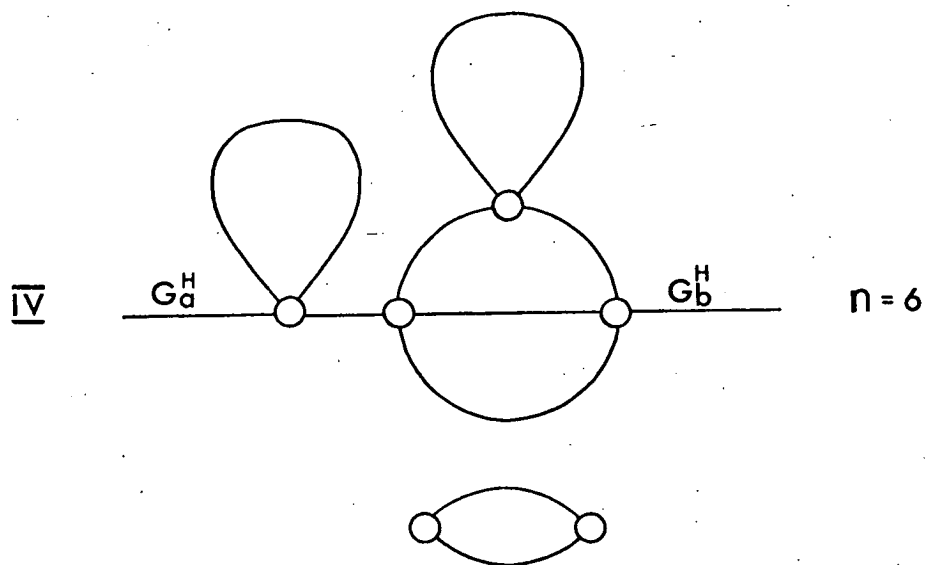
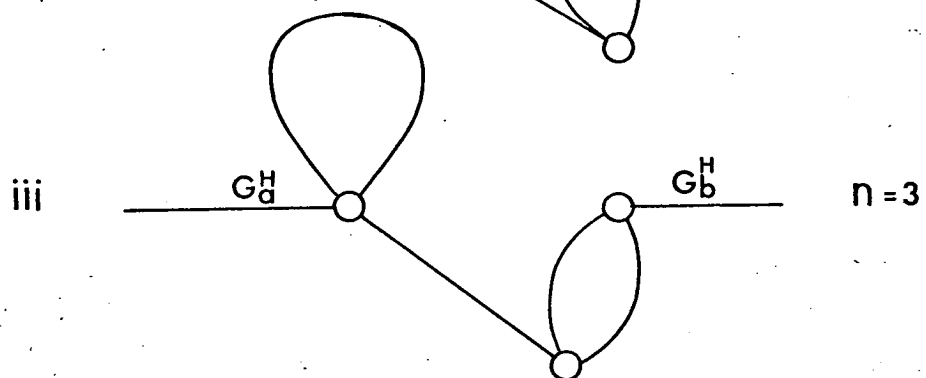
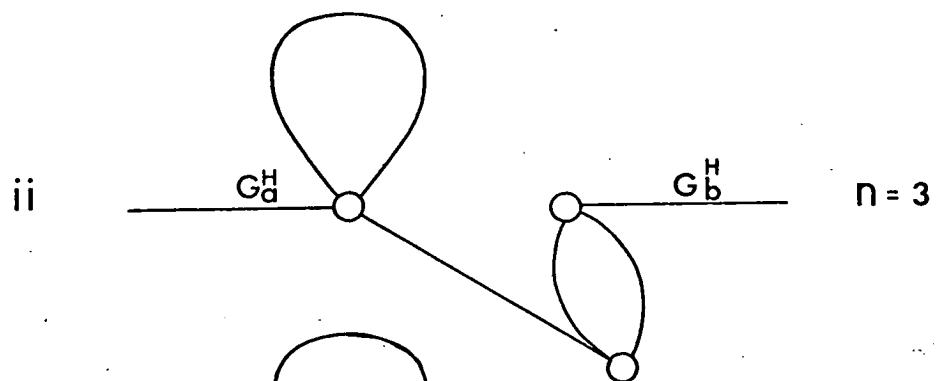
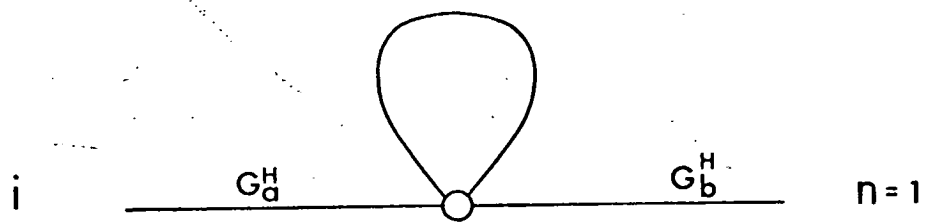
$$\begin{aligned}
 \text{Al.7} \quad G(\underline{y}_{ab}, i\omega_n) &= \delta_{ab} G_{aa}^H(\underline{y}, i\omega_n) - \sum_c \hbar G_{aa}^H(\underline{y}, i\omega_n) S(\underline{y}_{ac}, i\omega_n) G(\underline{y}_{cb}, i\omega_n)
 \end{aligned}$$

$S$  is called the (complex) self-energy. Al.7 reduces to 1.53 when  $S$  is written as  $\Delta + i\Gamma$ , and 1.51 is written for  $G^H$ . Equations Al.7 and Albv are equivalent, and are known as Dyson's equation.

FIGURE Ala: Some terms in the diagrammatic summation of the perturbation series for the frequency Greens function.

FIGURE Alb: The diagrammatic formulation of Dyson's equation for the one-phonon Greens function, equation A1.7.





i  $S$  =  $S$  +  $S G^H S$  +  $S G^H S G^H S$  + ...

ii  $G$  =  $\text{---}$  +  $\text{---}$   $\bullet$   $\text{---}$

iii =  $\text{---}$  +  $\text{---}$   $\left[ \begin{array}{l} \bullet + \bullet \text{---} \bullet \\ + \bullet \text{---} \bullet \text{---} \bullet + \dots \end{array} \right] \text{---}$

IV =  $\text{---}$  +  $\text{---}$   $\bullet$   $\left[ \begin{array}{l} \text{---} \\ + \text{---} \bullet \text{---} + \text{---} \bullet \text{---} \bullet \text{---} + \dots \end{array} \right]$

V  $G$  =  $G^H$  +  $G^H S G$

DYSON'S EQUATION

APPENDIX 2

TABLES

Tabulated values of the fitted parameters represented graphically in Chapters 3 and 4.

TABLE AIIa

The parameters of equation 2.12 for the  $167.1 \text{ cm}^{-1}$   $A_1$  mode in cubic Ni - I, with coupling to the  $76.8 \text{ cm}^{-1}$  mode.

Temperature (K)	$\omega_a \text{ (cm}^{-1}\text{)}$	$\Gamma_a \text{ (cm}^{-1}\text{)}$	$\omega_b \text{ (cm}^{-1}\text{)}$	$\Gamma_b \text{ (cm}^{-1}\text{)}$	$\Gamma_{ab}$
295	167.1	91.0	76.8	45.4	0.03
210	161.5	82.4	65.3	49.4	-21.18
165	163.1	84.0	69.8	56.5	-15.6
128	164.9	84.3	67.3	56.0	-10.3
122	157.5	84.9	64.3	55.6	-18.6
118	157.0	82.4	51.4	34.4	-40.0
115	152.2	82.9	67.2	47.4	-6.7
109	152.5	83.4	87.5	148.5	-2.1
98	152.1	81.5	61.1	51.7	-19.3
88	159.3	83.5	69.5	58.0	-16.2

TABLE AIIB

The parameters of equation 3.1 for the 655.0  $A_1$  mode in cubic Ni - I.

Temperature (K)	$\omega_0$ ( $\text{cm}^{-1}$ )	$\Gamma$ ( $\text{cm}^{-1}$ )
295	655.0	31.3
210	658.1	31.8
165	655.1	25.1
128	652.4	20.5
122	658.7	31.7
118	655.1	22.8
115	657.7	26.7
109	658.4	18.2
98	653.6	19.5
88	654.3	21.7

TABLE AIIc

The parameters of equation 3.1 for the  $1125.5 \text{ cm}^{-1}$  mode in  $Y'X'$  and  $X'X'$  polarisations.

Temperature (K)	$Y'X'$		$X'X'$	
	$\omega_0$	$\Gamma$	$\omega_0$	$\Gamma$
295	1125.5	43.2	1127.8	40.1
210	1130.3	38.9		
165	1130.8	36.9		
148	1131.1	34.6		
128	1125.8	39.4	1125.1	49.9
125	1133.8	34.6		
122	1134.4	32.3		
118	1136.0	29.1	1133.4	33.6
115	1135.6	30.4		
109	1136.1	30.4		
98	1136.2	30.5	1134.3	30.8
88	1136.0	29.0	1132.7	42.5
68	1140.0	16.9	1144.6	19.8
51	1142.0	15.2	1142.0	15.9
25	1143.8	12.0	1141.0	15.3
<7	1143.3	11.0	1144.3	8.8

TABLE AIId

The parameters of equation 2.12 for the  $863.5 \text{ cm}^{-1}$  mode in Y'X' and X'X' polarisations.

Temperature (K)	Y'X'		X'X'	
	$\omega_0$	$\Gamma$	$\omega_0$	$\Gamma$
295	863.3	15.6	863.0	15.5
210	866.1	13.6	867.2	14.0
165	866.9	13.0	865.5	16.5
148	866.3	12.1		
128	862.5	15.1	863.5	13.6
125	867.9	11.4		
122	868.3	11.3	868.8	9.3
118	869.0	10.1	867.0	10.4
115	869.0	10.8	868.5	15.3
109	869.5	11.4	867.6	11.1
98	869.7	10.9	867.3	10.5
88	869.7	10.1	868.3	14.5
73	873.9	6.8		
68	871.0	7.5	876.9*	5.2
51	872.7	6.5	872.7*	6.3
25	874.2	5.7	871.7	6.4
<7	873.9	5.7	874.3	4.8

\* - taken from poor quality spectrum.

TABLE AIIe

The parameters of equation 3.1. for the  $611.4 \text{ cm}^{-1}$  mode in Y'X' polarisation.

Temperature (K)	$\omega_0$	$\Gamma$
295	611.4	20.0
210	614.5	17.8
165	615.5	16.7
148	615.1	15.4
128	610.7	20.5
125	616.8	13.4
122	616.4	13.4
118	618.1	13.0
115	617.6	13.3
109	618.2	14.0
98	618.7	13.3
88	618.8	13.5
73	623.4	8.0
68	622.3	9.1
51	622.5	7.5
25	623.8	6.5
<7	623.0	7.3



TABLE AII f

The parameters of equation 3.1 for the  $1199.5 \text{ cm}^{-1}$  mode in Y'X' and X'X' polarisations.

Temperature (K)	Y'X'		X'X'	
	$\omega_0$	$\Gamma$	$\omega_0$	$\Gamma$
295	1199.3	73.6	1200.6	60.8
210	1204.0	57.2		
165	1204.1	66.9		
148	1203.1	51.7		
128	1201.2	60.3	1202.2	62.6
125	1207.2	46.3		
122	1206.8	44.1		
118	1207.8	37.5	1205.6	41.9
115	1207.8	42.2		
109	1208.0	41.3		
98	1208.3	43.0	1208.4	43.1
88	1208.0	44.4	1209.2	46.7
68	1210.7	21.3	1216.3	23.3
51	1213.0	16.1	1212.6	18.1
25	1213.8	13.6	1211.8	17.0
<7	1213.7	9.7	1213.7	8.25

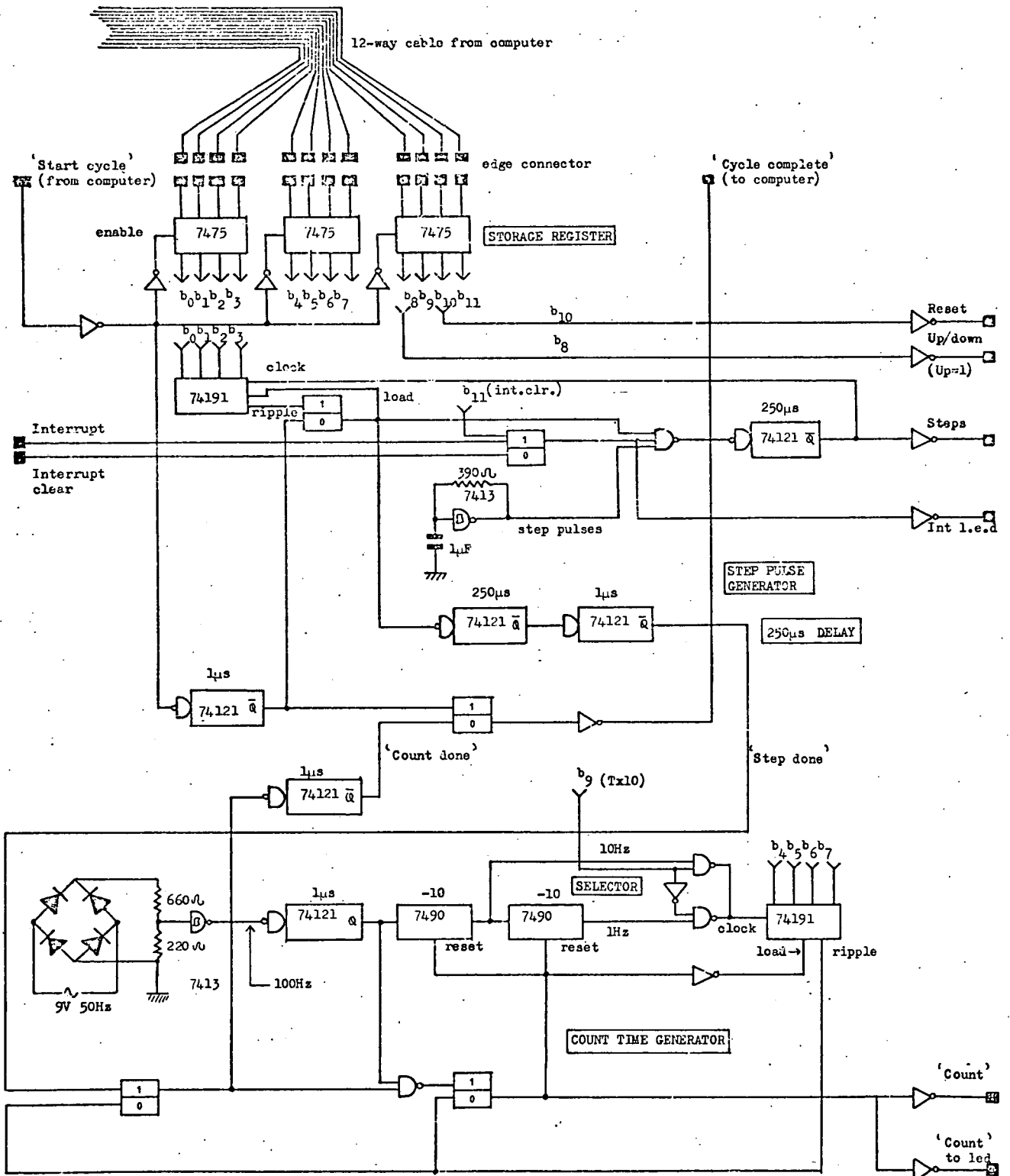
APPENDIX 3      CIRCUIT DIAGRAMS FOR THE BRILLOUIN SYSTEM

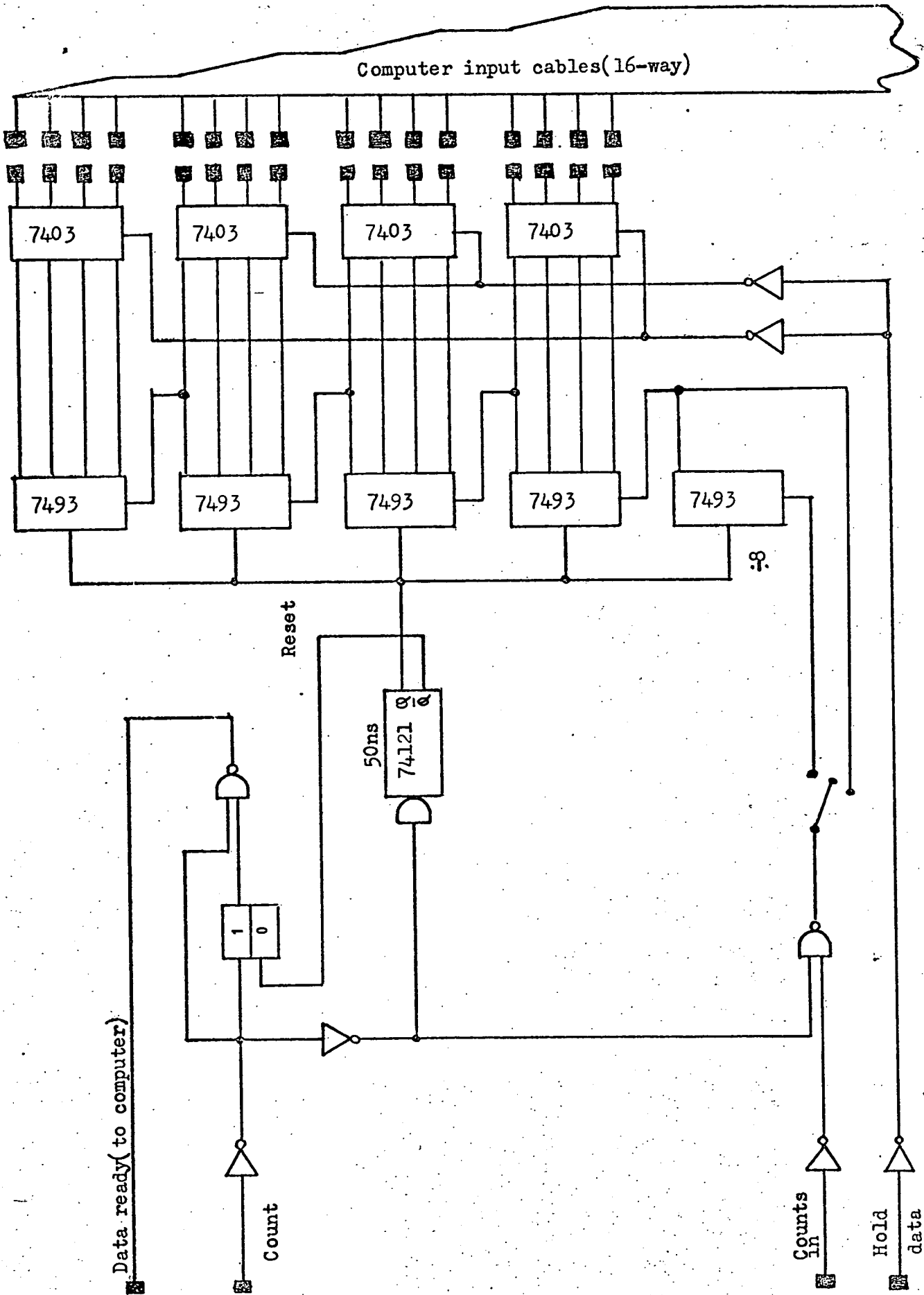
FIGURE A3a: The step control module of Figure 46.

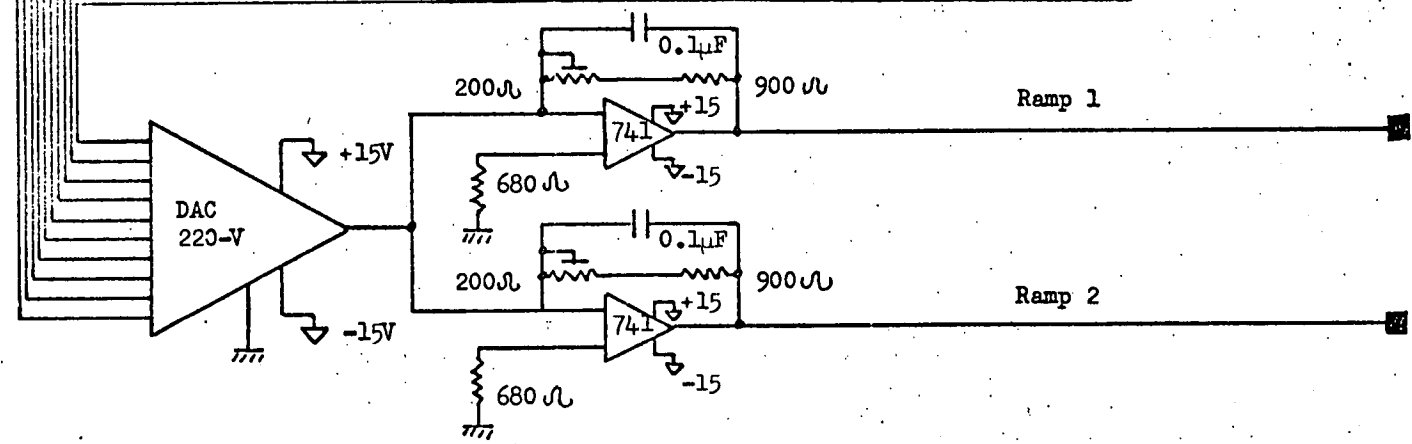
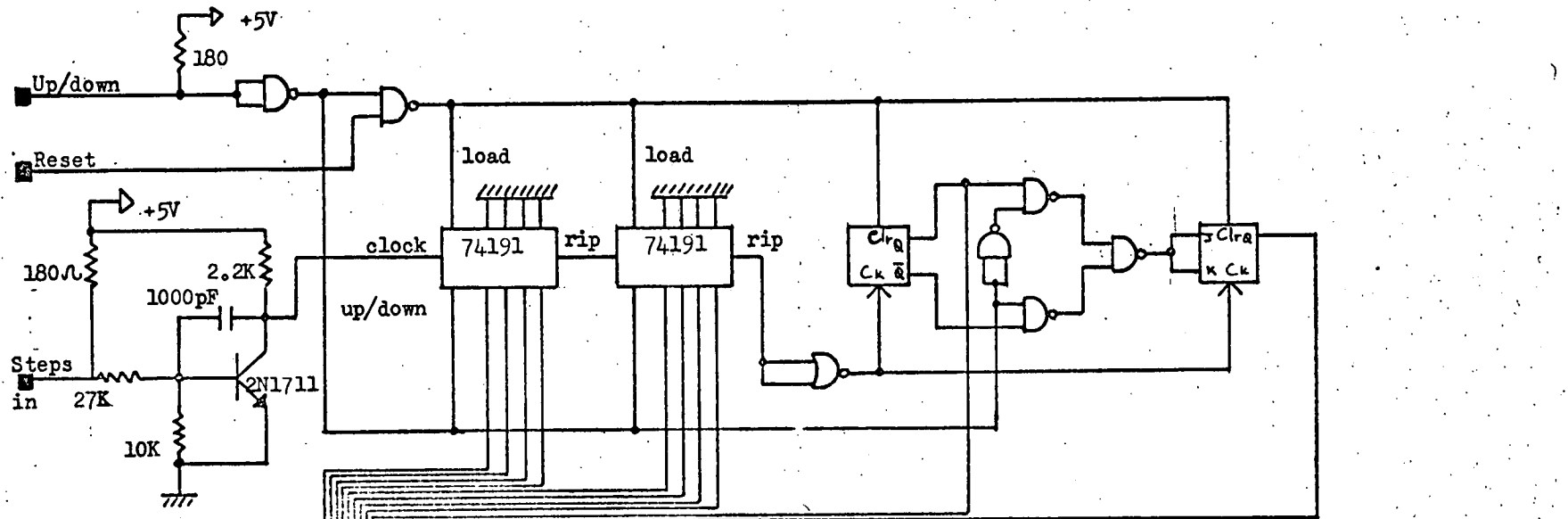
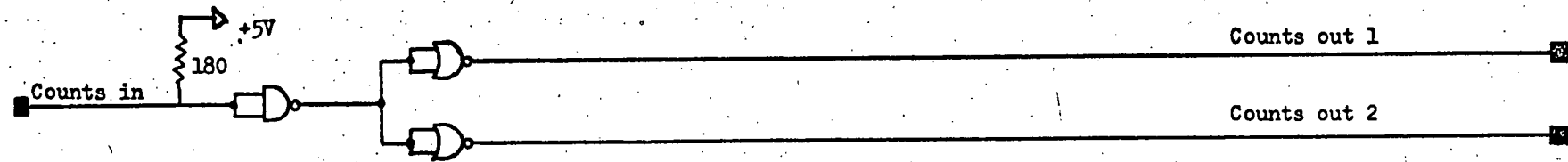
FIGURE A3b: The photon count scaler module of Figure 46.

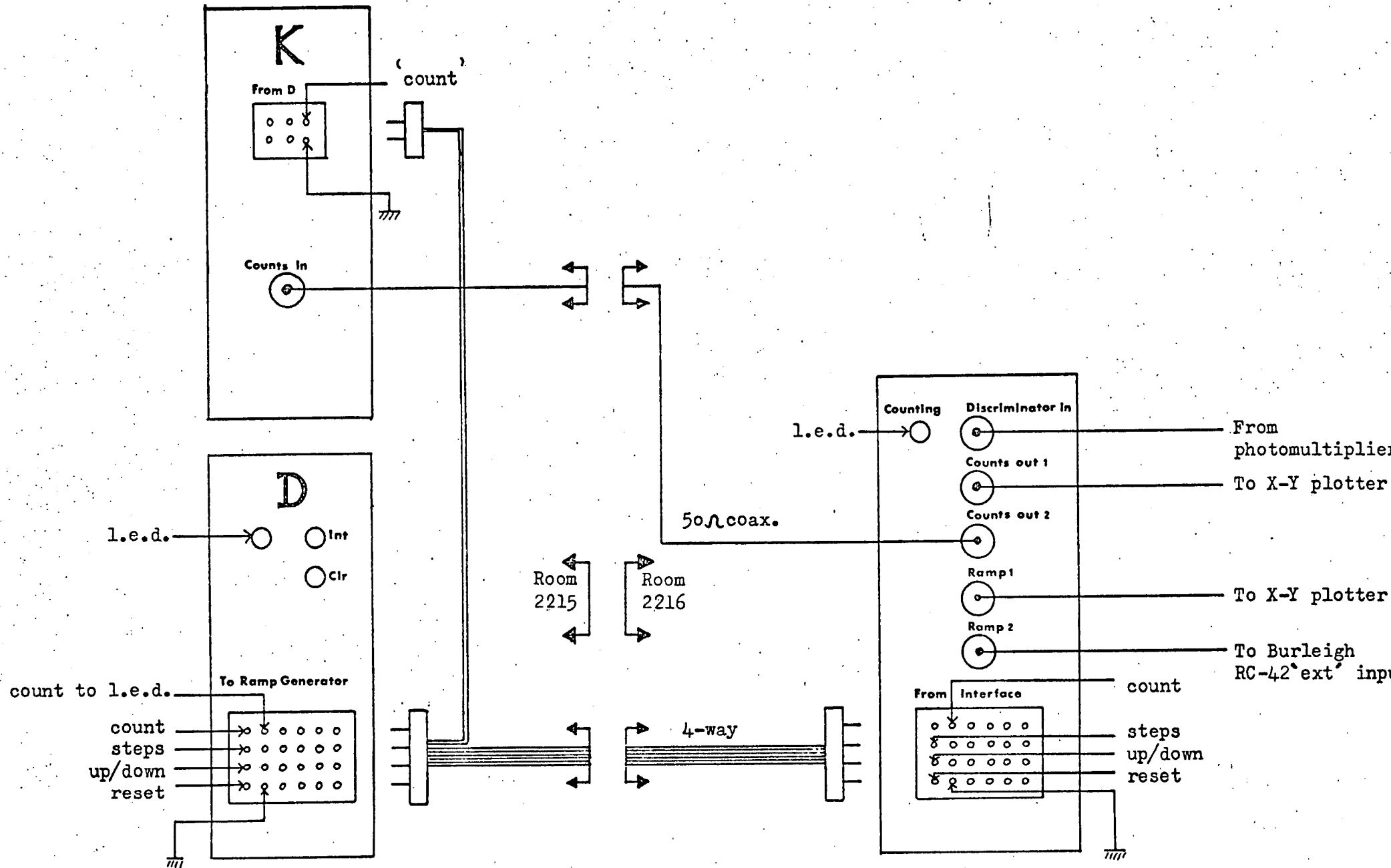
FIGURE A3c: The ramp generator module ( converts digital  
pulses to analogue voltage steps ).

FIGURE A3d: Front-panel connections of the step control (D) ,  
photon count scaler (K) and ramp generator modules.









REFERENCES

- 1) C.V. Raman and K.S. Krishnan, Indian J. Phys. 2, 387 (1928).
- 2) A. Smekal, Die Naturwiss. 11, 875 (1923).
- 3) T.H. Maiman, Nature 187, 493 (1960).
- 4) G. Plazcek, Handbuch der Radiologie 2, 209 (1934).
- 5) G. Landsberg and L. Mandelstam, Die Naturwiss. 16, 557 (1928),
- 6) J.M. Cassels, 'Basic Quantum Mechanics', (McGraw-Hill, 1970).
- 7) R.M. Loudon, 'The Quantum Theory of Light', (Clarendon, Oxford, 1973).
- 8) M. Born and K. Huang, 'Dynamical Theory of Crystal Lattices', (Clarendon, Oxford, 1954).
- 9) H. Goldstein, 'Classical Mechanics', (Addison-Wesley, 1950).
- 10) W. Cochran and R.A. Cowley, Handbuch der Physik XXV, 59 (1967).
- 11) R.H. Dicke and J.P. Wittke, 'Introduction to Quantum Mechanics', (Addison-Wesley, 1960).
- 12) J.W. Leech and D.J. Newman, 'How to use Groups', (Methuen, 1969).
- 13) R. McWeeny, 'Symmetry - an Introduction to Group Theory', Pergamon Press, 1963).
- 14) H. Montgomery, Proc. Roy. Soc. A309, 521 (1969).
- 15) R. Loudon, Adv. Phys. 13, 423 (1964).
- 16) H. Montgomery, private communication (1978).
- 17) R. Loudon, Adv. Phys. 14, 621 (1964).
- 18) W. Cochran, 'The Dynamics of Atoms in Crystals', (Arnold, 1973).
- 19) L.D. Landau and E.M. Lifshitz, 'Quantum Mechanics', (Pergamon Press, 1977).
- 20) A.A. Abrikosov, L.P. Gorkov and I.E. Dzyaloshinski, 'Methods of Quantum Field Theory in Statistical Physics', (Prentice-Hall, 1963).
- 21) R.A. Cowley, in 'Phonons in Perfect Lattices and Lattices with Point Imperfections', (Oliver & Boyd, 1966).

REFERENCES (Contd.)

- 22) T. Kinoshita, Prog. Theor. Phys. 5, 473 (1950).
- 23) J.W. Arthur, Ph.D. Thesis, University of Edinburgh (1974).
- 24) J.W. Arthur and A.F. Murray, J. Raman Spectrosc., to be published.
- 25) J.W. Arthur, J. Raman Spectrosc. 5, 9 (1976).
- 26) A.F. Murray and D.J. Lockwood, J. Phys. C. 9, 3691 (1976).
- 27) A.F. Murray and D.J. Lockwood, Proc. V Internat. Conf. on Raman Spectroscopy, Freiburg (Hans Ferdinand Schulz Verlag, 1976).
- 28) A.F. Murray and D.J. Lockwood, J. Phys. C. 11, 387 (1978).
- 29) P. Smith, S. Garcia-Blanco and L. Rivoir, Z. Kristallogr. 119, 375 (1964).
- 30) M. Martinez-Ripoll, S. Martinez-Carrera, and S. Garcia-Blanco, Acta Cryst. B27, 677 (1971).
- 31) A. Perloff and S. Block, Acta Cryst. 20, 274 (1966).
- 32) M. Marezio, J.P. Remeika and P.D. Dernier, Acta Cryst. B25, 965 (1969).
- 33) D.J. Lockwood, J. Raman Spectrosc. 2, 555 (1974).
- 34) H. Schmid, J. Phys. Chem. Solids 26, 973 (1965).
- 35) S. Terol and M.J. Otero, Z. Naturf. 16, 920 (1961).
- 36) J. Krogh-Moe, Z. Kristallogr. 117, 166 (1962).
- 37) P. Tarte, private communication (1977).
- 38) G. Herzberg, 'Molecular spectra and molecular structure', Vol. II (Litton Ed. Pub., Inc., 1945).
- 39) H.C. Urey and C.A. Bradley, Jr., Phys. Rev. 38 (1931).
- 40) H. Schmid, private communication (1976).
- 41) J.F. Scott, Phys. Rev. Lett. 21, 907 (1968).
- 42) J.F. Scott, Phys. Rev. Lett. 24, 1107 (1970).
- 43) D.L. Rousseau and S.P.S. Porto, Phys. Rev. Lett. 20, 1354 (1968).
- 44) U. Fano, Phys. Rev. 124, 1866 (1961).
- 45) R.J. Nelmes, J. Phys. C. 7, 3840 (1974).



REFERENCES (Contd.)

- 46) H. Schmid, Growth of Crystals 7, 25 (1969).
- 47) D.J. Lockwood, J-P. Rivera and H. Schmid, to be published (1978).
- 48) L.D. Landau and E.M. Lifshitz, 'Statistical Physics',  
(Pergamon Press, 1951).
- 49) E. Ascher, H. Rieder, H. Schmid and H. Stössel, J. Appl. Phys.  
37, 1404 (1966).
- 50) R.J. Nelmes and F.R. Thornley, J. Phys. C. 9, 665 (1976).
- 51) F.R. Thornley, N.S.J. Kennedy and R.J. Nelmes, J. Phys. C.  
9, 681 (1976).
- 52) G. Will and H. Morche, J. Phys. C. 10, 1389 (1977).
- 53) W. Rehwald, to be published (1978).
- 54) J. Petzelt and I. Mayerová, Czech J. Phys. B23, 1277 (1973).
- 55) A.F. Murray and D.J. Lockwood, Proc. Internat. Conf. on Lattice  
Dynamics, Paris (Flammarion, 1978).
- 56) A.F. Murray and D.J. Lockwood. J. Phys. C. 11, 2349 (1978).
- 57) E. Dormann, J. Phys. Chem. Solids 31, 199 (1970).
- 58) D.J. Lockwood, Ferroelectrics 13, 353 (1976).
- 59) D.J. Lockwood and R.W.G. Syme, Ferroelectrics (to be published, 1978).
- 60) R.J. Nelmes and F.R. Thornley, J. Phys. C. 7, 3840 (1974).
- 61) N.S.J. Kennedy, Ph.D. thesis, University of Edinburgh (1977).
- 62) R.J. Nelmes, private communication (1977).
- 63) L.D. Landau, Physik Z. Sowjetunion 11, 26 (1937).
- 64) W. Cochran in 'Structural Phase Transitions and Soft Modes'  
(Universitetsforlaget, 1971).
- 65) V. Dvůrák, Ferroelectrics 7, 1 (1974).
- 66) V. Dvůrák and J. Petzelt, Czech. J. Phys. B21, 1141 (1971).
- 67) V. Dvůrák, Czech. J. Phys. B21, 1251 (1971).

REFERENCES (Contd.)

- 68) Y.M. Gufan and V.P. Sakhnenko, Sov. Phys.-Solid State 14, 1660 (1973).
- 69) I.S. Zheludev, T.M. Perekalina, E.M. Smirnovskaya, S.S. Fonton and Yu.N. Yarmakhamedov, J.E.T.P. Lett. 20, 129 (1974).
- 70) W. von Wartburg, Phys. Stat. Sol. (a) 21, 557 (1974).
- 71) H. Schmid, H. Rieder and E. Ascher, Solid State Comm., 3, 327 (1965).
- 72) J. Kaczer, T. Shalnikova and Z. Hauptman, Czech J. Phys. B18, 734 (1968).
- 73) B.I. Alshin and L.N. Baturon, Sov. Phys. Solid State 18, 2062 (1976).
- 74) J-P. Rivera, Ferroelectrics (to be published, 1978).
- 75) D.J. Lockwood, Solid State Comm. 18, 115 (1976).
- 76) D.J. Lockwood, Ind. J. Pure Appl. Phys. (to be published, 1978).
- 77) G. Quèzel and H. Schmid, Solid State Comm. 6, 447 (1968).
- 78) A.F. Murray and D.J. Lockwood, Ferroelectrics (to be published, 1978).
- 79) A.F. Murray and D.J. Lockwood, J. Phys. C. (to be published, 1978).
- 80) J.W. Arthur and D.J. Lockwood, J. Raman Spectrosc. 2, 53 (1974).
- 81) F.A. Jenkins and H.E. White, 'Fundamentals of Optics' (McGraw-Hill, 1957).
- 82) The TTL Data book for design engineers (Texas Instruments Ltd., 1975).
- 83) The PDP11/45 processor handbook (Digital Equipment Corporation, 1971).
- 84) T.J. Hosea (private communication, 1977).
- 85) D.R. McGlynn, 'Microprocessors - Technology, Architecture and Applications,' (Wiley, 1976).
- 86) J.D. Axe, Oak Ridge Laboratory report CONF-760601-P1, 353 (1976).
- 87) R.A. Cowley and A.D. Bruce, J. Phys. C. (to be published, 1978).
- 88) A.D. Bruce, R.A. Cowley and A.F. Murray, J. Phys. C. (to be published, 1978).

REFERENCES (Contd.)

- 89) A.D. Bruce and R.A. Cowley, J. Phys. C. (to be published, 1978).
- 90) D.E. Moncton, J.D. Axe and F.J. DiSalvo, Phys. Rev. Lett. 34, 734 (1975).
- 91) W. Kohn, Phys. Rev. Lett. 2, 393 (1959).
- 92) H.A. Mook and C.R. Watson Jr., Phys. Rev. Lett. 35, 801 (1976).
- 93) M. Iizumi, J.D. Axe, G. Shirane and K. Shimaoka, Brookhaven National Laboratory report BNL-21900 (1976).
- 94) W. McMillan, Phys. Rev. B14, 1496 (1976).
- 95) P. Bak and V.J. Emery, Phys. Rev. Lett. 36, 978 (1976).
- 96) E. Eisenriegler, Phys. Rev. B9, 1029 (1974).
- 97) See for instance: R.K. Bullough, Physics Bulletin 29, No. 2 (1978).
- 98) S.C. Ying, Phys. Rev. B3, 4160 (1971).
- 99) D.W. Bechtle and J.F. Scott, J. Phys. C. 10, 1209 (1977).

APPENDIX 4

PUBLICATIONS

- (1) Raman spectrum of  $Zn_4O(BO_2)_6$   
A.F. Murray and D.J. Lockwood, J. Phys. C. 9, 3691 (1976).
- (2) Phonon coupling in zinc metaborate  
A.F. Murray and D.J. Lockwood, Proc. 5th Int. Conf. on  
Raman spectroscopy, Freiburg, 636 (1976).
- (3) Phonon coupling in  $Zn_4O(BO_2)_6$  studied by Raman spectroscopy  
A.F. Murray and D.J. Lockwood, J. Phys. C. 11, 387 (1978).
- (4) Raman spectral study of cubic Nickel-Iodine Boracite  
A.F. Murray and D.J. Lockwood, Proc. Int. Conf. on Lattice  
Dynamics, Paris, 662 (1977).
- (5) Raman spectrum of the puzzling paraelectric phase of nickel-  
iodine boracite<sup>†</sup> A.F. Murray and D.J. Lockwood, J. Phys. C. 11,  
2349 (1978).
- (6) Structural and magnetic transitions in nickel-iodine boracite:  
a light scattering study, A.F. Murray and D.J. Lockwood,  
J. Phys. C. \*
- (7) Lattice dynamics of nickel-iodine boracite, D.J. Lockwood and  
A.F. Murray, Ferroelectrics \*
- (8) The theory of structurally incommensurate systems II: commensurate-  
incommensurate phase transitions, A.D. Bruce, R.A. Cowley and  
A.F. Murray, J. Phys. C. \*
- (9) Automation techniques for spectroscopy: computer control,  
J.W. Arthur and A.F. Murray, J. Raman Spectrosc. \*

<sup>†</sup> in press, proof copy attached.

\* to be published.

# Raman spectrum of the puzzling paraelectric phase of nickel-iodine boracite

A F Murray and D J Lockwood

Physics Department, University of Edinburgh, Edinburgh EH9 3JZ, UK

Received 4 November 1977

**Abstract.** The Raman spectrum of  $\text{Ni}_3\text{B}_7\text{O}_{13}\text{I}$  is reported and the number of  $q = 0$  phonon frequencies observed is compared with the group-theoretical prediction. Anomalies in the temperature dependence of phonon lifetimes and frequencies are correlated with abnormalities in the dielectric, magnetic and structural properties at  $\approx 130$  K. The Raman spectra at temperatures from 88 K to 300 K indicate cubic symmetry. The static and temperature dependent structure of the Raman spectra are compared and contrasted with their counterparts for other boracites. It is concluded that  $\text{Ni}_3\text{B}_7\text{O}_{13}\text{I}$  is unique among boracites in many ways, at least in its cubic phase.

## 1. Introduction

Nickel-iodine boracite,  $\text{Ni}_3\text{B}_7\text{O}_{13}\text{I}$  (Ni-I) undergoes an improper first-order transition from a high-temperature paraelectric phase of cubic symmetry ( $T_0^3$ ) to a ferroelectric phase at  $T_c \approx 68$  K, with a concomitant onset of weak antiferromagnetic ordering (Schmid 1969, Nelmes 1974, Lockwood *et al* 1978). The existence of ferroelectric and ferromagnetic transitions is a characteristic of the boracite family (Nelmes 1974), that is, those compounds of the form  $\text{M}_3\text{B}_7\text{O}_{13}\text{X}$ , where M represents a divalent metal, and X a halogen or chalcogen. Of the halogen boracites studied so far by various techniques, only Ni-I has been found to exhibit a simultaneous ferroelectric magnetic transition.

Ni-I is particularly interesting, however, for reasons additional to the usual boracite improper and therefore 'coupled' phase transition, involving more than one order parameter (Nelmes 1974). These are the existence of 'growth sectors', with the attendant optical anisotropy (Schmid 1969, Nelmes and Thornley 1976b), and the anomalous dielectric, magnetic and structural properties of the cubic phase at  $T \approx 130$  K. These anomalies, illustrated in figure 1, comprise broad maxima in the magnetic and dielectric susceptibilities (Ascher *et al* 1966) and an increase of about 0.1% in the lattice constant (Will and Morche 1977).

The light-scattering study reported in this paper is concerned with the cubic phase, as a first step in understanding the dynamics of this interesting compound. It could be anticipated that some manifestation of the abnormalities in the magnetoelectric and structural properties should occur in the Raman spectrum. Such an expectation is reinforced by the existence of a broad maximum at 115 K and a broad minimum at 140 K in the elastic coefficient  $C_{44}$ , given by shear-mode measurements (W Rehwald 1977, private communication), and a minimum at 120 K, with a maximum at 150 K.

in the elastic compliance (Lockwood *et al* 1978). The phenomenon of growth sectors should present no difficulties under the experimental conditions described below, involving a single [100] growth sector, where the birefringence is barely measurable (Schmid 1969).

An infrared study of Ni-I at 300 K and 100 K (Petzelt and Mayerová 1973) provides a useful basis for comparison of  $F_2$  scattering properties. Also, the published Raman spectra of the paraelectric phases of Cr-Cl (Lockwood 1976) and Cu-Cl (Lockwood and Syme 1978) may be collated with their counterparts for Ni-I, with a view to identifying equivalent bands.

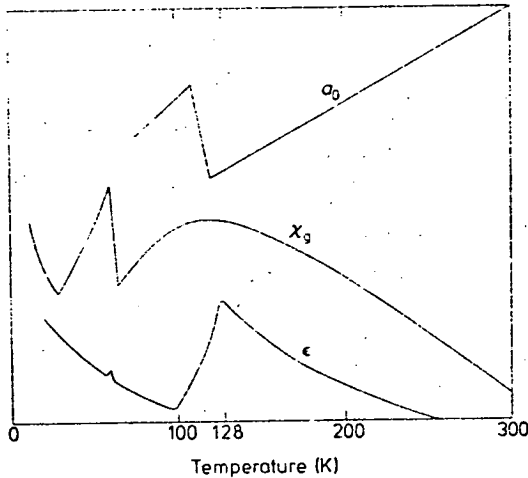


Figure 1. Temperature dependence of the dielectric ( $\epsilon$ ) and magnetic ( $\chi_g$ ) susceptibilities (Ascher *et al* 1966) and the lattice constant ( $a_0$ ) (Will and Morche 1977) of Ni-I in the cubic phase.

While the structure of the ferroelectric phase of Ni-I is not clear, the paraelectric phase has been shown to be cubic from a full structural analysis at room temperature and 77 K, by x-ray (Nelmes and Thornley 1976a, b) and neutron (Thornley *et al* 1976) diffraction respectively, and from powder diffraction studies of the lattice constant over the range 77 K to 300 K (Will and Morche 1977).

## 2. Experimental

The crystal used was the same  $^{11}\text{B}$ -enriched single crystal [100] growth sector used by Thornley *et al* (1976), supplied by Dr H Schmid, and grown by the vapour transport method (Schmid 1965). The sample formed a cuboid of dimensions  $2.2 \times 1.4 \times 0.55 \text{ mm}^3$ , these dimensions corresponding to the cubic  $\langle 110 \rangle$ ,  $\langle 1\bar{1}0 \rangle$  and  $\langle 001 \rangle$  directions respectively. Crystal faces were polished with  $1 \mu\text{m}$  diamond powder.

Ni-I appears dark green when viewed before white light, and is in fact almost opaque to all the resonant lines available from krypton and argon ion lasers. This can be confirmed from the published optical absorption spectrum (Dormann 1970). Trials showed that there is sufficient transmission for use of the 647.1 nm krypton laser line. Raman scattered light from Ni-I and other boracites is of low intensity and a photo-

multiplier tube of high sensitivity to red light is necessary to observe this. It is our experience that the RCA C31034A tube is essential for this criterion to be met. As absorption of radiation, with the corresponding heating involved, must be kept to a minimum axis of the sample proved most satisfactory. This orientation coincidentally shortest axis of the sample proved most satisfactory. This orientation coincidentally produced the strongest Raman signal. Consequently, the indices  $X'$ ,  $Y'$  and  $Z$  used to categorise scattering geometries refer to the  $\langle 110 \rangle$ ,  $\langle 110 \rangle$  and  $\langle 001 \rangle$  directions respectively.

Observation of the sample between the crossed polarisers of a polarising microscope revealed apparently negligible growth strains, a fact borne out by the conspicuous lack of mixing of spectra. There was therefore no necessity for subtraction of unwanted modes (Murray and Lockwood 1976).

Using 400 mW of the 647.1 nm krypton laser light, the  $90^\circ$  scattered radiation was dispersed by a Coderg T800 triple monochromator ( $T < 295$  K) and a Spex 1400 double monochromator ( $T = 295$  K) to a resolution of  $2.5 \text{ cm}^{-1}$  in both instruments. The scattered light was analysed with Polaroid sheet followed by a polarisation scrambler. The spectrometers were automatically controlled and data collected digitally (Arthur and Lockwood 1974, Arthur and Murray 1978). Temperature control was achieved by use of a Thor nitrogen vapour flow cryostat with a chromel-gold-iron thermocouple for temperature measurement. The laser beam was positioned as close as possible to the sample surface to maximise heat dissipation, but  $\approx 15$  K of laser heating was still detected at the thermocouple. This would seem to suggest that the temperature at the beam position was a few degrees higher than that measured by the thermocouple.

### 3. Results

A group-theoretical analysis of the zone-centre normal modes of the Ni-I structure predicts the following decomposition according to the irreducible representations of point group  $\bar{4}3m$

$$\Gamma = 4A_1 + 6A_2 + 10E + 18F_1 + 20F_2$$

of which, excluding acoustic modes,  $4A_1 + 10E + 19F_2$  should be Raman-active and  $19F_2$  infrared active.

The form of the Raman tensors (Loudon 1964) means that the  $Z(Y'Z)Y'$  spectrum contains modes of  $F_2$  symmetry (figure 2a), the  $Z(Y'X')Y'$  spectrum, modes of E symmetry (figure 2b), and the  $Z(X'X')Y'$  spectrum modes of  $A_1 + E + F_2$  symmetry (figure 2c). Subtraction of the spectrum of figure 2b from that of figure 2c with a suitable choice of scale factor reveals the  $A_1 + F_2$  spectrum (Murray and Lockwood 1976), (figure 2d). As the  $F_2$  scattering is roughly ten times weaker than the  $A_1 + E$  scattering, we have ignored its contribution to figure 2d. Subtraction is in this case quite impossible, no suitable 'scaling mode' being present. The resultant spectra are described below.

#### 3.1. The $A_1$ spectrum

This spectrum exhibits a Debye-like wing feature, common to all boracites (Lockwood 1976, Lockwood and Syme 1978) but less pronounced in this case, its influence on the cross-section being negligible beyond  $\approx 100 \text{ cm}^{-1}$ . There is a broad feature centred on  $\approx 154 \text{ cm}^{-1}$  with an indistinct but non-negligible broad feature peaking at  $100 \text{ cm}^{-1}$ .

Over the rest of the frequency range studied only two further discrete peaks are visible at  $378\text{ cm}^{-1}$  and  $655\text{ cm}^{-1}$ , with some structure in the  $900\text{--}1400\text{ cm}^{-1}$  range.

### 3.2. The E spectrum

This spectrum resembles the  $A_1$  spectrum in the region  $0\text{--}300\text{ cm}^{-1}$ , having a similar Debye-like wing, with broad modes peaking at  $160$  and  $84\text{ cm}^{-1}$ . There are, in addition, three discrete, isolated bands and a pair of high-frequency modes, characteristic of a cubic boracite.

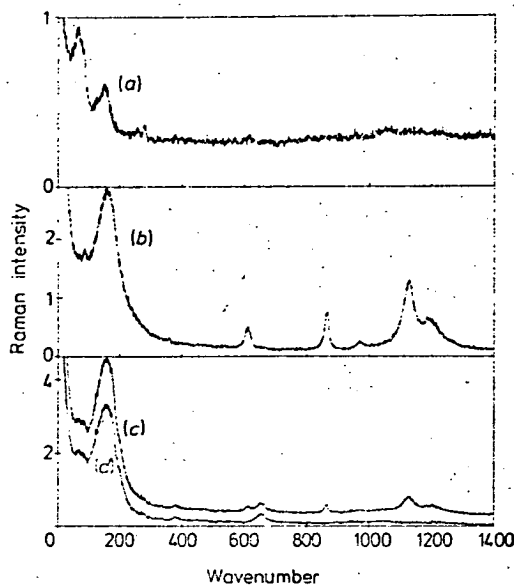


Figure 2. The room temperature Raman spectra of Ni-I in the different scattering geometries: (a)  $Z(Y'Z)Y'$ ,  $F_2$  modes; (b)  $Z(Y'X')Y'$ , E modes; (c)  $Z(X'X')Y'$ ,  $A_1 + E + F_2$  modes; (d) Subtracted spectrum (see §3),  $A_1 + F_2$  modes. N.B. The ordinate calibration is given in units of  $\text{counts s}^{-1} \div 80$ .

### 3.3. The $F_2$ spectrum

The scattering of  $F_2$  symmetry is very weak. Again, a narrow Debye wing feature is present, with an oddly shaped scattering profile below  $200\text{ cm}^{-1}$ , comprising apparently two bands, plus two very weak bands at  $255\text{ cm}^{-1}$  and  $280\text{ cm}^{-1}$ . It is impossible to decide at this stage whether the broad structure around  $600\text{ cm}^{-1}$  and  $1000\text{--}1200\text{ cm}^{-1}$  is a result of some superposition of weak first-order bands or of second or higher order. The  $Z(Y'Z)Y'$  spectrum contains TO and LO features, the  $Z(X'Z)Y'$  spectrum differing only in the absence of LO modes.

In table 1 the frequencies and linewidths (where appropriate) are presented for Ni-I at room temperature, along with the results of the infrared investigation at  $300\text{ K}$  (Petzelt and Mayerová 1973).

In figures 3 and 4 we present a selection of spectra of E and  $A_1$  symmetries respectively, recorded at various temperatures. From a visual scrutiny of these figures it is apparent that no change in the composition of the spectrum occurs as the temperature is varied



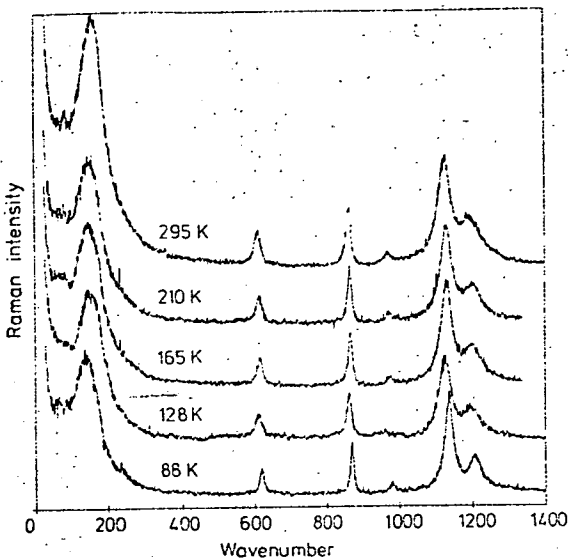


Figure 3. The E symmetry Raman spectrum of Ni-I at different temperatures.

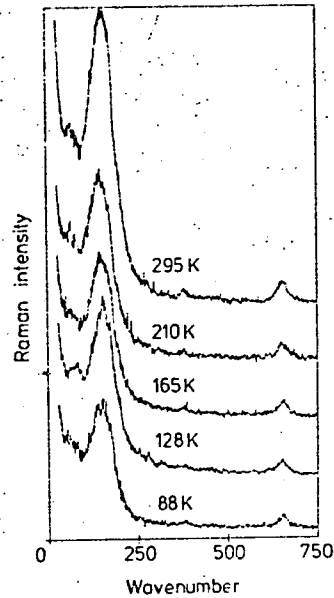


Figure 4. The  $A_1 (+ F_2)$  symmetry Raman spectrum of Ni-I at different temperatures.

from 295 K to 88 K. The only obvious modification to the scattering cross-section is a sharpening of the peaks. A computer fitting procedure proved essential in order that the true behaviour of the Raman spectrum as a function of temperature could be explored. The  $F_2$  spectrum was studied over the region  $0-300\text{ cm}^{-1}$  at temperatures between 88 K and 300 K but the signal-attenuating effects of cryostat windows rendered the results too weak for detailed analysis.

Table 1. Resonant frequencies  $\omega_0(\text{cm}^{-1})$ , damping parameters  $\Gamma(\text{cm}^{-1})$  and assignments for the Raman-active modes and frequencies for the infrared-active modes (Peizelt and Mayerová 1973) of Ni-I.

$A_1$		E		$F_2$		$F_2$ (infrared)	
$\omega_0$	$\Gamma$	$\omega_0$	$\Gamma$	$\omega_0$	$\Gamma$	$\omega_0^{T^0}$	$\omega_0^{b^0}$
81.5	61	84.5	35	74.5	48	42	42
163.5	76	170.0	90	152.5	42	54	70
378.0 <sup>a</sup>	18 <sup>a</sup>	611.5	20	255.0	b	89	91
655.0	30	863.5	15	280.0		112	114
		943.0	36			135	136
		1125.5	43			168	168
		1199.5	74			195	198
						224	226
						258	286
						308	308
						320	322

All  $\omega_0$  and  $\Gamma$  are from computer fits except:

<sup>a</sup> Measured from spectrum;

<sup>b</sup> Measured from spectrum and too weak for assignment of  $\Gamma$ .

#### 4. Analysis of results

As mentioned in §3, a computer least-squares fitting procedure was used to investigate the temperature variation of the Raman spectra. Discussion of this procedure benefits from a segregation of the spectra into low-frequency (0–300  $\text{cm}^{-1}$ ) and high-frequency (300–1400  $\text{cm}^{-1}$ ) regions.

##### 4.1. The high-frequency spectra

The peaks in the high-frequency spectra may each be represented by the response function

$$G(\omega) = \frac{S\Gamma\omega}{(\omega_0^2 - \omega^2)^2 + \Gamma^2\omega^2}$$

where  $\omega_0$  represents the resonant frequency,  $\Gamma$  the damping constant and  $S$  the oscillator strength. Incorporating the appropriate thermal weighting factor, the parameters  $\omega_0$  and  $\Gamma$  for several E modes and the 655  $\text{cm}^{-1}$   $A_1$  mode were obtained. These are presented in figures 5 and 6 respectively.

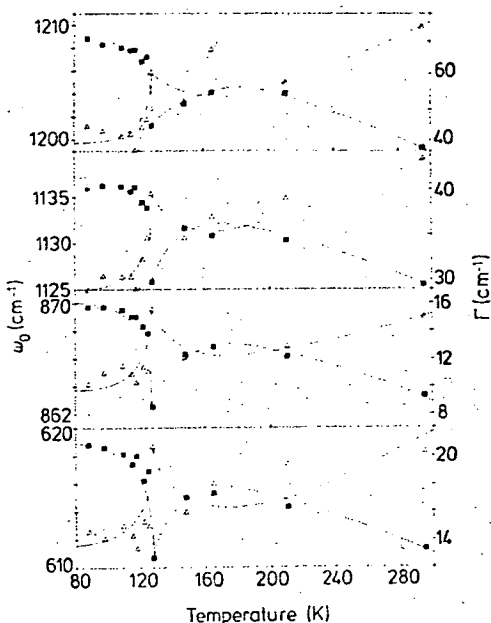


Figure 5. Temperatures variation of the resonant frequency  $\omega_0$  (squares) and damping  $\Gamma$  (triangles) of some E symmetry modes of Ni-I. The lines are intended merely as a guide to the eye.

##### 4.2. The low-frequency spectra

The model response function in this case proves more problematic. Firstly, a Debye-like wing feature with response function

$$G(\omega) = \frac{S\omega}{\omega^2 + \gamma^2}$$

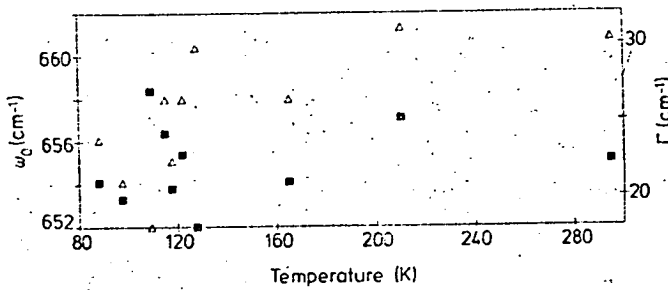


Figure 6. Temperature variation of the resonant frequency  $\omega_0$  (squares) and damping  $\Gamma$  (triangles) of the  $655.0 \text{ cm}^{-1} A_1$  symmetry mode.

must be added to two functions of the form presented in §4.1, where  $S$  is again a strength parameter and  $\gamma$  a width. The resultant function, when fitted to the observed data, produced the fitted profiles represented by the smooth curves in figure 7 and the parameters for the E and  $A_1$  spectra presented in figures 8 and 9.

Secondly, if coupling is presumed to occur between the low-frequency modes, an inverse response function having matrix form

$$g^{-1}(\omega) = \begin{bmatrix} \omega_1^2 - \omega^2 + i\Gamma_1\omega & i\gamma\omega \\ i\gamma\omega & \omega_2^2 - \omega^2 + i\Gamma_2\omega \end{bmatrix}$$

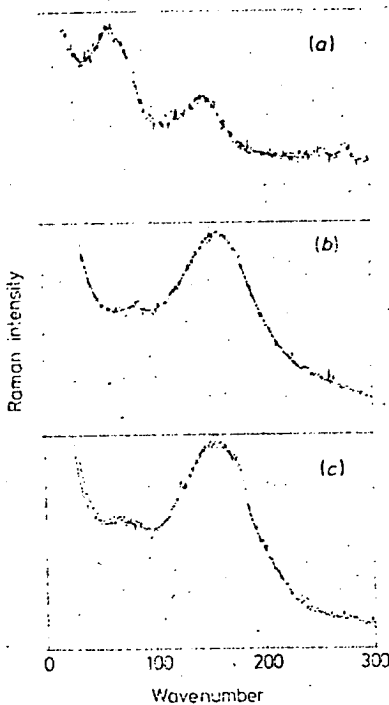


Figure 7. The low-frequency spectra of Ni-I with theoretical fits (smooth lines) in terms of two oscillators plus a Debye-like wing (a)  $F_2$  symmetry; (b) E symmetry; (c)  $A_1(+F_2)$  symmetry.

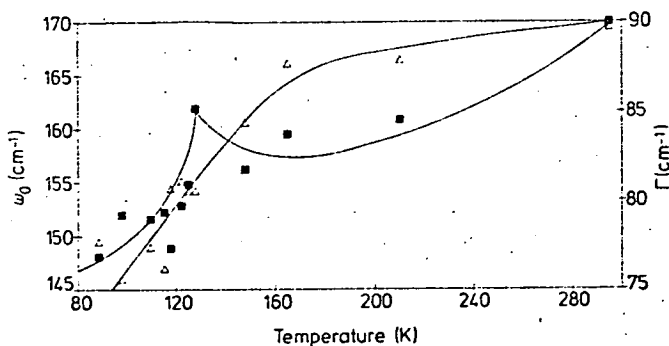


Figure 8. Temperature variation of the resonant frequency  $\omega_0$  (squares) and damping  $\Gamma$  (triangles) of the  $170.0 \text{ cm}^{-1}$  E symmetry mode. The lines are intended merely as a guide to the eye.

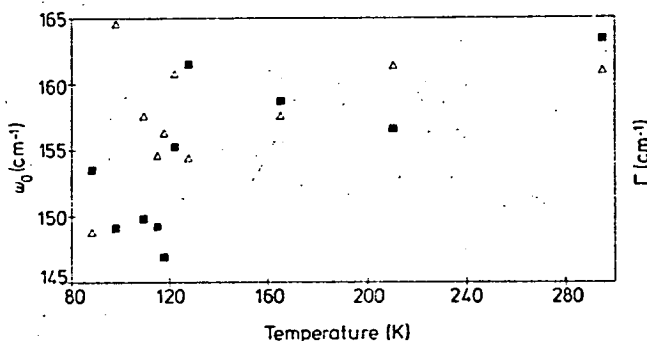


Figure 9. Temperature variation of the resonant frequency  $\omega_0$  (squares) and the damping  $\Gamma$  (triangles) of the  $163.5 \text{ cm}^{-1}$  A $_1$  symmetry mode.

must be postulated, having a response function given by

$$G(\omega) = \sum_{i,j} S_i S_j g_{ij}(\omega).$$

The motivation for such an ansatz comes from the poor agreement between the observed and calculated lineshapes in the A $_1$  and F $_2$  symmetries (figures 7a and c). In fact, coupling did not improve the fitted description of the data and, in some cases, produced considerably poorer fits.

#### 4.3. Errors

As the channel width for all the spectra was  $1 \text{ cm}^{-1}$ , an estimated error in  $\omega_0$  of  $\pm 0.5 \text{ cm}^{-1}$  seems reasonable, in agreement with the uncertainty values calculated by the fitting routine. Fitted values of  $\Gamma$  are accurate to approximately  $\pm 1 \text{ cm}^{-1}$ . These errors are not incorporated in the diagrams for reasons of clarity.

## 5. Discussion

### 5.1. Classification of room temperature modes

From table 1 it is evident that, while the correct number of A $_1$  symmetry bands are present, there is a dearth of both E and F $_2$  peaks. There are seven E peaks clearly visible

along with, we suspect, a very weak feature around  $360\text{ cm}^{-1}$  (see discussion below). This is a shortfall of two upon the predicted ten E modes. The most serious deficiency occurs in the  $F_2$  symmetry, where only four peaks are found, the bracketed pair in table 1 being a TO-LO pair. This assertion is confirmed by comparison of the Raman frequencies at  $255.0\text{ cm}^{-1}$  and  $280.0\text{ cm}^{-1}$  with the infrared peaks at  $258\text{ cm}^{-1}$  (TO) and  $286\text{ cm}^{-1}$  (LO). The infrared spectra also indicate that the  $F_2$   $0-300\text{ cm}^{-1}$  spectrum does not merely compromise two peaks, and is far more complex than it appears at first sight (see table 1). This would account for the peculiar low-frequency line profile in figure 2(a).

Some clue as to the whereabouts of 'missing' bands can be gained from a comparison of the  $BO_4$  molecular vibration frequencies obtained by fitting a generalised force field model for  $XY_4$  molecules (Urey and Bradley 1931) to the vibrational frequencies of  $Zn_4O(BO_2)_6$  and Cr-Cl (Murray and Lockwood 1976). These frequencies should be relatively insensitive to change of halogen or metal in the boracite formula, as such a change does not drastically disturb the B-O framework (Nelmes 1974, Nelmes and Thornley 1974). Comparison with Cr-Cl and  $Zn_4O(BO_2)_6$  results suggest that the  $378\text{ cm}^{-1}$  ( $A_1$ ) and  $255\text{ cm}^{-1}$  ( $F_2$ ) modes can be associated with B-O framework vibrations. Furthermore, the existence of vibrations at frequencies around  $300\text{ cm}^{-1}$  (E) and  $1100\text{ cm}^{-1}$  ( $F_2$ ) is suggested by this comparison. This would reinforce the presence of an E band at about  $360\text{ cm}^{-1}$  and support the notion that the structure around  $1100\text{ cm}^{-1}$  alluded to in §3.3 contains first-order peaks. The comparable modes in Cr-Cl are at  $375\text{ cm}^{-1}$  ( $A_1$ ),  $232\text{ cm}^{-1}$  (E) and  $1160\text{ cm}^{-1}$ ,  $252\text{ cm}^{-1}$  ( $F_2$ ) (Murray and Lockwood 1976) and in Cu-Cl at  $385\text{ cm}^{-1}$  ( $A_1$ ),  $239\text{ cm}^{-1}$  (E) and  $1167\text{ cm}^{-1}$ ,  $264\text{ cm}^{-1}$  ( $F_2$ ) (Lockwood and Syme 1978). The insensitivity to metal substitution is clearly demonstrated.

The low-frequency modes in all spectra are more heavily damped than their counterparts in Cr-Cl and Cu-Cl, particularly in the E symmetry, where the damping is roughly ten times greater for Ni-I. The lowering of frequencies from Cr-Cl and Cu-Cl to Ni-I produces a low-frequency total cross-section of great complexity, which may contribute to the shortening of the phonon lifetimes, and consequently higher damping. The frequency lowering also confirms that these vibrations are largely attributable to motions of the metal and halogen ions, in particular the latter.

The  $A_1$  Debye wing is considerably narrower than in Cr-Cl and Cu-Cl, where the wing was conjectured as being due to disorder (Lockwood 1976). X-ray structural studies have shown that this disorder, if extant, is associated mainly with the Cl ion, being most obvious in Cu-Cl, and corresponds to a displacement of the halogen ions along the [111] axes (Nelmes and Thornley 1974, Kennedy 1977). The Raman results for Ni-I suggest that any disorder is much less than in Cl boracites, in accord with structural results for cubic Cr-Cl, Cu-Cl, and Ni-I (Nelmes and Thornley 1974, 1976a, b, Thornley *et al* 1976, Kennedy 1977). In addition, the Ni-I spectra contain a Debye wing in the E and  $F_2$  symmetries, suggesting that the disorder lack definite symmetry, and is consequently more homogeneous than in Cl boracites, where no such wing was observed.

From the fitted spectra in figure 7 it is apparent that the A and  $F_2$  low-frequency spectra are not adequately described by the model of §4.2. In the case of  $F_2$  symmetry this is undoubtedly due to the complexity of the low-frequency  $F_2$  lineshape revealed by the infrared results (Petzelt and Mayerová 1973). Inspection of the two-mode fit of figure 7(a) suggests, in fact, the presence of at least four bands. In the  $A_1$  spectrum, where the numbers of observed and predicted modes agree, such an explanation is not valid. As the coupled mode analysis described in §4.2 did not improve the fits, the additional

structure must be due to the small admixture of  $F_2$  modes introduced by the form of the Raman tensors.

### 5.2. Temperature dependence of the modes

The normal behaviour of the parameters  $\omega_0$  and  $\Gamma$  as temperature is decreased consists of a steady rise in  $\omega_0$  with a drop in  $\Gamma$ , as the lattice contracts and anharmonic effects reduce. From figure 5 it can be seen that this behaviour is interrupted by an anomalous decrease in  $\omega_0$  and increase in  $\Gamma$  for the high-frequency E modes around 128 K. In figure 6 a similar effect is observed for the  $655\text{ cm}^{-1}$   $A_1$  feature, although its proximity to the  $611.5\text{ cm}^{-1}$  E mode made fitting less exact. This unusual phenomenon suggests that, in agreement with the x-ray work of Will and Morche (1977), the unit cell dimension expands and contracts again over the interesting temperature region.† The calibration of the Raman spectra can be verified by studying the laser frequency, the krypton emission lines, and the duplication of E-symmetry peaks in the  $Z(X'X')Y'$  and  $Z(Y'X')Y'$  spectra.

The low-frequency modes behave even more oddly. Figures 8 and 9 reveal frequency  $\omega_0$  falling with decreasing temperature, with an anomalous rise at 128 K, and the damping  $\Gamma$  decreasing more or less smoothly with decreasing temperature. Again, the parameters for the  $A_1$  symmetry mode are more scattered due to the subtraction process, and are possibly somewhat unreliable due to the underlying  $F_2$  component. Firstly, however, it can be gleaned from figures 8 and 9 that some disturbance in the lattice occurs at around 128 K. Secondly, the  $\approx 20\text{ cm}^{-1}$  (E) and  $\approx 15\text{ cm}^{-1}$  ( $A_1$ ) mode softenings are completely uncharacteristic of boracite behaviour. This can be seen from the Cr-Cl and Cu-Cl spectra where only the  $A_1$  Debye wing has strong temperature dependence, the other modes behaving normally. Such a softening is usually precursive to a displacive phase transition. Since the low-frequency modes can be attributed largely to motions of the Ni and I atoms as described in § 5.1, a transition to a phase with these atoms repositioned seems likely at some low temperature, in addition to the known 68 K transition (Murray and Lockwood 1978).

## 6. Conclusion

The Raman spectrum of Ni-I displays reasonable agreement with group theoretical predictions, considering the highly absorptive nature of the material, and indicates a cubic space group from 88 K to 300 K. The anomalies in the frequencies and linewidths of the Raman bands must be associated with the irregularities in the magnetic and dielectric properties. These anomalies are also consistent with the expansion of the lattice at around 128 K. The dielectric response is especially related to the  $F_2$  modes and no useful

† Note that our results do not agree with Will and Morche (1977) with regard to the temperature dependence of thermal motion. They report an overall increase in thermal motion from room temperature to 77 K, and quote in support the results of von Wartburg (1974) which have subsequently been shown, conclusively, to be incorrect by Thornley *et al* (1976). The latter authors find that all thermal amplitudes decrease from room temperature to 77 K, in accord with the normal temperature dependence of  $\omega_0$  and  $\Gamma$  (apart from the anomaly around 128 K) found by us. The x-ray powder-diffraction technique used by Will and Morche (1977) is likely to yield unit cell dimensions much more accurately than it yields thermal parameters (R J Nemes, private communication).

predictions concerning dielectric variations can be obtained from our weak  $F_2$  spectra. Such information should, however, result from an exhaustive infrared study of cubic Ni-I.

Our Raman results have confirmed the puzzling temperature dependent behaviour of Ni-I. The dielectric and magnetic susceptibility data suggests a phase transition but we find no evidence of this. All modes shift anomalously as temperature is lowered through 128 K, but the crystal subsequently exhibits 'normal' temperature dependence, and remains firmly cubic throughout. This is very strange phenomenon, of which there is as yet no explanation. The interesting dynamic changes occur in the low-frequency boracite spectra. This region for Ni-I contains many modes, and the complex interatomic interactions which are required to explain the observed temperature dependence cannot be determined from the Raman spectra alone. There is a need for further lattice dynamical studies using inelastic neutron scattering and infrared spectroscopy together with more detailed structural studies.

Work is in-progress to investigate further both the unusual  $A_1$  and E mode softening and the dynamics of the ferroelectric transition.

#### Acknowledgments

We are grateful to Dr H Schmid for invaluable discussions on the physical properties of boracites and to Dr R J Nelmes for discussions on structural aspects of Ni-I. This work was supported by the SRC (AFM), the Battelle Research Centre, Geneva, and the US Army Research and Development Group (Europe) (DJL).

#### References

- Arthur J W and Lockwood D J 1974 *J. Raman Spectrosc.* **2** 53-69  
 Arthur J W and Murray A F 1978 to be published  
 Ascher E, Rieder H, Schmid H and Stössel H 1966 *J. Appl. Phys.* **37** 1404-5  
 Dormann E 1970 *J. Phys. Chem. Solids* **31** 199-214  
 Kennedy N S J 1977 *PhD thesis* University of Edinburgh  
 Lockwood D J 1976 *Ferroelectrics* **13** 353-4  
 Lockwood D J, Rivera J-P and Schmid H 1978 to be published  
 Lockwood D J and Syme R W G 1978 *Ferroelectrics* to be published  
 Loudon R 1964 *Adv. Phys.* **13** 423-82 (erratum **14** 621)  
 Murray A F and Lockwood D J 1976 *J. Phys. C: Solid St. Phys.* **9** 3691-700  
 — 1978 *Ferroelectrics* to be published  
 Nelmes R J 1974 *J. Phys. C: Solid St. Phys.* **7** 3840-54  
 Nelmes R J and Thornley F R T 1974 *J. Phys. C: Solid St. Phys.* **7** 3855-74  
 — 1976a *J. Phys. C: Solid St. Phys.* **9** 655-80  
 — 1976b *Ferroelectrics* **13** 355-6  
 Petzelt J and Mayerová I 1973 *Czech. J. Phys.* **B 23** 1277-80  
 Schmid H 1965 *J. Phys. Chem. Solids* **26** 973-88  
 — 1969 *Growth of Crystals* Vol 7 (New York: Consultants Bureau) pp 25-52  
 Thornley F R T, Kennedy N S J and Nelmes R J 1976 *J. Phys. C: Solid St. Phys.* **9** 681-92  
 Urey H C and Bradley C A 1931 *Phys. Rev.* **38** 1969-78  
 von Wärtburg W 1974 *Phys. Stat. Solidi (a)* **21** 557-68  
 Will G and Morche H 1977 *J. Phys. C: Solid St. Phys.* **10** 1389-94

# Phonon coupling in $\text{Zn}_4\text{O}(\text{BO}_2)_6$ studied by Raman spectroscopy

A F Murray and D J Lockwood

Department of Physics, University of Edinburgh, Edinburgh EH9 3JZ, Scotland

Received 9 August 1977

**Abstract.** The Raman spectrum of cubic zinc metaborate contains an interference feature at  $122.5\text{ cm}^{-1}$  in both the  $A_1$  and E symmetries. The lineshape is analysed using models involving either the interaction between a one-phonon state and a continuum of multi-phonon states, or anharmonic coupling between one-phonon states. Both models describe the results adequately, but the former is preferred on theoretical grounds.

## 1. Introduction

Evidence of strong coupling between phonon excitations in solids has been reported in numerous materials such as  $\text{BaTiO}_3$  (Rousseau and Porto 1968), quartz (Scott 1968) and  $\text{AlPO}_4$  (Scott 1970). Coupling is most commonly observed when a soft mode associated with a phase transition overlaps in frequency another phonon of the same symmetry as a result of a change in pressure or temperature. Resonant interference has only rarely been observed (e.g.  $\text{SiO}_2$  and  $\text{AlPO}_4$ ). We have measured the room temperature Raman spectrum of cubic zinc metaborate and have recorded an interference feature of this type at  $122.5\text{ cm}^{-1}$ . We describe in this paper the analysis of the resultant Raman cross section in terms of two distinct models.

The first model, outlined in section two, was developed by Fano (1961) to describe the phase shifts in atomic state wavefunctions, and the corresponding excitation spectra, due to the configuration interaction between a discrete state and a continuum of states (or a number of continua). This interaction produces asymmetric peaks in the continuous absorption spectra of atomic or molecular systems. We have used this formalism to describe the Raman spectral lineshape due to interaction between a well defined phonon and a broad second or higher-order background.

The second model involves coupling, via anharmonic terms in the crystal Hamiltonian, of two phonons. This predicts a lineshape similar to that observed in  $\text{Zn}_4\text{O}(\text{BO}_2)_6$  when the lifetime of one of the phonons is much greater than that of the other (see for instance Cowley 1966). The details of this model are outlined in section three.

We compare the results of two different applications of the Fano model, involving different assumptions, and the application of the coupled oscillator model, in §4.

## 2. The Fano model

Strictly, this model describes the lineshape due to a discrete state which decays only into



the continuum. This means that the configuration interaction is wholly responsible for the finite lifetime of the state.

If we represent the discrete state by  $|p\rangle$ , the continuum states by  $\{|\psi_E\rangle\}$ , and the perturbed wavefunction of eigenvalue  $E$  by  $|\phi_E\rangle$ , we wish to study  $\sigma_1(E)$ , the scattering cross section for transitions from initial state  $|i\rangle$  to final state  $|\phi_E\rangle$ , which for a transition operator component  $\alpha_{xy}$ , is proportional to  $|\langle\phi_E|\alpha_{xy}|i\rangle|^2$ . With the following definitions in terms of total Hamiltonian  $H$ ,

$$H|p\rangle = E_p|p\rangle, \quad (2.1)$$

$$\langle\psi_E|H|p\rangle = V_E, \quad (2.2)$$

$$\langle\psi_{E'}|H|\psi_{E''}\rangle = E'\delta(E' - E''), \quad (2.3)$$

it can be shown that

$$|\langle\phi_E|\alpha_{xy}|i\rangle|^2 = |\langle\psi_E|\alpha_{xy}|i\rangle|^2 \left( \frac{\langle\tilde{p}|\alpha_{xy}|i\rangle}{\pi V_E^* \langle\psi_E|\alpha_{xy}|i\rangle} + \frac{E - E_0}{\pi |V_E|^2} \right)^2 \left[ 1 + \left( \frac{E - E_0}{\pi |V_E|^2} \right)^2 \right]^{-1}, \quad (2.4)$$

where

$$|\tilde{p}\rangle = |p\rangle + P \int V_{E'} |\psi_{E'}\rangle dE' / (E - E'), \quad (2.5)$$

$$E_0 = E_p + P \int |V_{E'}|^2 dE' / (E - E') \quad (2.6)$$

and  $P$  denotes 'principal part'.

Writing

$$q = \frac{\langle\tilde{p}|\alpha_{xy}|i\rangle}{\pi V_E^* \langle\psi_E|\alpha_{xy}|i\rangle} \quad (2.7)$$

and

$$\frac{E - E_0}{\pi |V_E|^2} = \frac{\omega - \omega_0}{\frac{1}{2}\Gamma} \quad (2.8)$$

the cross section ( $\sigma_1$ ) for scattering to the perturbed state of energy  $E$  in terms of the cross section ( $\sigma_0$ ) for scattering to the unperturbed state  $|\psi_E\rangle$  is given by

$$\sigma_1(\omega) = \sigma_0(\omega) \left( q + \frac{\omega - \omega_0}{\frac{1}{2}\Gamma} \right)^2 \left[ 1 + \left( \frac{\omega - \omega_0}{\frac{1}{2}\Gamma} \right)^2 \right]^{-1}. \quad (2.9)$$

Some of the family of curves defined by this function are plotted in figure 1. Fano (1961) has shown that when more than one continuum of states is present, the scattering cross section may be written as

$$\sigma(\omega) = \sigma_1(\omega) + \sigma_2(\omega), \quad (2.10)$$

where  $\sigma_2(\omega)$  corresponds to the underlying noninteracting continuum, and  $\sigma_0(\omega)$  is redefined as one linear combination of the continua.

### 3. Coupled modes

The application of one phonon Green function techniques to the analysis of coupling

between optical phonons is now commonplace (e.g. Cowley 1966, Scott 1971). Only the briefest survey need be given here to define the notation used.

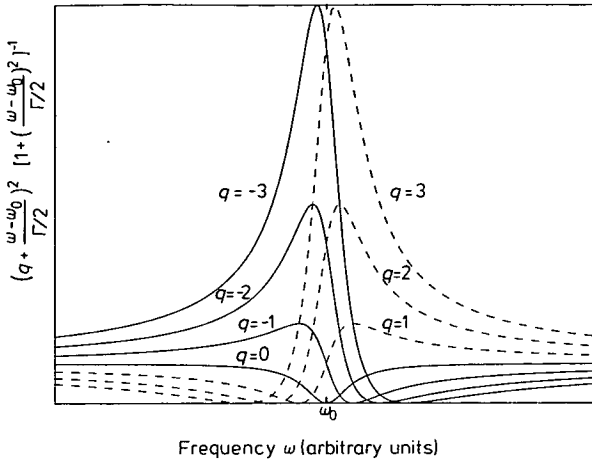


Figure 1. Shape of function (2.9) for different values of  $q$ .

The cross section for light scattering from optical phonons may be written:

$$\sigma(\omega) = (\bar{n}(\omega) + 1) \sum_{i,j=1}^N S_i S_j \text{Im}(G_{ij}(\omega)), \tag{3.1}$$

where  $\bar{n}(\omega) + 1$  is the Bose population factor,  $G_{ij}(\omega)$  the one phonon Green function matrix, and  $S_i, S_j$  may be loosely termed the scattering strengths of the uncoupled modes. They include the polarisability tensor elements, the input field strength,  $\omega^2$ , and other constant factors. It can be shown that the inverse of  $G(\omega)$  in the case of two modes (a and b), coupled by anharmonic terms in the crystal Hamiltonian, may be written:

$$G^{-1}(\omega) = \begin{pmatrix} \omega_a^2 - \omega^2 + i\omega\Gamma_a & \Delta + i\gamma\omega \\ \Delta + i\gamma\omega & \omega_b^2 - \omega^2 + i\omega\Gamma_b \end{pmatrix}. \tag{3.2}$$

By choice of a suitable unitary transformation, either the real or imaginary part of  $G^{-1}(\omega)$  may be diagonalised, corresponding to purely imaginary or real coupling respectively. If the other oscillator parameters are redefined suitably, the cross section is unaffected by this transformation. The distinction between real and imaginary coupling only becomes apparent when a soft mode is involved, so we may arbitrarily choose imaginary coupling in this case. Inversion of  $G^{-1}(\omega)$  leads to a complicated function in which the parameters of oscillators a and b may not be decoupled, and there is an anti-resonance dip between  $\omega_a$  and  $\omega_b$  when  $\Gamma_b \gg \Gamma_a$ . This function corresponds to coupling between one-phonon states, and therefore differs in concept from the Fano model.

#### 4. Comparison with experiment

Three functions were used to perform a computerised least squares fit to the observed room temperature  $A_1$  and E spectra of zinc metaborate (Murray and Lockwood 1976).

These are as follows.

#### 4.1. Coupled modes

A lineshape of the form (3.1) with  $N = 3$  and  $G_{23}^{-1} = G_{13}^{-1} = 0$  corresponds to two coupled modes and one uncoupled mode. A flat continuous background must be included to account for noninteracting continua and the photomultiplier dark current. If  $\omega_c$ ,  $\Gamma_c$  are the resonant frequency and linewidth of the uncoupled mode, table 1 summarises the results of this analysis.

Table 1. Coupled oscillator parameters

	$\omega_a$ (cm <sup>-1</sup> )	$\Gamma_a$ (cm <sup>-1</sup> )	$\omega_b$ (cm <sup>-1</sup> )	$\Gamma_b$ (cm <sup>-1</sup> )	$\gamma$	$\omega_c$ (cm <sup>-1</sup> )	$\Gamma_c$ (cm <sup>-1</sup> )
A <sub>1</sub>	124.4	4.3	143.1	73.6	12.4	94.9	11.8
E	123.8	1.8	163.8	103.2	7.2	90.2	12.2

The resulting functions, along with the experimental results, are presented in figure 2. The fine detail of this description in the vicinity of the resonance feature is represented by the broken line in the inset to figure 2.

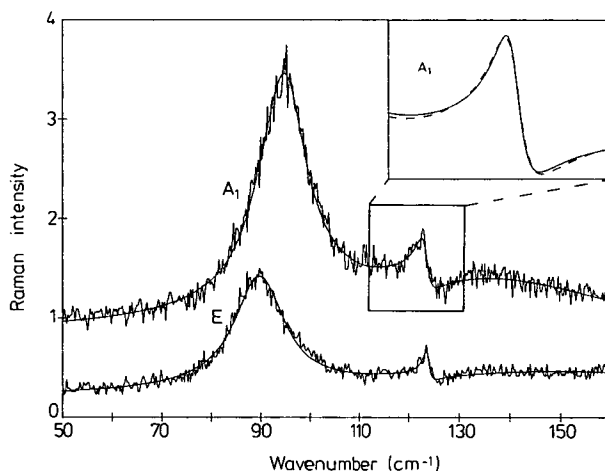


Figure 2. Experimental and theoretical forms for the room temperature A<sub>1</sub> and E spectra of Zn<sub>4</sub>O(BO<sub>2</sub>)<sub>6</sub> in the frequency region 50 cm<sup>-1</sup>–160 cm<sup>-1</sup>.

#### 4.2. Fano interference

If Fano interference between a discrete state and a featureless continuum of states is assumed, a diagonal  $2 \times 2$  Green function must be included to describe the noninteracting modes, and an additive constant, again to account for the noninteracting continua and the dark current. This model involves the same number of variable parameters as 4.1. If  $\omega_b$ ,  $\Gamma_b$ ,  $\omega_c$ ,  $\Gamma_c$  are the noninteracting oscillator parameters, the fitted results are given by table 2.

The parameters describing the noninteracting modes are in good agreement with those of table 1, although they now describe uncoupled excitations. The fitted spectrum obtained

is indistinguishable from that of §4.1 to the scale of the large graph in figure 2, but the detail is shown in the inset as a full curve.

Table 2. Fano model parameters.

	$q$	$\omega_0$ (cm <sup>-1</sup> )	$\Gamma$ (cm <sup>-1</sup> )	$\omega_b$ (cm <sup>-1</sup> )	$\Gamma_b$ (cm <sup>-1</sup> )	$\omega_c$ (cm <sup>-1</sup> )	$\Gamma_c$ (cm <sup>-1</sup> )
A <sub>1</sub>	-1.59	123.5	3.06	141.5	63.4	95.0	12.0
E	-2.26	123.9	1.49	163.2	101.6	90.2	12.3

### 4.3. Modified Fano interference

Following the reasoning of Rousseau and Porto (1968), an analysis was attempted involving Fano interference with  $\sigma_0(\omega)$  in (2.10) represented by an oscillator function and  $\sigma_1(\omega)$  by a constant, with a single uncoupled oscillator to describe the 95 cm<sup>-1</sup> mode. This led to values of  $q = -0.5$ ,  $\omega_0 = 125.0$  cm<sup>-1</sup> and  $\Gamma = 1.2$  cm<sup>-1</sup> for the A<sub>1</sub> spectrum, corresponding to figure 3. Convergence proved impossible in the case of E symmetry.

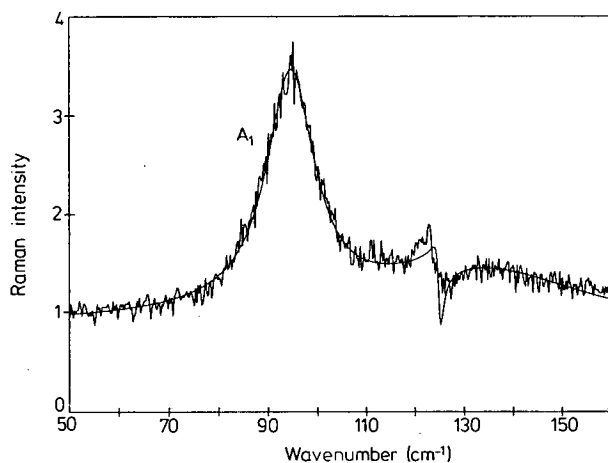


Figure 3. Experimental and theoretical forms for the A<sub>1</sub> spectrum of  $Zn_4O(BO_2)_6$  in the frequency region 50 cm<sup>-1</sup>–160 cm<sup>-1</sup>, using the model described in §4.3.

## 5. Conclusion

Firstly, function 4.3 may be dismissed as an inadequate description of this phenomenon in the case of zinc metaborate. The function involves fewer variable parameters. The results obtained from functions 4.1 and 4.2 are almost indistinguishable in figure 2. The goodness of fit test indicates that the Fano description is as good as the coupled mode description in the E symmetry, and less than one per cent better in the A<sub>1</sub> case. This is hardly significant. Physically, the Fano model would appear to be the more suitable, as the coupled oscillator analysis involves assuming that the broad background peak is first order. This would contradict the group theoretical prediction (Murray and Lockwood 1976). For this reason, we believe the Fano description to be more significant, although the experiment is not accurate enough to discriminate between the two theories.

A study of the temperature dependence of this feature revealed little change in the spectral lineshape as far as 130 K, with no evidence of decoupling.

### Acknowledgment

AFM thanks the SRC for the award of a Research Studentship.

### References

- Cowley R A 1966 *Phonons in Perfect Lattices and Lattices with Point Imperfections* ed Stevenson R W H (Edinburgh: Oliver and Boyd) pp 170–207
- Fano U 1961 *Phys. Rev.* **124** 1866–78
- Murray A F and Lockwood D J 1976 *J. Phys. C: Solid St. Phys.* **9** 3691–700
- Rousseau D L and Porto S P S 1968 *Phys. Rev. Lett.* **20** 1354–57
- Scott J F 1968 *Phys. Rev. Lett.* **21** 907–10
- 1970 *Phys. Rev. Lett.* **24** 1107–10
- 1971 *Light Scattering in Solids* ed Balkanski M (Paris: Flammarion) pp 387–92

2

**PROCEEDINGS  
OF THE  
FIFTH INTERNATIONAL CONFERENCE  
ON  
RAMAN SPECTROSCOPY**

**UNIVERSITÄT FREIBURG  
2-8 SEPTEMBER 1976**



**EDITED BY: E. D. SCHMID  
J. BRANDMÜLLER  
W. KIEFER  
B. SCHRADER  
H. W. SCHRÖTTER**

A.F. MURRAY, D.J. LOCKWOOD

Physics Department, Edinburgh  
University, Edinburgh EH9 3JZ,  
Scotland

Evidence of coupling between phonon states has been reported in the Raman spectra of  $\text{BaTiO}_3$ <sup>1</sup> and quartz<sup>2</sup>. We have measured the room temperature Raman spectrum of  $\text{Zn}_4\text{O}(\text{BO}_2)_6$  and have recorded a feature similar to that found at  $175\text{cm}^{-1}$  in  $\text{BaTiO}_3$ . Group theory predicts that the Raman spectrum of  $\text{Zn}_4\text{O}(\text{BO}_2)_6$  should contain  $3A_1 + 5E + 10F_2$  modes. These have been identified, along with an additional interference feature present in the  $A_1$  and E spectra.<sup>3</sup>

The quantum mechanical formalism surrounding resonant interference (Auger processes)<sup>4</sup> can be summarised as follows. If a discrete one-phonon state ( $\phi$ ) is superimposed on a continuum of states  $\{\psi_E\}$  they may interact via anharmonic terms in the potential function to cause a perturbation of  $\phi$ . The (perturbed) wavefunction of the coupled state ( $\bar{\psi}_E$ ) consists of a mixture of the discrete state wavefunction and the continuum wavefunctions. If the transition operator between initial state  $\psi_0$  and the state  $\bar{\psi}_E$  is  $\alpha_{ij}$ , the Raman cross-section depends on the matrix element  $\langle \bar{\psi}_E | \alpha_{ij} | \psi_0 \rangle$ . Fano<sup>4</sup> has shown that the ratio of the probability of such a transition to the probability of transition to the unperturbed continuum is

$$\frac{|\langle \bar{\psi}_E | \alpha_{ij} | \psi_0 \rangle|^2}{|\langle \psi_E | \alpha_{ij} | \psi_0 \rangle|^2} = \frac{(q + \epsilon)^2}{1 + \epsilon^2} \quad \text{where } \epsilon = \frac{E - E_r}{\pi |V_E|^2} = \frac{h(\nu - \nu_r)}{\frac{1}{2}\Gamma}$$

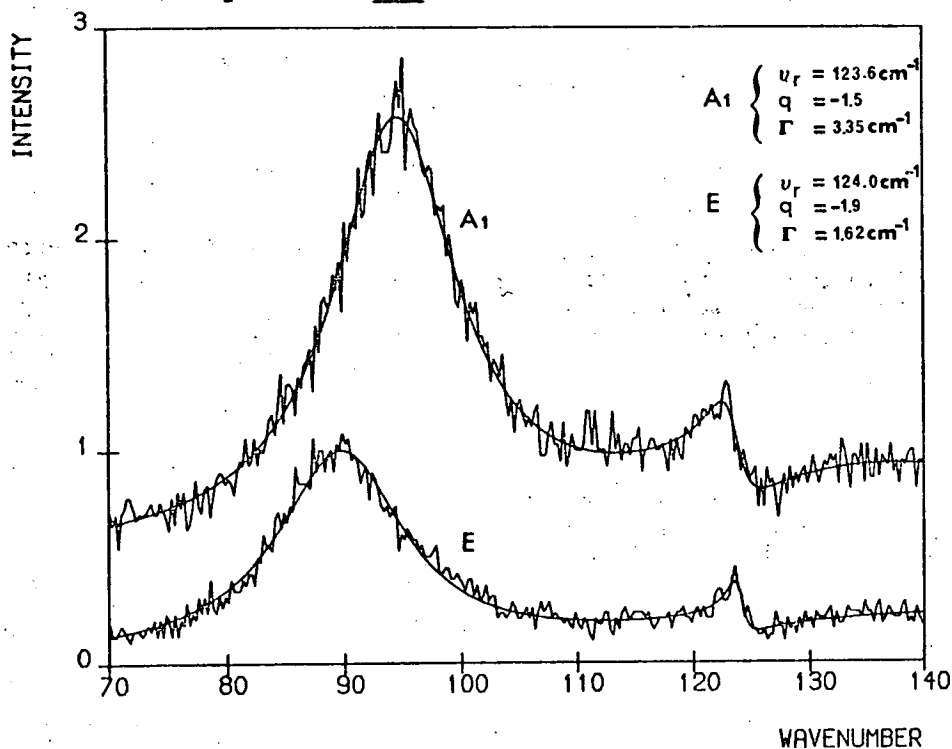
The width parameter  $V_E$  depends on coupling strength, and the line profile parameter  $q$  on the transition probability to a modified  $\phi$  state. As the frequency  $\nu$  of emitted photons studied is varied through  $\nu_r$ , the scattering cross-section is of the form<sup>1</sup>

$$\sigma = \sigma_0 + \sigma_1 \frac{(q + \epsilon)^2}{1 + \epsilon^2}$$

A computerised curve fitting to this function produced the

smooth lines in the diagram, along with the tabulated optimal values of  $\nu_r$ ,  $q$  and  $\Gamma$ . In the E spectrum, an underdamped simple harmonic oscillator was fitted to the  $89.4 \text{ cm}^{-1}$  mode, and in the  $A_1$  spectrum, to the  $94.7 \text{ cm}^{-1}$  mode. The fitted  $A_1$  and E profiles also incorporate a heavily damped harmonic oscillator function to describe the multi-phonon background empirically. It can be inferred from the values of  $\Gamma$  that the Fano-type interference in the  $A_1$  spectrum is due to a stronger coupling to the background than in the E symmetry. As for  $\text{BaTiO}_3$ , where again there is interference between one- and two-phonon states, the Fano model is a good fit to the data. The interference feature does, however, have mixed symmetry, and is thought to be due to some iodine species trapped as an impurity in the lattice, or to resonant Raman scattering from a manganese impurity content.<sup>3</sup>

1. D. Rousseau & S. Porto, Phys. Rev. Letters 20, 1354 (1968)
2. J.F. Scott, Phys. Rev. Letters 21, 907 (1968)
3. A.F. Murray & D.J. Lockwood, J. Phys. C. to be published
4. U. Fano, Phys. Rev. 124, 1866 (1961)





## Raman spectrum of $\text{Zn}_4\text{O}(\text{BO}_2)_6$

A F Murray and D J Lockwood

Department of Physics, University of Edinburgh, Edinburgh, EH9 3JZ, Scotland

Received 5 April 1976

**Abstract.** The first-order Raman spectrum of cubic zinc metaborate has been measured at room temperature, and the number of  $q = 0$  phonon frequencies found exceeds the group theoretical prediction by one. The additional band appears as an interference feature at  $122.5 \text{ cm}^{-1}$  and is thought to be attributable to some impurity introduced during crystal growth. The results are in reasonable agreement with an earlier qualitative investigation of the infrared transmission spectrum of this material, and the reported fluorescent properties are verified. A comparison between the Raman results for zinc metaborate and those for  $\text{Cr}_3\text{B}_7\text{O}_{13}\text{Cl}$  shows some correlations. A simple force-constant calculation identified four bands in each compound that can be associated with vibrations of  $\text{BO}_4$  tetrahedra contained within the boron-oxygen framework.

### 1. Introduction

The crystal  $\text{Zn}_4\text{O}(\text{BO}_2)_6$  is unusual in that it is one of the few anhydrous metaborates with all the boron atoms in fourfold coordination. In general, stability demands threefold coordination in anhydrous metaborates at atmospheric pressure. Crystals of basic zinc metaborate are cubic, having a bimolecular unit cell of edge length  $7.48 \text{ \AA}$ . Boron and oxygen atoms are bound together to form an infinitely extended three-dimensional framework based on  $(\text{B}_6\text{O}_{12})^{6-}$  rings (Smith *et al* 1964). Each boron atom is at the centre of four tetrahedrally distributed oxygen atoms, with a boron-oxygen distance of  $1.52 \text{ \AA}$  and a boron-boron distance of  $2.64 \text{ \AA}$ . The zinc atoms lie inside irregular tetrahedra whose corners are occupied by three oxygen atoms from metaborate ions and one 'free' oxygen atom.

All the crystals thought to contain boron atoms in exclusively fourfold coordination are of the form  $(\text{MeO})_m \cdot (\text{B}_2\text{O}_3)_n$ , where Me is a divalent metal. These are  $\text{CuO} \cdot \text{B}_2\text{O}_3$  (Martinez-Ripoll *et al* 1971),  $\text{SrO} \cdot (\text{B}_2\text{O}_3)_2$  and  $\text{PbO} \cdot (\text{B}_2\text{O}_3)_2$  (Perloff and Block 1966) and  $(\text{ZnO})_4 \cdot (\text{B}_2\text{O}_3)_3$  (Smith *et al* 1964). There are, however, several materials having all boron atoms in fourfold coordination in a high-pressure phase. These are  $\text{SrB}_2\text{O}_4$  (IV) (Dernier 1969),  $\text{B}_2\text{O}_3$  (II) (Prewitt and Shannon 1968),  $\text{HBO}_2$  (III) (Zachariasen 1963),  $\text{LiBO}_2$  (III) (Marezio and Remeika 1966) and  $\text{CaB}_2\text{O}_4$  (IV) (Marezio *et al* 1969). In addition, there are several compounds with mixed threefold and fourfold coordination, some of which are listed by Marezio *et al* (1969). The boracites (Nelmes 1974) are another example of this type of compound.

Apart from a qualitative examination of the infrared spectrum (Krogh-Moe 1962), there is no detailed investigation of the lattice vibrations of zinc metaborate. Here we report the Raman spectrum of this material with a view to characterizing the  $q = 0$

vibrations of a crystal lattice involving a boron–oxygen framework with fourfold coordination. While the results are of interest in their own right, they are also of value for comparison with some current work on the lattice vibrations of boracites. The dynamics of the ferroelectric phase transition exhibited by boracites are being investigated using Raman spectroscopy, and as part of this study, the lattice vibrations of the cubic phase of  $\text{Cr}_3\text{B}_7\text{O}_{13}\text{Cl}$  have been measured (Lockwood 1974, 1976). The elements common to the structures of zinc metaborate and boracite may produce common features in the Raman spectrum, which would facilitate a definite assignment.

## 2. Experiments and results

### 2.1. Group theory

A group theoretical analysis of the normal modes of vibration of the zinc metaborate structure at  $q = 0$  predicts the following decomposition according to the irreducible representation of point group  $\bar{4}3m$ :

$$\Gamma = 3A_1 + 2A_2 + 5E + 7F_1 + 11F_2.$$

The polarizability tensors for crystals of cubic symmetry are of the form (Loudon 1964)

$$A_1 \begin{bmatrix} a & - & - \\ - & a & - \\ - & - & a \end{bmatrix} \quad E \begin{bmatrix} b & - & - \\ - & b & - \\ - & - & -2b \end{bmatrix} \quad \text{and} \quad \begin{bmatrix} \sqrt{3}b & - & - \\ - & -\sqrt{3}b & - \\ - & - & - \end{bmatrix}$$

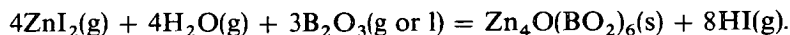
$$F_2 \begin{bmatrix} - & - & - \\ - & - & d \\ - & d & - \end{bmatrix}, \begin{bmatrix} - & - & d \\ - & - & - \\ d & - & - \end{bmatrix} \quad \text{and} \quad \begin{bmatrix} - & d & - \\ d & - & - \\ - & - & - \end{bmatrix}.$$

The Raman activities are indicated by the appropriate non-zero components of the polarizability tensor. Excluding acoustic modes, therefore, the Raman spectrum should comprise  $3A_1 + 5E + 10F_2$  normal modes of vibration. Only modes of  $F_2$  symmetry are infrared active.

The problem of distinguishing modes of  $A_1$  symmetry from those of  $E$  symmetry is readily solved (Lockwood 1974). Briefly, the solution involves aligning the incident light along an axis, say  $x'$ , at  $45^\circ$  to the cubic  $x$  and  $y$  axes, and observing the light scattered in direction  $y'$ , orthogonal to  $x'$ . The  $E$  spectrum is obtained by measuring the polarizability tensor element  $\alpha_{y'y'}$ . A point for point subtraction of the spectrum corresponding to tensor element  $\alpha_{y'y'}$  from that of  $\alpha_{zz}$  leaves a spectrum of pure  $A_1$  symmetry modes, provided an appropriate scaling factor is used.

### 2.2. Experimental details

The single crystal of  $\text{Zn}_4\text{O}(\text{BO}_2)_6$  was grown by the vapour transport method (Schmid 1965) as a byproduct in the attempted growth of Zn-I-boracite, the reaction mechanism being



The formation of zinc metaborate instead of the boracite is a result of an insufficient quantity of  $\text{ZnI}_2$  vapour (Schmid 1965). The crystal formed was a rhombic dodecahedron of approximate size 2 mm. The natural growth faces of the crystal were  $\{110\}$ , and con-

sequently faces perpendicular to the  $\langle 100 \rangle$  directions were cut and polished (using 1  $\mu$ m diamond powder) for use in the conventional Raman scattering measurements. Inspection of the crystal under a polarizing microscope revealed considerable growth strains, which lead to inhomogeneous optical properties. As a result, spectra of any polarization may contain additional features attributable to admixtures from spectra of other polarizations. A minor degree of mixing of spectra always occurs due to the wide collection angle of the lens used to gather the scattered light, but in this experiment the depolarization problem was more troublesome because of the strain birefringence. Adopting the approach that any spectrum is a combination of the true spectrum and small proportions of other spectra, the subtraction process described above may be used to remove unwanted modes. Provided a clear spectral feature can be used to determine a scale factor, a point for point subtraction should reveal the pure spectrum. It is, however, impossible to use this method when the spurious modes are attributable to the  $F_2$  spectrum, due to TO-LO intensity effects.

Zinc metaborate is known to exhibit fluorescence (Terol and Otero 1961), and a broad emission band peaked at 537.2 nm was observed in survey spectra excited by the 514.5 nm radiation from an argon laser. Therefore, in order that the Raman spectrum should not be confused with the broad fluorescent background, 350 mW of 476.5 nm argon laser light was used to excite all the spectra presented here. The Raman spectrum was recorded at room temperature from both  $90^\circ$  and  $180^\circ$  scattering geometries using a Coderg T800 triple monochromator with a spectral slit width of 1.0 and 1.5  $cm^{-1}$  for the 0–500  $cm^{-1}$  and 500–1500  $cm^{-1}$  frequency regions respectively. The spectrometer is connected via an interface to a PDP11 computer (Arthur and Lockwood 1974) which enables spectra to be stored in digital form. The data may be subsequently transferred to a time-sharing multi-access computer in order that the subtraction routine, along with other data handling routines (Arthur 1974, 1976) may be performed in an interactive manner.

In the following description of results, the labels  $X$ ,  $Y$  refer to the  $[100]$  and  $[010]$  directions and  $X'$ ,  $Y'$  to the  $[110]$  and  $[\bar{1}10]$  directions.

### 2.3. The $A_1$ spectrum

This spectrum was isolated, as described earlier, by subtracting the  $X'(Y'X')Y'$  E symmetry spectrum from the  $X'(ZZ)Y'$  spectrum which contains features of both  $A_1$  and E symmetry. These latter spectra are shown in figures 1 and 2. A first approximation to the scaling factor was found by comparing the relative intensities of the distinct E peak at 414.5  $cm^{-1}$  in both spectra, and then adjusting the factor for complete cancellation. This led to the isolated  $A_1$  spectrum of figure 3. The theoretical intensity scaling factors of  $4b^2$  and  $3b^2$  for the  $ZZ$  and  $Y'X'$  spectra, respectively, indicate that cancellation should be achieved when the  $Y'X'$  spectrum is multiplied by 1.33 and subtracted from the  $ZZ$  spectrum (Lockwood 1974). In fact, due to crystal and experimental imperfections, the scaling factor was found to be  $1.03 \pm 0.07$ . In figure 3, the disappearance of a mode of E symmetry is marked by an increase in the level of noise, for obvious reasons, and in places by a sharp differential feature due to a slight mismatch in the wavenumber calibration between  $ZZ$  and  $Y'X'$  spectra. There are, apart from some broad second-order structure, four sharp features. One of these takes the form of a resonance interference at 122.5  $cm^{-1}$  between a sharp peak and a broader second-order background. The peaks at 249.3  $cm^{-1}$  and 421.9  $cm^{-1}$  are clearly of  $A_1$  symmetry, but the nature of the feature at 94.7  $cm^{-1}$  is partially disguised by the proximity of E and  $F_2$  features. The different nor-

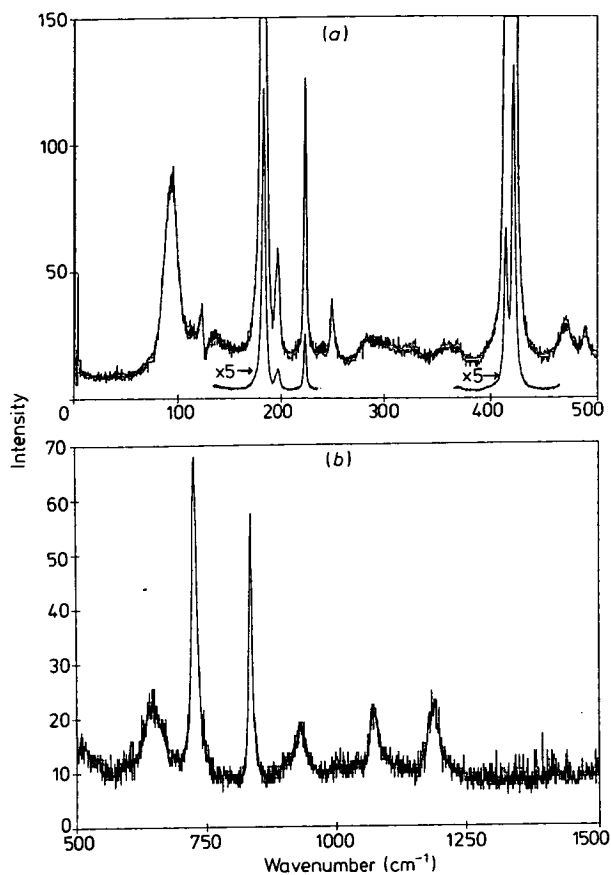


Figure 1. The  $X'(ZZ)Y'$  spectrum of  $Zn_4O(BO_2)_6$  in the regions  $0-500\text{ cm}^{-1}$  and  $500-1500\text{ cm}^{-1}$ .

mal-mode frequencies in this closely spaced trio are revealed by the use of the subtraction process and a computerized peak-finding routine (Arthur 1976), whereas visual inspection of the spectra suggests only one mode to be present. Table 1 shows all the measured frequencies, assignments, and linewidths where appropriate.

#### 2.4. The $E$ spectrum

From the  $X'(YX')Y'$  spectrum of figure 2, assignments of  $E$  symmetry modes are fairly straightforward, apart from the interference feature mentioned above.  $F_2$  symmetry modes appearing in this spectrum cannot be subtracted out due to the TO-LO intensity variations. The frequencies are tabulated in table 1.

#### 2.5. The $F_2$ spectrum

Identification of modes of  $F_2$  symmetry is complicated by splitting between the transverse

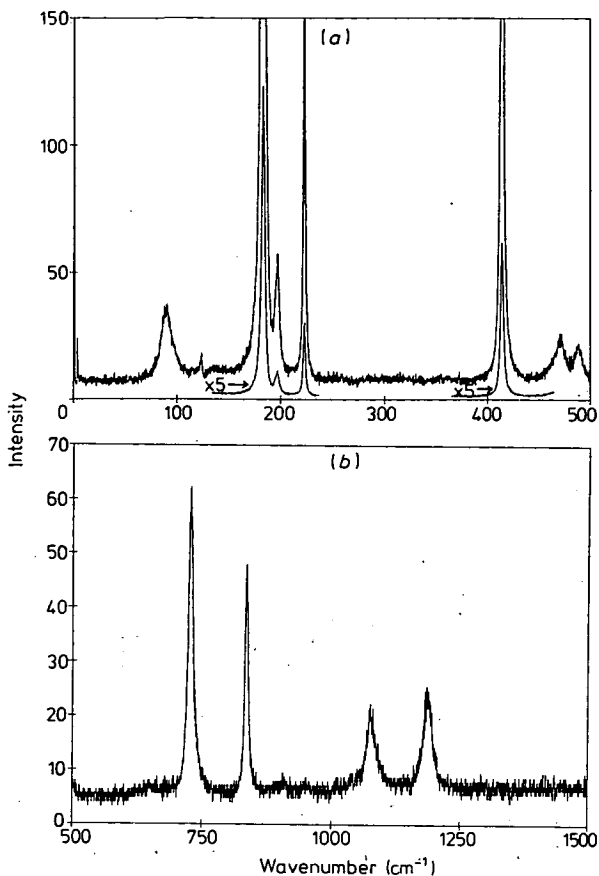


Figure 2. The  $X'(Y'X')Y'$  spectrum of  $Zn_4O(BO_2)_6$  in the regions  $0-500\text{ cm}^{-1}$  and  $500-1500\text{ cm}^{-1}$ .

and longitudinal components of some  $F_2$  modes. The  $X(YX)Y$  spectrum contains  $F_2$  modes of transverse character only, and this spectrum is shown in figure 4. Other  $90^\circ$  scattering off-diagonal spectra such as  $X(YZ)Y$  (see figure 5) contain both TO and LO features. In order to clarify the assignment of  $F_2^{LO}$  modes, the  $X(YZ)\bar{X}$  backscattering spectrum was measured; this spectrum contains only longitudinal modes. The signal in this spectrum was weak, and the argon laser plasma lines strong, but the assignments in table 1, taken from the  $X(YZ)Y$  spectrum of figure 5, were confirmed. Once again the subtraction routine was used, in this case to remove the admixture of modes of  $A_1$  and  $E$  symmetry to give figure 5. This involved subtraction from the  $YZ$  spectrum of the  $ZZ$  and  $Y'X'$  spectra with scale factors 0.045 and 0.2 respectively. This procedure reveals otherwise partially hidden spectral features of definite  $F_2$  symmetry at  $93.1\text{ cm}^{-1}$  and  $181.6\text{ cm}^{-1}$ . The peak-finding computer routine again proved invaluable in detecting small wavenumber differences and very weak modes, such as the peak at  $284.2\text{ cm}^{-1}$ .

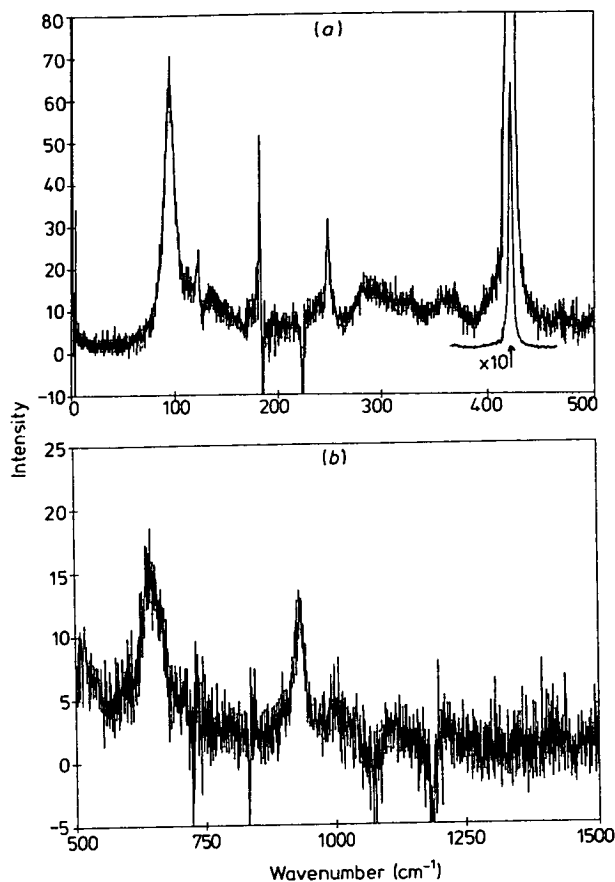


Figure 3. The  $A_1$  spectrum of  $Zn_4O(BO_2)_6$  in the regions  $0-500\text{ cm}^{-1}$  and  $500-1500\text{ cm}^{-1}$ .

Table 1. Peak frequencies  $\omega$  ( $\text{cm}^{-1}$ ), linewidths  $\gamma$  ( $\text{cm}^{-1}$ ) and assignments for the Raman-active modes of  $Zn_4O(BO_2)_6$ .

$A_1$		E		$F_2$	
$\omega$	$\gamma$	$\omega$	$\gamma$	$\omega$	$\gamma$
94.7	$11.5 \pm 1.5^a$	89.4	$12 \pm 1^a$	93.1	$15 \pm 2^a$
122.5		122.5			
249.3	$3 \pm 0.6^a$	183.0	$4 \pm 0.5^a$	181.6	$4 \pm 0.5^a$
421.9	$3 \pm 0.6^a$	414.5	$3.3 \pm 0.3^a$	196.7	$5 \pm 0.5^a$
		727.2	$12.5 \pm 1.5^b$	222.4	$2 \pm 0.5^a$
		835.9	$9 \pm 1.5^b$	278.0	$6.5 \pm 2^a$
				284.2	$6.5 \pm 2^a$
				471.1	$14 \pm 1.5^a$
				488.2	$9.5 \pm 1.5^a$
				653	$20 \pm 6^b$
				906.2	$14 \pm 2^b$
				1005	— <sup>c</sup>
				1040	— <sup>c</sup>
				1074.4	$19 \pm 1.5^b$
				1189.0	$23.5 \pm 1.5^b$

<sup>a</sup> Spectral slit width  $1.0\text{ cm}^{-1}$ .

<sup>b</sup> Spectral slit width  $1.5\text{ cm}^{-1}$ .

<sup>c</sup> Not sufficiently resolved for meaningful measurement.

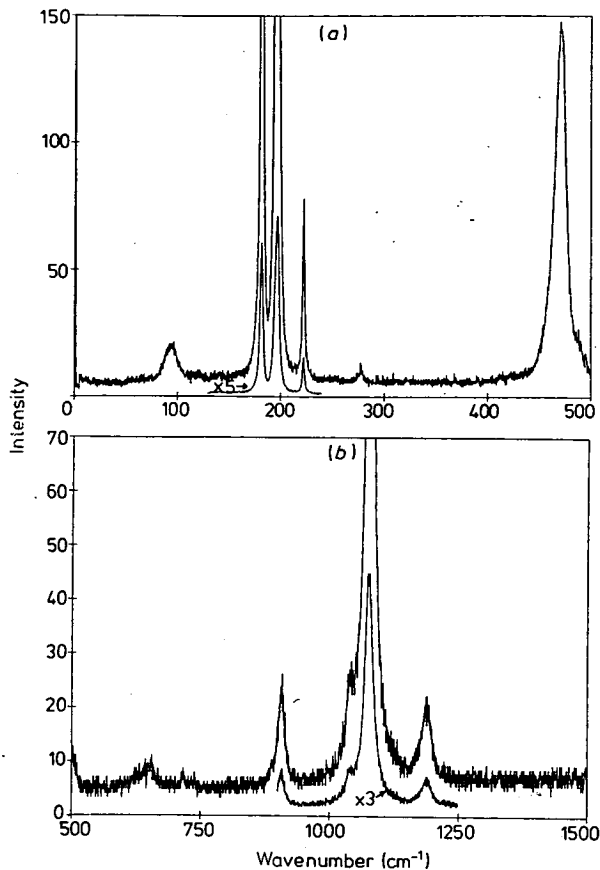


Figure 4. The  $X(YX)Y$  spectrum of  $Zn_4O(BO_2)_6$  in the regions  $0\text{--}500\text{ cm}^{-1}$  and  $500\text{--}1500\text{ cm}^{-1}$ .

### 3. Discussion

From the assignments in table 1 it is clear that the  $A_1$  and  $E$  spectra are not totally in agreement with group theoretical predictions. While the  $F_2$  spectrum contains ten distinct peaks as predicted by theory, the  $A_1$  spectrum contains four peaks and the  $E$  spectrum contains six, both of which exceed the predicted number of modes by one. There are two possible explanations of this discrepancy. It is conceivable that the broad peak appearing in both the  $E$  and  $A_1$  spectra (figures 2 and 3) around  $90\text{--}94\text{ cm}^{-1}$  is spurious. This feature has been clearly resolved into three peaks of  $E$ ,  $F_2$  and  $A_1$  symmetry at  $89.4\text{ cm}^{-1}$ ,  $93.1\text{ cm}^{-1}$  and  $94.7\text{ cm}^{-1}$  respectively. This near-degeneracy is quite remarkable, but these *distinct* frequencies, together with the intensities of the individual bands (figures 2, 3, 4 and 5) suggest that this is an intrinsic property. Therefore, it is anticipated that the interference feature at  $122.5\text{ cm}^{-1}$  is the spurious mode. The intensity of this mode is comparable, and has the same frequency, in both the  $A_1$  and  $E$  spectra.

The  $F_2$  spectrum of figures 4 and 5 contains ten modes, allowing for splitting between transverse and longitudinal components, and should show some agreement with the infrared spectrum. The only published infrared investigation of the lattice vibrations of zinc metaborate (Krogh-Moe 1962) is very qualitative and no frequency assignments are

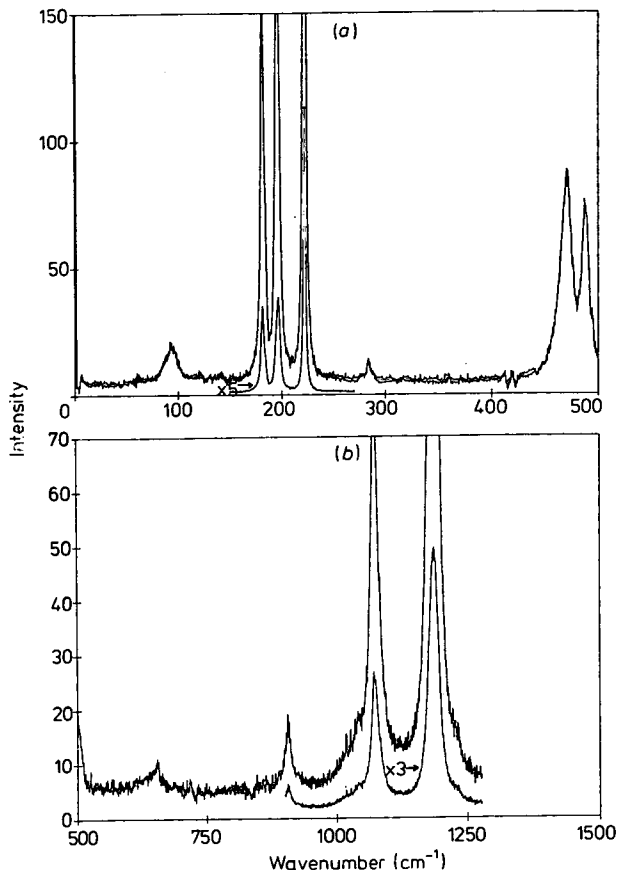


Figure 5. The X(YZ)Y spectrum of  $\text{Zn}_4\text{O}(\text{BO}_2)_6$  in the regions  $0\text{--}500\text{ cm}^{-1}$  and  $500\text{--}1500\text{ cm}^{-1}$ .

tabulated. This makes detailed comparison difficult, but measurements on the published spectrum from  $670$  to  $5000\text{ cm}^{-1}$  do reveal some correlations. There are strong absorption peaks at  $1040 \pm 6\text{ cm}^{-1}$  and  $1080 \pm 6\text{ cm}^{-1}$  and a broader feature stretching from  $915\text{ cm}^{-1}$  to  $945\text{ cm}^{-1}$ , while there are shoulder features at  $990\text{ cm}^{-1}$  and  $1140\text{ cm}^{-1}$  which could correspond to longitudinal components. It seems reasonable to assume that the two sharper features correspond to the tabulated Raman frequencies of  $1040\text{ cm}^{-1}$  and  $1074.4\text{ cm}^{-1}$  and the broader feature to the  $906.2\text{ cm}^{-1}$  mode, with longitudinal components where appropriate. There is, however, a strong infrared absorption at  $720\text{ cm}^{-1}$ , which is completely absent in the Raman spectrum. This could arise from second-order absorption, or may indicate the presence of an impurity in the sample used for the infrared measurements due to the different method of preparation (crystallization from the melt of fused zinc oxide and boric acid).

It is interesting and informative to compare the observed fluorescence band at  $537\text{ nm}$  with the luminescence data of Terol and Otero (1961). Terol and Otero observed that pure cubic zinc borate is luminescent under  $253.7\text{ nm}$  excitation with the emission comprising a narrow band peaked at  $435\text{ nm}$  with a weaker secondary band peaked at  $535\text{ nm}$ . The luminescent response to  $365\text{ nm}$  excitation was very weak. The luminescence is ascribed to trapped electrons (or positive holes) due to absences of 'free' oxygen (or zinc) atoms in the crystal structure: oxygen vacancies in the  $\text{BO}_4$  tetrahedra are not likely because of the



high strength of the B–O framework. Activation with a small amount of Mn produces a strong green luminescence, peaked at 540 nm, under ultraviolet excitation: the Mn is divalent and is assumed to substitute for Zn. The fluorescence observed in the Raman experiments is presumed to be excited by the near-ultraviolet light characteristically produced in the argon laser plasma discharge. As noted above, low-energy excitation produces only weak luminescence in pure zinc borate. Therefore, even though there is good agreement between the peak position at 537 nm found here and the sideband at 535 nm reported by Terol and Otero, it seems unlikely that the emission is from the pure crystal, particularly as we found no evidence of the contiguous band at 435 nm. A more likely explanation, confirmed by H Schmid (1976, private communication), is the presence of some Mn in the crystal carried over as an impurity from the starting materials (see §2.2); the  $Mn^{2+}$  luminescence is strong and peaks at 540 nm, which agrees well with our observations.

Terol and Otero (1961) note that the multiple closed chains of linked  $(BO_2)_6$  groups form a basket-like framework containing many cavities that are large enough to accommodate positive and negative ions. Some of these cavities are, of course, occupied by the zinc and 'free' oxygen atoms that make up the chemical formula. However, there is the possibility of other species occupying these cavities and, in particular, the growth mechanism (§2.2) suggests that HI or some other iodine species may be trapped in these sites. The presence of iodine during crystal growth could also result in  $I^-$  substituting for cavity oxygen. The spurious interference band at  $122.5\text{ cm}^{-1}$  is, therefore, tentatively assigned to a local mode vibration of some iodine species trapped within the lattice. (The Mn ion concentration would be too small to observe an impurity mode from this ion in the absence of resonant Raman scattering.) The variation of the interference band profile with temperature and excitation frequency is being studied in an attempt to divine its origin and to obtain more information on the coupling mechanism to the phonon bath.

Any explanation of the origin of the interference feature must resolve the puzzling fact that the mode has  $A_1$  and E symmetry.

The Raman results obtained for zinc metaborate may be compared with the  $q = 0$  frequencies of chromium chlorine boracite (Lockwood 1974, 1976) with a view to determining common features arising from vibrations of the B–O framework. There are a large number of normal modes in both crystals, and some simplifications are needed to facilitate the comparison. We assume that the basic  $BO_4$  molecular units within each crystal are independent. The vibrations of this tetrahedral molecule transform as  $A_1 + E + 2F_2$ , and these are considered to be internal modes in the cubic crystal. Unfortunately, the vibrational frequencies of the free  $BO_4^{5-}$  ion are unknown, and therefore no ready comparison and assignment can be made. An indirect approach was adopted. Using the known values for the vibrational frequencies of the tetrahedral ions  $SiO_4^{4-}$ ,  $PO_4^{3-}$ ,  $SO_4^{2-}$  and  $ClO_4^-$  as a guide, possible  $A_1$ , E and  $F_2$  frequencies for borate were selected from the results for zinc metaborate and chromium chlorine boracite. Appropriate combinations of these frequencies were then used to obtain force constants for two different models representing the forces in tetrahedral molecules. One model assumed central forces only, and the other was the more sophisticated generalized force field model of the Urey–Bradley (1931) type. The force constants were calculated on a computer from a simultaneous least-squares fit to the four equations connecting frequencies and force constants. Different combinations from the previously selected  $A_1$ , E and  $F_2$  frequencies were tried until the best fit was obtained. The best and most sensible fits were obtained from the same data sets for both models. These data sets are shown in table 2. The frequencies in each column are remarkably similar. Furthermore, the relative intensities show close

Table 2. Data sets for the two models (frequencies in  $\text{cm}^{-1}$ ).

	$A_1(\nu_1)$	$E(\nu_2)$	$F_2(\nu_3)$	$F_2(\nu_4)$
$\text{Zn}_4\text{O}(\text{BO}_2)_6$	421	183	1075	278
$\text{Cr}_3\text{B}_7\text{O}_{13}\text{Cl}$	375	232	1160	252

agreement: the  $\nu_1$ ,  $\nu_2$  and  $\nu_3$  bands are strong, while the  $\nu_4$  band is weak in both cases. The force constants obtained are somewhat different from those calculated for a free molecule like  $\text{SiO}_4^{4-}$ , as can be expected. In particular, the  $\nu_1$  band in the crystal is undoubtedly much lower in frequency than one would anticipate for the free molecule. Nevertheless, it appears that frequencies at about  $A_1 = 400 \text{ cm}^{-1}$ ,  $E = 200 \text{ cm}^{-1}$ ,  $F_2 = 1100 \text{ cm}^{-1}$  and  $F_2 = 260 \text{ cm}^{-1}$  are characteristic of a B-O framework comprising or containing  $\text{BO}_4$  tetrahedra.

### Acknowledgments

We wish to thank H Schmid for considerable advice and for providing the crystal growing facilities, and H Tippmann for technical assistance in the growth of the zinc metaborate crystal. The work was supported by the Science Research Council and the Battelle Research Centre, Geneva. One of us (AFM) acknowledges the support of an SRC student-ship.

### References

- Arthur J W 1974 *PhD thesis* University of Edinburgh  
 — 1976 *J. Raman Spectrosc.* to be published  
 Arthur J W and Lockwood D J 1974 *J. Raman Spectrosc.* **2** 53–69  
 Dernier P D 1969 *Acta Crystallogr. B* **25** 1001–3  
 Krogh-Moe J 1962 *Z. Kristallogr.* **117** 166–70  
 Lockwood D J 1974 *J. Raman Spectrosc.* **2** 555–62  
 — 1976 to be published  
 Loudon R 1964 *Adv. Phys.* **13** 423–82 (erratum **14** 621)  
 Marezio M and Remeika J P 1966 *J. Chem. Phys.* **44** 3348–53  
 Marezio M, Remeika J P and Dernier P D 1969 *Acta Crystallogr. B* **25** 965–70  
 Martinez-Ripoll M, Martinez-Carrera S and Garcia-Blanco S 1971 *Acta Crystallogr. B* **27** 677–81  
 Nelmes R J 1974 *J. Phys. C: Solid St. Phys.* **7** 3840–54  
 Perloff A and Block S 1966 *Acta Crystallogr.* **20** 274–9  
 Prewitt C T and Shannon R D 1968 *Acta Crystallogr. B* **24** 869–74  
 Schmid H 1965 *J. Phys. Chem. Solids* **26** 973–88  
 Smith P, Garcia-Blanco S and Rivoir L 1964 *Z. Kristallogr.* **119** 375–83  
 Terol S and Otero M J 1961 *Z. Naturf.* **16** 920–7  
 Urey H C and Bradley C A 1931 *Phys. Rev.* **38** 1969–78  
 Zachariasen W H 1963 *Acta Crystallogr.* **16** 385–9

PROCEEDINGS  
OF THE  
INTERNATIONAL CONFERENCE

on

LATTICE DYNAMICS

(Paris, September 5-9, 1977)

edited by

M. BALKANSKI

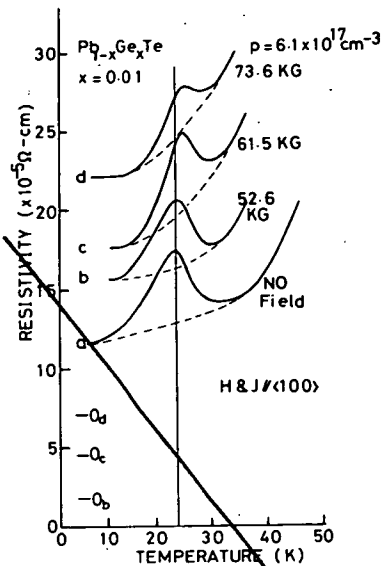


Fig. 3. Resistivity anomalies of  $Pb_{1-x}Ge_xTe$  for  $x=0.01$  under magnetic field. The peak of the anomaly moves upward with magnetic field.

be much larger than the value for SnTe used to explain the carrier dependence of soft phonon frequency, which was 5.6 eV. However, if we take into account that the Fermi energy for SnTe specimens with carrier concentrations of  $\sim 4 \times 10^{20} \text{ cm}^{-3}$  is about  $\sim 0.6$  eV, the reducing factor  $(1+2E/E_g)^{-1}$  becomes  $\sim 0.2$  ( $E_g=0.3$  meV). If we allow of the shift of the lowest Landau level, taking account of the effect of spin-splitting, these parameters would change.

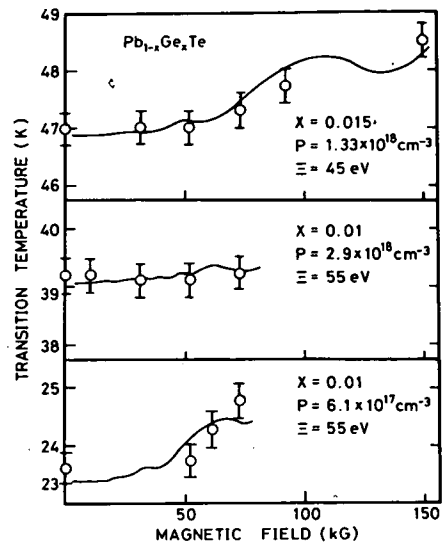


Fig. 4. Transition temperature vs. magnetic field. The open circles are obtained from the peak of the resistance anomaly. The solid lines are obtained from the calculation.

There is a possibility that the lattice vacancies accompanying the free carriers will affect the lattice instability<sup>12</sup>. However, the effect of magnetic field on the lattice instability will give a definitive evidence for the importance of the electronic excitation.

This work is partially supported by a Grant by the Department of Education.

#### REFERENCES

1. COCHRAN, W., Phys. Letters **13**, 193 (1964).
2. KRISTOFFEL, N. and KONSIN, P., Phys. Stat. Sol. **28**, 731 (1968).
3. KAWAMURA, H., KATAYAMA, S., TAKANO, S. and HOTTA, S., Solid State Commun. **14**, 259 (1974).
4. PAWLEY, G., COCHRAN, W., COWLEY, R.A. and DOLLING, G., Phys. Rev. Lett. **17**, 753 (1966).
5. ALPERIN, H.A., PICKART, S.J., RHYNE, J.J. and MINKIEWICZ, K.H., Phys. Letters **40A**, 295 (1972).
6. DOLLING, G. and BUYERS, W.J.L., J. Nonmetals **1**, 159 (1973).
7. SUGAI, S., MURASE, K. and KAWAMURA, H., Solid State Commun. **23**, 127 (1977).
8. SUGAI, S., MURASE, K., KATAYAMA, S., TAKAOKA, S., NISHI, S. and KAWAMURA, H., Solid State Commun., to be published.
9. KOBAYASHI, K.L.I., KATO, Y., KATAYAMA, Y. and KOMATSUBARA, K.F., Solid State Commun. **17**, 875 (1975).
10. KATAYAMA, S., Solid State Commun. **19**, 381 (1976).
11. MURASE, K., SUGAI, S., TAKAOKA, S. and KATAYAMA, S., Proc. Int. Conf. Phys. Semicond., Rome, (1976), p. 305.
12. JANTSCH, W. and LOPEZ-OTERO, A., Proc. Int. Conf. Phys. Semicond., Rome, (1976), p. 487.

## RAMAN SPECTRAL STUDY OF CUBIC NICKEL-IODINE BORACITE

A.F. Murray and D.J. Lockwood

Physics Department, University of Edinburgh,  
Edinburgh, EH9 3JZ, Scotland.

The Raman spectrum of cubic nickel-iodine boracite is reported for temperatures between 88 and 295 K. Anomalies in the temperature dependence of E and  $A_1$  symmetry modes at 128 K are interpreted as being related to anomalies in the structural, magnetic, and electrical properties of this material. A  $20\text{ cm}^{-1}$  softening of a broad E symmetry mode is also noted. The 88 to 295 K results for this system are all characteristic of a material with a cubic space group.

Nickel iodine boracite,  $\text{Ni}_3\text{B}_7\text{O}_{13}\text{I}$  (Ni - I), has a first order transition from a high temperature paraelectric cubic phase to an orthorhombic improper ferroelectric phase at  $T_c = 64\text{ K}$ , at which temperature Ni - I also becomes weakly ferromagnetic.<sup>1</sup> Both the dielectric constant and magnetic susceptibility exhibit a broad maximum at around  $125\text{ K}$ <sup>1</sup>, while the lattice constant increases anomalously by about 0.1%.<sup>2</sup> Apart from a tentative suggestion that this behaviour may be due to short-range magnetic ordering associated with localised structural ordering<sup>1</sup>, the microscopic origin of this phenomenon is not understood.

We have studied the Raman spectrum of Ni - I using the same single [100] growth sector B<sup>11</sup> enriched sample examined in reference 3. With 400 mW of 647.1 nm krypton laser light aligned

along the [001] crystal axis the Raman scattering along the [110] axis was analysed in all polarisations. The sample temperature was varied between 88 K and 295 K by use of a nitrogen vapour flow cryostat, and the scattered light dispersed by a Spex 1400 double monochromator (295 K) and a Coderg T800 triple monochromator (88 K - 210 K) with a spectral slit width of  $2.5\text{ cm}^{-1}$  in both cases.

The room temperature Raman spectra are presented in Figure 1. E and  $F_2$  symmetry modes are active in the  $Z(Y'X')Y'$  and  $\bar{Z}(Y'Z)Y'$  polarisations respectively, where  $X', Y', Z$  refer to the crystal [110], [110], [001] directions. Allowing that the  $F_2$  spectrum is relatively weak, the  $A_1$  spectrum is isolated by subtracting the  $Z(Y'X')Y'$  spectrum from the  $Z(X'X')Y'$  spectrum<sup>4</sup>. The results between 88 K and room temperature are con-

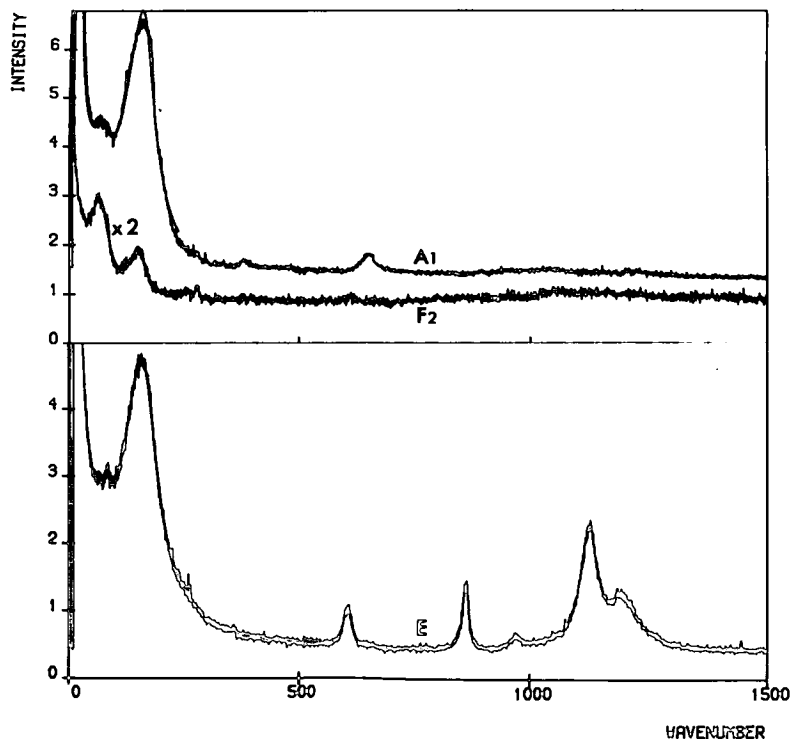


Figure 1. The room temperature Raman spectrum of Ni - I.

sistent with a cubic crystal space group throughout this temperature range, in agreement with X-ray results at 77 K and room temperature<sup>3,5</sup>, and are also consistent with a structure containing  $BO_4$  groups.<sup>4</sup> The low frequency  $F_2$  and  $A_1$  symmetry line profiles are characteristic of a cubic boracite<sup>6</sup> but the expected  $A_1$  wing is far less well-defined, and the low frequency  $A_1$  and E symmetry modes more heavily damped than their counterparts in the spectra of other boracites (e.g. Cu - Cl, Cr - Cl).

Part of the work concerning the temperature variation of the Raman spectra is illustrated in Figures 2 and 3. In Figure 2 the peak position of

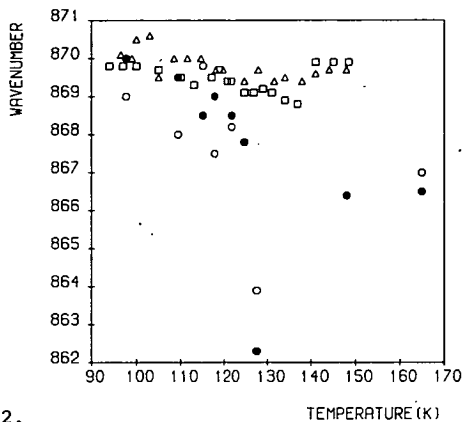


Figure 2. Temperature dependence of an E mode peak frequency.

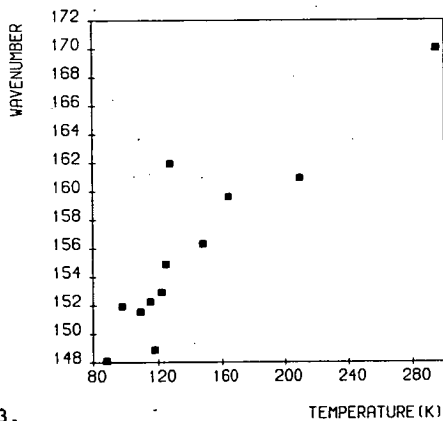


Figure 3. Temperature dependence of the broad E mode natural frequency.

one of the higher frequency E modes is plotted as a function of temperature, from experiments performed at different times and in different polarisations. The black circles represent  $Z(Y'X')Y'$  results and the open circles,  $Z(X'X')Y'$  spectra. The triangles and squares illustrate later experiments in  $Z(Y'X')Y'$  geometry, with temperature increasing and decreasing respectively. From these results it is clear that the natural frequency rises with decreasing temperature, dropping anomalously at about 128 K. This effect became less pronounced as the sample 'deteriorated' after several temperature cycles, but was characteristic of all the high frequency E modes. The linewidths of these bands show the opposite behaviour, decreasing with falling temperature and increasing at 128 K. In contrast, the broad  $170\text{ cm}^{-1}$  E mode frequency decreases with temperature, increasing anomalously at 128 K as shown in Figure 3. There is no corresponding linewidth anomaly for this mode in the given temperature range. The frequencies and linewidths for this feature are taken from a computerised least squares fitting of an anharmonically damped oscillator line-shape over the region  $30 - 240\text{ cm}^{-1}$ . Examples of fitted  $A_1$ , E and  $F_2$  spectra are shown in Figure 1. The broad  $A_1$  peak at  $166\text{ cm}^{-1}$  exhibits a similar, if less dramatic, temperature variation. No significant temperature variation can be attributed to the very weak  $F_2$  spectrum.

From these results it is apparent that there is some disturbance of the structure at around 128 K, but there is no spectroscopic evidence for either a structural transition, or long range antiferromagnetic ordering. These results are in accord with the suggestion of short range magnetic ordering giving rise to the susceptibility maximum. The softening of the heavily damped E mode is unlike the results in Cr - Cl and Cu - Cl, and suggests that the 64 K transition differs from the usual boracite behaviour. The low frequency modes are mostly related to vibrations involving motion of the nickel and iodine ions. Softening of these modes would therefore indicate a repositioning of one or more of these ions. Such displacements must, however, retain the overall cubic symmetry, as verified in reference 2. At all temperatures in our study of Ni - I, the Raman spectrum indicates that the system is cubic.

We acknowledge the support of the S.R.C. (A.F.M.) and U.S. Army Research and Development Group (Europe) (D.J.L.).

#### REFERENCES

- See the review by NELMES, R.J., J. Phys. C. **7**, 3840 (1974).
- WILL, G., and MORCHE, H., J. Phys. C. **10**, 1389 (1977).
- THORNLEY, F.R., KENNEDY, N.S.J., and NELMES, R.J., J. Phys. C. **9**, 681 (1976).
- MURRAY, A.F., and LOCKWOOD, D.J., J. Phys. C. **9**, 3691 (1976).
- NELMES, R.J., and THORNLEY, F.R., J. Phys. C. **9**, 665 (1976).
- LOCKWOOD, D.J., Ferroelectrics **13**, 353 (1976).

RAMAN-SCATTERING MEASUREMENTS OF THE EFFECT OF UNIAXIAL STRESS  
ON THE FERROELECTRIC TRANSITION IN  $Gd_2(MoO_4)_3$ \*

Q. Kim, F. G. Ullman, R. D. Kirby, and J. R. Hardy  
University of Nebraska, Lincoln, Nebraska 68588

The 50 and 75  $cm^{-1}$  lines of the  $A_1$  Raman spectrum of ferroelectric  $Gd_2(MoO_4)_3$  were found to vary identically with uniaxial stress up to 1.0 kbar in the temperature range  $(T - T_c) < 20C$ . The force constant parameter,  $\omega$ , of the 75  $cm^{-1}$  line was independent of stress while its damping constant  $\Gamma$  decreased by 50%, similar to the behavior of the 50  $cm^{-1}$  line reported previously. These results are offered as further confirmation of the identification of the 75  $cm^{-1}$  line as one of the two unstable modes of the ferroelectric phase.

The ferroelectric rare-earth molybdates, the first improper ferroelectrics<sup>1</sup> to be studied, undergo their ferroelectric transition at  $T_c = 160C$ . This cell-doubling transition is believed to originate from the softening of a doubly degenerate,  $T_1$ , zone boundary mode of the paraelectric phase<sup>2</sup>; below  $T_c$ , the degeneracy is removed and the two modes transform to  $A_1$  symmetry and move to the zone center.

Infrared<sup>3</sup> and Raman-scattering<sup>4,5</sup> studies of the low frequency  $A_1$  spectrum have isolated three modes that exhibit abnormal behavior with temperature. At 80K, they peak at 44.5, 51.5, and 83  $cm^{-1}$ . At 300K, the broadened 51.5  $cm^{-1}$  line obscures the 44.5  $cm^{-1}$  line, and the 83  $cm^{-1}$  line is broadened and its peak downshifted to 75  $cm^{-1}$  where it remains up to  $T_c$ ; above  $T_c$ , all three are absent from the  $A_1$  spectrum. In back-scattering, however, in the configuration  $z(xx)z$ , the symmetry changes from  $A_1$  below  $T_c$ , to  $B_2$  above. The 51.5  $cm^{-1}$  line does not vanish above  $T_c$  in this case and so has been identified as a zone-center mode<sup>5</sup> (the other two vanish and so must be zone boundary modes). There has been some recent controversy<sup>6,7</sup> over this assignment since the 44.5 and 51.5  $cm^{-1}$  modes had been suggested previously<sup>3</sup> to be the soft modes that degenerate into the soft zone boundary mode of the paraelectric phase.

Prior to the discovery of the abnormal behavior of the 83  $cm^{-1}$  line, measurements of the effect of uniaxial stress on the 51.5  $cm^{-1}$  line at temperatures near  $T_c$  showed a nearly constant  $\omega$  but a steep, non-linear decrease in  $\Gamma$  with increasing stress<sup>8</sup>.

In this paper, we describe uniaxial stress measurements on the  $A_1$  Raman spectrum in the temperature range  $(T - T_c) < 20C$ . Three lines, which for clarity are designated here as peaking at 50, 75, and 100  $cm^{-1}$ , were studied over a stress range of 0-1.0 kbar. The apparatus and other experimental details were as described previously<sup>8</sup>. Typical results are shown in Fig. 1. It can be seen that the 50 and 75  $cm^{-1}$  lines narrow and increase in peak height with increasing stress whereas the 100  $cm^{-1}$  line is essentially unchanged. The overlap of the 75 and 100  $cm^{-1}$

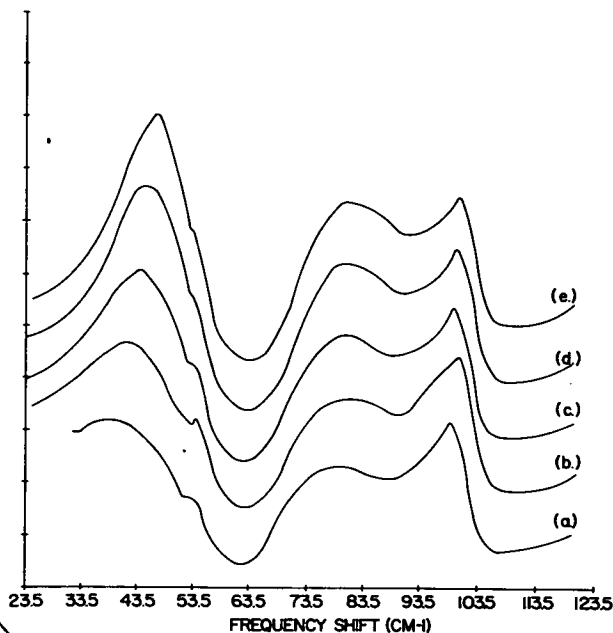


Fig. 1  $A_1$  Raman spectra for different applied stress.  $T \sim 140C$ , scattering configuration  $X(ZZ)Y$ , stress in  $X$  direction. Piston force: a) 0 lb, b) 50 lb, c) 100 lb, d) 150 lb, e) 200 lb. A constant background was subtracted from the original data.

lines, the difficulty in estimating the background, and the contributions from minor unresolved lines, permitted only a crude Lorentzian analysis of the 75 and 100  $cm^{-1}$  lines. For both lines,  $\omega$  was found to be independent of stress (varying by less than 2%) as found previously for the 50  $cm^{-1}$  line. On the other hand,  $\Gamma$  decreased by about 50% for the 75  $cm^{-1}$  line but stayed constant ( $\pm 20\%$ ) for the 100  $cm^{-1}$  line.

For a constant  $\omega$ , the Lorentzian line-width is proportional to its peak height, so we have examined peak height ratios as shown in Table I below.

\*Supported by the Army Research Office.